Plasma Physics Reports, Vol. 30, No. 5, 2004, pp. 353–362. Translated from Fizika Plazmy, Vol. 30, No. 5, 2004, pp. 387–397.

TOKAMAKS

Drift-Alfvén Turbulence in a Tokamak Wall Plasma

R. V. Shurygin

Russian Research Centre Kurchatov Institute, pl. Kurchatova 1, Moscow, 123182 Russia

Received July 7, 2003

Abstract—The behavior of turbulent fluxes in the vicinity of a resonant point $m/n = q(x_{res})$ in a plane wall plasma layer in a tokamak is studied by numerically analyzing the nonlinear MHD equations in a four-field electromagnetic model. Simulations show that, as the electron temperature at the plasma edge increases, the intensity of turbulent particle flux decreases, reaching its minimum value, and then increases. Such behavior is found to be due to the stabilizing effect of the electron drift velocity ($V_{y0} \sim dT_{e0}/dx$) in the equation for the longitudinal component of the magnetic potential. It is shown that, at a strong toroidal magnetic field, turbulent transport processes conform to the gyro-Bohm scaling, which gradually passes over to the Bohm scaling as the field decreases. © *2004 MAIK "Nauka/Interperiodica".*

1. INTRODUCTION

One of the challenging problems in controlled thermonuclear fusion research is that of obtaining reliable estimates for transport fluxes at the plasma edge in a tokamak. Besides being of general theoretical significance, this problem is important from the standpoint of overcoming technological and engineering difficulties that may arise in designing future facilities. One of the most powerful approaches in this way is to simulate turbulent plasma dynamics numerically. In recent years, many groups of theoreticians have succeeded in constructing numerical codes capable of adequately simulating complicated physical processes in a tokamak plasma. The first codes were based on solving the MHD equations in the electrostatic approximation, which is valid for $\beta \ll 1$ and in which the magnetic field fluctuations in the plasma are ignored. Although this approach makes it possible to obtain reliable estimates for the anomalous transport coefficients, it fails to describe such phenomena as L–H transitions, the formation of magnetic islands, coherent self-oscillations at the plasma edge, and so on. From an analysis of recent numerical results, it has become clear that, in order provide an adequate description of the behavior of a turbulent plasma, it is necessary to take into account magnetic fluctuations. Theory [1] shows that electromagnetic effects play an important role when the parameter $\beta_M = \beta(M_i/m_e)$, with $\beta = 4\pi NT/B^2$, is larger than unity. Thus, for parameters typical of a low-temperature wall plasma, $N = 4 \times 10^{13}$ cm^{-3}, $T = 150$ eV, and $B = 2$ T, we have $\beta_M = 1.107$, which indicates that the magnetic field fluctuations should be taken into consideration.

This paper presents the results of numerical simulations of the turbulent plasma dynamics in a plane wall layer in a tokamak. The simulations are based on solving the reduced nonlinear quasi-two-dimensional Braginskii equations with allowance for the electron dynamics in an electromagnetic field and with the longitudinal differentiation operator, which was modified nonlinearly to include the magnetic field fluctuations (the magnetic flatter effect). One of the goals of the present work is to investigate the dependence of turbulent fluxes on the temperature of the edge plasma. It is shown that, as the electron temperature at the plasma edge (the so-called "pedestal" temperature) increases, the intensity of the turbulent particle flux decreases until the plasma remains in the electrostatic regime and then, after the plasma has evolved into the electromagnetic regime, it begins to increase. Simultaneously, the turbulent heat flux increases monotonically as the edge temperature increases.

Numerical calculations of the dependence of the turbulent transport coefficients on the magnitude of the toroidal magnetic field show that, in the parameter range under consideration, the wall plasma turbulence at a strong toroidal magnetic field B_0 conforms to the gyro-Bohm scaling, which gradually passes over to the Bohm scaling as the field decreases. Also, the results of calculating the scalings of turbulence transport coefficients in terms of magnetic shear are presented, along with the results of investigations of the role of the zonal magnetic field B_{y0}. The computations were carried out with an electromagnetic version of the numerical code developed in [2].

2. BASIC EQUATIONS

Based on the reduced two-fluid Braginskii equations that have been derived recently by Zeiler *et al.* [3], we assume that $T_i \ll T_e$ and ignore both the longitudinal ion velocity ($u_\parallel = 0$) and thermal current to obtain the following set of nonlinear four-field $\{\phi, n, T_e, A\}$ MHD

1063-780X/04/3005-0353$26.00 © 2004 MAIK "Nauka/Interperiodica"

equations describing the behavior of a low-temperature plasma in a plane wall layer in a tokamak:

$$m\left\{\frac{\partial W}{\partial t} + \mathbf{V}_E \cdot \nabla W\right\} = \frac{B\nabla_\parallel J_\parallel}{c} - \frac{2}{R_0}\frac{\partial p_e}{\partial y} + mn\mu_\perp \Delta_\perp W, \quad (1)$$

$$\frac{\partial n}{\partial t} + \mathbf{V}_E \cdot \nabla n = \frac{\nabla_\parallel J_\parallel}{e} + \frac{2n}{R_0}\frac{c\partial\phi}{B\partial y} + D_\perp \Delta_\perp n, \quad (2)$$

$$\left(\frac{\partial T_e}{\partial t} + \mathbf{V}_E \cdot \nabla T_e\right) = \frac{T_e \nabla_\parallel J_\parallel}{en} + \frac{2T_e}{R_0}\frac{c\partial\phi}{B\partial y} + \chi_\perp \Delta_\perp T_t + \nabla_\parallel(\chi_\parallel \nabla_\parallel T_e), \quad (3)$$

$$\frac{1}{c}\frac{\partial A}{\partial t} = -\eta J_\parallel - \nabla_\parallel \phi + \frac{\nabla_\parallel p_e}{en}, \quad (4)$$

$$J_\parallel = -\frac{c}{4\pi}\Delta_\perp A, \quad W = \frac{c}{B}\nabla \cdot (n\nabla_\perp \phi). \quad (5)$$

In deriving Eqs. (1)–(5), we used the following representation of the tokamak magnetic field in a Cartesian coordinate system (x, y, z):

$$\mathbf{B} = \mathbf{B}_{\text{eq}} + \mathbf{b}_{\text{turb}}, \quad \mathbf{b}_{\text{turb}} = \nabla A \times \mathbf{e}_z,$$
$$\mathbf{B}_{\text{eq}} = B_0\left[\left(1 - \frac{x}{R_0}\right)\cdot \mathbf{e}_z + \frac{\varepsilon}{q(x)}\mathbf{e}_y\right], \quad (6)$$

where $\mathbf{B}_{\text{eq}}$ is the equilibrium tokamak magnetic field, q is the safety factor, $\varepsilon = r/R_0$, and r and R_0 are the minor and major radii of the torus. The rest of the notation in Eqs. (1)–(6) is as follows: $n(x, y, t)$ is the density; $T_e(x, y, t)$ is the temperature; $\phi(x, y, t)$ and $A(x, y, t)$ are the electrostatic and vector potentials, describing the oscillations of the electric and magnetic fields; $\mathbf{V}_E = \frac{c[\mathbf{B}\times\nabla\phi]}{B^2}$, $\Delta_\perp = \frac{\partial^2}{\partial x^2} + \frac{\partial^2}{\partial y^2}$, $\nabla_\parallel = \mathbf{b}\cdot\nabla$; and $\mu_\perp$, $D_\perp$, and $\chi_{\perp,\parallel}$ are the dissipation coefficients.

It is convenient to nondimensionalize Eqs. (1)–(5) by switching to the new variables

$$t \longrightarrow t/t_*, \quad (x, y) \longrightarrow (x/x_*, y/x_*), \quad \phi \longrightarrow e\phi/T_*,$$
$$n \longrightarrow n/n_*, \quad T \longrightarrow T_e/T_*, \quad A \longrightarrow A/A_*,$$
$$A_* = B_0 x_* \beta, \quad q_\parallel \longrightarrow q_\parallel/(n_* T_* V_*), \quad k_y \longrightarrow k_y x_*,$$

where $t_* = \frac{x_*^2}{\rho_S^2 \omega_{ci}}$, $\rho_S = \frac{V_*}{\omega_{ci}}$, $V_* = \sqrt{\frac{T_*}{m_i}}$, $\omega_{ci,e} = \frac{eB}{m_{i,e}c}$, $\eta = \frac{m_e \nu_{ei}}{e^2 n_0}$, ν_{ei} is the electron–ion collision frequency, and x_* is the width of the computation region. The normalizing density and normalizing electron temperature were taken to be $n_* = 10^{13}$ cm^{-3} and $T_* = 100$ eV. Singling out the zeroth harmonics in the expression for the convective term (see below), we convert Eqs. (1)–(5) into the form

$$\frac{DW}{Dt} = -\nabla_\parallel J - \frac{U_{y0}}{\rho}\frac{\partial W}{\partial y} + \rho(N_0 U_{y0})''\frac{\partial\phi}{\partial y} - g_B\frac{\partial p}{\partial y} + \mu_\perp \Delta_\perp W, \quad (7)$$

$$\frac{Dn}{Dt} = -\nabla_\parallel J - \frac{U_{y0}}{\rho}\frac{\partial n}{\partial y} + N_0'\frac{\partial\phi}{\partial y} + g_B N_0\frac{\partial\phi}{\partial y} + D_\perp \Delta_\perp n, \quad (8)$$

$$\frac{DT}{Dt} = -\frac{T_{e0}}{N_0}\nabla_\parallel J - \frac{U_{y0}}{\rho}\frac{\partial T}{\partial y} + T_{e0}'\frac{\partial\phi}{\partial y} + g_B T_{e0}\frac{\partial\phi}{\partial y} + \nabla_\parallel(\chi_\parallel \nabla_\parallel T) + \chi_\perp \Delta_\perp T, \quad (9)$$

$$\beta\frac{\partial A}{\partial t} = \eta_0 J - \nabla_\parallel \phi - \frac{\nabla_\parallel p}{N_0}, \quad (10)$$

$$J = \Delta_\perp A, \quad W = \rho^2 \nabla(N_0 \nabla\phi), \quad (11)$$

where

$$\frac{D}{Dt} = \frac{\partial}{\partial t} + \{\phi, \}, \quad \{A, B\} = \mathbf{e}_z \nabla A \times \nabla B,$$

$$\rho = \frac{\rho_S}{x_*}, \quad g_B = \frac{2x_*}{R_0}, \quad \beta = \frac{4\pi n_* T_*}{B^2}, \quad \eta_0 = \frac{\nu_{ei}}{\omega_{ce}},$$

$\chi_\parallel = \frac{3.16\omega_{ei}}{\nu_{ei}}$, and $p = T_{e0}n + N_0 T$. Note that the dimensionless poloidal ion velocity U_{0y} is related to the radial electric field by the relationship $U_{y0} = -\frac{cE_x}{B_0 V_*} = \rho\frac{\partial\phi_0}{\partial x}$ and that, by virtue of the assumption $T_i \ll T_e$, the ion pressure in calculations was ignored.

The numerical technique used in the code is a quasi-spectral approach based on the Galerkin method. All functions $f = \{n, \phi, T, A\}$ are chosen to be the sum of helical waves with the same helicity, $f(x, y, z, t) = \sum f_{ky,kz}(x, t)\exp[i(k_y y - k_z z)]$, where $k_z/k_y = \text{const}$. It is well known that this approach reduces the problem of solving three-dimensional equations to that of solving two-dimensional equations. We switch to the new helical variable $Y \longrightarrow y - \frac{k_z}{k_y}z$ and assume that the follow-

ing Fourier series is valid for each of the above functions f:

$$f(x, Y, t) = f_0(x, t) + \sum_{m=1}^{M} [f_{Sm}(x, t)\sin(mk_{y0}Y) + f_{Cm}(x, t)\cos(mk_{y0}Y)], \quad (12)$$

where $k_{y0} = m_0 x_*/a$, a is the tokamak minor radius, and m_0 is the minimum number of a Fourier harmonic.

Substituting Fourier series (12) into Eqs. (7)–(11), we obtain a set of equations for the poloidal harmonics $\{f_{Sm}, f_{Cm}\}$.

The equations for the zeroth harmonics $f_0 = \{N_0, U_{y0}, T_{e0}, A_0\}$ (which are usually referred to as background quantities) can easily be obtained by averaging Eqs. (7)–(11) over Y and by supplementing the right-hand sides of the resulting equations with the necessary dissipative and source terms:

$$\frac{\partial N_0}{\partial t} + \frac{\partial \Gamma}{\partial x} = D_0 \frac{\partial^2 N_0}{\partial x^2}, \quad (13)$$

$$\frac{\partial T_{e0}}{\partial t} + \frac{\partial (Q + q_\parallel)}{\partial x} = \chi_0 \frac{\partial^2 T_{e0}}{\partial x^2}, \quad (14)$$

$$\frac{\partial U_{y0}}{\partial t} + \frac{\partial \Pi}{\partial x} = \mu_0 \frac{\partial^2 U_{y0}}{\partial x^2} - \nu_{\mathrm{NEO}} U_{y0}, \quad (15)$$

$$\frac{\partial B_{y0}}{\partial t} - \frac{\partial^2 \Gamma_A}{\partial x^2} = \frac{\partial}{\partial x}\eta_0 \frac{\partial B_{y0}}{\partial x}. \quad (16)$$

The diffusion coefficient D_0 and thermal conductivity χ_0 were calculated from their neoclassical formulas in the plateau regime. The quantity ν_{neo} was calculated from the following formula, obtained by Su *et al.* [4]:

$$\nu_{\mathrm{neo}} = \frac{\nu_{ii}}{\varepsilon^{3/2}(1 + \nu_*)(1 + \varepsilon^{3/2}\nu_*)}, \quad \nu_* = \frac{qRV_{ti}}{\varepsilon^{3/2}\nu_{ii}}.$$

With allowance for the zeroth harmonics, the operator of differentiation in the longitudinal direction can be written as

$$\nabla_\parallel f = \nabla_{\parallel 0} f - \beta A_0' \frac{\partial f}{\partial y} + \beta f_0' \frac{\partial A}{\partial y} - \beta\{A, f\}. \quad (17)$$

Under the assumption that the waves are of the same helicity, we can use the expansion $k_z/k_y = \varepsilon/q(x_{\mathrm{res}})$ at the resonant point to obtain the following representation for $\nabla_{\parallel 0} f$ in a thin plane layer:

$$\nabla_{\parallel 0} f = \frac{\varepsilon}{q(x)}\frac{\partial f}{\partial y} + \frac{\partial f}{\partial z} \approx -\frac{x_*}{L_s}(x - x_{\mathrm{res}})\frac{\partial f}{\partial Y}, \quad L_s = \frac{qR_0}{s}, \quad s = \frac{rq'}{q}. \quad (18)$$

With allowance for the second term on the right-hand side of formula (17) for $\nabla_\parallel$, we obtain

$$\nabla_\parallel f = \gamma_\parallel \frac{\partial f}{\partial Y} + b_x f_0' - \beta\{A, f\}, \quad b_x = \beta\frac{\partial A}{\partial Y}, \quad (19)$$

where

$$\gamma_\parallel = -\frac{x_*}{L_s}(x - x_{\mathrm{res}}) + B_{y0}, \quad B_{y0} = -\beta A_0'. \quad (20)$$

Taking into account formula (19), we write Eq. (10) as

$$\beta\left[\frac{\partial A}{\partial t} + \frac{V_{y0}}{\rho}\frac{\partial A}{\partial Y} + \{\phi, A\} - \frac{1}{N_0}\{p, A\}\right] = \eta_0 J - \gamma_\parallel \frac{\partial}{\partial Y}(\phi - p/N_0), \quad (21)$$

$$V_{y0} = U_{y0} + V_{yDe}, \quad V_{yDe} = -\rho(\kappa_0 N_0' + T_{e0}'). \quad (21a)$$

Note that the velocity V_{y0} in the induction equation corresponds to the poloidal electron velocity and represents the sum of the poloidal ion velocity and the poloidal electron drift velocity. To convince ourselves of this, we merely need to calculate the diamagnetic current density j_y from the equilibrium equation $\mathbf{j} \times \mathbf{B} = c\nabla p_e$ (recall that $p_i = 0$). The calculations give

$$j_y = en(u_{iy} - u_{ey}) = \frac{c}{B_0}\frac{dp_e}{dx}.$$

Nondimensionalizing this equality in the above manner yields relationships (21a) with $V_{y0} = u_{ey}/V_*$, $U_{y0} = u_{iy}/V_*$, and $V_{yDe} = -\frac{\rho}{N_0}\frac{dp_{e0}}{dx}$, where $p_{e0} = N_0 T_{e0}$.

It can be seen that formula (20) contains not only the familiar term that is proportional to $\sim\Delta x/L_S$ and is responsible for the magnetic shear stabilization effect, but also the term that is associated with the magnetic field B_{y0} and accounts for the zeroth harmonic of the vector potential $A_0(x, t)$. It will be shown below that it is this term in formula (20) for $\gamma_\parallel$ that describes an increase in turbulent fluxes.

In Eqs. (13)–(16), the turbulent fluxes are described by the following expressions:

the particle flux is

$$\Gamma = \langle nV_x\rangle_Y + \langle b_x J\rangle_Y,$$

the heat flux is

$$Q = \langle TV_x\rangle_Y + \langle b_x J\rangle_Y,$$

the momentum flux is

$$\Pi = \rho\langle V_x V_Y\rangle_Y - \frac{1}{\beta\rho}\langle b_x b_Y\rangle_Y,$$

the longitudinal heat flux is

$$q_\parallel = -\chi_\parallel\left[\gamma_\parallel\langle b_x T_Y'\rangle_Y + \langle b_x^2\rangle_Y\frac{dT_{e0}}{dx} - \langle b_x\{A, T\}\rangle_Y\right],$$

and the flux of the longitudinal component of the vector potential is

$$\Gamma_A = \beta\left\langle A\frac{\partial}{\partial y}(p/N_0 - \phi)\right\rangle_Y.$$

Here, the angular brackets denote averaging over the periodic coordinate Y: $\langle f\rangle_Y = \frac{1}{L_Y}\int_0^{L_Y} f(Y)dY$, with $L_Y = 2\pi/k_{0y}$. Obviously, the contribution to the fluxes comes only from the harmonics $\{f_{Sm}, f_{Cm}\}$. Although the zeroth harmonics do not contribute to the fluxes, they nevertheless play an important role in the turbulent plasma dynamics because they act as driving sources for turbulence.

In order to analyze the relative effects of the processes described by different terms in the set of Eqs. (7)–(11) on the turbulent plasma dynamics, it is expedient to write the energy equation for this set. Because Eqs. (9) and (10) contain the parameter $T_{e0}/N_0 = \kappa_0(x, t)$, which depends on the coordinate and time, the energy conservation law cannot be written in a compact form. However, this can readily be done in the case $\kappa_0 = \text{const}$. Performing the required averaging procedures, we arrive at the following evolutionary equation for the energy density of fluctuations:

$$\frac{\partial W_{FL}}{\partial t} = S_N + S_T + S_U + S_J - S_\parallel - D_J - S_{\text{diss}}. \qquad (22)$$

Here, we have introduced the notation

$$W_{FL} = \frac{1}{2}\left\langle\left\langle \rho^2 N_0|\nabla\phi|^2 + \beta|\nabla A|^2 + \kappa_0 n^2 + \frac{T^2}{\kappa_0}\right\rangle\right\rangle,$$

$$S_N = -\left\langle\left\langle \frac{dN_0}{dx}\Gamma\right\rangle\right\rangle, \quad S_T = -\left\langle\left\langle \frac{dT_{e0}}{dx}Q\right\rangle\right\rangle,$$

$$S_U = -\left\langle\left\langle \frac{dU_0}{dx}\Pi\right\rangle\right\rangle, \quad S_J = -\left\langle\left\langle \left(\frac{dJ_0}{dx} + \frac{dJ_{00}}{dx}\right)\Gamma_A\right\rangle\right\rangle,$$

$$J_0 = \frac{dB_{y0}}{dx}, \quad D_J = \langle\langle \eta_0 J^2\rangle\rangle, \quad S_\parallel = \langle\langle \chi_\parallel(\nabla_\parallel T)^2\rangle\rangle,$$

$$\langle\langle \ldots\rangle\rangle = \int_0^1 dx\frac{1}{L_y}\int_0^{L_y}(\ldots)dY,$$

where $J_0(x, t)$ and $J_{00}(x)$ are the longitudinal current driven by fluctuations and the equilibrium longitudinal current, respectively, and S_{diss} is the sum of the dissipative terms that account for collisional processes associated with viscosity, diffusion, and heat conduction. The double angular brackets denote averaging over two coordinates.

Computations were carried out over the region $0 < x < 1$ for parameters close to those of the DIII-D tokamak: $R_0 = 170$ cm, $a = 67$ cm, $B_0 = 2$ T, $x_* = 4$ cm, $Z_{\text{eff}} = 1.6$, and $m_i = 2m_h$. The resonant point x_{res} was such that $q(x_{\text{res}}) = 4$ was at the center of the computation region, $x_{\text{res}} = 0.5$. The dimensionless wave vector $k_{y0} = m_0 x_*/a$ determined the minimum widths of the f_m harmonics along the Y coordinate. In calculations, the minimum harmonic number was $m_0 = 20$. The harmonic number was varied within the interval $1 < m < M$, and the maximum number of harmonics was varied within the interval $M = 13$-21. The boundary conditions were chosen to be

$$\phi(0) = w(0) = n(0) = T(0) = A(0) = 0,$$
$$\phi(1) = w(1) = n(1) = T(1) = A(1) = 0$$

for $m \neq 0$ and

$$T_{e0}(0) = T_b, \quad N_0(0) = N_b, \quad U_{y0}(0) = 0, \quad B_{y0}(0) = 0,$$
$$T_{e0}(1) = T_s, \quad N_0(1) = N_s, \quad U_{y0}(1) = 0, \quad B_{y0}(1) = 0$$

for $m = 0$.

The main goal of the simulations was to investigate the dependence of the parameters of turbulent processes on the so-called pedestal temperature T_b. The remaining parameters in the boundary conditions were set to be $N_b = 2$–3, $N_s = 0.6$, and $T_s = 0.2T_b$. In the equations for the harmonics, the dissipation coefficients were chosen to be equally small, $D_\perp = \chi_\perp = \mu_\perp = 0.002$.

Numerical simulations were carried out based on a simple two-level predictor–corrector scheme:

$$\frac{X_i^{n+1/2} - X_i^n}{\tau/2} = \hat{L}(X_{i-1}^{n+1/2}, X_i^{n+1/2}, X_{i+1}^{n+1/2}) + N(X_i^n),$$

$$\frac{X_i^{n+1} - X_i^n}{\tau} = \hat{L}(X_{i-1}^{n+1}, X_i^{n+1}, X_{i+1}^{n+1}) + N(X_i^{n+1/2}),$$

where $\hat{L}$ and $\hat{N}$ are the linear and nonlinear operators in Eqs. (7)–(10). At each time step, the difference equations were solved by the sweep method.

According to the Fourier series method used in this paper, the set of equations describing the drift-Alfvén (DA) turbulence can be regarded as being composed of the two subsets of equations that describe two interacting subsystems of turbulent modes. The first subsystem is represented by the small-scale harmonics $f_m(x, t)$, which determine the dependence on the poloidal coordinate Y, and the second subsystem is represented by the evolving large-scale harmonics $f_0(x, t) = \{N_0, T_{e0}, U_{y0}, B_{y0}\}$, which are independent of Y. As follows from Eqs. (13)–(16), these large-scale harmonics are generated by the gradients of the corresponding turbulent fluxes, which are expressed in terms of the nonlinear sums over small-scale harmonics. In turn, the harmonics f_0 influence the generation of the small-scale harmonics f_m. Calculations show that, in the range of actual tokamak parameters, the equations describing the dynamic system in question have no solutions in a traditional sense ($\partial/\partial t = 0$). In such a system, all the quantities are oscillating; moreover, the oscillations are irregular and chaotic. As a result of the interaction of

the above two subsystems of turbulent modes, the dynamic system evolves into a self-consistent regime with incoherent self-oscillations; this regime is such that, during the evolution of the oscillating and background quantities, the turbulence becomes self-sustaining.

That a mechanism for generating self-sustaining turbulence does indeed exist is readily seen from Eq. (22), which describes the evolution of the fluctuation energy. Over the width of the computation region, the time-averaged turbulent fluxes of heat and particles remain positive, $\Gamma > 0$ and $Q > 0$, whereas the time-averaged density and temperature gradients are negative, $dN_0/dx < 0$ and $dT_{e0}/dx < 0$. In this case, the source terms are positive, $S_N > 0$ and $S_T > 0$, which indicates that the fluctuations are generated by turbulent fluxes; i.e., we can speak of the existence of a plasma state with self-sustaining turbulence. The source term S_J, containing the current density gradient, plays a role analogous to that of the terms S_N and S_T. However, for the plasma edge, this source term is so small that, in calculations, it had little influence on the final results. The physical meaning of the source term S_U is that it accounts for the work done by the turbulent force (turbulent Reynolds stress) on the turbulent flux. Since the quantities dU_0/dx and Π are not of fixed sign, the sign of the term S_U can generally be arbitrary. The quantity $D_J > 0$ corresponds to the power of the Joule dissipation of the longitudinal turbulent current.

3. NUMERICAL RESULTS

First, we consider the effect of the temperature T_{e0} on turbulent transport at different values of the pedestal temperature $T_b = T(x = 0)$. The pedestal temperature T_b and pedestal density N_b are among the most important parameters of the tokamak wall plasma because it is known from experiments that, depending on the values of these two parameters, the plasma can be confined in essentially different modes.

Figure 1 shows the dependence of the time-averaged transverse turbulent fluxes of particles and heat, $\{\langle\Gamma\rangle\}$ and $\{\langle Q\rangle\}$, on the pedestal temperature T_b. Here, the braces and angular brackets indicate averaging over the computation time t and over the transverse coordinate x of the plane layer:

$$\{\langle A\rangle\} = \frac{1}{T}\int_0^T dt\int_0^1 A(x,t)dx,$$

$$\{A(x)\} = \frac{1}{T}\int_0^T A(x,t)dt, \quad \langle A(t)\rangle = \int_0^1 A(x,t)dx.$$

According to Fig. 1, the dependence of the turbulent particle flux $\{\langle\Gamma\rangle\}$ on the temperature T_b has the shape of a well, while the turbulent heat flux increases with pedestal temperature. This behavior of the fluxes is

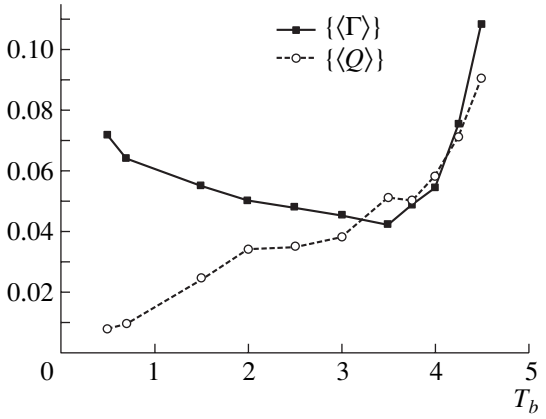

Fig. 1. Dependence of the particle and heat turbulent fluxes on the pedestal temperature T_b.

caused by two factors: the dependence of the terms $\nabla_\parallel J$ in Eqs. (7)–(9) on temperature and the presence of the term proportional to $\sim V_{y0}(x, t)$ in the induction equation. The contribution of the terms with the current J can be estimated by considering the temperature dependence of the Joule dissipation power D_J in Eq. (22) for the fluctuation energy density W_{FL}. Keeping only the leading-order terms in this equation, we rewrite it as

$$\frac{\partial W_{FL}}{\partial t} \approx S_N + S_T - D_J - S_\parallel. \tag{23}$$

For negative gradients of the density and temperature, the first two terms describe the generation of fluctuations and the last two terms describe their suppression. We first consider the electrostatic regime ($T_b < 3$, $\beta_M < 1$). Omitting the terms proportional to $\sim\beta$ in Eq. (20), we arrive at the following expression for the current J:

$$J \approx \frac{1}{\eta_0}\gamma_\parallel \partial(\phi - p/N_0)/\partial Y. \tag{24}$$

With Eq. (23), the expression for D_J becomes

$$D_J = \left\langle \frac{1}{\eta_0}\left|\gamma_\parallel \partial(\phi - p/N_0)/\partial Y\right|^2 \right\rangle. \tag{25}$$

Since $\eta_0 \propto T_{e0}^{-3/2}$, it is clear that the Joule dissipation power D_J increases with the pedestal temperature T_b, which leads to a decrease in the fluctuation energy and, accordingly, in turbulent fluxes. Figure 2 shows how the averaged fluctuation amplitudes $\{\langle A\rangle\}$, $\{\langle\phi\rangle\}$, $\{\langle n\rangle\}$, and $\{\langle T\rangle\}$ depend on the pedestal temperature T_b. We can see that the amplitude of the density fluctuations decreases, while the temperature fluctuations increases. A decrease in $\{\langle n\rangle\}$ with temperature stems from an increase in the term $\nabla_\parallel J$ (because of the increase in $\{\langle A\rangle\}$) in Eq. (8) for the density. On the other hand, despite the presence of an analogous term in Eq. (9) for the temperature, the amplitude $\{\langle T\rangle\}$ of the temperature fluctuations increases. This behavior of the temperature

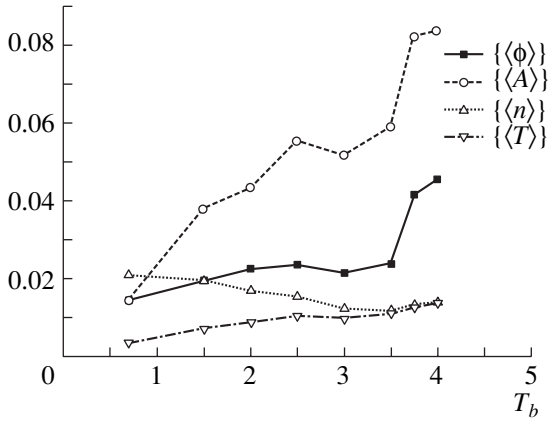

Fig. 2. Dependence of the averaged amplitudes $\{\langle\phi\rangle\}$, $\{\langle A\rangle\}$, $\{\langle n\rangle\}$, and $\{\langle T\rangle\}$ on the pedestal temperature T_b.

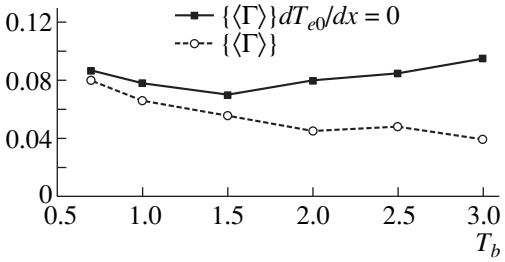

Fig. 3. Dependence of the particle turbulent flux on the pedestal temperature T_b at $dT_{e0}/dx = 0$.

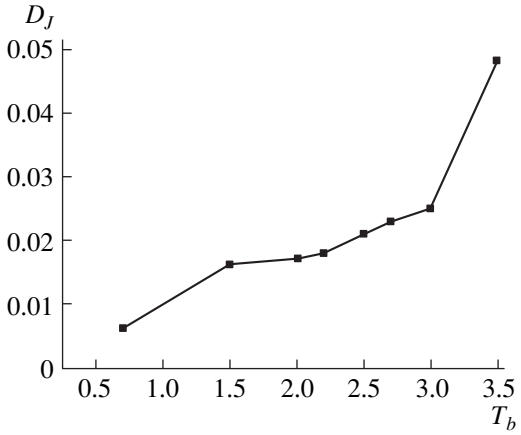

Fig. 4. Dependence of the Joule dissipation power D_J on the pedestal temperature T_b.

fluctuations is attributed to the presence of the term $T'_{e0}\partial\phi/\partial y$ in Eq. (9): an increase in this term increases the amplitude $\{\langle T\rangle\}$. Hence, a decrease in $\{\langle n\rangle\}$ reduces the turbulent particle flux, while an increase in $\{\langle T\rangle\}$ causes the turbulent heat flux to become higher.

In order to consider the electromagnetic regime ($T_b > 3$, $\beta_M > 1$), we must systematically take into account magnetic fluctuations and calculate the fluctuation-driven current from Ampére's law $J = \Delta_\perp A$. An analysis of the results of the corresponding computations shows that, in this case, a new effect that is associated with the poloidal electron velocity $V_{y0}(x, t) = U_{y0} + V_{yDe}$ in the induction equation comes into play. It is known from linear theory [5, 6] that the electron drift velocity suppresses the tearing instability. Nonlinear calculations are also capable of capturing this effect. As a result, the electron drift velocity V_{yDe} also increases with temperature, thereby stabilizing the turbulence; decreasing the fluctuation amplitudes; and, accordingly, reducing the turbulent particle flux. For $T > 3.5$, the destabilizing effect of magnetic field line curvature, which is described by the term proportional to $\sim g_B$, predominates over the above stabilizing effect of the electron drift velocity V_{yDe}, so that the development of a linear instability enhances the turbulent flux.

Figure 3 shows the dependence of the turbulent particle flux on the pedestal temperature for the following two cases:

(i) the term dT_{e0}/dx in the expression $V_{yDe} = -\rho(\kappa_0 N'_0 + T'_{e0})$ for the electron drift velocity [see formulas (21a)] is taken into account in a conventional manner (curve *1*) and

(ii) this term in the expression for V_{yDe} is ignored, $dT_{e0}/dx = 0$ (curve *2*).

We can see that, in the second case, in which the temperature gradient is zero (the velocity V_{yDe} is low), the particular flux $\langle\Gamma\rangle$ is far more intense than in the first case. This result confirms the conclusion about the stabilizing effect of the electron drift velocity.

The effect of the term in question on the amplitude of the magnetic fluctuations is analogous to that of the poloidal sheared velocity $U_{y0}(x, t)$, which is accounted for by the term $U_{y0}\partial W/\partial y$ in Eq. (7). As is well known [7–9], the poloidal sheared velocity acts to break the convective cells into smaller cells, thus eventually reducing the turbulent flux. Analogously, the temperature gradient, described by the term T'_{e0} in the expression $V_{y0} = U_{y0} - \rho(\kappa_0 N'_0 + T'_{e0})$ for the poloidal electron velocity [see the term $V_{y0}\partial A/\partial y$ in Eq. (21)], initiates the breaking of the tearing-mode magnetic islands into smaller islands and, as a consequence, increases the current $J = A''_{xx} + A''_{yy}$. As was explained above, the result of this increase in J is a decrease in the turbulent particle flux $\langle\Gamma\rangle$.

Note that the current J increases in such a way that the Joule dissipation power $D_J = \langle\eta_0 J^2\rangle$ also increases with T_b. According to Eq. (22), this increase leads to a decrease in the fluctuation energy density. However, it can be seen from Fig. 4 that, in the range $1.5 < T_b < 2.2$,

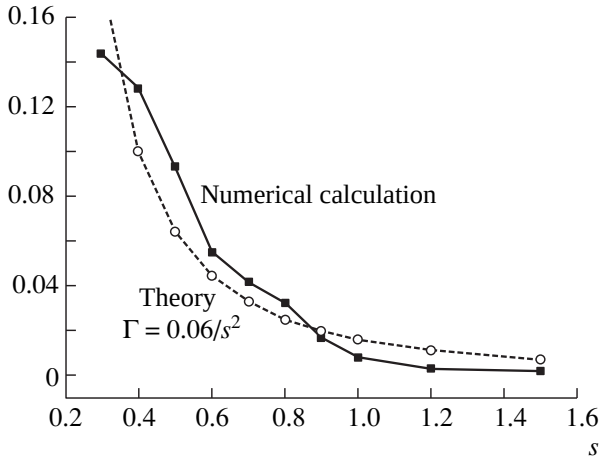

Fig. 5. Dependence of the particle turbulent flux on the magnetic field shear *s*.

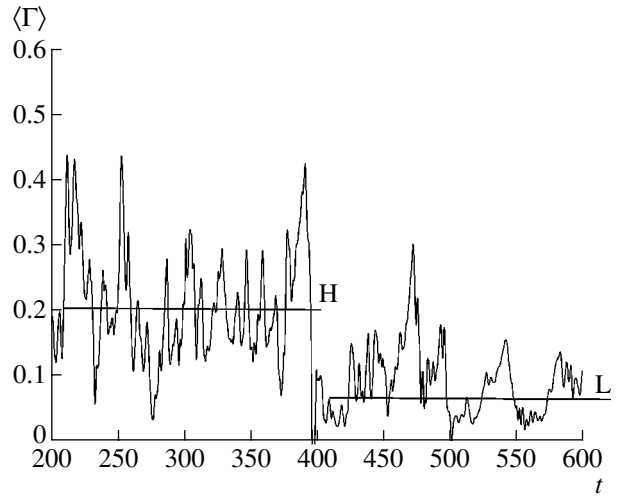

Fig. 6. L–H transition during a jumplike change in magnetic shear.

D_J increases more slowly because, in this range, the resistance decreases according to the law $\eta_0 \propto T_{e0}^{-3/2}$, which results in a more gradual decrease in the turbulent particle flux $\langle\Gamma\rangle$ in the electromagnetic regime.

It is well known that, in the linear approximation, the DA modes are stabilized by the magnetic field shear [5, 6]. Let us consider the numerical results that illustrate the effect of the shear on the nonlinear transport processes. The solid curve in Fig. 5 shows the turbulent particle flux $\{\langle\Gamma\rangle\}$ calculated as a function of the magnetic shear parameter *s*. The dotted curve is the analytic approximation $\{\langle\Gamma\rangle\} \approx 0.016/s^2$, indicating that the particle flux decreases in inverse proportion to the squared shear *s*. A theoretical estimate confirming this dependence is easy to obtain. To do this, we consider the electrostatic regime with $\beta \ll 1$ and assume for simplicity that $T \ll n$. In this case, Eq. (10) yields the following formula for the longitudinal current *J*:

$$J \approx \frac{\gamma_\parallel}{\eta_0}\left(\frac{\partial\phi}{\partial Y} - \frac{T_{e0}}{N_0}\frac{\partial n}{\partial Y}\right). \quad (26)$$

Omitting the nonlinear term $\{\phi, W\}$ in Eq. (7), we reduce this equation to the quasi-steady equation

$$-\nabla_\parallel J - g_B T_{e0}\frac{\partial n}{\partial Y} \approx 0.$$

With formula (26), this equation gives the following expression for V_x:

$$V_x = -\rho\frac{\partial\phi}{\partial Y} = \rho\left(\frac{\eta_0 g_B T_{e0}}{\gamma_\parallel^2}n - \frac{T_{e0}}{N_0}\frac{\partial n}{\partial Y}\right).$$

We average the product nV_x over *Y* to arrive at

$$\langle nV_x\rangle = \frac{\rho\eta_0 g_B T_{e0}}{\gamma_\parallel^2}\langle n^2\rangle. \quad (27)$$

We thus have derived approximate formula (26) for the turbulent particle flux. With allowance for formula (20), which gives $\gamma_\parallel \sim s$, formula (26) yields the dependence $\Gamma \sim 1/s^2$. This strong dependence on *s* shows that a change in the current profile can trigger the L–H transition. Figure 6 illustrates the possibility of such a transition when the shear increases instantaneously from $s = 0.5$ to 0.75 at $t = 400$.

Note that the shear term $\Delta x/L_S$ enters into the expression for the function $\gamma_\parallel(x, t)$, which also contains the zonal magnetic field B_{y0}. It is clear that the changes in the function $\gamma_\parallel(x, t)$ at the expense of the magnetic field B_{y0} and of the magnetic shear *s* should have an equally strong impact on turbulent fluxes.

In order to check this conclusion, a series of numerical simulations was carried out in which the quantity $S_A = \partial^2\Gamma_A/\partial x^2$ in Eq. (16) was multiplied by a certain coefficient, α_B. Since the quantity S_A describes a source that generates the field B_{y0} (the turbulent dynamo effect), the values $\alpha_B > 1$ should increase B_{y0}. Figures 7 and 8 show how the quantities $\{B_{y0}(x)\}$ and $\{\gamma_\parallel(x)\}$ depend on the *x* coordinate for $\alpha_B = 0.2$, 1, and 2. We can see that the magnetic field B_{y0} at $\alpha_B = 2$ is stronger than that at $\alpha_B = 0.2$. The profile $B_{y0}(x)$ is such that the quantity $\gamma_\parallel$ decreases; this indicates that the stabilizing shear term is canceled by the field term B_{y0}. Calculations show that the value of the zonal magnetic field is too small to substantially change $\gamma_\parallel$. As a result, a small decrease in $\gamma_\parallel$ leads to a slight increase in the turbulent fluxes of particles and heat: $\{\langle\Gamma\rangle\}$ $(\alpha_B = 0.2) = 0.75$, $\{\langle\Gamma\rangle\}$ $(\alpha_B = 1) = 0.9$, and $\{\langle\Gamma\rangle\}$ $(\alpha_B = 2) = 0.12$.

Note, however, that the field B_{y0} can in principle be changed significantly at the expense of the external steady-state poloidal field. We can therefore conceive of a situation in which the field B_{y0} precisely cancels the shear term $\Delta x/L_S$. In this case, the magnetic shear loses

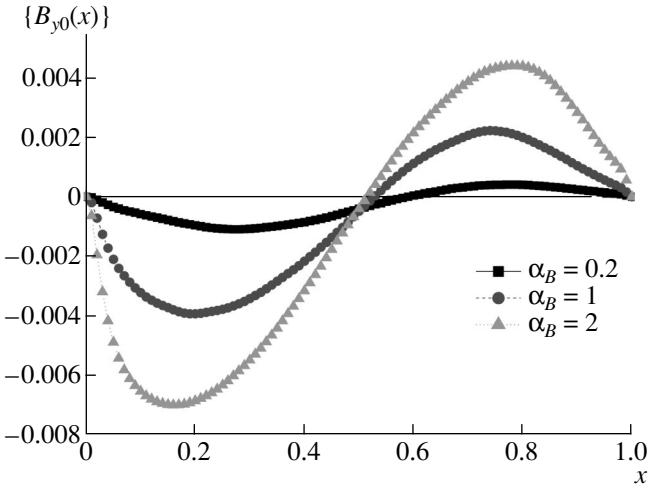

Fig. 7. Coordinate dependence of the averaged magnetic field $\{B_{y0}(x)\}$ for different values of the parameter α_B: 0.2, 1, and 2.

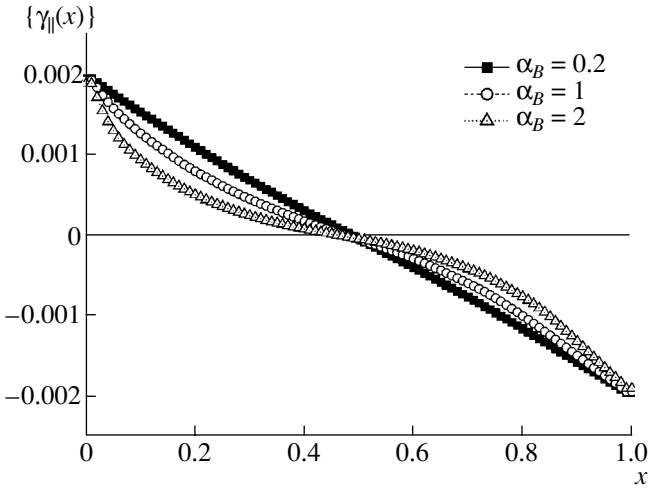

Fig. 8. Coordinate dependence of the averaged quantity $\{\gamma_{\|}(x)\}$ for different values of the parameter α_B: 0.2, 1, and 2.

its stabilizing effect and the turbulence becomes much stronger. Another possible (at least theoretically) situation is that in which $|B_{y0}| \gg |\Delta x/L_s|$. In this case, the role of the stabilizing term in the expression for $\gamma_{\|}$ is played by the field B_{y0} (rather than by the magnetic shear term) and turbulence is suppressed. An example of the numerical calculations of such external influence under the conditions of DA wall plasma turbulence was presented in my earlier paper [10], in which the field B_{y0} was changed by changing the boundary condition $B_{y0}(x = 1) = b_{\text{ext}}$ at the plasma surface. Hence, numerical simulations show that, under actual conditions, the large-scale poloidal magnetic field generated in a tokamak wall plasma is too weak to have any appreciable effect on turbulence. However, it should be kept in mind that, if the zonal magnetic field B_{y0} is subject to an external influence, then, depending on the extent of this influence, turbulent fluxes can be either markedly enhanced or markedly reduced.

One more scaling that was investigated numerically is the dependence of turbulent fluxes on the toroidal magnetic field B_0. In the case under consideration, the dimensionless turbulent particle flux $\Gamma = \langle nV_x \rangle$ is related to the dimensional physical flux Γ_{ph} by the expression $\Gamma = \Gamma_{ph}/\Gamma_B$. Here, the Bohm flux is given by the formula

$$\Gamma_B = (n_*/x_*)D_B, \quad D_B = cT_*/eB_0 = \rho_S V_*.$$

The problem of investigating the dependence of the turbulent transport coefficients on the magnetic field usually reduces to that of searching for the dependence $\Gamma = f(\rho)$, where $\rho = \rho_S/x_*$. Then, if f = const, turbulent diffusion conforms to the Bohm scaling (in terms of the normalized fluxes); i.e., $\Gamma_{ph} \sim \Gamma_B \sim 1/B_0$. If $f = \text{const}\,\rho$, we are dealing with a plasma in the gyro-Bohm regime, in which case the fluxes scale as $\Gamma_{ph} \sim \rho\Gamma_B \sim 1/B_0^2$. In actuality, the dependence $f(\rho)$ is more complicated because it incorporates transitions from one regime to another. Recently, Ottaviani and Manfredi [11] carried out MHD simulations of a turbulent tokamak plasma with ion-temperature-gradient driven instability. They showed that, over a wide parameter range, transport processes conform to the gyro-Bohm scaling; this is in contrast to linear theory, which predicts the Bohm scaling.

In the present paper, a study is also made of a fully developed plasma turbulence far from the instability threshold. Figure 9 shows the dependence of the turbulent fluxes of particles and heat on the parameter $\rho \sim 1/B$ for two values of the pedestal temperature: T_B = 1 and T_B = 3. We see that, at large values of B_0 (i.e., at

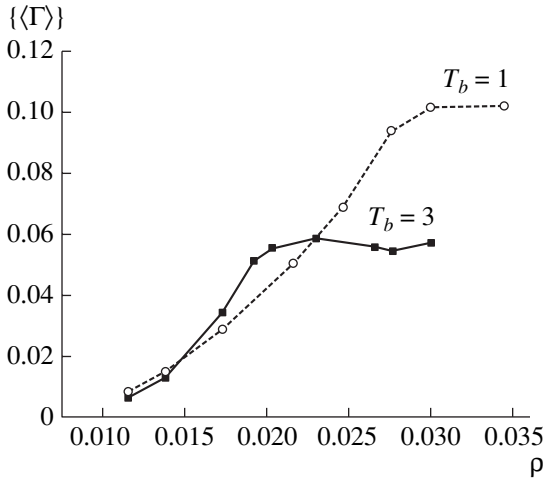

Fig. 9. Dependence of the turbulent particle flux on the parameter ρ for two values of the pedestal temperature: T_b = 1 and 3.

small ρ values), the turbulent fluxes increase almost linearly, which indicates that the plasma is in the gyro-Bohm regime. At small values of the toroidal magnetic field (i.e., at large ρ values), the turbulent fluxes are independent of ρ, which indicates a transition to the Bohm regime. Figure 10 presents contours of constant electrostatic potential, $\phi(x, y) = \text{const}$, for $T_B = 1$ and for two values of the toroidal magnetic field: $B_0 = 1$ and 3 T. We can be seen that, at small values of B_0 (in the Bohm regime), turbulent plasma is characteristically dominated by large-size convective cells stretched in the X direction. Such structures with $k_x \ll 1$ are customarily called streamers. It is known that the presence of these structures in the edge plasma enhances turbulent transport. On the other hand, at large values of B_0 (in the gyro-Bohm regime), the convective cells are smaller in size and are stretched in the Y direction.

Calculations show that an increase in the field B_0 leads to an increase in the zonal flow velocity U_{y0}. In this case, the vortices break into smaller vortices by the known mechanism [6, 7] associated with the shear of the velocity U_{y0}. Figure 11 depicts the correlation function $C(\Delta)$ calculated from the formula

$$C(\Delta) = \left\{\int_0^1 \phi_{s1}(x, t)\phi_{s1}(x + \Delta, t)dx\right\} / \left\{\int_0^1 \phi_{s1}^2(x, t)dx\right\},$$

for two magnitudes of the toroidal magnetic field. We see that, as the field increases from $B_0 = 1$ T to $B_0 = 3$ T, the correlation function becomes narrower and the correlation length decreases from $\Delta_0(1) = 0.32$ to $\Delta_0(3) = 0.26$. These numerical results agree with the results obtained by Ottaviani and Manfredi [11], who showed that, in the regime of fully developed plasma turbulence, the behavior of the nonlinear eigenfunctions differs greatly from that of the linear eigenfunctions. In this case, an increase in B_0 (a decrease in ρ) gives rise to a fairly intense poloidal zonal flow, which stimulates the vortices to break into smaller vortices and shortens the mean correlation length of a convective cell. As a result, turbulent transport decreases.

It follows from Fig. 9 that, as the pedestal temperature increases from $T_b = 1$ to $T_b = 3$, and as the parameter ρ increases, the transition to the Bohm regime of turbulence occurs at larger values of the field B_0. In other words, as B_0 decreases (i.e., as ρ increases), the transition to the Bohm regime occurs first at a higher pedestal temperature, $T_b = 3$ (when $B_0 \approx 1.75$ T and $\rho \approx 0.02$). At a lower pedestal temperature, $T_b = 1$, and at the above B_0 values, the plasma still remains in the gyro-Bohm regime. The transition to the Bohm regime occurs when the field B_0 has decreased to about $B_0 \approx 1.3$ T ($\rho \approx 0.027$). Hence, it is clear that, at low pedestal temperatures, the sheared flow velocity U_{y0}, which governs transitions from one regime to another, has a greater stabilizing effect than it does at high pedestal temperatures. Moreover, simulations show that, although the poloidal velocity U_{y0} at a higher plasma temperature ($T_b = 3$) somewhat exceeds that at a lower temperature ($T_b = 1$), the stabilization in the latter case is nevertheless more efficient. In order to explain such a property of transitions from one regime to another, we recall [12]

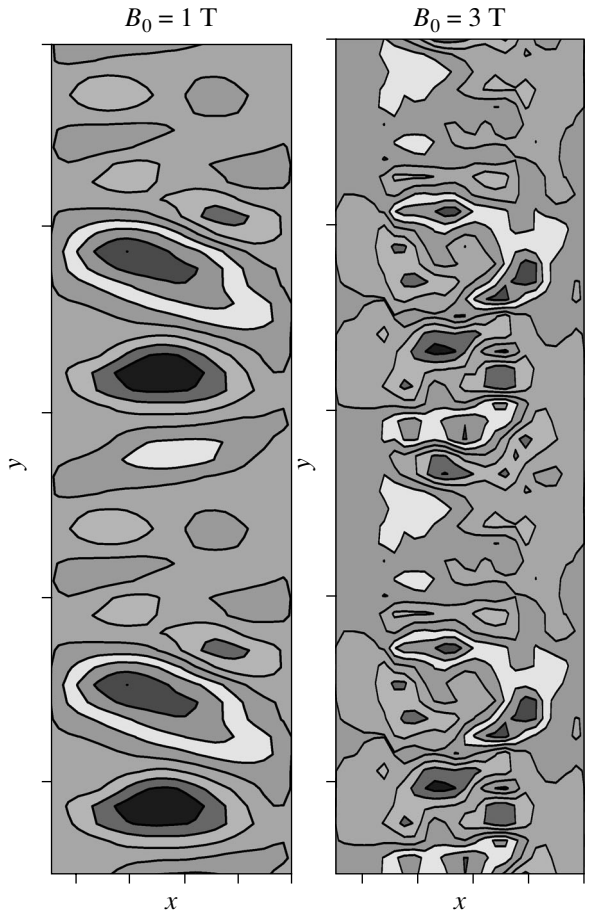

Fig. 10. Contours of constant potential $\phi(x, y)$ for two values of the toroidal magnetic field: $B_0 = 1$ and 3 T.

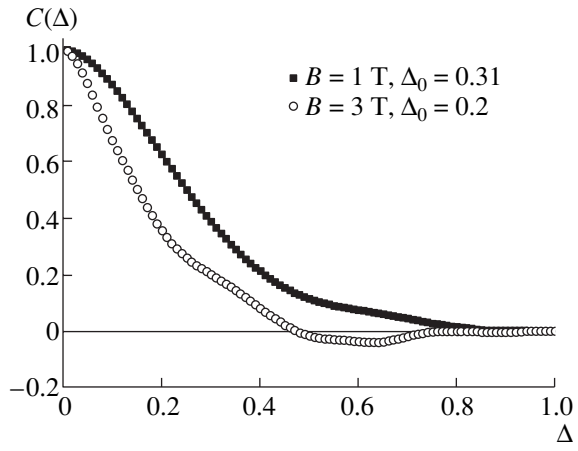

Fig. 11. Correlation function $C(\Delta)$ for two values of the toroidal magnetic field: $B_0 = 1$ and 3 T.

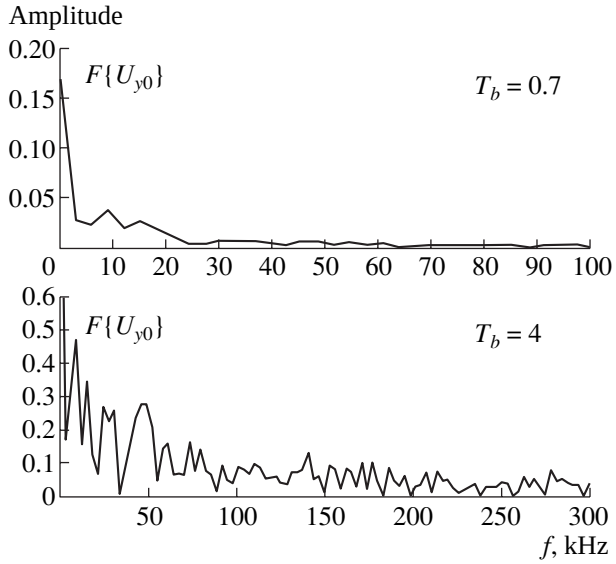

Fig. 12. Time Fourier spectra of the velocity U_{y0} for two values of the pedestal temperature: $T_b = 0.7$ and 4.0.

that, along with the flow velocity $U_{y0}(x, t)$, an important parameter determining the stabilizing effect of the sheared flow is also the rate of change of the flow velocity. Physically, it is clear that, if the rate of change of the sheared flow velocity is higher than the rotation rate of a vortex cell, then the effect of breaking the cells into smaller cells is far less pronounced. Figure 12 shows the frequency Fourier spectra $F\{U_{y0}(x, t)\}$ of the velocity $U_{y0}(x_0, t)$ at $x_0 = 0.5$ for two different pedestal temperatures, $T_b = 0.7$ and 4.0. It can be seen that, at the higher temperature, the mean rate of oscillations of the velocity U_{y0} exceeds that at the lower temperature. Hence, we arrive at the following qualitative conclusion: the reduction in the efficiency of stabilization by a sheared flow is presumably associated with the fact that the rate of oscillations in the flow velocity increases with plasma temperature. To obtain the quantitative characteristics of this phenomenon requires more detailed computations; this, however, goes beyond the scope of the present paper.

4. CONCLUSIONS

Numerical simulations of the nonlinear turbulent plasma dynamics in a wall layer in a tokamak have been carried out using an electromagnetic MHD model based on the reduced four-field $\{\phi, A, n, T_e\}$ Braginskii equations with cold ions ($T_i \ll T_e$). The behavior of turbulent fluxes in the vicinity of a resonant point such that $m/n = q(x_{\text{res}})$ has been investigated in the plane layer approximation. The simulations show that, as the electron temperature at the plasma edge increases, the intensity of turbulent particle flux decreases, reaching its minimum value, and then increases. Such behavior is found to be due to the stabilizing effect of the poloidal electron drift velocity ($V_{yDe} \sim dT_{e0}/dx$) in the equation for the longitudinal component of the magnetic potential. It is shown that, at a strong toroidal magnetic field B_0, turbulent transport processes conform to the gyro-Bohm scaling, which gradually passes over to the Bohm scaling as the field decreases. In the Bohm regime, turbulent plasma convection is dominated by vortices stretched in the radial direction ($k_x \ll 1$). During the transition to the gyro-Bohm regime, the velocity of the zonal flow (the poloidal velocity U_{y0}) increases; as a result, the vortex cells break into smaller cells, their correlation length decreases, and turbulent transport is reduced. As the plasma temperature in the wall layer increases, the frequency of oscillations in the sheared velocity becomes higher, so that the sheared velocity progressively loses its stabilizing effect on turbulent fluctuations. As a consequence, the transition to the Bohm regime occurs at a stronger toroidal magnetic field.

It follows from the results of numerical modeling that, in the range of plasma parameters under analysis, the intensity of turbulent fluxes decreases abruptly as the magnetic field shear increases. The simulations show that the strength of the large-scale (zonal) magnetic field B_{y0} is insignificant, so that this field does not substantially affect turbulent transport processes.

ACKNOWLEDGMENTS

This work was supported in part by the Federal Program for State Support of Leading Scientific Schools (project no. NSh-2024.2003.2) and the Department of Atomic Science and Technology of the Ministry of Atomic Industry of the Russian Federation.

REFERENCES

1. B. D. Scott, Plasma Phys. Controlled Fusion **39**, 1635 (1997).
2. R. V. Shurygin, Fiz. Plazmy **27**, 19 (2001) [Plasma Phys. Rep. **27**, 18 (2001)].
3. A. Zeiler, J. F. Drake, and B. Rogers, Phys. Plasmas **4**, 2134 (1997).
4. X. N. Su, P. N. Yushmanov, J. Q. Dong, and W. Horton, Phys. Plasmas **1**, 1905 (1994).
5. B. D. Scott, J. F. Drake, and A. B. Hassam, Phys. Rev. Lett. **54**, 1027 (1985).
6. T. M. Antonsen, Phys. Rev. Lett. **41**, 33 (1978).
7. H. Biglari, P. H. Diamond, and P. W. Terry, Phys. Fluids B **2**, 1 (1990).
8. Y. Z. Zhang and S. M. Mahajian, Phys. Fluids **4**, 1385 (1992).
9. S. J. Camargo, D. Biskamp, and B. D. Scott, Phys. Plasmas **2**, 48 (1995).
10. R. V. Shurygin, in *Proceedings of the 29th EPS Conference on Plasma Physics and Controlled Fusion, Montreux, 2002*, p. 1.108.
11. M. Ottaviani and G. Manfredi, Phys. Plasmas **6**, 3267 (1999).
12. P. W. Terry, Rev. Mod. Phys. **72**, 109 (2000).

Translated by I.A. Kalabalyk

Plasma Physics Reports, Vol. 30, No. 5, 2004, pp. 363–369. Translated from Fizika Plazmy, Vol. 30, No. 5, 2004, pp. 398–405.

TOKAMAKS

Peripheral Fluctuations and Particle Transport during an L–H Transition in the FT-2 Tokamak

S. V. Shatalin*, E. O. Vekshina*, P. R. Goncharov*, L. A. Esipov, and S. I. Lashkul****

**St. Petersburg State Technical University, Politekhnicheskaya ul. 29, St. Petersburg, 195251 Russia*

***Ioffe Physicotechnical Institute, Russian Academy of Sciences, Politekhnicheskaya ul. 26, St. Petersburg, 194021 Russia*

Received April 22, 2003; in final form, September 15, 2003

Abstract—Experimental data on the processes in edge plasma that accompany the transition to an improved confinement regime during lower hybrid heating in the FT-2 tokamak are presented. The poloidal and radial distributions of the plasma parameters and drift particle fluxes were measured with the use of mobile mulitielectrode Langmuir probes and were found to be substantially nonuniform in the poloidal direction. The evolution of the plasma parameters in the course of heating and during an L–H transition is investigated. It is shown that, in FT-2 experiments, the drift of plasma particles in a slowly varying (quasi-steady) electric field and the fluctuation-induced particle fluxes make comparable contributions to the radial particle transport, whereas the contribution of fluctuations to poloidal plasma fluxes is negligibly small. The effective coefficient of radial diffusion is determined. The measurement results show that the L–H transition is accompanied by a substantial decrease in this coefficient. © *2004 MAIK "Nauka/Interperiodica".*

1. INTRODUCTION

The edge plasma in magnetic confinement systems is characterized by complicated physical processes that are closely related to the confinement parameters in the plasma core and can play a decisive role under certain experimental conditions. The scrape-off layer (SOL)—the plasma region lying outside the last closed flux surface (LCFS)—presents some problem for the diagnostics and interpretation of experimental data. Unlike the plasma core, where the plasma parameters can be assumed to depend on the radius of the magnetic-flux surface only (as is usually assumed in modeling and diagnostics), the SOL plasma is two-dimensional in the poloidal cross section. The full mapping of this region is a rather difficult task, one which is usually almost impossible to accomplish in large devices. At the same time, the poor understanding of the processes occurring in SOL plasma is a serious obstacle on the way to controlled fusion [1]. In this context, the plasma of small tokamaks, which is a more flexible and quite easily diagnosed subject, can provide useful experimental information.

In this paper, the main results are presented of a long-term experimental study of the particle transport in the edge plasma and its evolution during the transition to an improved confinement regime (L–H transition). The data were obtained from probe measurements in the FT-2 tokamak with a major radius of R = 55 cm and a radius of the poloidal limiter of a = 7.9 cm. L–H transitions were observed in experiments on additional on-axis lower hybrid heating (LHH) under conditions of the efficient absorption of the electromagnetic wave energy (f = 920 MHz, $P \le 120$ kW) in the resonance region. The LHH pulse with a duration of Δt_{LHH} = 5 ms was switched on during the steady-state phase of the discharge at the following values of the main experimental parameters: the toroidal magnetic field was B_{tor} = 22 kG, the plasma current was I_{pl} = 22 kA, and the duration of the steady-state phase was Δt_{pl} = 40 ms. During LHH, we observed substantial variations in the profiles of the plasma density (n) and the electron and ion temperatures (T_e, T_i), an increase in the plasma energy (W), and a decrease in the emission intensity of neutral hydrogen (H_β). An analysis of the experimental data allowed us to conclude that an external transport barrier had formed by the end of the LHH pulse. The values of T_e and n and the energy confinement time τ_{pl}, which increased during the LHH phase by a factor of 2 to 3, retained in the post-heating phase of the discharge. This fact, along with a decrease in the intensity of the H_β line, testifies to an L–H transition [2–4].

As an illustration of a typical change in the discharge parameters during LHH, Fig. 1 shows the evolution of the loop voltage, the average plasma density, the intensity of the H_β line, and the plasma energy. The vertical dashed lines indicate the beginning and end of the radio-frequency (RF) LHH pulse. The displacement of the flux surface with a radius of 13 cm (where the Mirnov coils were located) along the major radius R is also shown. We note that the change in the equilibrium state (ΔR) is caused not only by the change in the plasma energy W, but also by the control fields that hold the plasma column at the axis of the vacuum vessel. The displacement ΔR reflects the general features of the W

1063-780X/04/3005-0363$26.00 © 2004 MAIK "Nauka/Interperiodica"

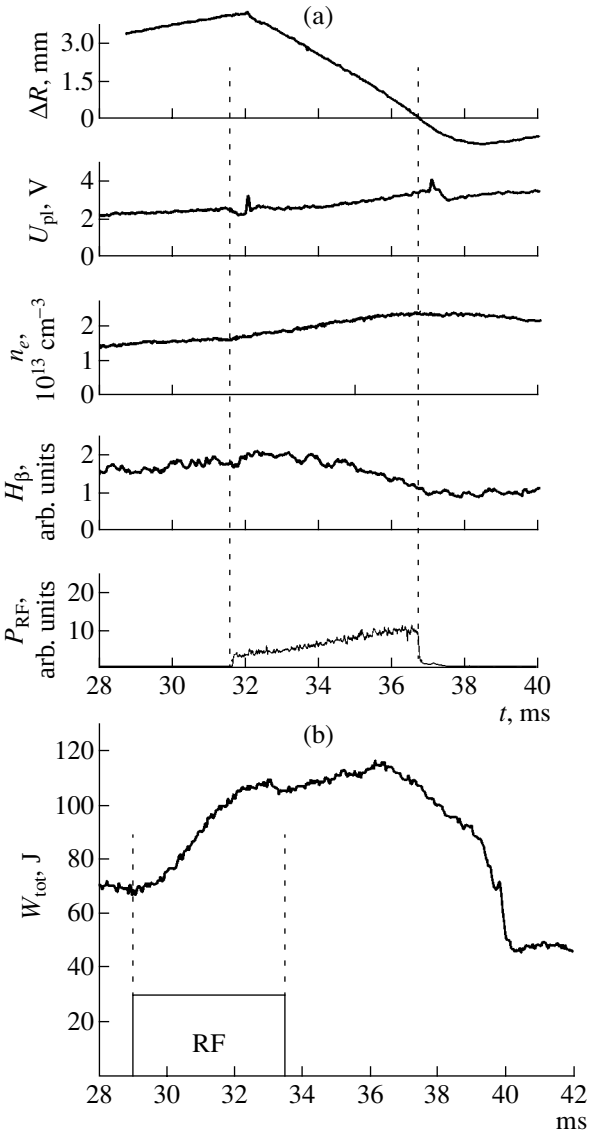

Fig. 1. (a) Typical waveforms of the discharge parameters: ΔR is the shift of the center of a magnetic flux surface with a radius of $r = 13$ cm (where the Mirnov coils were located), U_{pl} is the loop voltage, n_e is the average charged particle density, H_β is the intensity of the H_β line, P_{RF} is the power of the RF pulse. (b) A typical waveform of a diamagnetic signal (plasma energy) during additional heating [4] (the RF pulse starts at 29 ms).

variations related to the rapid increase in the plasma energy during auxiliary heating and to the subsequent action of the control fields.

2. SCHEME OF THE EXPERIMENT

The processes in the SOL that accompany the L–H transition were studied using three mobile multielectrode probes that were arranged along the poloidal direction in the same cross section of the chamber and provided information about the peripheral region of the plasma (Fig. 2). This diagnostics allowed us to study the evolution of the local values of the plasma potential and the electron density and temperature, as well as the two-dimensional (in the poloidal section) particle flux caused by the drift in the crossed poloidal electric field **E** and toroidal magnetic field **B** [5–7]. This flux can be represented as a sum of a quasi-steady and a fluctuating component. The density of the quasi-steady flux is given by the expression

$$\mathbf{\Gamma}_0(t) = cn_0(t)[\mathbf{E}_0(t) \times \mathbf{B}]/B^2. \quad (1)$$

The fluctuation-induced flux is caused by the correlation of the particle density fluctuations $n^{\sim}$ and the electric field $\mathbf{E}^{\sim}$,

$$\mathbf{\Gamma}^{\sim}(t) = c[\langle n^{\sim}(t)\mathbf{E}^{\sim}(t)\rangle \times \mathbf{B}]/B^2. \quad (2)$$

Here, the angle brackets stand for time averaging. To determine the density of quasi-steady flux (1), we used slowly varying (smooth) components of the probe signals. The processing of these signals allowed us to determine the time dependence of the local values of T_e, n, and $\mathbf{E}_0$ [5]. Fluctuating component (2) could be found using either analog or digital processing of the signals. In the former case, we used the analog multiplication of the fluctuating component (in the frequency band of up to 500 kHz) of the ion saturation current at the probe by a fluctuating component of the potential difference between two floating electrodes, after which the results were averaged. The floating electrodes were located symmetrically on both sides of the point at which the ion current was measured. This procedure allowed us to determine two orthogonal components of flux (2), assuming that T_e fluctuations are small. In the case of digital processing, the signals were recorded at a sampling rate of 1 MHz.

The probe measurements were performed with a step of 20°–30° in the poloidal direction and a step of 1 mm along the minor radius, which allowed us to measure the time evolution of the poloidal and radial distributions of the plasma parameters and particle fluxes in the SOL. When measuring these distributions, the poloidal angle Θ was counted from the equatorial plane on the low-field side of the plasma column in the direction of the electron diamagnetic drift (upward in the poloidal cross section, as is shown in Fig. 2). The design features of the tokamak did not allow us to perform probe measurements near the equatorial plane on the high-field side of the plasma column (at poloidal angles of $\Theta = 160°$–$190°$). As was mentioned above, the plasma column in the heating phase shifted outward along the major radius of the tokamak (Fig. 1). The position of the LCFS in this case was determined by the point at which the plasma contacted the high-field side of the poloidal limiter in the preheating (ohmic heating) phase, while in the post-heating phase (H-mode), it was determined by the point at which the plasma contacted the low-field side of the poloidal limiter. Thus, probe measurements could not be performed over the entire region overlapped by the moving LCFS. In the poloidal

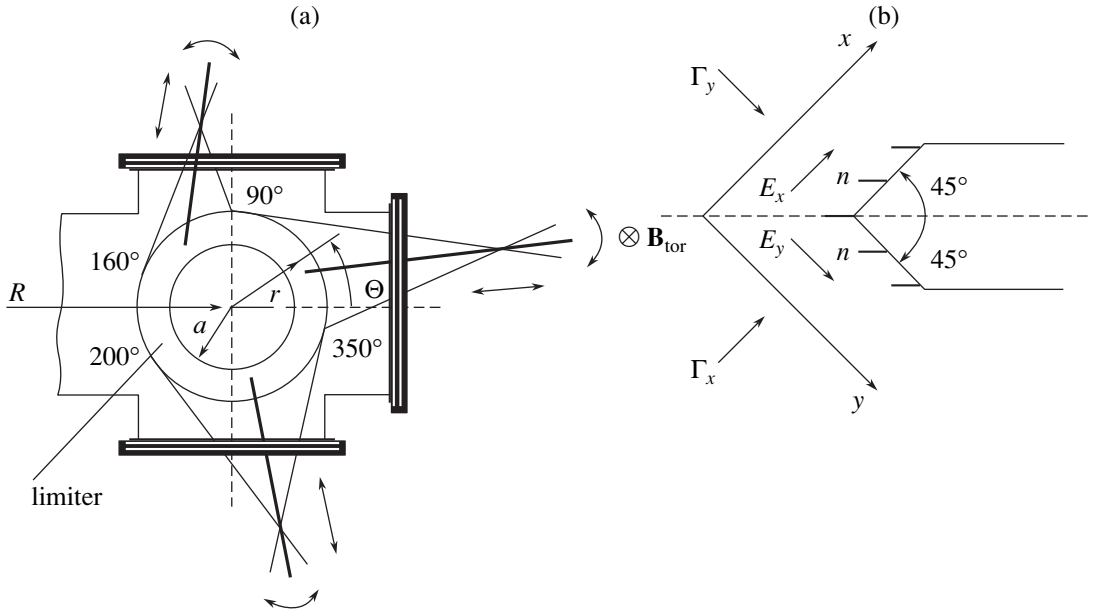

Fig. 2. (a) Arrangement of three mobile five-electrode probes in the poloidal cross section of the chamber and (b) a schematic of the measuring head of the probe. The central and two side electrodes are intended to measure the floating potential. The electrodes labeled with *n* were connected as a single or double probe and were used to measure the plasma density and temperature.

cross section, this region was a superposition of all the instantaneous positions of a circle of radius $r < a$, which moved from the high-field to the low-field side of the limiter. In the course of measurements, a mobile probe was displaced from shot to shot along the minor radius toward the axis of the plasma column until an appreciable influence on the discharge parameters (an increase in the particle density measured by an interferometer, a change in the equilibrium state, or partial disruptions) was detected. This influence was interpreted as the fact that the probe reached the boundary of the region overlapped by the LCFS (or, probably, a magnetic surface close to the LCFS) in the course of its motion along the major radius. The positions of such "boundary" points corresponding to the minimal values of the minor radius at which the measurements could be performed fit well with the horizontal motion of a circle with a radius of 70–71 mm and with the center located somewhat below (~4 mm) the geometrical center of the poloidal cross section of the chamber. Obviously, this diagnostics of the LCFS position is rather rough; however, the hypothesis of the motion of a circle with a radius of ~70 mm does not contradict the data of the interferometric and magnetic measurements. We note that this evolution of the plasma column substantially complicates the interpretation of experimental data.

3. EXPERIMENTAL RESULTS

The poloidal and radial distributions of the plasma parameters in the SOL were found to be highly inhomogeneous in the poloidal direction. The LHH and the subsequent L–H transition were accompanied by an appreciable redistribution of the plasma parameters.

3.1. Charged Particle Density

In the ohmic heating (OH) phase of the discharge, the charged particle density was maximum at poloidal angles of $\Theta = 100°–150°$ and was about (6–8) ×

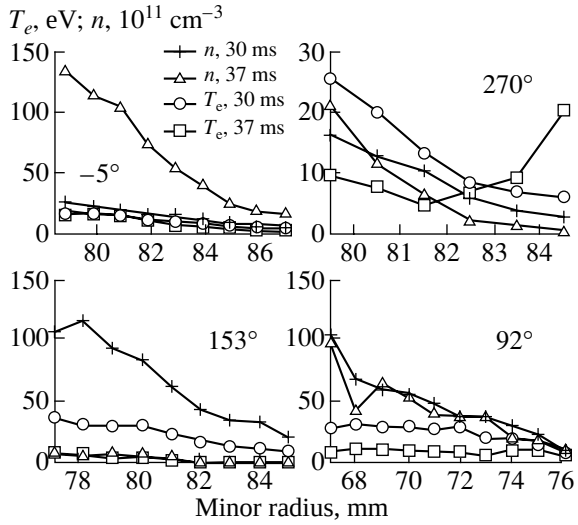

Fig. 3. Radial profiles of the density and temperature in the SOL for four values of the poloidal angle Θ that correspond to the maxima of the local density in the OH phase (t = 30 ms, $\Theta = 153°$) and in the *H*-mode (t = 37 ms, $\Theta = -5°$) and to the regions outside the local maxima (92° and 270°).

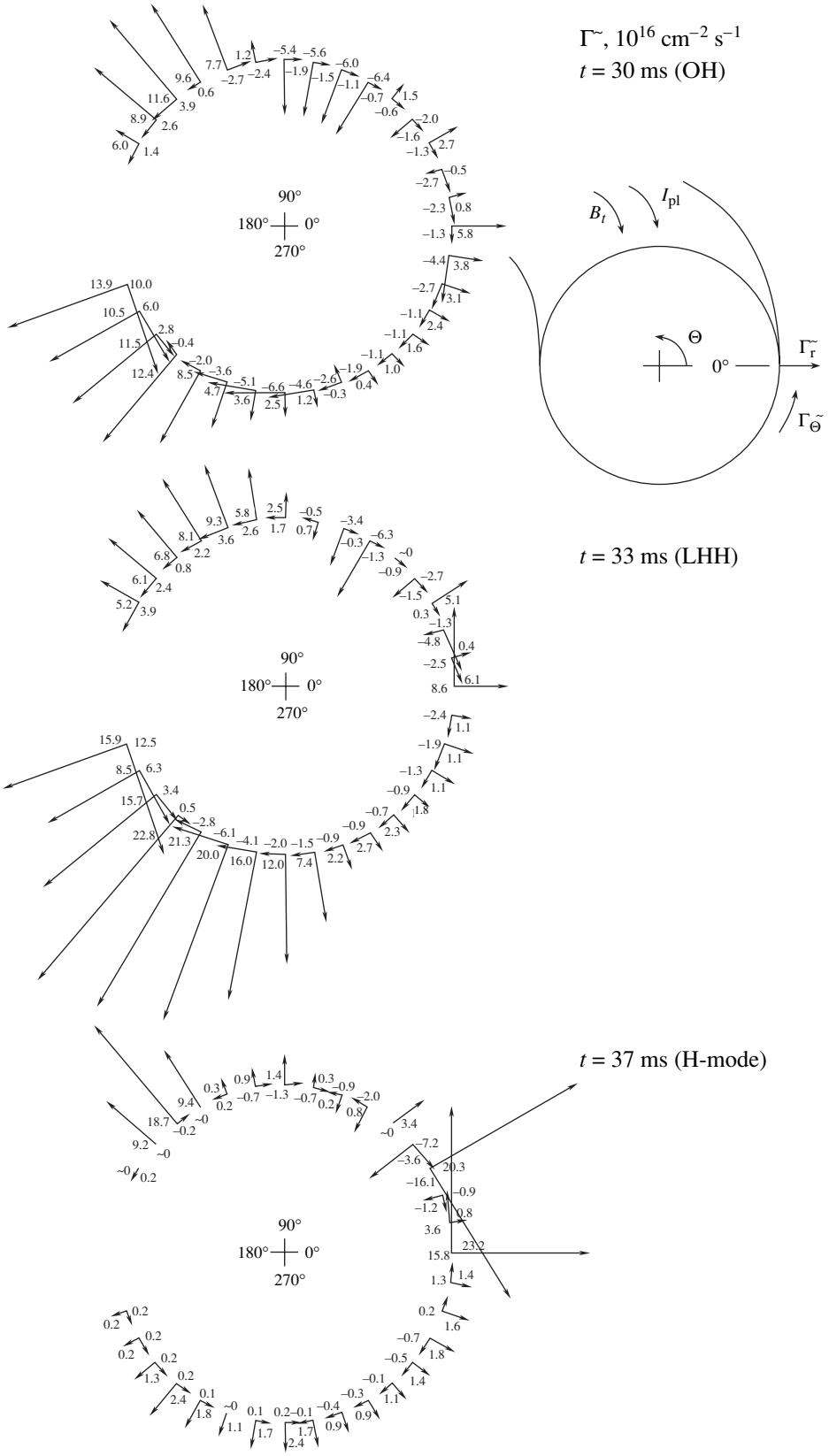

Fig. 4. Diagram of fluctuation-induced particle fluxes, illustrating the poloidal distribution of the two orthogonal components of the particle-flux density $\tilde{\Gamma}_r$ and $\tilde{\Gamma}_\Theta$ at the boundary points.

10^{12} cm^{-3} at the boundary points, while the central plasma density was $\approx 4 \times 10^{13}$ cm^{-3}. The second region with an increased density of (2–4) $\times 10^{12}$ cm^{-3} was observed at $\Theta = 200°$–$240°$. Taking into account that measurements in the region $\Theta = 160°$–$190°$ were not performed, we can conclude that, in the OH phase, the particle density was higher on the high-field side. During LHH, the particle density on the low-field side increased substantially, and, by the end of the RF pulse, the density became maximum there. Thus, at $\Theta = 0°$, the value of n at the boundary point increased from $\approx 3 \times 10^{12}$ cm^{-3} to $\approx 1.3 \times 10^{13}$ cm^{-3}, and this value was retained for several milliseconds after the end of an RF pulse. The central density in this case also increased (to $\approx 5 \times 10^{13}$ cm^{-3}). The particle density at the boundary points lying outside the local maxima was (1–3) $\times 10^{12}$ cm^{-3} and varied insignificantly in the course of LHH and during an L–H transition. At the same time, the radial gradient of n increased substantially at almost all values of Θ. Figure 3 shows the change in the radial density profiles in the SOL for four values of Θ corresponding to four characteristic regions: a local maximum in the OH phase (153°), a local maximum in the H-mode (–5°), and regions outside local maxima (92° and 270°). Different radial ranges in these plots are explained by the motion of the LCFS, as was discussed above.

3.2. Electron Temperature

The poloidal and radial distributions of T_e also varied substantially in the course of LHH and during an L–H transition. In general, these variations can be described as follows. In the OH phase, the maximum values of the electron temperature (up to 40 eV at the boundary points) were observed at angles of $\Theta = 90°$–$150°$ and 220°–250°, where the density was maximum. A less pronounced peak ($T_e^{\max} \approx 20$ eV) was observed on the low-field side ($\Theta \sim 0°$). During LHH, the temperature distribution became more flattened in the poloidal direction, whereas the value of T_e, on average, increased; 3 ms after the beginning of the heating pulse, the average value of T_e increased from ≈10 eV in the OH phase to ≈20 eV. All three of the above regions of local maxima with nearly the same values of $T_e^{\max} \approx$ 40 eV retained in this phase. In the post-heating phase (H-mode), the distribution of T_e was strongly inhomogeneous with a pronounced maximum on the low-field side ($T_e^{\max} \approx 20$ eV). The value of T_e decreased, on average, to 8–10 eV. We note that the cooling of the edge plasma was accompanied by an increase in T_e in the plasma core by a factor of 1.5–2 [2–4]. The evolution of the radial profiles of the electron temperature for four values of the poloidal angle is shown in Fig. 3. We also note that the radial profile of T_e at $t = 37$ ms and $\Theta = 270°$ is nonmonotonic with a minimum at $r =$ 81.5 mm. Similar distributions of T_e were also observed in other SOL regions, which indicates that the plasma parameters in the SOL are governed not only by radial heat fluxes, but also by other factors (e.g., poloidal particle fluxes).

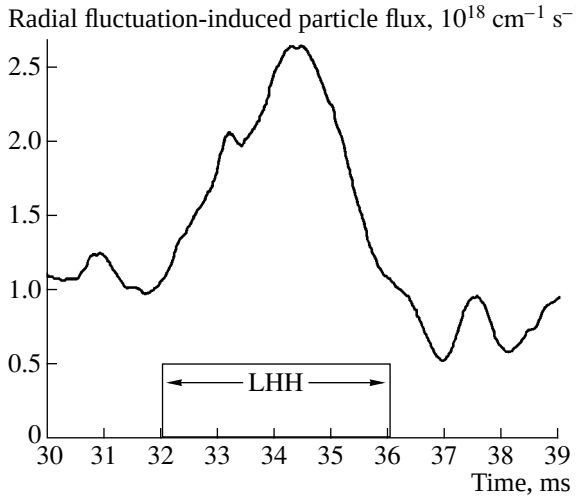

Fig. 5. Time evolution of the fluctuation-induced particle flux per unit length of the contour passing through the boundary points. The LHH pulse lasts from 32 to 36 ms.

3.3. Fluctuation-Induced Particle Fluxes

The results of measurements of fluctuation-induced particle fluxes are presented in Fig. 4 in the form of diagrams illustrating the poloidal distribution of two orthogonal components of the particle-flux density $\tilde{\Gamma}_r$ and $\tilde{\Gamma}_\Theta$ at the boundary points. When constructing these diagrams, the step in Θ was chosen to be 10°. At the angles at which measurements were not performed, the flux density was calculated as the mean of two values measured at the neighboring angles Θ. The diagrams correspond to three instants: 30, 33, and 37 ms, corresponding to the OH phase, LHH, and H-mode, respectively.

It can be seen from Fig. 4 that, in the OH phase, the region with an enhanced fluctuation-induced radial transport is located on the high-field side. The radial particle flux in this region increases substantially during the first half of the RF pulse (33 ms). Note that the fluxes are negative (directed to the center of the plasma column) in the region $\Theta = 60°$–$90°$. These fluxes also vary substantially during LHH. We also note that such flux behavior at nearly the same values of Θ was observed in the previous FT-2 experiments on studying the OH regime [6]. In the post-heating phase (*H*-mode), the average radial fluctuation-induced flux decreased; however, some local regions with enhanced transport were retained in this case too (at $\Theta = 0°$, 30°, and 120°–140°).

The results obtained allow us to calculate the radial fluctuation-induced particle flux through the entire

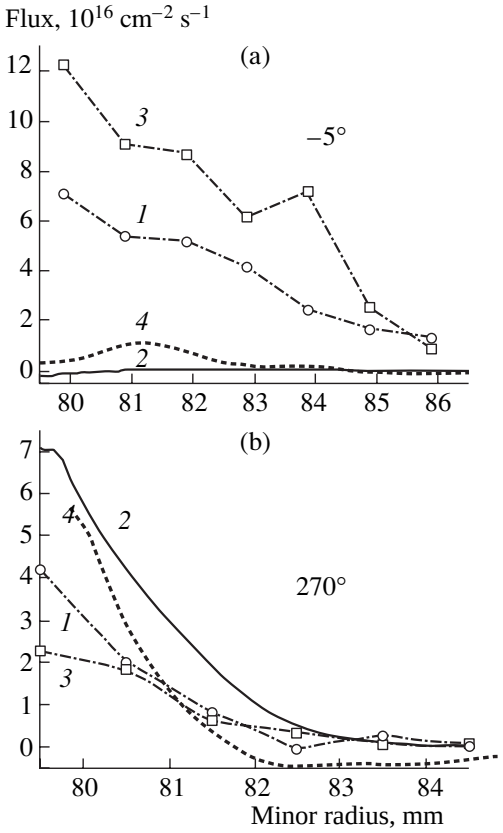

Fig. 6. Comparison of the radial profiles of the radial quasi-steady flux Γ_{0r} and the radial component of the fluctuation-induced flux $\Gamma_r^{\sim}$ for two values of the poloidal angle Θ = –5° and 270°: (*1*) fluctuation-induced flux, 30 ms; (*2*) quasi-steady flux, 30 ms; (*3*) fluctuation-induced flux, 37 ms; and (*4*) quasi-steady flux, 37 ms.

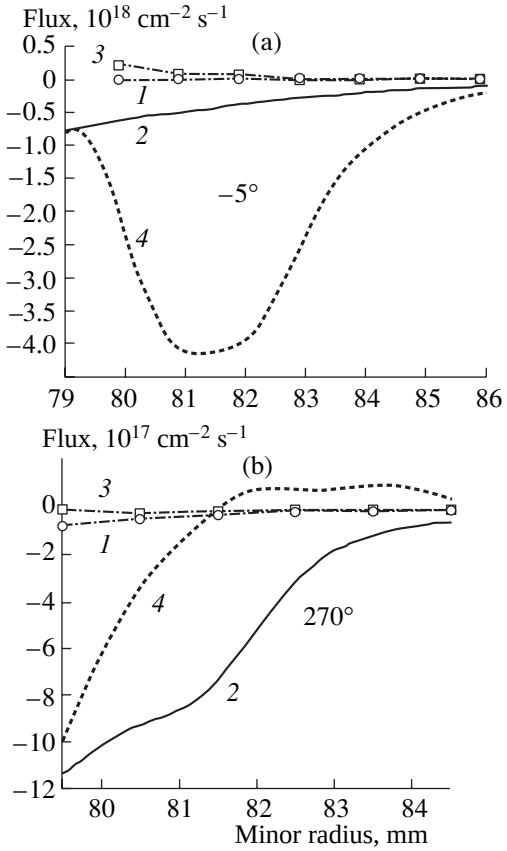

Fig. 7. Comparison of the radial profiles of the poloidal quasi-steady flux $\Gamma_{0\Theta}$ and the poloidal component of the fluctuation-induced flux $\Gamma_\Theta^{\sim}$ for two values of the poloidal angle Θ = –5° and 270°: (*1*) fluctuation-induced flux, 30 ms; (*2*) quasi-steady flux, 30 ms; (*3*) fluctuation-induced flux, 37 ms; and (*4*) quasi-steady flux, 37 ms.

poloidal contour (the sum of the products of the measured flux density by the length of the corresponding segment of the poloidal contour). The time behavior of this flux, which is the total fluctuation-induced particle flux per unit length of the major circumference, is shown in Fig. 5. This flux increases during the first half of the LHH pulse and then decreases. In the *H*-mode, the value of the total radial flux is reduced by nearly one-half in comparison with the preheating phase of the discharge.

The evolution of the poloidal component of the fluctuation-induced particle flux $\Gamma_\Theta^{\sim}$ can also be traced in Fig. 4. We note that there are oppositely directed fluxes both on the low-field side and on the high-field side in the OH and LHH phases. In the *H*-mode, the poloidal fluctuation-induced transport is almost totally suppressed (except for local regions on the low-field side).

3.4. Contribution from Quasi-Steady Fluxes

Similar distributions were also obtained for quasi-steady components $\mathbf{\Gamma}_0$ of the drift particle fluxes in the SOL. Figure 6 illustrates, as an example, the radial distributions of the fluxes Γ_{0r} and $\Gamma_r^{\sim}$ for two values of the poloidal angle, so we can compare the quasi-steady and fluctuation-induced particle fluxes. This figure demonstrates a complicated structure of the drift fluxes in the SOL. Two components of the radial flux at different spatial points can differ not only in the magnitude, but also in the direction. Since both components are of the same order of magnitude, they make comparable contributions to the total particle transport.

The radial profiles of the poloidal fluxes $\Gamma_{0\Theta}$ and $\Gamma_\Theta^{\sim}$ are shown in Fig. 7. This figure illustrates the dominant contribution of the quasi-steady flux to the total poloidal flux and a substantial increase in $\Gamma_{0\Theta}$ in the *H*-mode. Note that the quasi-steady flux changes its sign at r = 81.5 mm (Θ = 270°). This could be the reason for a nonmonotonic T_e profile with a minimum at r = 81.5 mm (Fig. 3).

3.5. Effective Coefficient of Radial Diffusion

Using the measured poloidal and radial distributions of the charged particle density and radial drift fluxes

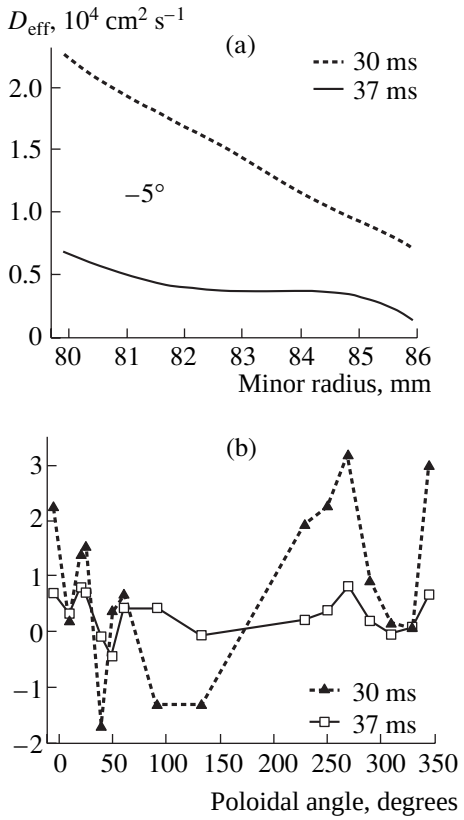

Fig. 8. Effective coefficient of radial diffusion $D_{\text{eff}} = -\Gamma_r/\text{grad}_r n$ as a function of (a) the radius and (b) the poloidal angle. The poloidal profiles are presented for the boundary points.

(both quasi-steady and fluctuation-induced), we can determine the effective coefficient D_{eff} of radial diffusion in the SOL from the expression $\Gamma_r = -D_{\text{eff}} \cdot \text{grad}_r n$, where $\Gamma_r = \Gamma_{0r} + \tilde{\Gamma_r}$ (the classical diffusion transport is negligibly small and can be ignored). Such a description implies that the particle transport in the SOL is a diffusion process in spite of the fact that drift fluxes (at least, the quasi-steady drift) are not related to the actual diffusion of particles. Figure 8 shows the radial and poloidal profiles of D_{eff} calculated by this formula for two instants in the OH phase and in the *H*-mode. It can be seen from the figure that the coefficient of radial diffusion decreases substantially after the transition to the improved confinement regime. The presence of negative values of D_{eff} indicates once again the complicated structure of the drift fluxes in the SOL.

4. CONCLUSIONS

A large amount of experimental data on the evolution of the poloidal and radial distributions of the plasma parameters and particle fluxes in the SOL during an L–H transition have been obtained in the course of probe measurements in the FT-2 tokamak.

It is shown that, under our experimental conditions, the fluctuation-induced and quasi-steady drift fluxes make comparable contributions to the radial particle transport, whereas the contribution of fluctuations to poloidal plasma fluxes in the SOL is negligibly small.

The L–H transition is accompanied by a substantial decrease in the effective coefficient of radial diffusion.

The results obtained, as well as the data from other (few in number) studies, show that the processes in the SOL are characterized by a fairly complicated structure of plasma flows. Fluctuation-induced fluxes contribute significantly to the total radial particle transport. The understanding of these processes and the search for ways of controlling the particle fluxes require further theoretical and experimental investigations. It is also necessary to study the nature of plasma fluctuations and the mechanism of fluctuation-induced transport. Probe measurements still remain one of the basic diagnostic tools in these studies.

ACKNOWLEDGMENTS

We thank E.L. Gurevich and A.P. Sharpenok for their assistance in processing the experimental results and preparing the paper for publication. This work was supported in part by the Ministry of Education of the Russian Federation (grant no. TO 2-7.4-2694), the Russian Foundation for Basic Research (project nos. 01-02-17926, 02-02-17589, 02-02-17684), INTAS (grant no. 2001-2056), and the RF Program for State Support of Leading Scientific Schools (grant no. 2216.2003.2).

REFERENCES

1. P. C. Stangeby, in *Proceedings of the International Atomic Energy Agency (IAEA) Technical Committee Meeting Workshop on Divertor Concepts, Provence, 2001*.
2. V. N. Budnikov, V. V. D'yachenko, L. A. Esipov, *et al.*, Pis'ma Zh. Éksp. Teor. Fiz. **59**, 651 (1994) [JETP Lett. **59**, 685 (1994)].
3. S. I. Lashkul, V. N. Budnikov, E. O. Vekshina, *et al.*, Fiz. Plazmy **27**, 1059 (2001) [Plasma Phys. Rep. **27**, 1001 (2001)].
4. S. I. Lashkul, V. N. Budnikov, A. D. Gurchenko, *et al.*, Czech. J. Phys. **52**, 1149 (2002).
5. A. N. Levitskiĭ, I. E. Sakharov, and S. V. Shatalin, Prib. Tekh. Éksp., No. 5, 153 (1992).
6. L. A. Esipov, I. E. Sakharov, E. O. Chechik, *et al.*, Zh. Tekh. Fiz. **67** (4), 48 (1997) [Tech. Phys. **42**, 367 (1997)].
7. E. O. Vekshina, P. R. Goncharov, S. V. Shatalin, *et al.*, Pis'ma Zh. Tekh. Fiz. **26** (10), 52 (2000) [Tech. Phys. Lett. **26**, 873 (2000)].

Translated by N.F. Larionova

Plasma Physics Reports, Vol. 30, No. 5, 2004, pp. 370–375. Translated from Fizika Plazmy, Vol. 30, No. 5, 2004, pp. 406–411.

Empirical Mode Decomposition Method for Investigating the Structure of Large-Scale MHD Instabilities in a Tokamak

A. M. Kakurin and I. I. Orlovsky

Russian Research Centre Kurchatov Institute, pl. Kurchatova 1, Moscow, 123182 Russia

Received August 14, 2003; in final form, October 1, 2003

Abstract—A new approach to the processing of experimental data from MHD diagnostics is developed for the purpose of investigating the spatial structure of large-scale MHD instabilities in a tokamak. The empirical mode decomposition method is applied to expand a multimode MHD perturbation in individual modes, which are then identified by constructing a spatial analytic signal with the help of the Hilbert transform. The method can be used to analyze the structure of the tearing instability and of the resistive wall modes. © *2004 MAIK "Nauka/Interperiodica".*

1. INTRODUCTION

The problem of identifying the mode composition of large-scale MHD perturbations in a tokamak has recently attracted increased interest because of the development of active research aimed at determining the restrictions imposed on the possible operating regimes of large tokamak devices by the onset of the neoclassical tearing modes and resistive wall modes (RWMs). One way of stabilizing these dangerous instabilities is to use feedback control systems. In order to provide such systems, it is necessary to develop methods by which the mode composition of an instability can be identified in real time.

The mode composition of an MHD instability is usually derived by analyzing the data from probe measurements of the spatiotemporal evolution of the perturbations of the poloidal magnetic field of a plasma column.

The distortions of the spatial structure of the perturbations due to toroidicity and due to some other factors limit the possibilities for identifying the mode composition of the instability by standard spectral methods. In some cases, an approach based on the representation of the experimental data under analysis in the form of a so-called analytic signal [1] may be considered as a viable alternative to the spectral methods. Such a representation makes it possible to correctly determine the instantaneous amplitudes and phases of the unsteady oscillating functions. In our earlier paper [2], we successfully applied this approach to identify the spatial structure of a single mode of a tearing instability. However, the approach is subject to a serious restriction: the basic oscillating function should be monocomponent [3].

The analysis of an MHD instability that occurs in the form of several modes with different spatial structures requires the use of mode decomposition. This problem can be solved by the recently developed empirical mode decomposition (EMD) method, in which a basic polyharmonic function $f(x)$ is decomposed into the components $\mathrm{imf}_i(x)$ having the shape of oscillations simultaneously modulated in amplitude and in frequency [3]. Each of these components, called intrinsic mode functions (IMFs), has the following properties: (i) the number of its local extremes and the number of points where it intersects its zero level differ by no more than unity and (ii) its upper and lower envelopes are symmetric with respect to its zero level. By constructing an analytic signal for each of the IMFs, it is possible to identify instability modes with the help of the algorithm proposed earlier in [2]. The attractiveness of the EMD method for MHD diagnostics is that, in a tokamak, the spatial distribution of the tearing perturbations in the poloidal direction has the shape of oscillations with a variable amplitude and variable frequency—a feature peculiar to IMFs.

2. EMPIRICAL MODE DECOMPOSITION ALGORITHM

An algorithm for decomposing the function $f(x)$, $x \in [a, b]$, was proposed by Huang *et al.* [3]. It involves the following steps:

(i) Initialization: $i = 0$, $r_i(x) = f(x)$, $x \in [a, b]$.

(ii) Initialization: $j = 0$, $g_j(x) = r_i(x)$, $x \in [a, b]$.

(iii) Determination of the extremes of $g_i(x)$.

(iv) Calculation of the envelopes $\max_j(x)$ and $\min_j(x)$ by spline-interpolation using the extremes obtained.

(v) Calculation of the mean envelope: $m_j(x) = (\max_j(x) + \min_j(x))/2$.

1063-780X/04/3005-0370$26.00 © 2004 MAIK "Nauka/Interperiodica"

(vi) Elimination of the local trend: $g_{j+1}(x) = g_j(x) - m_j(x)$.

(vii) Determination of whether or not $g_j(x)$ satisfies a *stopping criterion*. If not, the $j = j + 1$ iterate is taken and step (iii) is repeated.

(viii) Extraction of the IMF: $\mathrm{imf}_i(x) = g_j(x)$.

(ix) Elimination of the extracted IMF: $r_{i+1}(x) = r_i(x) - \mathrm{imf}_i(x)$.

(x) If $r_i(x)$ is not sufficiently small or is monotonic, the $i = i + 1$ iterate is taken and step (ii) is repeated.

The algorithm yields the decomposition $f(x) = \sum \mathrm{imf}_j(x) + r_n(x)$ in terms of the resulting set of n IMFs and the trend $r_n(x)$. The stopping criterion (step (vii)) has the form $\langle |a_i(x) - a_{i+1}(x)|^2 \rangle / \langle a_i(x)^2 \rangle < \varepsilon$, where ε is specified in advance (we have adopted $\varepsilon = 0.01$).

The mean frequency of oscillations of the first IMF is maximum, and the mean frequency of each of the next IMFs is lower than that of the previous one. Hence, each IMF is characterized by its own frequency scale, and the problem of calculating the IMF reduces to that of eliminating the local trend corresponding to its frequency scale.

Assigning to the expansion of the function $f(x)$ the analytic signal $Z(x) = \sum A_j(x)\exp(i\varphi_j(x))$, where $A_j(x) = (\mathrm{imf}_j^2(x) + (\mathbf{H}[\mathrm{imf}_j(x)])^2)^{1/2}$, $\varphi_j(x)) = \arctan(\mathbf{H}[\mathrm{imf}_j(x)]/\mathrm{imf}_j(x))$, and $\mathbf{H}[\ldots]$ is an operator defining the Hilbert transform (HT), we can generalize the algorithm proposed in [2] to a multimode MHD instability.

One of the difficulties arising in the practical implementation of the algorithm is the fact that, in calculating the upper and lower envelopes of the IMFs, the functions grow without bound at the end portions of the closed intervals on which they are defined. As the algorithm operates, these end portions become increasingly longer, which distorts the shapes of the resulting IMFs. For IMFs defined on short closed intervals, the algorithm produces uncertain expansions. One possible way of eliminating this numerical effect is to extrapolate the IMF beyond the closed interval by the method of neuron grids [4].

Our numerical algorithm is free of this drawback, because the spatial perturbation of the magnetic field is periodic in the poloidal angle θ, which allows the EMD method to be used with periodic cubic splines.

3. EXAMPLES OF THE MODE DECOMPOSITION OF TEST DISTRIBUTIONS

As an example, we show how to identify the mode composition of the tearing instability. In a multimode case, the modes of the perturbation of the poloidal magnetic field can be identified unambiguously because the perturbed field can be expanded into spatial components, each of which corresponds to the specific structure of the magnetic islands (i.e., to the intrinsic tearing mode). In the general case, such an identification is problematic; however, in the vast majority of standard discharge regimes with $q \le 3.5$ in tokamaks, the most probable tearing modes are those with m/n = 2/1, 3/1, 3/2, and 5/2. The modes with different n can easily be singled out by a spatial Fourier analysis. The modes with m/n = 2/1 and 3/1, as well as the modes with m/n = 3/2 and 5/2, can be resolved by the EMD method.

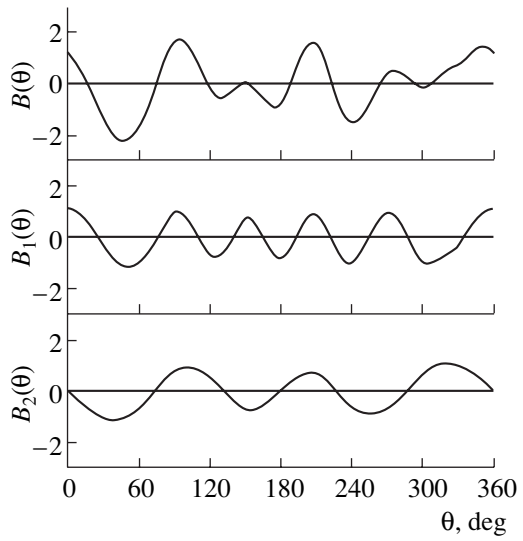

Fig. 1. First test distribution $B(\theta)$ and its components $B_1(\theta)$ and $B_2(\theta)$.

The EMD algorithm was checked against the test distributions that model the toroidal and ballooning distortions of MHD perturbations. The poloidal magnetic field was described by the distribution $B(\theta) = B_1(\theta) + B_2(\theta)$, where $B_i(\theta) = A(\theta)\cos(m_i(\theta - \lambda_i\sin\theta) - \alpha_i)$; $A(\theta) = 1 + k\cos\theta$ is the amplitude variation, m_i is the number of the mode, λ_i is the parameter determining the level of the distortions, and α_i is the phase shift. Figure 1 shows the distribution $B(\theta)$ with the parameters $m_1 = 5$, $m_2 = 3$, $\lambda_1 = 0.33$, $\lambda_2 = 0.3$, $k = 0.2$, $\alpha_1 = 0$, and $\alpha_2 = \pi/2$. The results of applying the EMD algorithm to this distribution $B(\theta)$ are illustrated in Fig. 2, which shows the upper and lower envelopes, the mean of the envelopes, and the extracted components $\mathrm{imf}_0(\theta)$ and $\mathrm{imf}_1(\theta)$. We can see that the extracted IMFs coincide almost completely with the prescribed components $B_1(\theta)$ and $B_2(\theta)$. Each IMF was processed by the algorithm for identifying an individual mode on the basis of the HT [2]. The mode composition obtained in this way is given in Fig. 3. For comparison, the figure also presents the mode composition obtained by the method of expansion in cylindrical Fourier harmonics, which possess a far richer spatial spectrum. We can see that the algorithm proposed here produces more reliable results than the conventional Fourier expansion method, which

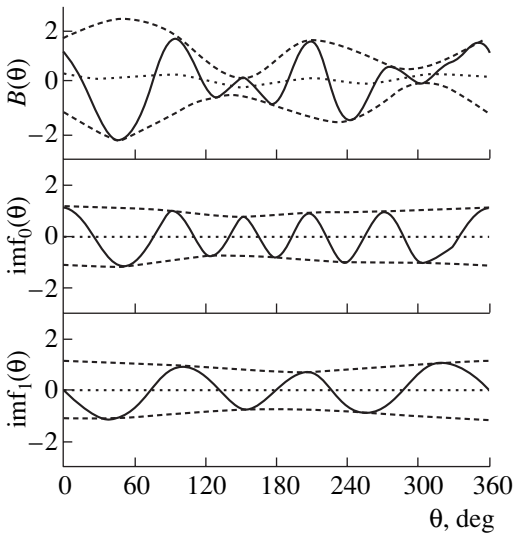

Fig. 2. Distribution $B(\theta)$ and the components $\mathrm{imf}_0(\theta)$ and $\mathrm{imf}_1(\theta)$ extracted by the EMD method.

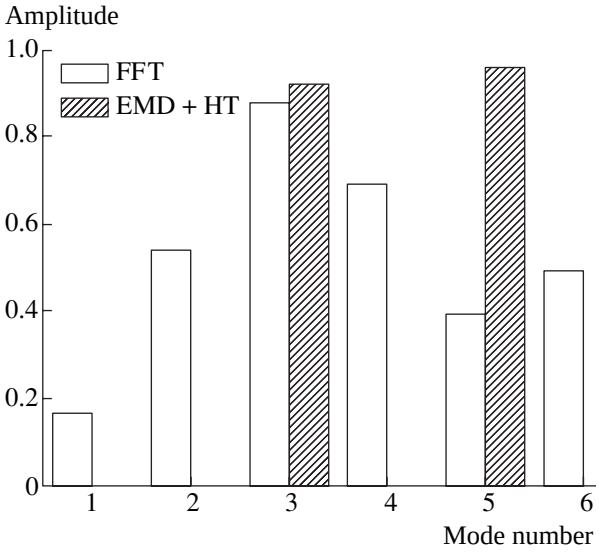

Fig. 3. Comparison between the mode compositions of the test distribution $B(\theta)$ obtained by the fast Fourier transform (FFT) and by the EMD + HT method.

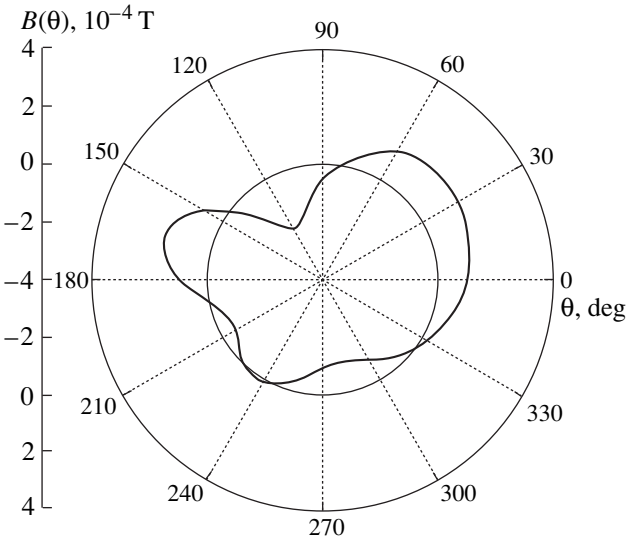

Fig. 4. Second test distribution $B(\theta)$.

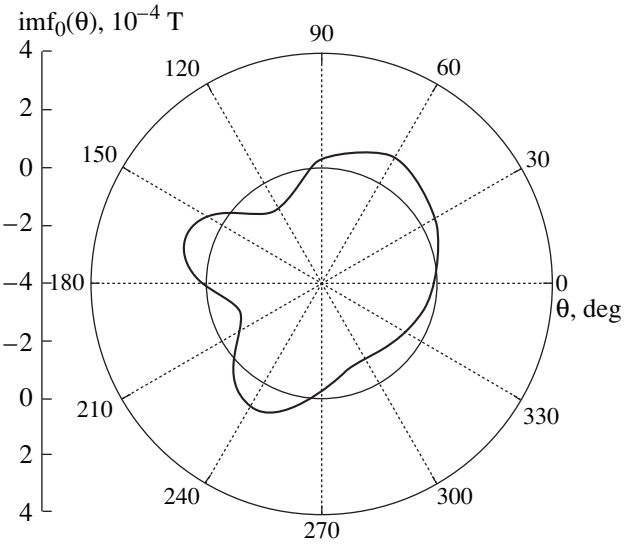

Fig. 5. Zeroth IMF component of $B(\theta)$.

yields a large number of harmonics in comparison with that contained in the initial distribution $B(\theta)$.

The algorithm described above was also applied to the test distribution $B(\theta)$ with the parameters $m_1 = 3$, $m_2 = 2$, $\lambda_1 = 0.6$, $\lambda_2 = 0.4$, $k = 0$, $\alpha_1 = \pi/2$, and $\alpha_2 = 0$ (Fig. 4). The extracted components (which are plotted in polar coordinates in Figs. 5, 6) are also seen to coincide with the prescribed components to within several percent. The mode compositions obtained by the proposed algorithm and by the conventional Fourier expansion method are depicted in Fig. 7. As in the previous case, the results of the algorithm are certainly more reliable than those of the conventional Fourier expansion.

4. EXAMPLE OF THE PROCESSING OF AN EXPERIMENTAL DISTRIBUTION OF MHD PERTURBATIONS

The algorithm was also used to process experimental signals from the magnetic pick-up coils (Mirnov probes) in the T-10 tokamak. The measurements were

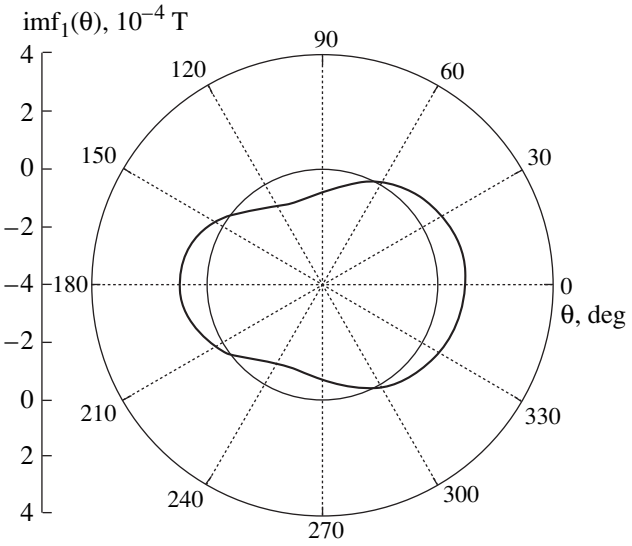

Fig. 6. First IMF component of $B(\theta)$.

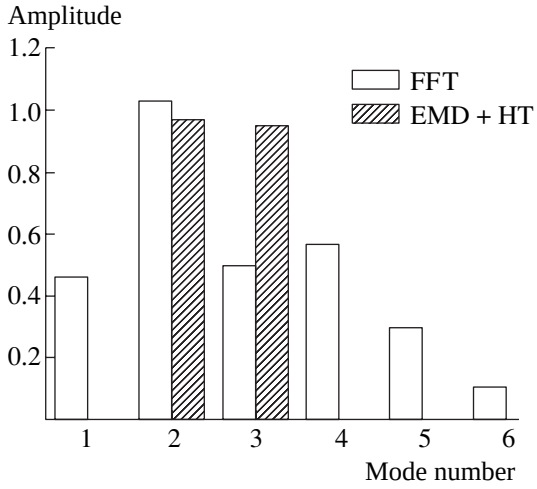

Fig. 7. Mode compositions of $B(\theta)$ obtained by the fast Fourier transform (FFT) and by the EMD + HT method.

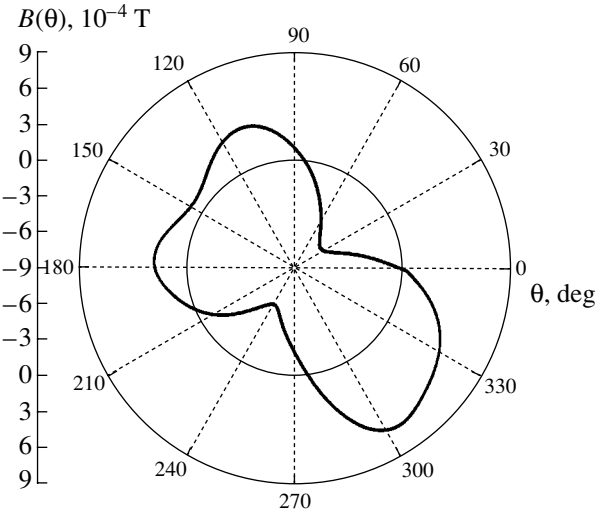

Fig. 8. Experimental distribution $B(\theta)$.

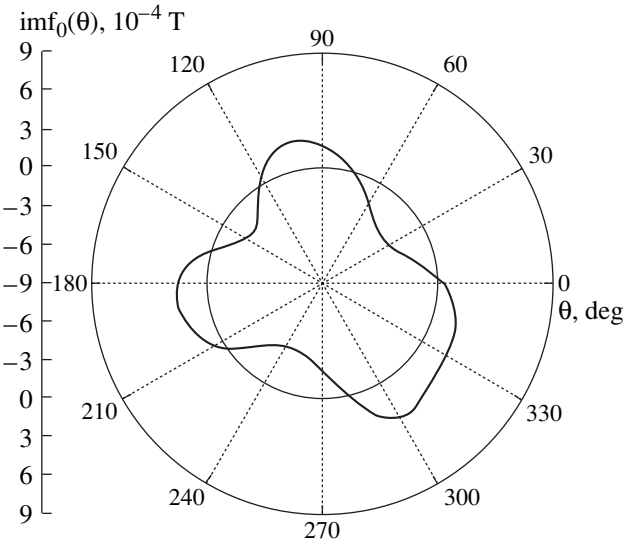

Fig. 9. Zeroth IMF component of the experimental distribution.

carried out in a discharge with the following parameters: the magnetic field was $B_T = 2.5$ T, the discharge current was $I_P = 250$ kA, the mean plasma density was $\langle n_e \rangle \approx 1.2 \times 10^{19}$ m^{-3}, the plasma minor radius was $a = 0.27$ m, and the safety factor at the plasma boundary was $q(a) = 2.4$. During the discharge, the poloidal magnetic field was strongly perturbed, the perturbation amplitude being $B \approx 5 \times 10^{-4}$ T. The signals from Mirnov probes were recorded at the time $t = 763$ ms after the beginning of the discharge.

The results of signal processing by the algorithm and by the method of expansion in cylindrical Fourier harmonics are demonstrated in Figs. 8–12. The algorithm shows that the perturbation is largely dominated by the second and third modes, whereas the Fourier expansion contains a far larger number of harmonics. Since, in this discharge regime, $q \approx 2.4$ and the $m/n = 3/1$ tearing mode cannot be excited, this result presumably indicates the simultaneous development of the $m/n = 2/1$ and 3/2 tearing modes.

To obtain additional information that would provide a more reliable identification of the tearing modes present in the perturbation, we consider how MHD perturbations evolve over time. Figure 13 shows the time evolutions of the second and third spatial Fourier harmonics of a perturbed poloidal magnetic field, obtained

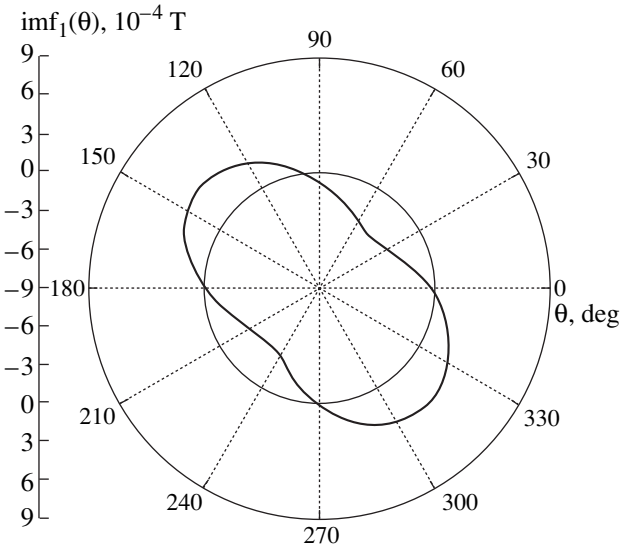

Fig. 10. First IMF component of the experimental distribution.

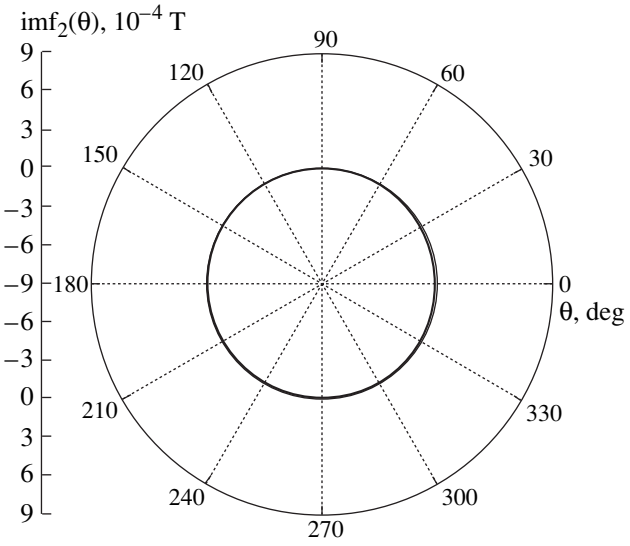

Fig. 11. Second IMF component of the experimental distribution.

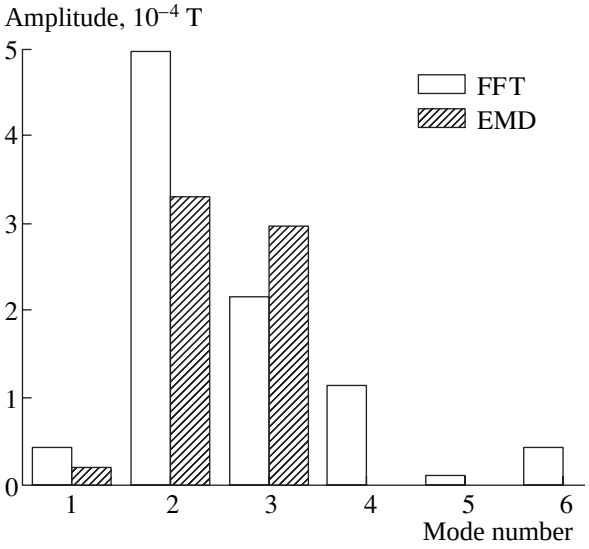

Fig. 12. Mode compositions of the experimental distribution $B(\theta)$ obtained by the fast Fourier transform (FFT) and by the EMD + HT method.

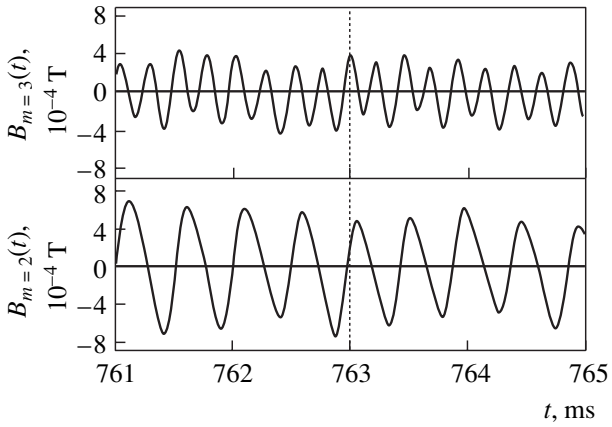

Fig. 13. Time evolutions of the second ($B_{m=2}$) and third ($B_{m=3}$) Fourier harmonics, obtained by processing the signals from Mirnov probes by analog schemes.

by processing the signals from Mirnov probes by analog schemes. The frequencies of the main components of each of the signals are different, which indicates the presence of at least two tearing modes. The frequency of the main component of the signal corresponding to the third spatial Fourier harmonic is two times higher than that corresponding to the second harmonic. Assuming that the plasma rotates predominantly in the toroidal direction, we can conclude that the signal with the higher frequency corresponds to the tearing mode whose toroidal number n is two times larger. This conclusion agrees with the above experimental result about the simultaneous detection of the m/n = 2/1 and 3/2 tearing modes.

5. CONCLUSIONS

The algorithm described in the present paper is based on a combination of the EMD method and the method developed earlier in [2]. This algorithm, which

makes it possible to resolve the individual modes in an MHD perturbation and to identify them, produces far more reliable results than the conventional method of expansion in cylindrical Fourier harmonics. Also, the algorithm can be implemented to operate in real time and thus is potentially applicable in systems for controlling tearing modes and RWMs. This feature gives the algorithm a distinct advantage over the singular value decomposition (SVD) method [5], which requires a time sample of several milliseconds. Although a rigorous mathematical justification of the EMD method is still lacking, it has been actively developed in recent years and has rapidly found increasingly wider application [6–8].

ACKNOWLEDGMENTS

This work was supported in part by the Department of Atomic Science and Technology of the Ministry of Atomic Industry of the Russian Federation.

REFERENCES

1. L. Franks, *Signals Theory* (Prentice-Hall, Englewood Cliffs, 1969; Sov. Radio, Moscow, 1974).
2. A. M. Kakurin and I. I. Orlovsky, Fiz. Plazmy **29**, 891 (2003) [Plasma Phys. Rep. **29**, 826 (2003)].
3. N. E. Huang, Z. Shen, S. Long, *et al.*, Proc. R. Soc. London, Ser. A **454**, 903 (1998).
4. Y. J. Deng, W. Wang, C. C. Qian, *et al.*, Chin. Sci. Bull. **46**, 954 (2001).
5. J. S. Kim, D. H. Edgell, J. M. Greene, *et al.*, Plasma Phys. Controlled Fusion **41**, 399 (1999).
6. P. Flandrin, G. Rilling, and P. Goncalves, in *Proceedings of the IEEE–EURASIP Workshop on Nonlinear Signal and Image Processing, Grado-Gorizia, Italy, 2003*; http://perso.ens-lyon.fr/patrick.flandrin/NSIP03.pdf.
7. S. T. Quek, P. S. Tua, and Q. Wang, Smart Mater. Struct. **12**, 447 (2003).
8. J. C. Nunes, O. Niang, Y. Bouaoune, *et al.*, Lecture Notes in Computer Science **2749**, 171 (2003).

Translated by O.E. Khadin

Plasma Physics Reports, Vol. 30, No. 5, 2004, pp. 376–382. Translated from Fizika Plazmy, Vol. 30, No. 5, 2004, pp. 412–418.

PLASMA ELECTRONICS

Influence of the Electrons Reflected from the Collector on the Parameters of a High-Current Relativistic Electron Beam

I. L. Bogdankevich, P. S. Strelkov, V. P. Tarakanov, and D. K. Ul'yanov

Prokhorov Institute of General Physics, Russian Academy of Sciences, ul. Vavilova 38, Moscow 119991 Russia

Received May 28, 2003; in final form, September 15, 2003

Abstract—In plasma microwave oscillators, electrons fall onto the surface of a graphite collector, which leads to the generation of secondary electrons. The influence of the electrons reflected from the collector on the parameters of a high-current relativistic electron beam propagating in a strong longitudinal magnetic field was studied experimentally and by numerical simulations. It is shown that the penetration of the reflected electrons into the drift space can lead to a substantial increase in the depth of the potential well in the drift space, a decrease in the velocity of the beam electrons, and a broadening of the electron energy distribution function. *© 2004 MAIK "Nauka/Interperiodica".*

1. INTRODUCTION

The efficiency of a microwave device depends largely on the quality of an electron beam. High efficiency can be achieved by using a monoenergetic beam with a small angular spread in velocity space. It is also important that the beam potential related to the beam space charge be low. For this reason, thin-walled annular high-current relativistic electron beams (REBs) are usually used in relativistic microwave electronics. The beam is transported in a strong uniform magnetic field and is separated from the wall of the electrodynamic structure by a rather narrow gap comparable to the beam wall thickness. It is desirable that the wall thickness of the annular beam be as small as possible, because when this thickness is sufficiently small, all the electrons are uniformly decelerated by the space-charge electric field and, in the case of an azimuthally symmetric microwave field, they interact identically with the exited electromagnetic field. This makes it possible to create highly efficient microwave devices.

It is well known that, when the beam electrons fall onto the collector, they cause secondary electron emission. If the secondary-electron energy is higher than the work needed to overcome the electron beam potential, these electrons can penetrate into the drift space and substantially affect the beam parameters: the spread of electrons over energy, the angular spread in velocity space, and the beam wall thickness. Since the beam potential in all relativistic microwave electronics devices is higher than 1 kV, original secondary electrons (with energies lower than 50 eV) do not affect the REB parameters. In contrast, secondary electrons with energies close to the energy of incident electrons, namely, the electrons that undergo elastic or inelastic reflections, can penetrate into the drift space of the beam. The influence of the reflected electrons on the parameters of a high-current REB was studied in [1, 2]. In [2], an REB was investigated in the absence of a magnetic field, whereas in [1], the beam propagated in a strong longitudinal magnetic field and the experimental conditions were similar to those used in the present study. It was experimentally shown in [1] that the penetration of the reflected electrons into the drift space leads to a 5–10% decrease in the beam current and to a 30% increase in the space-charge density of the beam. In that paper, an analytical model that offered a qualitative explanation of the observed effects was developed; this model, however, did not provide quantitative agreement with experiment. Moreover, in [1], the beam current was fixed and equal to $0.65I_0$, where I_0 is the limiting current in a vacuum [3].

In the present study, the influence of the reflected electrons on the beam parameters is investigated at beam currents from I_0 to $0.45I_0$. It is shown that the influence of the reflected electrons is higher at low beam currents. For example, at a current of $0.45I_0$, the reflected electrons can increase the beam space charge in the drift space by 100%. The experimental results are compared with numerical simulations. The numerical model includes some effects that were not taken into account in [1]. The experimental data are in quantitative agreement with calculations.

2. EXPERIMENT

A schematic of the experimental setup is shown in Fig. 1. Thin-walled electron beam *1* was formed at cylindrical explosive-emission cathode *2* with a radius of $r_2 = 0.5$ cm and propagated in a uniform magnetic field of $B = 1.5$ T along the axis of the vacuum chamber. The metal vacuum chamber consisted of anode tube *4*, transition tube *5*, and drift tube *6*, whose radii satisfied

1063-780X/04/3005-0376$26.00 © 2004 MAIK "Nauka/Interperiodica"

the inequalities $r_4 > r_6 > r_5$ ($r_4 = 5.6$ cm, $r_5 = 0.7$ cm, and $r_6 = 1.8$ cm). The beam electrons arrived at collector *7*. The experiments were performed with three types of collectors made of different materials: graphite, stainless steel, and tungsten.

The voltage pulse with an amplitude of 540 kV and a full width at half-maximum of 35 ns was applied to the accelerator cathode. The beam current was varied by varying the distance *d* between cathode *2* and anode plane *3*. When the condition $d \gg r_4 - r_2$ is satisfied, the beam current is limited by the beam space charge in tube *4*. This current, which is usually referred to as the limiting current of a coaxial magnetically insulated diode, is equal to [4]

$$I_m = \frac{8.5}{\ln r_4/r_2}\frac{(\gamma-\gamma_0)\sqrt{\gamma_0^2-1}}{\gamma_0}\ \text{[kA]}, \qquad (1)$$

where $\gamma = 1 + eU/(mc^2)$, e is an electron charge, U is the cathode potential, mc^2 is the electron rest energy, and $\gamma_0 = \sqrt{2\gamma + 0.25} - 0.5$. The current I_m is the minimum beam current that can be achieved using the system shown in Fig. 1a. Figure 1b qualitatively shows the profile of the beam potential along the system axis. In tubes *5* and *6*, the external electric field is low; therefore, the beam potential is primarily determined by the field of the beam space charge. The beam potential is equal to

$$\Phi = 2Q\ln r/r_b, \qquad (2)$$

where Q is the charge per unit length of the beam, r is the tube radius, and r_b is the beam radius. It follows from this that the absolute value of the beam potential is minimum in tube *5* (Fig. 1).

As the gap *d* decreases, the current injected in tube *5* increases; however, the current cannot exceed the vacuum limiting current [3] for drift tube *6*:

$$I_0 = \frac{8.5}{\ln r_6/r_b}(\gamma^{2/3}-1)^{3/2}\ \text{[kA]}. \qquad (3)$$

In this case, the beam potential in drift tube *6* cannot be higher than

$$\Phi_0 = -511(\gamma - \gamma^{1/3})\ \text{[kV]}. \qquad (4)$$

Strictly speaking, the above formulas are valid in the case of an infinitely strong magnetic field. It was also assumed in deducing formulas (3) and (4) that a metal foil perfectly transparent to electrons and electrically connected to tube *6* is installed at the entrance to tube *6* and the electron energy at the entrance to this tube is equal to eU. In our case, these formulas are approximately valid only if $r_5 \approx r_2$. Under this condition, the decrease in the potential in tube *5* is small and the electron kinetic energy at the entrance to tube *6* is close to eU; i.e., conditions of experiments with a foil in which the electron kinetic energy at the entrance to tube *6* is exactly equal to eU are approximately satisfied.

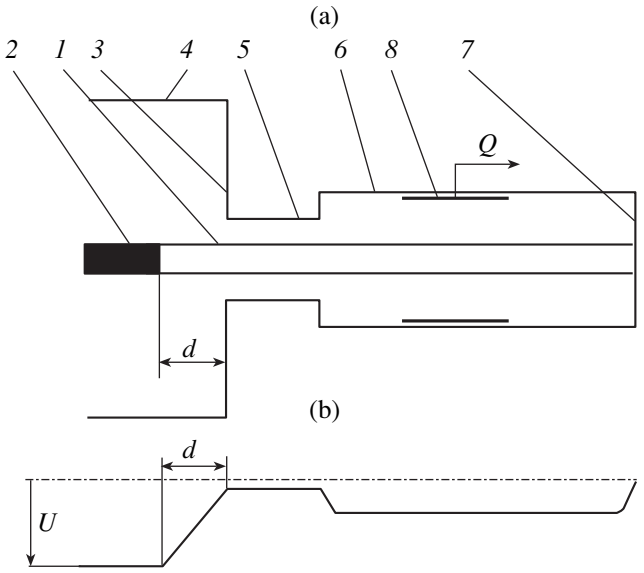

Fig. 1. (a) Schematic of the experimental setup: (*1*) REB, (*2*) cathode, (*3*) anode plane, (*4*) anode tube, (*5*) transition tube, (*6*) drift tube, (*7*) collector, and (*8*) beam space charge meter, and (b) the REB potential profile along the system axis.

The problem of the limiting current in a metal chamber consisting of two tubes with different diameters was considered in [5].

The scheme of the REB formation shown in Fig. 1 is widely used in relativistic microwave electronics. The electrodynamic structure of a microwave device was located in drift tube *6*. Since the microwave oscillator efficiency decreases with increasing beam current at a fixed electron energy, the beam currents in straight relativistic vacuum microwave-electronics devices are usually no higher than $0.2I_0$, which is achieved by adjusting the distance *d* and the ratio r_4/r_2.

In our experiments, the beam space charge in the central part of the drift tube was measured by capacitive divider *8* (see Fig. 1) with a length of 10 cm. The transverse size of the electron beam was measured from its print on a dielectric target that was transparent to the beam electrons and was also installed in the central part of the drift tube.

From the measured beam space charge per unit length Q, the potential Φ at the outer beam radius $r = r_b$ can be estimated by formula (2), assuming that the beam charge density is uniform in the longitudinal and azimuthal directions. At typical parameter values $R/r_b = 3$ and $Q = -10^{-7}$ C/cm, we find $\Phi = -200$ kV.

3. EXPERIMENTAL RESULTS

Figure 2a shows the beam current at the collector as a function of the distance *d* between the cathode and plane *3* (Fig. 1). One can see that the current reaches its

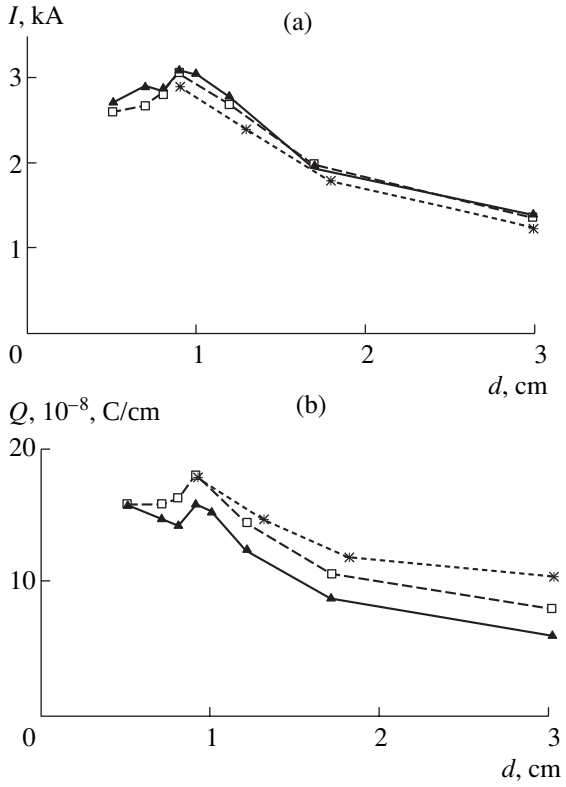

Fig. 2. Measured dependences of the (a) beam current and (b) beam space charge per unit length on the distance d for different collector materials. Triangles, squares, and asterisks correspond to graphite, stainless steel, and tungsten, respectively.

maximum value equal to 3.1 kA at $d = 0.9$ cm and then decreases to 1.4 kA at $d = 3$ cm. The beam current depends on the collector material. When a collector made of graphite (which has a low electron reflection coefficient) is replaced with a collector made of tungsten (which has a high electron reflection coefficient), the beam current decreases by 6–10%.

In every measurement of the beam current, we simultaneously measured the beam space charge (see Fig. 2b). One can see that, when graphite is replaced with tungsten, the increase in the flux of reflected electrons leads to an increase in the beam space charge. This effect is most pronounced at low currents ($d = 3$ cm), $Q_w/Q_c = 1$, where Q_w and Q_c are the beam charge densities per unit length for collectors made of tungsten and graphite, respectively.

The dependence shown in Fig. 2a can be explained as follows: As was mentioned above, for $d \gg r_4 - r_2$, the current of the beam entering tube *6* is equal to the current of a magnetically insulated diode for tube *4* [see formula (1)]. At $\gamma = 2.06$, $r_2 = 0.5$ cm, and $r_4 = 5.6$ cm, we have $I_m = 1.28$ kA. At $d = 3$ cm (i.e., at $d \approx r_4 - r_2$), the beam current should be higher than the current of a magnetically insulated diode. Calculations show, however, that this difference is small, so that for $d = 3$ cm $< r_4 - r_2 = 5.1$ cm, the measured current turns out to be close to the current of a magnetically insulated diode. As the gap becomes narrower ($d < 3$ cm), the current injected into tube *6* increases; however, the current measured at the collector cannot exceed the vacuum limiting current for tube *6*. According to formula (3), for $\gamma = 2.06$, $r_2 = 0.5$ cm, and $r_6 = 1.8$ cm, the vacuum limiting current is $I_0 = 3.2$ kA. Thus, the increase in the beam current from 1.4 kA to 3.1 kA as the distance d decreases from 3 cm to 0.9 cm finds a natural explanation.

At $d > 0.9$ cm, the beam current is limited by the space charge in the diode (tube *4*). The electrons reflected from the collector can penetrate into the diode; as a result, the beam space charge increases, whereas the beam current decreases. This fact explains the decrease in the beam current when a graphite collector is replaces with a tungsten collector.

The influence of the reflected electrons on the beam space charge should be more pronounced at low beam currents. The point is that, at a high beam current equal to I_0, the beam potential in the drift tube Φ_0 is close to the cathode potential. According to formula (4), this potential is equal to –400 kV when the cathode potential is –540 kV. Therefore, only a small fraction of the reflected electrons, namely, the electrons that have energies above 400 keV and escape from the collector at small angles to the tube axis, can enter the drift tube. When the beam current is low, the potential in the drift tube is low and the fraction of the reflected electrons that can enter the drift tube increases.

Figure 2 also shows the results obtained with a stainless-steel collector. One can see that, when a graphite collector is replaced with a stainless-steel collector, the beam current changes only slightly, while the space charge varies significantly. Since the reflection coefficient for iron is smaller than for tungsten and is larger than for carbon, the curves for stainless steel lie between those for tungsten and graphite.

4. NUMERICAL SIMULATIONS

In simulations of the electron reflection from a solid surface, we used the data presented in [6]. These data include experimental dependences of the electron reflection coefficient, the energy E of the reflected particles, and the angle at which they leave the surface on the energy E_0 and the angle of incidence of the incident particles. For example, when electrons with an energy of $E_0 = 540$ keV are incident normally onto a surface (i.e., the angle of incidence is zero), the total electron reflection coefficient equals 0.45 for tungsten, 0.22 for iron, and 0.08 for graphite. As the angle of incidence increases, the total electron reflection coefficient for all materials increases to unity. The distribution function of the reflected electrons over energy E depends on the target material. Thus, when electrons are incident normally onto a tungsten surface, this function equals zero

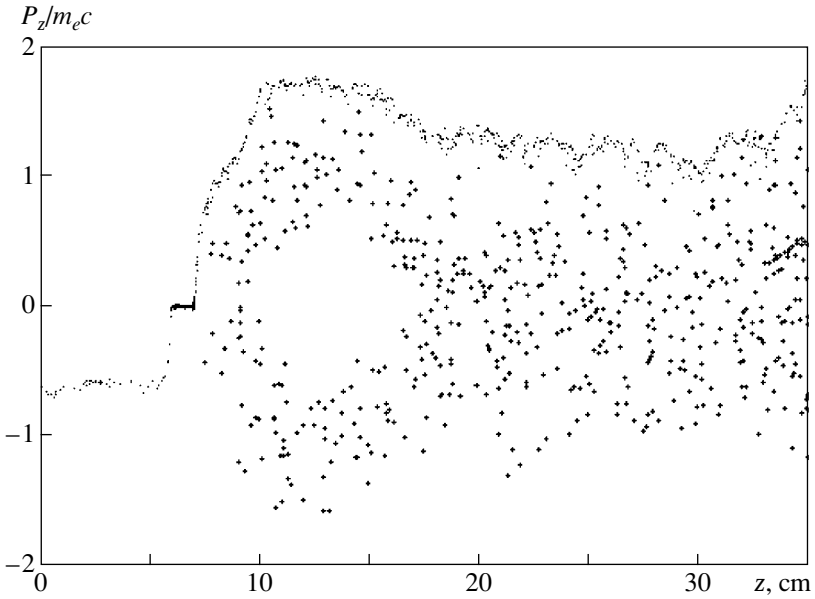

Fig. 3. Electron phase portrait (z, P_z) calculated for d = 3 cm and a tungsten collector. The points refer to the primary beam electrons, while the crosses indicate the reflected and re-reflected electrons.

at an energy equal to the energy of incident electrons, reaches its maximum at $E = 0.9E_0$, and then decreases to 0.1 of its maximum value at $E = 0.3E_0$. The dependence is qualitatively similar for all materials; however, the maximum shifts toward lower energies and is less pronounced for low-Z materials. For example, for iron, the electron energy distribution function reaches its maximum at $E = 0.7E_0$ and decreases to 0.5 of its maximum value at $E = 0.3E_0$. The angle at which the reflected electrons leave the surface depends only slightly on the target material. For normal incidence, the angular distribution of the reflected electrons is close to a cosine function.

Numerical simulations were performed using the two-dimensional axisymmetric version of the KARAT particle-in-cell electromagnetic code [7]. The code solved a set of Maxwell's equations and the relativistic equations of motion for electrons. The geometry of the cathode and vacuum chamber was the same as in the experiment. The magnetic induction was 1.5 T. The shape of the cathode voltage pulse was close to that used in the experiment: the duration of the leading edge was 10 ns, and the duration of the plateau was 20 ns. The pulse amplitude was 540 kV. Note that in both the experiments and simulations, the REB parameters were determined during the plateau of the voltage pulse (from 15 to 25 ns).

A boundary condition corresponding to the reflection of a fraction of incident particles was set at the collector surface. The energies and angles at which the reflected electrons left the surface were chosen by the Monte Carlo method and were used as initial values for calculating the trajectories of these electrons. After the reflected particles returned to the collector (after being re-reflected from the cathode or a potential well in the drift tube near the collector), they again underwent a partial reflection according to the above simulation procedure.

A typical electron phase portrait (z, P_z) calculated for a tungsten collector and d = 3 cm ($I = 0.45I_0$) is shown in Fig. 3. Let us trace the behavior of electrons using this phase portrait. The emitted electrons are accelerated to the maximum energy in the gap between the cathode and plane d in the positive direction along the z axis (Fig. 1). After entering the drift tube, they are slightly decelerated. Note that the beam current and the energy of the beam electrons are unsteady in this cross section. This fact requires additional study; however, we can conclude that, when the beam current is comparable to the limiting current, the regions where the beam is accelerated and decelerated act as a virtual cathode modulating the current and energy of electrons. After arriving at the collector (z = 35 cm), electrons can be reflected with a certain probability, after which they begin to move in the opposite direction (in Fig. 3, these electrons are marked by crosses). When the reflected electrons pass from the drift tube to the narrow drift tube *5* (Fig. 1), they are accelerated and are then re-reflected from the cathode, after which they follow the path of the primary electrons; however, they have a lower energy and a significant spread in transverse velocities. On the collector, they can be reflected again, and so on.

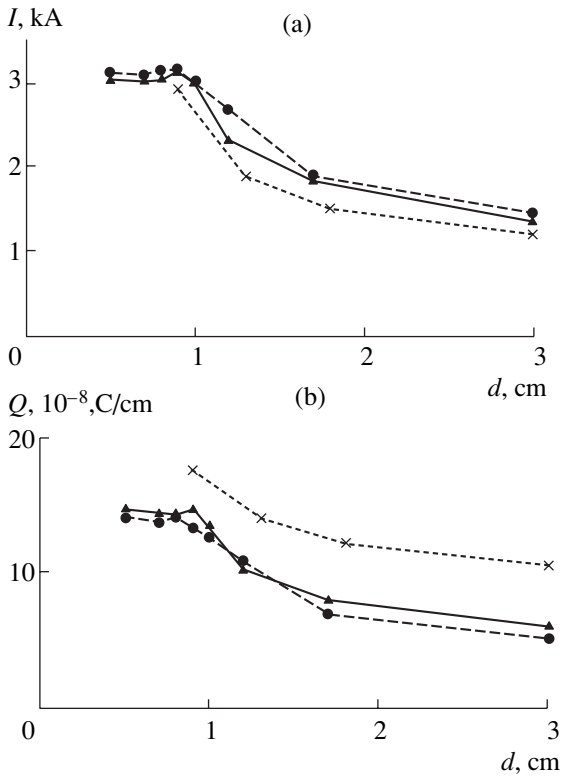

Fig. 4. Calculated dependences of (a) the beam current and (b) the beam space charge per unit length on the distance d for different collector materials. The circles refer to a material that does reflect electrons, the triangles refer to graphite, and the crosses refer to tungsten.

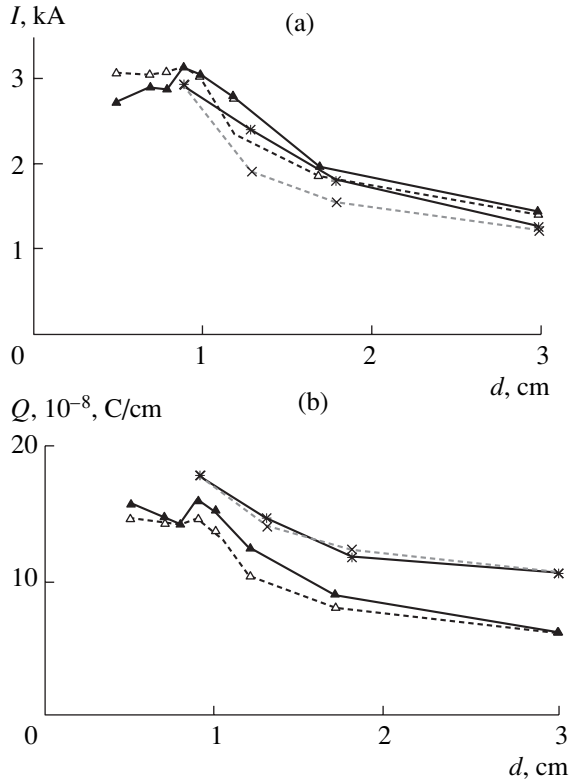

Fig. 5. Comparison of the measured and calculated dependences shown in Figs. 2 and 4 for a graphite collector (triangles) and a tungsten collector (asterisks and crosses). The solid lines show the experimental results, and the dashed lines show the results of calculations.

5. COMPARISON OF THE EXPERIMENTAL RESULTS WITH SIMULATIONS

Figure 4 shows the calculated beam current and space charge density per unit length as functions of the distance d for tungsten and graphite collectors and an ideal collector with a zero reflection coefficient. One can see that, for a graphite collector, the effect of the reflected electrons on the REB parameters is weaker. The electrons reflected from a graphite collector decrease the beam current by no more than 7% and increase the space charge by no more than 16%.

Let us compare the experimental dependences of the beam current to those calculated for graphite and tungsten (see Fig. 5a). The measured and calculated values of the beam current for $d = 0.9$ cm and $d = 3$ cm coincide for both graphite and tungsten. For intermediate values of d, the calculated current is lower than the experimental one for both materials. The maximum discrepancy is 17% for graphite and 25% for tungsten.

For tungsten, the measured and calculated values of the space charge almost coincide, whereas the calculated values for graphite are somewhat smaller than the experimental ones; however, the discrepancy does not exceed 20% (Fig. 5b). Thus, the simulations qualitatively agree with the experimental dependences of the beam current and the beam space charge on d and on the collector material. The discrepancy between the measured and calculated values does not exceed 25%.

In the experiments, the shape of the REB print on the target depended markedly on the collector material (see Fig. 6). This change can be explained by the increase in the wall thickness of an annular beam with increasing number of reflected electrons. However, in simulations, the thickness of an annular beam turned out to be independent of the collector material (see Fig. 7); the only difference is that the space charge density increased slightly near the beam axis in the case of a tungsten collector. A substantial difference between the prints in Fig. 6 can be explained by the fact that the reflected and re-reflected electrons have low kinetic energies. A 70-μm-thick heat-sensitive paper turns out to be opaque for these electrons, so that the paper is heated much more efficiently. The presence of a large number of low-energy reflected and re-reflected electrons in the drift tube is confirmed by the simulation results (Fig. 8).

The penetration of the reflected electrons to the drift space leads not only to a decrease in the average kinetic energy of the beam electrons, but also to a significant broadening of their energy distribution function (Fig. 8a). In the case of a graphite collector, these

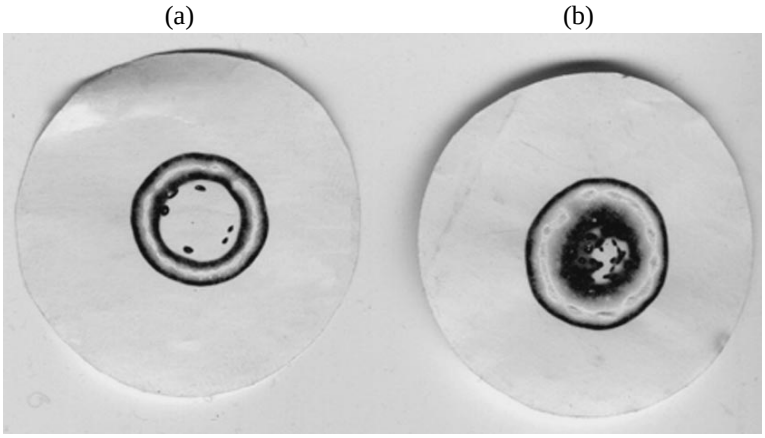

Fig. 6. Beam prints on a heat-sensitive paper for (a) a graphite collector and (b) a tungsten collector (d = 3 cm).

effects are reduced (Fig. 8b), but are not eliminated completely. The broadening of the energy distribution function in the presence of reflected electrons can be attributed to the onset of electron two-stream instability.

In vacuum relativistic microwave electronics, special precautions are usually taken in order to prevent the penetration of reflected electrons into the drift space. To this end, the collector is placed in the region of a weaker magnetic field, so that the electrons reflected from the collector have to pass through a magnetic mirror. This makes it possible to significantly decrease the number of reflected electrons in the drift space; however, the flux of reflected electrons cannot be completely eliminated in this way. On the other hand, the present study has demonstrated that, in principle, the reflected electrons can catastrophically deteriorate the beam parameters. The adverse effect of the reflected electrons on the operation of relativistic microwave devices was described, e.g., in [8, 9]. Note that, in [8], a method was proposed for completely eliminating the penetration of the electrons reflected from the collector into the drift space. However, the application of this method to actual microwave devices significantly complicates their design. For this reason, in existing vacuum microwave sources, the side wall of the metal cylindrical chamber that is situated in a weaker magnetic field serves as a beam collector. In plasma microwave oscillators [10], electrons are incident normally onto the graphite col-

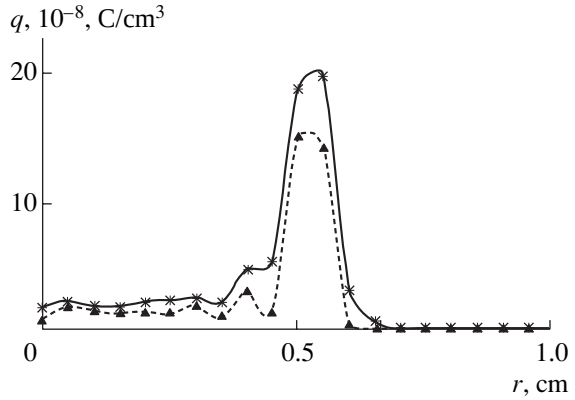

Fig. 7. Calculated radial profiles of the beam space charge density for a graphite collector (triangles) and a tungsten collector (asterisks) (d = 3 cm).

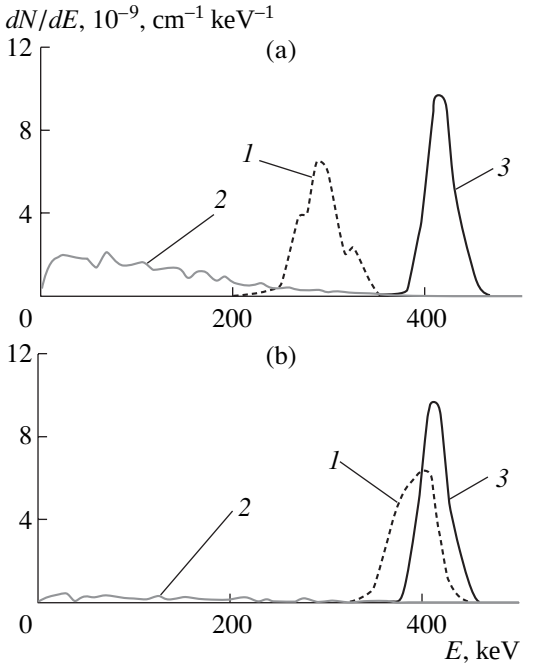

Fig. 8. Calculated energy distribution functions of the electron density per unit length at d = 3 cm for (a) a tungsten collector and (b) a graphite collector: (*1*) primary electrons and (*2*) reflected electrons. For comparison, curves *3* show the electron energy distribution functions in the absence of reflected electrons.

lector surface. Therefore, measurements and simulations similar to those described in our paper would be of interest for any study on relativistic microwave electronics.

ACKNOWLEDGMENTS

We thank V.E. Nechaev and O.T. Loza for useful discussions. This work was supported in part by the Ministry of Industry, Science, and Technologies of the Russian Federation under the Program for Supporting Unique Devices (registration no. 01-04), the Presidium of the Russian Academy of Sciences under the Nanosecond Relativistic High-Power Electronics Complex Program (Broadband Relativistic Cherenkov Plasma Maser Project), and the Russian Foundation for Basic Research (project no. 01-02-17265).

REFERENCES

1. N. I. Zaĭtsev, G. S. Korablev, I. S. Kulagin, and V. E. Nechaev, Fiz. Plazmy **8**, 918 (1982) [Sov. J. Plasma Phys. **8**, 515 (1982)].
2. V. Engelko, J. Mueller, and H. Bluhm, in *Proceedings of the 13th International Conference on High-Power Particle Beams, Nagaoka, 2000*, p. 188.
3. L. S. Bogdankevich and A. A. Rukhadze, Usp. Fiz. Nauk **103**, 609 (1971) [Sov. Phys. Usp. **14**, 163 (1971)].
4. A. I. Fedosov, E. A. Litvinov, S. Ya. Belomyttsev, and S. P. Bugaev, Izv. Vyssh. Uchebn. Zaved. Fiz., No. 10, 134 (1977).
5. A. A. Grishkov, S. Ya. Belomyttsev, S. D. Korovin, and V. V. Ryzhov, Pis'ma Zh. Tekh. Fiz. **29** (22), 46 (2003) [Tech. Phys. Lett. **29**, 944 (2003)].
6. M. I. Ryazanov and I. S. Tilinin, *Study of Surfaces Using Particle Backscattering* (Énergoatomizdat, Moscow, 1985).
7. V. P. Tarakanov, *User's Manual for Code KARAT* (Berkley, Springfield, 1992).
8. O. T. Loza, P. S. Strelkov, and S. N. Voronkov, Fiz. Plazmy **20**, 418 (1994) [Plasma Phys. Rep. **20**, 374 (1994)].
9. M. Fuks, E. Shamiloglu, and E. Abubakirov, in *Proceedings of the 28th IEEE International Conference on Plasma Science, 2001*, p. 498.
10. M. V. Kuzelev, O. T. Loza, A. A. Rukhadze, *et al.*, Fiz. Plazmy **27**, 710 (2001) [Plasma Phys. Rep. **27**, 669 (2001)].

Translated by E.L. Satunina

Plasma Physics Reports, Vol. 30, No. 5, 2004, pp. 383–397. Translated from Fizika Plazmy, Vol. 30, No. 5, 2004, pp. 419–433.

PLASMA ELECTRONICS

Nonlinear Theory of the Collective Cherenkov Interaction of a Dense Relativistic Electron Beam with a Dense Plasma in a Waveguide

Yu. V. Bobylev, M. V. Kuzelev, and A. A. Rukhadze

Prokhorov Institute of General Physics, Russian Academy of Sciences, ul. Vavilova 38, Moscow, 119991 Russia

Received July 2, 2003

Abstract—A nonlinear theory of the instability of a straight relativistic dense electron beam in a plasma waveguide is derived for conditions of the stimulated collective Cherenkov effect. A study is made of a waveguide with a dense plasma such that the plasma wave excited by the beam during the instability can be described, with a good degree of accuracy, as a potential wave. General relativistic nonlinear equations are obtained that describe the temporal dynamics of beam–plasma instabilities with allowance for plasma nonlinearity and the generation of harmonics of the initial perturbation. Under the assumption that the resonant interaction between the beam waves and the plasma waves is weak, the general equations are reduced to relativistic equations with cubic nonlinearities by using the method of expansion in small perturbations of the trajectories and momenta of the beam and plasma electrons. The reduced equations are solved analytically, the time scales on which the instability saturates are determined, and the nonlinear saturation amplitudes are obtained. A comparison between analytical solutions to the reduced equations and numerical solutions to the general nonlinear equations shows them to be in good agreement. Nonlinear processes caused by the relativistic nature of the beam are found to prevent stochastization of the system in the nonlinear stage of the well-developed instability. In contrast, a nonrelativistic electron beam is found to be subject to significant anomalous nonlinear stochastization. © *2004 MAIK "Nauka/Interperiodica".*

1. It is well known that the Cherenkov instability of an electron beam in a plasma waveguide can occur only when the plasma density is higher than a certain threshold value determined by the beam velocity and the geometry of the system. Thus, in a magnetized waveguide with a low-density beam, a necessary condition for the onset of the Cherenkov instability has the form [1]

$$\omega_p^2 > k_\perp^2 u^2 \gamma^2 \equiv \Omega_0^2, \tag{1}$$

where ω_p is the Langmuir frequency of the plasma electrons, u is the beam electron velocity, $\gamma = (1 - u^2/c^2)^{-1/2}$ is the relativistic factor, and $k_\perp$ is the smallest transverse wavenumber of the main plasma E wave in the waveguide. When the Langmuir frequency ω_p is close to the threshold frequency Ω_0, the instability develops in the long-wavelength range at a frequency ω that is low in comparison with the frequency ω_p. In this case, an unstable plasma wave excited by an electron beam propagating with a relativistic velocity u is essentially nonpotential. The long-wavelength beam–plasma instability is of interest in connection with the problem of creating relativistic plasma microwave oscillators and amplifiers [2, 3]. Under the condition

$$\omega_p \gg \Omega_0, \tag{2}$$

the instability develops in the short-wavelength range. The plasma wave excited during the instability is nearly potential and has a frequency close to ω_p. The short-wavelength beam–plasma instability may be of interest in solving such problems as plasma heating and raising the efficiency of energy input into plasma waves [4, 5].

Here, the plasma is considered to be dense if strong inequality (2) is satisfied. In such a plasma, the Cherenkov beam instability gives rise to quasi-potential plasma waves at a frequency of $\omega \sim \omega_p$. As an example, we consider a particular laboratory experiment with a circular waveguide of radius $R = 2$ cm and with an annular plasma that has an inner radius of $r_1 = 0.7$ cm and an outer radius of $r_2 = 1$ cm and is assumed to be completely magnetized by a strong external magnetic field directed along the waveguide axis. Figure 1 shows the ω_p dependence of the quantity

$$P = \frac{\omega_p - \omega_0}{\omega_p}, \tag{3}$$

where ω_0 is the frequency of the single-particle Cherenkov resonance between a plasma E_{01} wave in a waveguide and a beam propagating with the velocity $u = 2.6 \times 10^{10}$ cm/s ($\gamma = 2$). For the waveguide under consideration, the threshold frequency is equal to $\Omega_0 \approx 10^{11}$ rad/s. Figure 1 implies that the plasma in which the electron Langmuir frequency is only one order of magnitude higher than this threshold frequency can already be considered dense.

1063-780X/04/3005-0383$26.00 © 2004 MAIK "Nauka/Interperiodica"

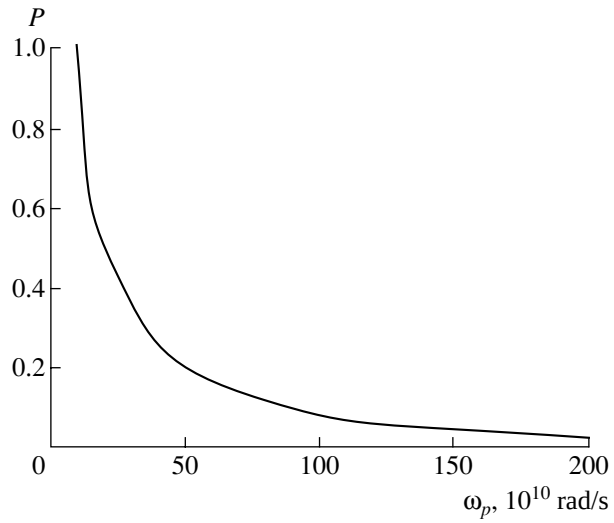

Fig. 1. Explanation of the notion of a dense plasma: dependence of the relative frequency P of the single-particle Cherenkov resonance on the Langmuir frequency of the plasma electrons.

The dispersion of a low-frequency E_{01} wave in a strong magnetic field in a plasma waveguide is determined by the relation [6]

$$\omega^2 = \Omega_p^2 \equiv \omega_p^2 G^2(\chi^2), \tag{4}$$

where $\chi^2 = k_z^2 - \omega^2/c^2$, $G^2(\chi^2)$ is a geometric factor, and k_z is the longitudinal wavenumber. For a waveguide in which the plasma is inhomogeneous over the cross section, the function $G^2(\chi^2)$ is transcendental and Eq. (4) is fairly complicated. In solving a nonlinear problem, when it is impossible to introduce the notion of the frequency ω (or of the longitudinal wavenumber k_z), dispersion relation (4) is a pseudodifferential equation [7] for determining the electric field vector in a plasma waveguide. Solving such an equation runs into serious mathematical difficulties. However, if the plasma is assumed to be dense, this can be done without difficulty. In fact, under inequality (2), the frequency is $\omega \sim \omega_p$. In this case, under the Cherenkov resonance condition $\omega \approx k_z u$, we have $\chi^2 \approx \omega_p^2/(u^2\gamma^2)$, which allows us to rewrite inequality (2) as

$$|\chi^2| \gg k_\perp^2. \tag{5}$$

In the most general case, it is possible to show [6, 8] that, under inequality (5), the transcendental function $G^2(\chi^2)$ is close to unity. This also follows from dispersion relation (4) with $\omega \sim \omega_p$. Accordingly, dispersion relation (4) reduces to an elementary algebraic relation and the corresponding pseudodifferential equation passes over to the equation for a harmonic oscillator. It is precisely for this purpose that we make the main simplifying assumption that the plasma density is high: under this assumption, the fields and the spectra in the nonlinear problem under study can be calculated analytically. This is also true in the case without an external magnetic field, the only difference being that, under inequality (5), the function $G^2(\chi^2)$ is close to 1/2.

2. We consider the evolution of an original harmonic perturbation driven at the time $t = 0$ in a waveguide with a fully magnetized thin-walled plasma and a fully magnetized thin-walled relativistic electron beam. We begin with the general nonlinear equations derived in our earlier paper [9]. In the case of a relativistic electron beam and under conditions (1) and (5), these equations take the form

$$\frac{d^2 y_p}{dt^2} = -\frac{1}{2} i \sum_{n=1}^{\infty} \left\{ \frac{1}{n} [g_{pn}\rho_{pn} + \tilde{\omega}_b^2 q_n \rho_{bn}] \exp(iny_p) - \text{c.c.} \right\},$$

$$k_z \frac{d}{dt}\left(\frac{v_b}{\sqrt{1 - v_b^2/c^2}} \right) \tag{6}$$

$$= -\frac{1}{2} i \sum_{n=1}^{\infty} \left\{ \frac{1}{n} [g_{bn}\rho_{bn} + \tilde{\omega}_p^2 q_n \rho_{pn}] \exp(iny_b) - \text{c.c.} \right\},$$

$$\frac{dy_b}{dt} = k_z v_b.$$

Here, k_z is the wavenumber of the original harmonic perturbation, $y_p(t, y_0) = k_z z_p(t, z_0)$, $y_b(t, y_0) = k_z z_b(t, z_0)$, $y_0 = k_z z_0$, $z_p(t, z_0)$ and $z_b(t, z_0)$ are the coordinates of the plasma and beam electrons that were at the point z_0 at the time $t = 0$, $v_b(t, z_0)$ is the velocity of a beam electron, $\tilde{\omega}_p^2 = S_p \omega_p^2$, $\tilde{\omega}_b^2 = S_b \omega_b^2$, ω_b is the Langmuir frequency of the beam electrons, S_p and S_b are the plasma and beam cross-sectional areas, the quantity g_{pn} denotes the right-hand side of Eq. (4), the quantity g_{bn} is the beam analogue of g_{pn}, and the parameter q_n determines the coupling between the plasma waves and the beam waves. Equations (6) account for the nonlinear excitation of the modes of the original perturbation, namely, the waves with the wavenumbers nk_z, where $n = 1, 2, \ldots$ is the mode number. The dimensionless amplitudes of the harmonics of the plasma and beam densities are given by the formulas

$$\rho_{\alpha n} = \frac{1}{\pi} \int_0^{2\pi} \exp(-iny_\alpha) dy_0, \quad \alpha = p, b. \tag{7}$$

It should be noted that, in terms of Eqs. (6), the plasma and the beam are described nonlinearly in a way

that is exactly equivalent to a description of the systems of charged particles in a model based on the Vlasov kinetic equation. Equations (6) themselves are derived from the Maxwell–Vlasov equations by integrating over the initial conditions [10]—a method that is widely used in the theory of plasma relativistic microwave electronics.

The above explanations concerning dispersion relation (4) imply that, for a waveguide with a dense plasma, we can set, with a good degree of accuracy, $g_{pn} = \omega_p^2$ (and, analogously, $g_{bn} = \omega_b^2$) for all modes of the original perturbation. However, we do not do so in order to treat the problem in the most general way. We also do not specify here the parameters q_n describing the coupling between the plasma waves and the beam waves. For a dense plasma, we can use the order-of-magnitude estimate $q_1 \sim S_w^{-1}\exp(-2\omega_p u^{-1}\gamma^{-1}|\mathbf{r}_b - \mathbf{r}_p|)$, where S_w is the cross-sectional area of the waveguide and $|\mathbf{r}_b - \mathbf{r}_p|$ is the radial separation between the beam and the plasma (of course, it is assumed that $|\mathbf{r}_b - \mathbf{r}_p| \neq 0$, because otherwise, the exponential in the expression for q_1 reduces to unity). If the plasma is dense, then, by virtue of inequality (2), the parameter q_1 is small, and the parameters q_n with $n \geq 2$ are even smaller. In addition to the assumption of a dense plasma, the second main assumption used in our analysis is that the coupling parameters q_n are small. For $q_n = 0$, the set of Eqs. (6) splits into two independent subsets, one for the plasma and one for the beam. Consequently, for small q_n values, we can speak of a weak interaction between the beam and the plasma. In plasma microwave electronics, such interaction is called interaction in the regime of the collective Cherenkov effect [2, 3, 6, 8]. Our problem now is to solve the set of complicated nonlinear equations (6) analytically. In this way, we utilize the expansion methods that were proposed in [11–13] and were described in detail in [8], specifically, the method of expansion in small perturbations of the trajectories and momenta of the beam and plasma electrons. In the expansions, we retain nonlinear terms up to third order, in which case, in the basic equations (6), it is sufficient to take into account only the first two ($n = 1, 2$) modes of the original perturbation.

3. We introduce the dimensionless variables and parameters

$$\tau = \sqrt{g_{b1}\gamma^{-3}}t, \quad \eta = \xi\frac{v_b - u}{u}, \quad p = \frac{1}{\sqrt{1-\mu_0\eta}},$$
$$\xi = \frac{k_z u}{\sqrt{g_{b1}\gamma^{-3}}}, \quad \mu_0 = 2\frac{u^2}{c^2}\gamma^2\frac{\sqrt{g_{b1}\gamma^{-3}}}{k_z u}, \tag{8}$$

and write the coordinates of the beam electrons as

$$y_b = \xi\tau + y(y_0, t) \tag{9}$$

in order to convert Eqs. (6) to the form

$$\frac{d^2 y_p}{d\tau^2} = -\frac{\gamma^3}{2}i\sum_{n=1}^{2}\left\{\frac{1}{n}\left[\frac{g_{pn}}{g_{b1}}\rho_{pn}\right.\right.$$
$$\left.\left. + \frac{\tilde{\omega}_b^2 q_n}{g_{b1}}\rho_n\exp(-in\xi\tau)\right]\exp(iny_p) - \text{c.c.}\right\},$$
$$\frac{dy}{d\tau} = \frac{1}{\mu_0}\left(1 - \frac{1}{p^2}\right), \tag{10}$$
$$\frac{dp}{d\tau} = -\frac{i}{4}\mu_0$$
$$\times\sum_{n=1}^{2}\left\{\frac{1}{n}\left[\frac{g_{bn}}{g_{b1}}\rho_n + \frac{\tilde{\omega}_p^2 q_n}{g_{b1}}\rho_{pn}\exp(in\xi\tau)\right]\exp(iny) - \text{c.c.}\right\}.$$

Here, p is the momentum of a beam electron and

$$\rho_n = \frac{1}{\pi}\int_0^{2\pi}\exp(-iny)dy_0. \tag{11}$$

Following the above expansion methods, we write the functions y_p, y, and p in the form

$$y_p = y_0 + w_p(\tau) + \frac{1}{2}\sum_{n=1}^{2}[a_{pn}(\tau)\exp(iny_0) + \text{c.c.}],$$
$$y = y_0 + w_b(\tau) + \frac{1}{2}\sum_{n=1}^{2}[a_{bn}(\tau)\exp(iny_0) + \text{c.c.}], \tag{12}$$
$$p = 1 - \delta(\tau) + \frac{1}{2}\sum_{n=1}^{2}[A_n(\tau)\exp(iny_0) + \text{c.c.}].$$

Here, the functions $w_p(\tau)$ and $w_b(\tau)$ describe the changes in the directed motion of plasma electrons in the laboratory frame of reference and in the directed motion of beam electrons in a reference frame moving with the velocity u. It may be said that the functions $w_p(\tau)$ and $w_b(\tau)$, as well as the function $\delta(\tau)$, account for the nonlinear excitation of zeroth spatial modes of the perturbations in the plasma and in the beam (i.e., the excitation of the constant components of the perturbations). In turn, the coefficients $a_{pm}(\tau)$, $a_{bn}(\tau)$, and $A_n(\tau)$ in expansions (12) account for nonzeroth spatial modes of the perturbations in the plasma and in the beam and describe the interaction between the plasma wave and the beam wave and the nonlinear excitation of the higher spatial modes of original perturbations.

Let us derive expressions for the expansion coefficients in representations (12). To do this, we combine

the second and third of Eqs. (10) into one equation:

$$\frac{d^2y}{d\tau^2} = -\frac{1}{2}i\frac{1}{p^3} \times\sum_{n=1}^{2}\left\{\frac{1}{n}\left[\frac{g_{pn}}{g_{b1}}\rho_{pn}+\frac{\tilde{\omega}_p^2 q_n}{g_{b1}}\rho_n\exp(in\xi\tau)\right]\exp(iny)-\text{c.c.}\right\}. \tag{13}$$

Substituting expansions (12) into Eqs. (7), (11), and (13) and assuming that the perturbations of the coordinates y_p and y and the momentum p are small, i.e.,

$$|y_p(y_0,\tau)-y_0-w_p(\tau)| \ll 1,$$
$$|y(y_0,\tau)-y_0-w_b(\tau)| \ll 1, \quad |p-1| \ll 1,$$

we expand the nonlinear terms in Eqs. (7), (11), (10), and (13) in powers of these perturbations and retain terms up to third order. Further, using the orthogonality of the functions $\exp(iny_0)$, we equate to zero the coefficients in front of these functions in Eqs. (7), (10), (11), and (13). As a result, we arrive at Eqs. (A.1)–(A.4) given in the Appendix (see also [8, 11] for details). We seek solutions to these equations in the form

$$a_{b1} = \tilde{a}_{b1}(\tau)\exp(i\tau), \quad a_{b2} = \tilde{a}_{b2}(\tau)\exp(2i\tau),$$
$$a_{p1} = \tilde{a}_{p1}(\tau)\exp\left(-i\sqrt{\frac{g_{p1}}{\gamma^{-3}g_{b1}}}\tau\right),$$
$$a_{p2} = \tilde{a}_{p2}(\tau)\exp\left(-2i\sqrt{\frac{g_{p1}}{\gamma^{-3}g_{b1}}}\tau\right), \tag{14}$$
$$A_1 = \tilde{A}_1(\tau)\exp(i\tau), \quad A_2 = \tilde{A}_2(\tau)\exp(2i\tau),$$

where $\tilde{a}_{p1}$, $\tilde{a}_{p2}$, $\tilde{a}_{b1}$, $\tilde{a}_{b2}$, $\tilde{A}_1$, and $\tilde{A}_2$ are slowly varying amplitudes. Inserting solutions (14) into Eqs. (A.1)–(A.4) yields Eqs. (A.5)–(A.10), which will serve as the basis for our analysis.

Equations (A.1)–(A.10) have the first integrals

$$\frac{dw_p}{d\tau} = \frac{1}{2}\sqrt{\frac{g_{p1}}{g_{b1}\gamma^{-3}}}(|\tilde{a}_{p1}|^2+4|\tilde{a}_{p2}|^2), \tag{15}$$

$$\frac{\mu_0\gamma^{-3}}{2}\tilde{\omega}_p^2\frac{dw_p}{d\tau} = \tilde{\omega}_b^2\delta, \tag{16}$$

the latter of which can be obtained directly from the first and third of Eqs. (10). In deriving integrals (15) and (16), we used the following initial conditions for Eqs. (A.5)–(A.10):

$$a_{p1}(0)=0, \quad a_{p2}(0)=0, \quad a_{b1}(0)=a_0,$$
$$a_{b2}(0)=0, \quad \delta(0)=0, \quad \frac{dw_p}{d\tau}(0)=\frac{dw_b}{d\tau}(0)=0. \tag{17}$$

These conditions imply that, first, the electron beam is initially modulated in density at the wavelength $2\pi/k_z$ (the relative modulation depth being $\sim a_0$) and, second, there are no other perturbations at the initial time. From Eqs. (A.3) and integral (16), we obtain the relationship

$$\delta = \frac{\mu_0\gamma^{-3}}{4}\frac{\tilde{\omega}_p^2}{\tilde{\omega}_b^2}\sqrt{\frac{g_{p1}}{g_{b1}\gamma^{-3}}}(|\tilde{a}_{p1}|^2+4|\tilde{a}_{p2}|^2). \tag{18}$$

This relationship and Eqs. (A.4) yield the following third-order equation:

$$\frac{dw_b}{d\tau} = -\frac{\gamma^{-3}}{2}\frac{\tilde{\omega}_p^2}{\tilde{\omega}_b^2}\sqrt{\frac{g_{p1}}{g_{b1}\gamma^{-3}}}|\tilde{a}_{p1}|^2-\frac{3}{2}\mu_0|\tilde{A}_1|^2. \tag{19}$$

4. Now, we take into account Eqs. (15) and (19) and make a change of variables in Eqs. (A.5)–(A.10):

$$\tilde{a}_{p1} = b_{p1}\exp(iw_p), \quad \tilde{a}_{b1} = b_{b1}\exp(iw_b),$$
$$\tilde{A}_1 = B_1\exp(iw_b),$$
$$\tilde{a}_{p2} = b_{p2}\exp(2iw_p), \quad \tilde{a}_{b2} = b_{b2}\exp(2iw_b), \tag{20}$$
$$\tilde{A}_2 = B_2\exp(2iw_b).$$

In view of the nonresonant nature of the excitation of the second modes, we neglect the derivatives of the slowly varying amplitudes $\tilde{a}_{p2}$, $\tilde{a}_{b2}$, and $\tilde{A}_2$. As a result, we arrive at the following set of three first-order equations with cubic nonlinearities:

$$2i\frac{db_{b1}}{d\tau} = \frac{\tilde{\omega}_p^2}{\tilde{\omega}_b^2}\sqrt{\frac{g_{p1}}{g_{b1}\gamma^{-3}}}|b_{p1}|^2b_{b1} + \frac{1}{2}\frac{3(g_{b2}-g_{b1})}{g_{b2}-4g_{b1}}|b_{b1}|^2b_{b1} + \frac{3}{2}i\mu_0\frac{g_{b1}-g_{b2}}{g_{b2}-4g_{b1}}|b_{b1}|^2B_1-3\mu_0|B_1|^2b_{b1}-\frac{\tilde{\omega}_p^2q_1}{g_{b1}}b_{p1}, \tag{21}$$

$$2i\sqrt{\frac{g_{p1}}{g_{b1}\gamma^{-3}}}\frac{db_{p1}}{d\tau} = \gamma^3\left\{\left(\frac{g_{p1}}{g_{b1}}-\frac{1}{2}\frac{(g_{p2}-g_{p1})^2}{(g_{b2}-4g_{b1})g_{b1}}+\frac{1}{2}\frac{g_{p2}-g_{p1}}{g_{b1}}\right)|b_{p1}|^2b_{p1} + \frac{\tilde{\omega}_b^2q_1}{g_{b1}}b_{b1}\right\}, \tag{22}$$

$$\frac{dB_1}{d\tau} = -\frac{i}{2}\frac{\tilde{\omega}_p^2}{\tilde{\omega}_b^2}\sqrt{\frac{g_{p1}}{g_{b1}\gamma^{-3}}}|b_{p1}|^2B_1 + \frac{3}{2}i\mu_0|B_1|^2B_1-iB_1-\frac{1}{2}\left(b_{b1}+\frac{\tilde{\omega}_p^2q_1}{g_{b1}}b_{p1}\right). \tag{23}$$

Before proceeding to a solution of Eqs. (21)–(23), we write them in the first-order approximation in the amplitudes, in which case Eq. (23) drops out of the analysis:

$$2i\frac{db_{b1}}{d\tau} = -\frac{\tilde{\omega}_p^2 q_1}{g_{b1}} b_{p1},$$
$$2i\sqrt{\frac{g_{p1}}{g_{b1}\gamma^{-3}}}\frac{db_{p1}}{d\tau} = \gamma^3\frac{\tilde{\omega}_b^2 q_1}{g_{b1}} b_{b1}. \quad (24)$$

The growing solution to Eqs. (24) describes the resonant beam–plasma instability in the regime of the collective Cherenkov effect:

$$b_{b1}, b_{p1} \sim \exp(\delta_0\tau) = \exp(\delta\omega t),$$
$$\delta_0 = \frac{1}{2}\frac{q_1\tilde{\omega}_p\tilde{\omega}_b\gamma^{3/4}}{\sqrt{g_{b1}}(g_{p1}g_{b1})^{1/4}}, \quad (25)$$

where δ_0 is the dimensionless growth rate of the beam instability in question and

$$\delta\omega = \frac{1}{2}\frac{q_1\tilde{\omega}_p\tilde{\omega}_b\gamma^{-3/2}}{(g_{p1}g_{b1}\gamma^{-3})^{1/4}} \quad (26)$$

is its dimensional growth rate. Obviously, the requirement that the amplitudes in solution (14) be slowly varying reduces to the inequality

$$\delta_0 \ll 1, \quad (27)$$

which indicates that the interaction between the plasma wave and the beam wave is weak.

Equations that are similar to Eqs. (21)–(23) and contain cubic nonlinearities are well known in nonlinear plasma theory (see, e.g., [14]). Their solutions are expressed in terms of elliptic functions and are rather complicated. However, in the form in which they are presented here, Eqs. (21)–(23) cannot be solved analytically. That is why we simplify the equations by keeping only their linear terms. Then, from Eq. (23), we obtain an approximate expression for B_1 ($B_1 \approx ib_{b1}/2$) and substitute this expression into Eqs. (21) and (22). As a result, taking into account initial conditions (17), we can reduce Eqs. (21) and (22) to a single equation for the quantity $x = |b_{b1}|^2$:

$$\left(\frac{dx}{dt}\right)^2 = A_4x^4 + A_3x^3 + A_2x^2 + A_1x + A_0. \quad (28)$$

Here, we have introduced the notation ($x_0 = a_0^2$)

$$A_0 = -\frac{1}{16}\left(\alpha_b - 2 - \frac{\tilde{\omega}_b^2}{\tilde{\omega}_p^2}\alpha_p\right)^2 x_0^4,$$

$$A_1 = \frac{q_1^2\tilde{\omega}_b^2\tilde{\omega}_p^2}{g_{b1}\sqrt{g_{b1}g_{p1}}}x_0 - \frac{1}{4}\left(\alpha_b - 2 - \frac{\tilde{\omega}_b^2}{\tilde{\omega}_p^2}\alpha_p\right)\left(\frac{\tilde{\omega}_b^2}{\tilde{\omega}_p^2}\alpha_p + 1\right)x_0^3,$$

$$A_2 = \frac{q_1^2\tilde{\omega}_b^2\tilde{\omega}_p^2\gamma^{\frac{3}{2}}}{g_{b1}\sqrt{g_{b1}g_{p1}}} - \frac{1}{4}\left(\alpha_b - 2 - \frac{\tilde{\omega}_b^2}{\tilde{\omega}_p^2}\alpha_p\right)\left(\frac{\tilde{\omega}_b^2}{\tilde{\omega}_p^2}\alpha_p + 1\right)^2 x_0^2, \quad (29)$$

$$A_3 = -\frac{1}{4}\left(\frac{\tilde{\omega}_b^2}{\tilde{\omega}_p^2}\alpha_p\gamma^3 + \alpha_b\right)\left(\frac{\tilde{\omega}_b^2}{\tilde{\omega}_p^2}\alpha_p + 1\right)x_0,$$

$$A_4 = -\frac{1}{4}\left(\frac{\tilde{\omega}_b^2}{\tilde{\omega}_p^2}\alpha_p\gamma^3 + \alpha_b\right),$$

where the quantities α_p and α_b are given by the formulas

$$\alpha_b = 1 - \frac{3}{2}\frac{g_{b2} - g_{b1}}{g_{b2} - 4g_{b1}} - \frac{9}{4}\mu_0\frac{g_{b1}}{g_{b2} - 4g_{b1}},$$
$$\alpha_p = 1 - \frac{3}{2}\frac{g_{p2} - g_{p1}}{g_{p2} - 4g_{p1}}. \quad (30)$$

Below, these quantities, which play an important role in our analysis, will be called the coefficients of nonlinear stabilization of the instability.

The terms in coefficients (30) are of different origins. For instance, the term proportional to μ_0 describes the nonlinear dependence of the frequency of the beam wave on its amplitude due to relativistic effects. An analogous term for the plasma is absent since the plasma is nonrelativistic. The terms containing the factor 3/2 account for the dependence of the frequencies of the beam wave and plasma wave on their amplitudes due to nonrelativistic effects. For a dense plasma such that inequality (2) is satisfied, we have $g_{b2} \approx g_{p1} \approx \omega_p^2$, $g_{b2} \approx g_{b1} \approx \omega_b^2$, so that, in coefficients (30), these terms are unimportant. This reflects the well-known fact that the frequency of a one-dimensional potential plasma wave is independent of its amplitude [15]. One more nonlinear mechanism for stabilization of the beam and plasma waves is the change in the mean velocity of the beam and plasma electrons, with the result that resonance condition fails to hold. In expansions (12), this mechanism is described by the terms $w_p(\tau)$ and $w_b(\tau)$, and, in coefficients (30), it is accounted for by the terms that are equal to unity.

Performing the corresponding manipulations, we reduce the solution to Eq. (28) to the form

$$x = |b_{b1}|^2 = \frac{2x_0\left(1+\frac{\tilde{\omega}_b^2}{\tilde{\omega}_p^2}\alpha_p\right)\left(x_0+\sqrt{x_0^2+\tilde{x}^2\left(1+\frac{\tilde{\omega}_b^2}{\tilde{\omega}_p^2}\alpha_p\right)^{-2}}\right)}{2\left(1+\frac{\tilde{\omega}_b^2}{\tilde{\omega}_p^2}\alpha_p\right)\left(x_0+\sqrt{x_0^2+\tilde{x}^2\left(1+\frac{\tilde{\omega}_b^2}{\tilde{\omega}_p^2}\alpha_p\right)^{-2}}\right)\mathrm{cn}^2(y,r)+x_0\,\mathrm{sn}^2(y,r)}. \quad (31)$$

Here, cn(y, r) and sn(y, r) are the Jacobian elliptic functions, whose argument and modulus are given by the expressions

$$y = \delta_0\tau;$$
$$r = 1-\frac{x_0}{2}\left(1+\frac{\tilde{\omega}_b^2}{\tilde{\omega}_p^2}\alpha_p\right)\tilde{x}^{-2}\sqrt{x_0^2+\tilde{x}^2\left(1+\frac{\tilde{\omega}_b^2}{\tilde{\omega}_p^2}\alpha_p\right)^{-2}}, \quad (32)$$

where δ_0 is defined in formulas (25) and the quantity $\tilde{x}^2$ is

$$\tilde{x}^2 = \frac{4q_1^2\tilde{\omega}_b^2\tilde{\omega}_p^6\gamma^{\frac{3}{2}}}{(\tilde{\omega}_b^2\alpha_p\gamma^3+\alpha_b\tilde{\omega}_p^2)^2 g_{b1}\sqrt{g_{b1}g_{p1}}}. \quad (33)$$

The instability saturation time, i.e., the time during which amplitude (31a) saturates, is determined by the expression

$$\tau_0 = \frac{1}{\delta_0}\ln\left[4\left(\frac{x_0}{\tilde{x}^2}\left(1+\frac{\tilde{\omega}_b^2}{\tilde{\omega}_p^2}\alpha_p\right)\sqrt{x_0^2+\tilde{x}^2\left(1+\frac{\tilde{\omega}_b^2}{\tilde{\omega}_p^2}\alpha_p\right)^{-2}}\right)^{-\frac{1}{2}}\right]. \quad (34)$$

Under the assumption that the field is switched on adiabatically (which corresponds to $x_0 = 0$ or, more precisely, to the switching-on of the field in the infinite past, $|b_{b1,\,p1}|_{\tau\to-\infty} \longrightarrow 0$), Eq. (28) simplifies substantially and its solution is given by the formula

$$x = |b_{b1}|^2 = \frac{4q_1\tilde{\omega}_p^2\gamma^{\frac{3}{4}}}{\alpha_p\tilde{\omega}_p^2+\alpha_p\tilde{\omega}_b^2\gamma^3}\sqrt{\frac{\tilde{\omega}_p^2\tilde{\omega}_b^2}{g_{b1}(g_{p1}g_{b1})^{\frac{1}{2}}}}\cosh^{-1}(2\delta_0\tau). \quad (35)$$

For both nonadiabatic and adiabatic initial conditions, the plasma wave amplitude $|b_{p1}|$ can be calculated using the following first integral of Eqs. (21) and (22):

$$\sqrt{\frac{g_{p1}}{g_{b1}\gamma^{-3}}}\tilde{\omega}_p^2|b_{p1}|^2 = \tilde{\omega}_b^2\gamma^3(|b_{b1}|^2-a_0^2). \quad (36)$$

For adiabatic initial conditions, we obtain

$$|b_{p1}|^2 = \frac{4q_1\tilde{\omega}_b^2\gamma^{\frac{9}{4}}}{\alpha_b\tilde{\omega}_p^2+\alpha_p\tilde{\omega}_b^2\gamma^3}\sqrt{\frac{\tilde{\omega}_p^2\tilde{\omega}_b^2}{g_{p1}(g_{p1}g_{b1})^{\frac{1}{2}}}}\cosh^{-1}(2\delta_0\tau). \quad (37)$$

For nonadiabatic initial conditions, the squared absolute value of the plasma wave amplitude is equal to

$$|b_{p1}|^2 = \frac{\tilde{\omega}_b^2\gamma^3}{\tilde{\omega}_p^2}\sqrt{\frac{g_{b1}\gamma^{-3}}{g_{p1}}}\left[\frac{2x_0\left(1+\frac{\tilde{\omega}_b^2}{\tilde{\omega}_p^2}\alpha_p\right)\left(x_0+\sqrt{x_0^2+\tilde{x}^2\left(1+\frac{\tilde{\omega}_b^2}{\tilde{\omega}_p^2}\alpha_p\right)^{-2}}\right)}{2\left(1+\frac{\tilde{\omega}_b^2}{\tilde{\omega}_p^2}\alpha_p\right)\left(x_0+\sqrt{x_0^2+\tilde{x}^2\left(1+\frac{\tilde{\omega}_b^2}{\tilde{\omega}_p^2}\alpha_p\right)^{-2}}\right)\mathrm{cn}^2(y,r)+x_0\,\mathrm{sn}^2(y,r)}-a_0^2\right]. \quad (31a)$$

Formula (31a) shows that, for $x_0 \ll x$, the maximum value of the solution is approximately equal to $x_{\max} \approx 2\tilde{x}$; i.e., we have $|b_{b1}|^2_{\max} = 2\tilde{x}$. Consequently, for $x_0 \ll \tilde{x}$, expression (35) for the time of the nonlinear saturation of the instability can be substantially simplified:

$$\tau_0 = \frac{1}{\delta_0}\ln\left[4\sqrt{\frac{\tilde{x}}{x_0}}\right] = \frac{1}{\delta_0}\ln\left[4\frac{|b_{b1}|_{\max}}{\sqrt{2}a_0}\right]. \quad (38)$$

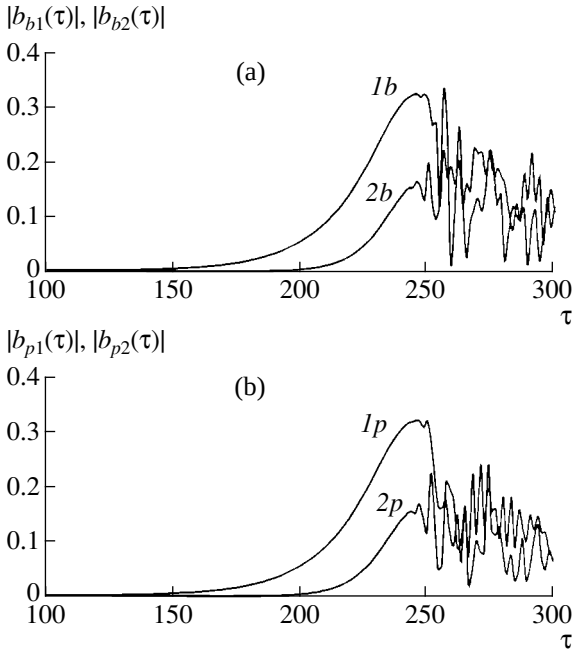

Fig. 2. Dependence of the amplitudes of the first and second harmonics of (a) the density of a nonrelativistic ($\gamma \longrightarrow 1$) beam and (b) the plasma density on the dimensionless time τ.

It follows from Eqs. (7), (9), (11), (12), (14), (20), and (36) that the maximum dimensionless amplitudes of the first modes of the beam wave and plasma wave have the form

$$|b_{b1}|^2_{\max} = \frac{4q_1\tilde{\omega}_p^2\gamma^{\frac{3}{4}}}{\alpha_b\tilde{\omega}_p^2 + \alpha_p\tilde{\omega}_b^2\gamma^3}\sqrt{\frac{\tilde{\omega}_p^2\tilde{\omega}_b^2}{g_{b1}(g_{p1}g_{b1})^{\frac{1}{2}}}},$$
$$|b_{p1}|^2_{\max} = \frac{4q_1\tilde{\omega}_b^2\gamma^{\frac{9}{4}}}{\alpha_b\tilde{\omega}_p^2 + \alpha_p\tilde{\omega}_b^2\gamma^3}\sqrt{\frac{\tilde{\omega}_p^2\tilde{\omega}_b^2}{g_{p1}(g_{p1}g_{b1})^{\frac{1}{2}}}}. \quad (39)$$

The maximum dimensional amplitudes, which determine the absolute depth of the nonlinear electron density modulation of the beam and the plasma, are obtained by multiplying expressions (39) by the unperturbed beam density n_{0b} and by the unperturbed plasma density n_{0p}, respectively. We thus arrive at the following applicability condition for the expansion method used in our study, namely, the method of expansion in small perturbations of the trajectories and momenta of the beam and plasma electrons:

$$|b_{b1}|_{\max} \ll 1, \quad |b_{p1}|_{\max} \ll 1. \quad (40)$$

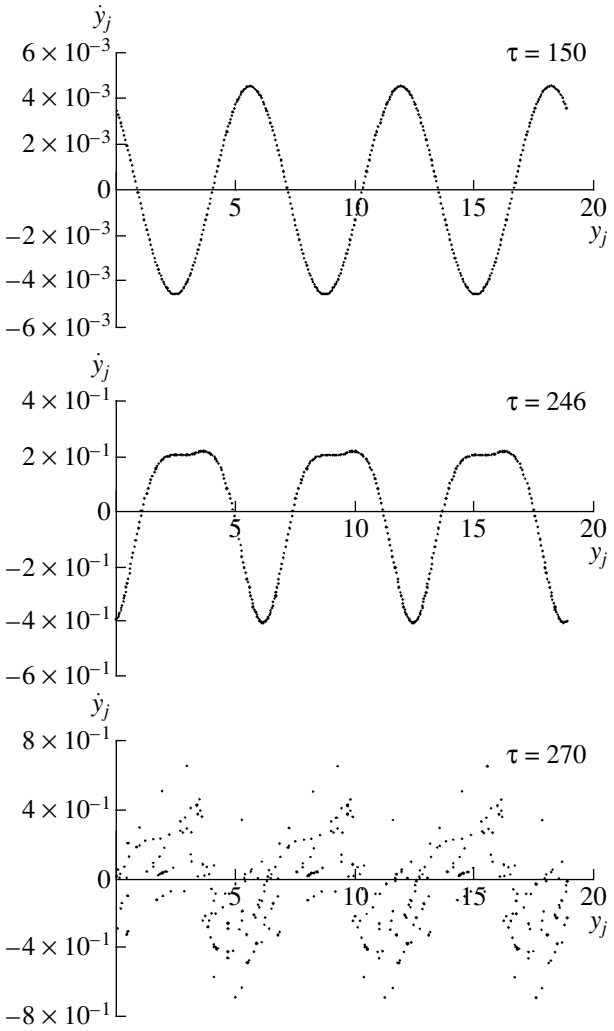

Fig. 3. Phase planes of the electrons of a nonrelativistic ($\gamma \longrightarrow 1$) beam before the instability saturation, at the time of saturation, and after the saturation. In this and other figures, $j = 1, 2, 3, \ldots$ is the number of the beam electron.

Formulas (39) for the maximum amplitudes of the beam wave and plasma wave are valid not only for the perturbations that are switched on adiabatically in the infinite past; they are also approximately valid in a general case [see solutions (32)] under the condition that the initial beam modulation depth is small, which reduces to the condition $x_0 \ll \tilde{x}$.

5. In order to determine more realistic applicability limits of the nonlinear analytic theory developed here, it is necessary to compare the exact solutions to Eqs. (6) or (10) with the solutions to Eqs. (21)–(23) that are obtained by means of the above expansion methods to within terms containing cubic nonlinearities. Equations of form (6) can only be solved numerically by using a macroparticle method [16]. To make the problem as simple as possible while still preserving all its main

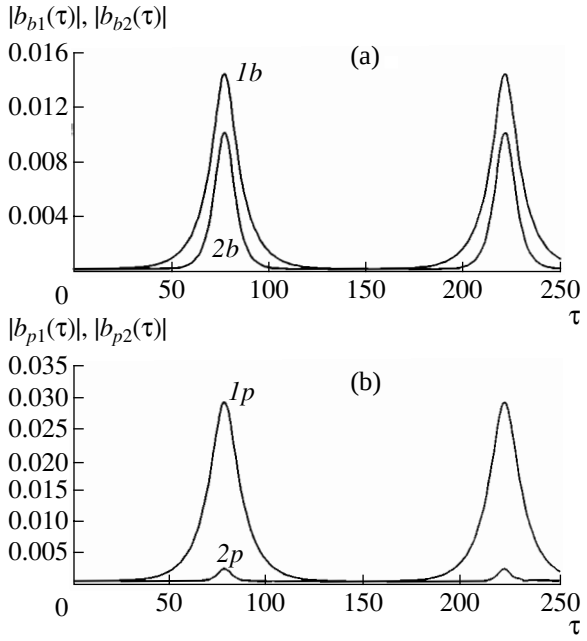

Fig. 4. Dependence of the amplitudes of the first and second harmonics of (a) the density of a beam with $\gamma = 3$ and (b) the plasma density on the dimensionless time τ.

mathematical properties, we reduce the number of free parameters. To do this, we set

$$g_{pn} = g_{bn}, \quad n = 1, 2, \ldots, \tag{41}$$

which, in fact, indicates that the beam and plasma densities are the same. In this case, we have $\mu_0 = 2(\gamma^2 - 1)(1 + \gamma^{3/2})$, $\xi = 1 + \gamma^{3/2}$, and Eqs. (6) or (10) take the form [see expressions (8), (9), (11)]

$$\frac{d^2 y_p}{d\tau^2} = -\frac{\gamma^3}{2} i \sum_{n=1}^{2} \left\{ \frac{1}{n} [\rho_{pn} + \tilde{q}_n \rho_n \exp(-in\xi\tau)] \exp(iny_p) - \text{c.c.} \right\},$$

$$\frac{d^2 y}{d\tau^2} = -\frac{i}{2}(1 - \mu_0 \eta)^{3/2} \times \sum_{n=1}^{2} \left\{ \frac{1}{n} [\rho_n + \tilde{q}_n \rho_{pn} \exp(in\xi\tau)] \exp(iny) - \text{c.c.} \right\}. \tag{42}$$

Here,

$$\tilde{q}_n = \left(\frac{\tilde{\omega}_b^2 \tilde{\omega}_p^2 q_n^2}{g_{bn} g_{pn}} \right)^{1/2} \tag{43}$$

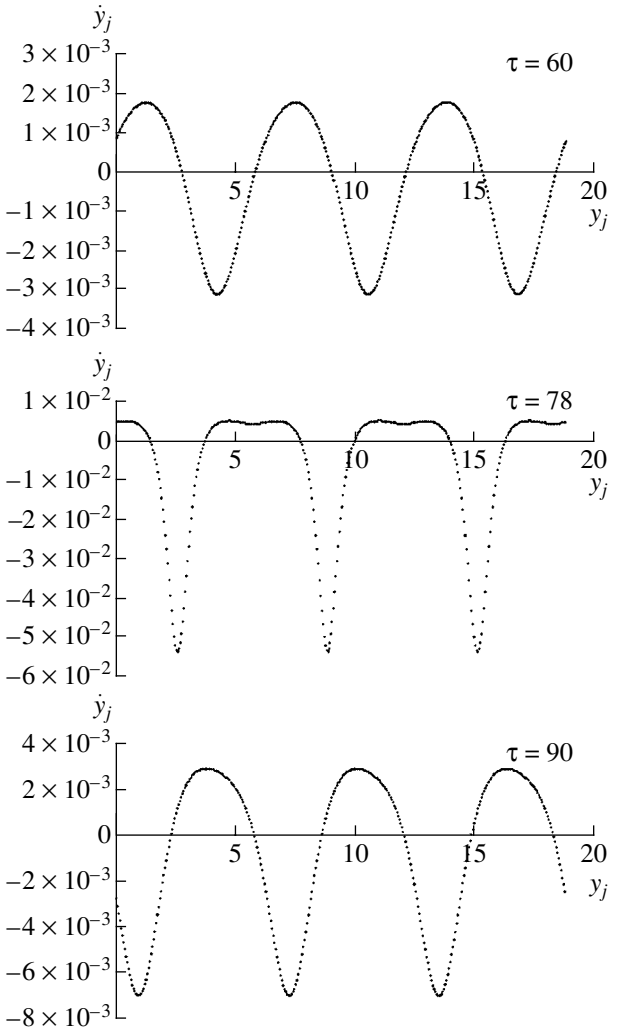

Fig. 5. Phase planes of the electrons of a beam with $\gamma = 3$ before the instability saturation, at the time of saturation, and after the saturation.

is the normalized parameter determining the coupling between the beam wave and the plasma wave. It can be shown that this parameter lies within the range $0 < \tilde{q}_n \le 1$ [6].

We also write out formulas (39) and inequality (27) for a particular case corresponding to conditions (41):

$$|b_{b1}|^2_{\max} = \frac{4\tilde{q}_1 \gamma^{3/4}}{\alpha_b + \alpha_p \gamma^3}, \quad |b_{p1}|^2_{\max} = \frac{4\tilde{q}_1 \gamma^{9/4}}{\alpha_b + \alpha_p \gamma^3}, \tag{39a}$$

$$\delta_0 = \frac{1}{2}\tilde{q}_1 \gamma^{3/4} \ll 1, \tag{27a}$$

where $\alpha_b = 1 + (3/4)\mu_0$ and $\alpha_p = 1$. The problem given by Eqs. (42), formulas (39a), and inequality (27a) contains only two parameters, γ and $\tilde{q}_1$. Let us analyze the

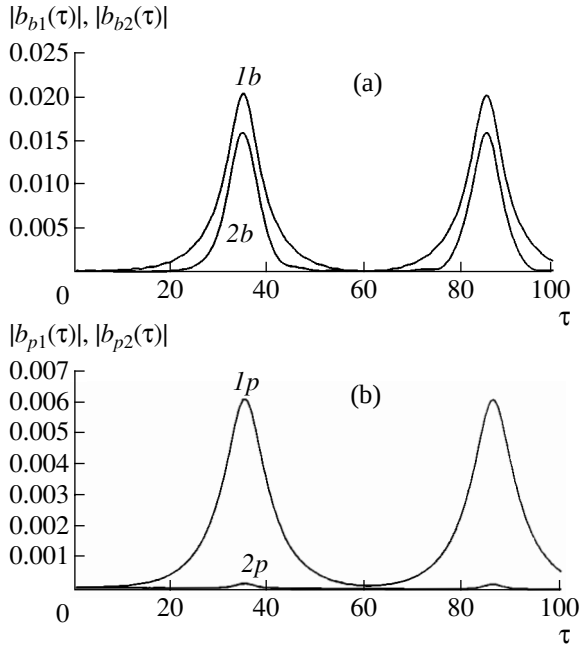

Fig. 6. Dependence of the amplitudes of the first and second harmonics of (a) the density of a beam with $\gamma = 6$ and (b) the plasma density on the dimensionless time τ.

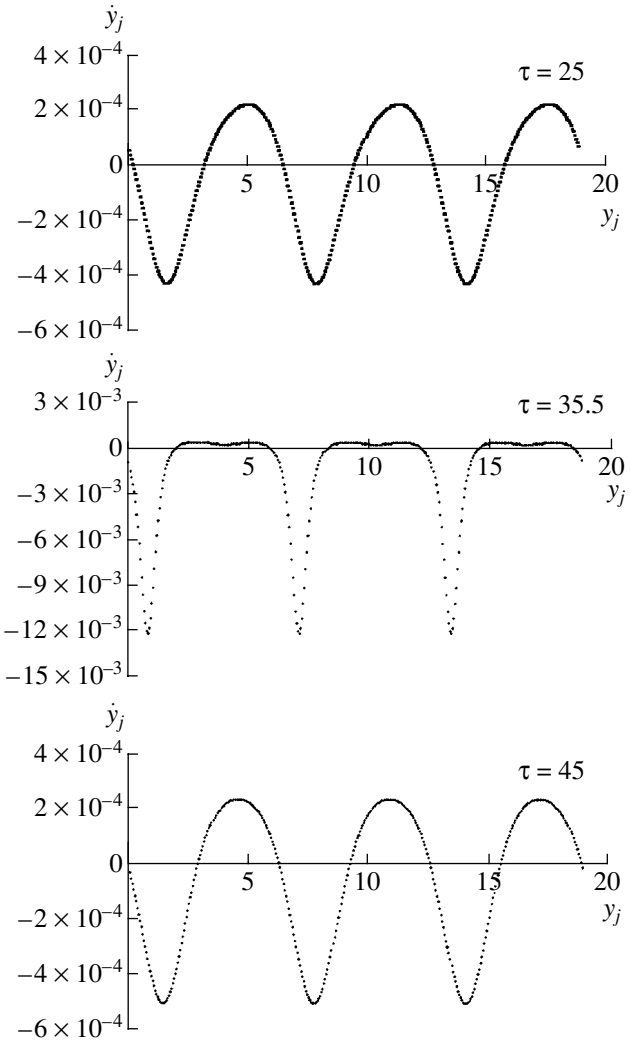

Fig. 7. Phase planes of the electrons of a beam with $\gamma = 6$ before the instability saturation, at the time of saturation, and after the saturation.

results of solving this problem numerically for $\tilde{q}_1 = 0.1$, for the initial beam modulation depth $a_0 = 10^{-5}$, and for different values of the relativistic factor γ of the beam.

Figures 2 and 3 illustrate the results of a numerical solution of Eqs. (42) for a nonrelativistic electron beam ($\gamma \longrightarrow 1$). Figure 2 shows how the dimensionless amplitudes of the harmonics of the beam and plasma densities depend on the dimensionless time τ. In this figure, curve *1b* is for $|\rho_1(\tau)| = |b_{b1}(\tau)|$, curve *2b* is for $|\rho_2(\tau)| = |b_{b2}(\tau)|$, curve *1p* is for $|\rho_{p1}(\tau)| = |b_{p1}(\tau)|$, and curve *2p* is for $|\rho_{p2}(\tau)| = |b_{p2}(\tau)|$. Figure 3 shows the phase planes of the beam electrons at three characteristic times. The vertical axis in the phase plane represents $\dot{y}_j(\tau)$ and the horizontal axis represents $y_j(\tau)$, where j is the number of a beam electron, or, more precisely, of a macroparticle that models the beam electrons. It can be seen in Fig. 2 that the amplitudes of the harmonics of the beam and plasma densities behave in essentially the same manner. The explanation for this result is quite clear: the beam is nonrelativistic ($\gamma \longrightarrow 1$) and the unperturbed electron densities of the beam and the plasma are the same [see conditions (41)]. On the time scales on which the instability saturates ($\tau < 240$–250), analytical solutions agree well with the numerical ones. However, just after the instability saturation, the beam–plasma system rapidly becomes completely stochastic. This stochastization (or phase mixing) is also seen in the phase planes of the beam electrons (Fig. 3). Thus, at $\tau = 150$ and $\tau = 240$, the distributions of the beam electrons over the phase planes are regular, which is characteristic of the linear and slightly nonlinear stages of the quasi-harmonic wave process. However, already at $\tau = 270$, the distribution is seen to be completely irregular. We do not yet know the causes of such an anomalous stochastization of the beam–plasma system, but we are sure that it does not stem from numerical effects in computations. The small values of the saturation amplitudes ($|b_{b1}| \approx |b_{p1}| < 0.4$) and the structure of the phase planes provide evidence that the anomalous stochastization cannot be associated with such well-studied nonlinear processes as trapping of the beam electrons by the plasma wave [17] or their self-trapping by the wave of the beam charge density [18].

The results of simulations of a relativistic beam with $\gamma = 3$ are illustrated in Figs. 4 and 5, which show the amplitudes of the harmonics of the beam and plasma densities and the phase planes of the beam electrons

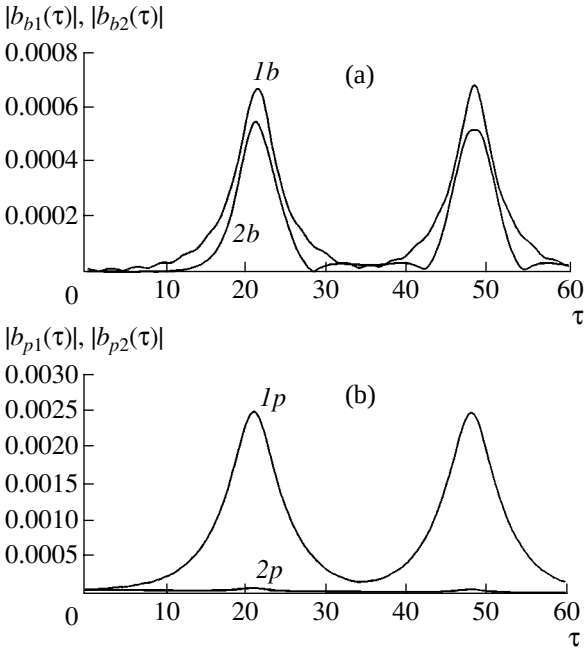

Fig. 8. Dependence of the amplitudes of the first and second harmonics of (a) the density of a beam with $\gamma = 9$ and (b) the plasma density on the dimensionless time τ.

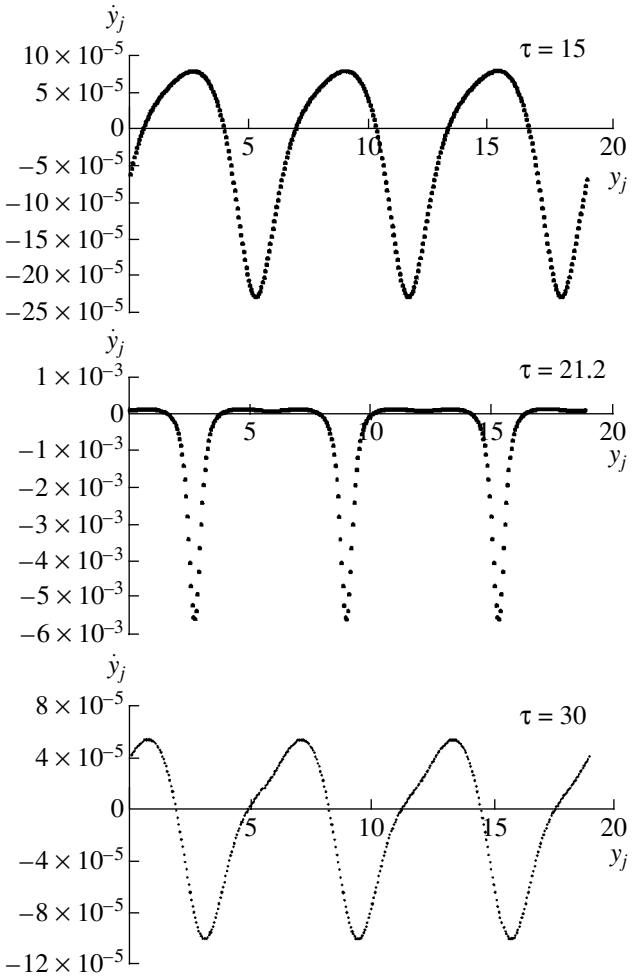

Fig. 9. Phase planes of the electrons of a beam with $\gamma = 9$ before the instability saturation, at the time of saturation, and after the saturation.

(the notation is the same as in Figs. 2, 3). The solutions are seen to differ radically from those for a nonrelativistic beam. In Fig. 4, the dependence of the amplitudes of the harmonics on the time τ is essentially regular and soliton-like in character. The time evolutions of the amplitudes are satisfactorily described by formulas (32). The maximum modulation depth of the beam density is less than that of the plasma density, for which the obvious reason is the relativistic nature of the beam. On the other hand, the amplitude of the second harmonic of the beam density is larger than the amplitude of the second harmonic of the plasma density. Since the higher harmonics are excited due to nonlinear effects, it can be expected that, for a beam with a large γ value, the relativistic nonlinearities will play a dominant role. That the system exhibits no stochastic behavior is also evidenced by the phase planes shown in Fig. 5. In this figure, the phase plane at $\tau = 78$ corresponds to the instability saturation. At a later time ($\tau = 90$), the beam electrons are distributed over the phase plane in essentially the same manner as in the stage before the saturation ($\tau = 60$). It can be said that, after the instability saturates, the electron beam tends to relax to its weakly perturbed initial state. The same is true of the plasma electrons, the phase planes of which are not presented here.

Figures 6 and 7 illustrate the results obtained for an electron beam with a larger relativistic factor, $\gamma = 6$. All of the above features of the behavior of a plasma waveguide system with such a beam are seen to be even more pronounced. Generally, the best agreement (not only qualitative but also quantitative) between the predictions of the analytic theory developed here and the solution to the exact nonlinear problem is observed for beams with relativistic factors in the range $\gamma \approx 2$–6.

Figures 8 and 9 refer to an electron beam with $\gamma = 9$. The solutions are seen to be similar in character to those obtained above. This is especially true for the time evolutions of the amplitudes of the harmonics of the plasma density (curves *1p*, *2p*). However, some features of the time evolutions of the amplitudes of the harmonics of the beam density (curves *1b*, *2b*) cannot be described in terms of solution (32a). The phase planes of the beam electrons in Fig. 9 also differ from those in Figs. 7 and 5: the electron distributions before ($\tau = 15$) and after ($\tau = 30$) the instability saturation are both seen to be highly asymmetric. The larger the relativistic factor γ, the more pronounced the difference between analytical and numerical solutions.

The discrepancy between analytical and numerical solutions for large γ values cannot be explained either

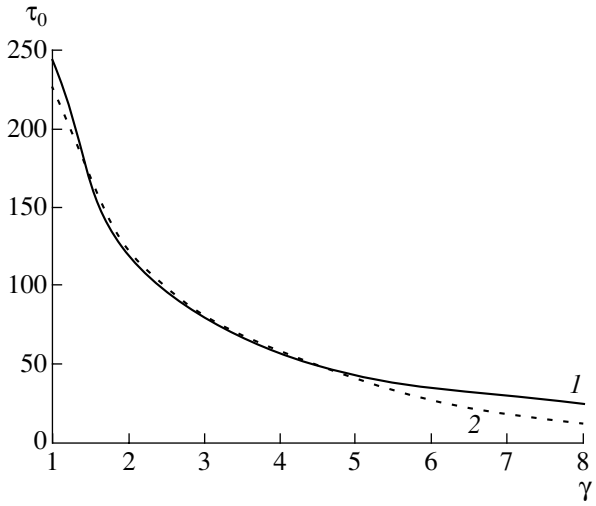

Fig. 10. Dependence of the dimensionless time τ_0 of the instability saturation on the relativistic factor γ. Curve *1* shows the results of numerical simulations, and curve *2* is calculated from formula (35).

in terms of the violation of inequality (27a) (for $\gamma = 9$, this inequality is still satisfied by a large margin) or in terms of the increase in the modulation depth of the beam density (as can be seen from the figures, the modulation depth decreases as γ increases). The reason is that, for $\gamma \gg 1$, the perturbation $\tilde{p}$ in the representation $p = 1 + \tilde{p}$ of the momentum is large [see the third of expansions (12)]. In this case, it is mathematically illegitimate to expand the right-hand side of the second of Eqs. (10) in powers of $\tilde{p}$. Hence, the problem is to develop a correct description of the relativistic nonlinearities in the equation of motion for beam electrons. This problem is postponed to a future paper.

Nevertheless, there exists a considerable range of γ values in which analytical solutions agree fairly well with the numerical ones. To complete the analysis, we present some results that confirm the efficiency and reliability of the analytic methods developed above. The dependence of the instability saturation time on γ is demonstrated in Fig. 10, in which curve *1* shows the results of numerical simulations and curve *2* shows the results of analytical calculations from expression (35). At $\gamma \longrightarrow 1$, the discrepancy between analytical and numerical results is slight, but it becomes significant at large γ values. Moreover, the instability saturation time calculated from formula (35) becomes negative at a sufficiently large value of γ. That is why the instability in a plasma waveguide with an ultrarelativistic electron beam requires a separate study.

In order not to come to the erroneous conclusion that the time scale on which the instability develops decreases as the relativistic factor of the beam increases, recall that the dimensional time t is related to the dimensionless time τ by the formula $t = \text{const}\gamma^{3/2}\tau$ [see expressions (8)]. Figure 11 illustrates the numerically calculated dependence of the instability saturation time on the relativistic factor γ. In this figure, curve *2*, which coincides with the corresponding curve in Fig. 10, shows the dimensionless saturation time, and curve *1* was computed with allowance for the multiplication factor $\gamma^{3/2}$. The actual instability saturation time is given precisely by curve *1*; i.e., it increases with increasing γ.

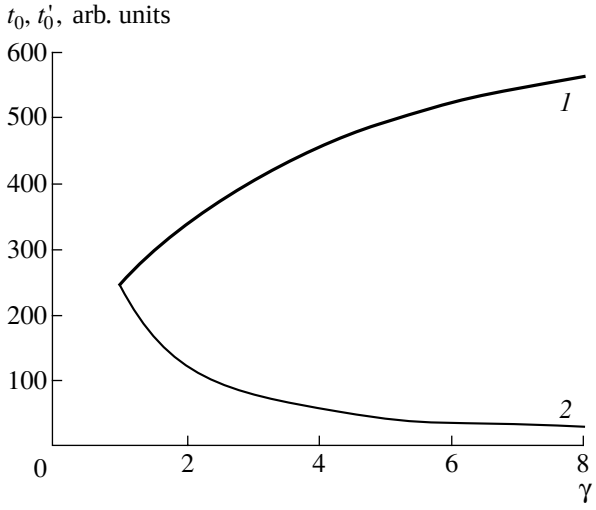

Fig. 11. Instability saturation time calculated numerically as a function of the relativistic factor γ without (t_0, curve *1*) and with (t_0', curve *2*) allowance for the multiplication factor $\gamma^{3/2}$.

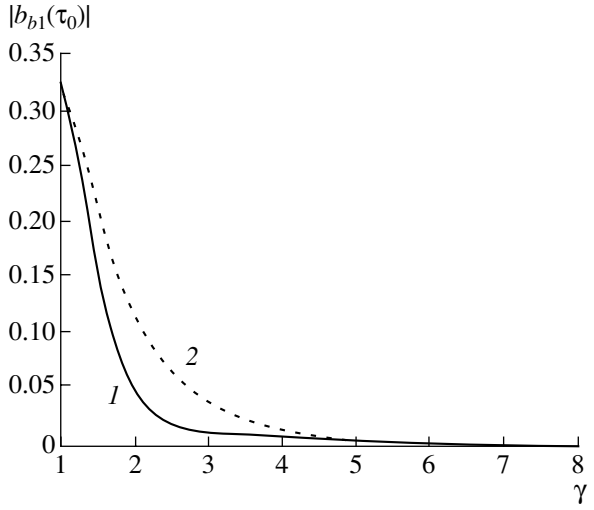

Fig. 12. Dependence of the amplitude of the first harmonic of the beam density at the time of saturation of the instability on the relativistic factor γ. Curve *1* shows the results of numerical simulations, and curve *2* was calculated analytically from the first of formulas (39).

Finally, the dependence of the amplitude of the first harmonic of the beam density in the instability saturation stage is illustrated in Fig. 12, in which curve *1* was obtained numerically and curve *2* was calculated from the first of formulas (39). The fact that these curves differ somewhat in shape is associated with the assumptions that were made in transforming Eq. (23). On the whole, we can conclude that the methods of expansion in small perturbations of the trajectories and momenta of the beam and plasma electrons provide an efficient and effective tool for the analytic description of the radiative instabilities of relativistic dense electron beams in dense plasmas in the regime of the collective Cherenkov effect.

ACKNOWLEDGMENTS

This work was supported in part by the Ministry of Education of the Russian Federation (project no. E02-3.2-447), the Russian Foundation for Basic Research (project no. 01-02-17265), the RF Ministry of Industry, Science, and Technologies (project no. NSh-1962.2003.2), and the Universities of Russia program (project no. 01.03.073).

APPENDIX

By equating to zero the coefficients in front of the exponentials $\exp(iny)$, we obtain the equations

$$\frac{d^2a_{b1}}{d\tau^2} = -i\Big\{-ia_{b1} + i\Big(1-\frac{g_{b2}}{g_{b1}}\Big)a_{b1}^*a_{b2} + \frac{1}{2}\Big(1-\frac{g_{b2}}{g_{b1}}\Big)|a_{b1}|^2a_{b1} - 3i\delta a_{b1} - \frac{9}{4}\mu_0(A_1|a_{b1}|^2 + A_1^*a_{b1}^2) - \frac{3}{2}i\mu_0a_{b1}^*(\mu_0A_1^2 - A_2) + \frac{\tilde\omega_p^2q_1}{g_{b1}}\Big(-ia_{p1} - \frac{1}{2}ia_{p1}^*a_{p2} + \frac{i}{8}|a_{p1}|^2a_{p1} + \frac{i}{4}|a_{b1}|^2a_{p1} - 3ia_{p1}\Big(\delta + \mu_0^2|A_1|^2 - i\frac{\mu_0}{4}(A_1a_{b1}^* + A_1^*a_{b1})\Big)\Big) \times \exp(i(\xi\tau + w_b - w_p)) + i\frac{\tilde\omega_p^2q_1}{2g_{b1}}a_{p1}^*\Big(ia_{b2} + \frac{1}{4}a_{b1}^2 - 3\mu_0(\mu_0A_1^2 - A_2)\Big)\exp(-i(\xi\tau + w_b - w_p)) + \frac{3}{4}\frac{g_{b2}}{g_{b1}}\mu_0A_1^*(2ia_{b2} + a_{b1}^2) - \frac{\tilde\omega_p^2q_2}{4g_{b1}}(2ia_{p2} + a_{p1}^2)(2ia_{b1}^* - 3\mu_0A_1^*) \times \exp(2i(\xi\tau + w_b - w_p))\Big\}, \quad \text{(A1)}$$

$$\frac{d^2a_{b2}}{d\tau^2} = -\frac{g_{b2}}{g_{b1}}a_{b2} + \frac{1}{2}i\Big(\frac{g_{b2}}{g_{b1}} - 1\Big)a_{b1}^2 + \frac{3}{2}\mu_0a_{b1}A_1 - \frac{1}{2}i\frac{\tilde\omega_p^2q_1}{g_{b1}}a_{p1}(a_{b1} + 3i\mu_0A_1)\exp(i(\xi\tau + w_b - w_p)) - \frac{\tilde\omega_p^2q_2}{g_{b1}}\Big(a_{p2} - \frac{1}{2}ia_{p1}^2\Big)\exp(2i(\xi\tau + w_b - w_p)).$$

In the same way, from the first of Eqs. (10), we obtain the following equations for a_{p1} and a_{p2}:

$$\frac{d^2a_{p1}}{d\tau^2} = \gamma^3\Big\{-\frac{g_{p1}}{g_{b1}}a_{p1} + \frac{i}{g_{b1}}(g_{p1} - g_{p2})a_{p1}^*a_{p2} + \frac{1}{2g_{b1}}(g_{p1} - g_{p2})|a_{p1}|^2a_{p1} - \frac{\tilde\omega_b^2q_1}{g_{b1}}\Big(a_{b1} - \frac{1}{2}ia_{b1}^*a_{b2} - \frac{1}{8}|a_{b1}|^2a_{b1} - \frac{1}{4}|a_{p1}|^2a_{b1}\Big) \times \exp(-i(\xi\tau + w_b - w_p)) + \frac{\tilde\omega_b^2q_1}{2g_{b1}}\Big(ia_{b1}^*a_{p2} + \frac{1}{4}a_{b1}^*a_{p1}^2\Big)\exp(i(\xi\tau + w_b - w_p)) - \frac{\tilde\omega_b^2q_2}{g_{b1}}\Big(ia_{b1}^*a_{b2} + \frac{1}{2}a_{p1}^*a_{b1}^2\Big)\exp(-2i(\xi\tau + w_b - w_p))\Big\}, \quad \text{(A2)}$$

$$\frac{d^2a_{p2}}{d\tau^2} = \gamma^3\Big\{\Big(-\frac{g_{p2}}{g_{b1}}a_{p2} + \frac{i}{2g_{b1}}(g_{p2} - g_{p1})a_{p1}^2 - \frac{1}{2}\frac{\tilde\omega_b^2q_1}{g_{b1}}a_{b1}a_{p1}\exp(i(w_p - w_b - \xi\tau)) - \frac{\tilde\omega_b^2q_2}{g_{b1}}\Big(a_{b2} - \frac{1}{2}ia_{b1}^2\Big)\exp(-2i(\xi\tau + w_b - w_p))\Big\}.$$

Substituting representations (12) into the third of Eqs. (10) yields the equations for the coefficients A_1 and A_2 and for the nonoscillating momentum component δ:

$$\frac{dA_1}{d\tau} = \frac{1}{2}\Big\{-a_{b1} + i\Big(1-\frac{g_{b2}}{g_{b1}}\Big)a_{b1}^*a_{b2} + \frac{1}{2}\Big(1-\frac{g_{b2}}{g_{b1}}\Big)|a_{b1}|^2a_{b1} - \frac{\tilde\omega_p^2q_1}{g_{b1}}\Big(a_{p1} - \frac{1}{2}ia_{p1}^*a_{p2}$$

$$-\frac{1}{8}|a_{p1}|^2 a_{p1} - \frac{1}{4}|a_{b1}|^2 a_{p1}\Big)\exp(i(\xi\tau + w_b - w_p))$$

$$+\frac{\tilde{\omega}_p^2 q_1}{2g_{b1}} a_{p1}^*\Big(ia_{b2} - \frac{1}{4}a_{b1}^2\Big)\exp(-i(\xi\tau + w_b - w_p))$$

$$-\frac{\tilde{\omega}_p^2 q_2}{g_{b1}}\Big(ia_{p2} + \frac{1}{2}a_{p1}^2\Big)a_{b1}^*\exp(2i(\xi\tau + w_b - w_p))\Big\},$$

$$\frac{dA_2}{d\tau} = \frac{1}{2}\Big\{-\frac{g_{b2}}{g_{b1}}a_{b2} + \frac{1}{2}i\Big(\frac{g_{b2}}{g_{b1}} - 1\Big)a_{b1}^2$$

$$-\frac{i}{2}\frac{\tilde{\omega}_p^2 q_1}{g_{b1}} a_{p1}a_{b1}\exp(i(\xi\tau + w_b - w_p)) \quad \text{(A3)}$$

$$-\frac{\tilde{\omega}_p^2 q_2}{g_{b1}}\Big(a_{p2} - \frac{1}{2}ia_{p1}^2\Big)\exp(2i(\xi\tau + w_b - w_p))\Big\},$$

$$\frac{d\delta}{d\tau} = \frac{i}{8}\frac{\mu_0\tilde{\omega}_p^2}{g_{b1}}\Big\{q_1\Big(a_{p1}a_{b1}^*\Big(1 - \frac{1}{8}|a_{b1}|^2 - \frac{1}{8}|a_{p1}|^2\Big)$$

$$+\frac{i}{2}a_{p1}a_{b1}a_{b2}^* - \frac{i}{2}a_{b1}^* a_{p1}^* a_{p2}\Big)\exp(i(\xi\tau + w_b - w_p))$$

$$+\frac{q_2}{2}(4a_{p2}a_{b2}^* + 2ia_{p2}a_{b1}^{*2} - 2ia_{p1}^2 a_{b2}^* + a_{p1}^2 a_{b1}^{*2})$$

$$\times\exp(2i(\xi\tau + w_b - w_p)) - \text{c.c.}\Big\}.$$

Finally, from the first and second of Eqs. (10), we obtain the equations for w_p and w_b:

$$\frac{d^2 w_p}{d\tau^2} = -\frac{i}{4}\frac{\tilde{\omega}_b^2\gamma^3}{g_{b1}}\Big\{q_1\Big(a_{b1}a_{p1}^* + \frac{1}{2}ia_{b1}a_{p1}a_{p2}^*$$

$$-\frac{1}{8}|a_{p1}|^2 a_{b1}a_{p1}^* - \frac{1}{2}ia_{p1}^* a_{b1}^* a_{b2}$$

$$-\frac{1}{8}|a_{b1}|^2 a_{b1}a_{p1}^*\Big)\exp(-i(\xi\tau + w_b - w_p)) \quad \text{(A4)}$$

$$+\frac{1}{2}q_2(4a_{b2}a_{p2}^* + 2ia_{b2}a_{p1}^{*2} - 2ia_{b1}^2 a_{p2}^* + a_{b1}^2 a_{p1}^{*2})$$

$$\times\exp(-2i(\xi\tau + w_b - w_p)) - \text{c.c.}\Big\},$$

$$\frac{dw_b}{d\tau} = -\frac{1}{\mu_0}\Big(2\delta + \frac{3}{2}\mu_0^2|A_1|^2 - 3\delta^2\Big).$$

We analyze Eqs. (A.1)–(A.4) for the case of nonresonant excitation of the second harmonics of the beam-density and plasma-density perturbations: $g_{p2} \neq 4g_{p1}$ and $g_{b2} \neq 4g_{b1}$ (i.e., $\omega^2(2k_z) \neq 4\omega^2(k_z)$, where $\omega(k_z)$ is the dispersion law). Note that, for a dense plasma, these conditions are satisfied automatically, because, under inequality (2), we have $g_{p2} \approx g_{p1} \approx \omega_p^2$ and, analogously, $g_{b2} \approx g_{b1} \approx \omega_b^2$. We seek solutions to Eqs. (A.1)–(A.4) in the form of expressions (14). The physical meaning is conveyed predominantly by the first and third of expressions (14) and can easily be understood from Eqs. (A.1) and (A.2). In the linear approximation and for $q_n = 0$, Eq. (A.1) describe free linear Langmuir oscillations of an electron beam that proceed according to the law $q_{b1} = \text{const}\exp(i\tau)$. Using the definition of the dimensionless time τ [see expressions (8)] and ignoring the Doppler shift $k_z u$, we find that the frequency of the beam wave is equal to $\sqrt{g_{b1}\gamma^{-3}}$. Consequently, the first of expressions (14) describes the beam wave, in which case the amplitude $\tilde{a}_{b1}(\tau)$ is slowly varying because the interaction of the beam with the plasma is weak. The same considerations apply to the Eq. (A.2) and the third of expressions (14), because free linear plasma oscillations proceed according to the law $a_{p1} = \text{const}\exp(-i\sqrt{g_{p1}\gamma^3 g_{b1}^{-1}}\,\tau) = \text{const}\exp(-i\sqrt{g_{p1}}\,t)$.

In order to derive reduced equations for the slowly varying amplitudes, we substitute expressions (14) into Eqs. (A.1)–(A.4) and take into account the condition of the collective Cherenkov resonance between the plasma wave and the slow beam wave,

$$\sqrt{\frac{g_{p1}}{\gamma^{-3}g_{b1}}} = \frac{k_z u}{\sqrt{\gamma^{-3}g_{b1}}} - 1$$

or, in terms of the dimensional frequencies, $\sqrt{g_{p1}} = k_z u - \sqrt{g_{b1}\gamma^{-3}}$. As a result, we arrive at the following reduced equations, in which we discard the second derivatives of the slowly varying amplitudes with respect to τ:

$$2i\frac{d\tilde{a}_{b1}}{d\tau} = i\Big(1 - \frac{g_{b2}}{g_{b1}}\Big)\tilde{a}_{b1}^*\tilde{a}_{b2} - \frac{1}{2}\Big(1 - \frac{g_{b2}}{g_{b1}}\Big)|\tilde{a}_{b1}|^2\tilde{a}_{b1}$$

$$-3\delta a_{b1} + \frac{9}{4}i\mu_0(\tilde{A}_1|\tilde{a}_{b1}|^2 + \tilde{A}_1^*\tilde{a}_{b1}^2)$$

$$-\frac{3}{2}\mu_0\tilde{a}_{b1}^*(\mu_0\tilde{A}_1^2 - \tilde{A}_2) - \frac{\tilde{\omega}_p^2 q_1}{g_{b1}}\Big(\tilde{a}_{p1} - \frac{1}{2}i\tilde{a}_{p1}^*\tilde{a}_{p2}$$

$$-\frac{1}{8}|\tilde{a}_{p1}|^2\tilde{a}_{p1}-\frac{1}{4}|\tilde{a}_{b1}|^2\tilde{a}_{p1}+3\tilde{a}_{p1}\Big(\delta+\mu_0^2|\tilde{A}_1|^2 - i\frac{\mu_0}{4}(\tilde{A}_1\tilde{a}_{b1}^*+\tilde{A}_1^*\tilde{a}_{b1})\Big)\Big)\exp(i(w_b-w_p)) - \frac{\tilde{\omega}_p^2 q_1}{2g_{b1}}\tilde{a}_{p1}^*\Big(i\tilde{a}_{b2}+\frac{1}{4}\tilde{a}_{b1}^2-3\mu_0(\mu_0\tilde{A}_1^2-\tilde{A}_2)\Big) \times\exp(-i(w_b-w_p))+\frac{3}{4}i\frac{g_{b2}}{g_{b1}}\mu_0\tilde{A}_1^*(2i\tilde{a}_{b2}+\tilde{a}_{b1}^2) -i\frac{\tilde{\omega}_p^2 q_2}{4g_{b1}}(2i\tilde{a}_{p2}+\tilde{a}_{p1}^2)(2i\tilde{a}_{b1}^*-3\mu_0\tilde{A}_1^*)\exp(2i(w_b-w_p)) \quad (A5)$$

$$4i\frac{d\tilde{a}_{b2}}{d\tau} = \frac{1}{2}i\Big(\frac{g_{b2}}{g_{b1}}-1\Big)\tilde{a}_{b1}^2+\frac{3}{2}\mu_0\tilde{a}_{b1}\tilde{A}_1 -\frac{1}{2}i\frac{\tilde{\omega}_p^2 q_1}{g_{b1}}\tilde{a}_{p1}(\tilde{a}_{b1}+3i\mu_0\tilde{A}_1)\exp(i(w_b-w_p)) \quad (A6) -\frac{\tilde{\omega}_p^2 q_2}{g_{b1}}\Big(\tilde{a}_{p2}-\frac{1}{2}i\tilde{a}_{p1}^2\Big)\exp(2i(w_b-w_p)),$$

$$\frac{d\tilde{A}_1}{d\tau} = -i\tilde{A}_1+\frac{1}{2}\Big\{-\tilde{a}_{b1}+i\Big(1-\frac{g_{b2}}{g_{b1}}\Big)\tilde{a}_{b1}^*\tilde{a}_{b2} +\frac{1}{2}\Big(1-\frac{g_{b2}}{g_{b1}}\Big)|\tilde{a}_{b1}|^2\tilde{a}_{b1}-\frac{\tilde{\omega}_p^2 q_1}{g_{b1}}\Big(\tilde{a}_{p1}-\frac{1}{2}i\tilde{a}_{p1}^*\tilde{a}_{p2} -\frac{1}{8}|\tilde{a}_{p1}|^2\tilde{a}_{p1}-\frac{1}{4}|\tilde{a}_{b1}|^2\tilde{a}_{p1}\Big)\exp(i(w_b-w_p)) \quad (A7) +\frac{\tilde{\omega}_p^2 q_1}{2g_{b1}}\tilde{a}_{p1}^*\Big(i\tilde{a}_{b2}-\frac{1}{4}\tilde{a}_{b1}^2\Big)\exp(-i(w_b-w_p)) -\frac{\tilde{\omega}_p^2 q_2}{g_{b1}}\Big(i\tilde{a}_{p2}+\frac{1}{2}\tilde{a}_{p1}^2\Big)a_{b1}^*\exp(2i(w_b-w_p))\Big\},$$

$$\frac{d\tilde{A}_2}{d\tau} = -2i\tilde{A}_2+\frac{1}{2}\Big\{-\frac{g_{b2}}{g_{b1}}\tilde{a}_{b2}+\frac{1}{2}i\Big(\frac{g_{b2}}{g_{b1}}-1\Big)\tilde{a}_{b1}^2 -\frac{i}{2}\frac{\tilde{\omega}_p^2 q_1}{g_{b1}}\tilde{a}_{p1}\tilde{a}_{b1}\exp(i(w_b-w_p)) \quad (A8) -\frac{\tilde{\omega}_p^2 q_2}{g_{b1}}\Big(\tilde{a}_{p2}-\frac{1}{2}i\tilde{a}_{p1}^2\Big)\exp(2i(w_b-w_p))\Big\},$$

$$-2i\sqrt{\frac{g_{p1}}{g_{b1}\gamma^{-3}}}\frac{d\tilde{a}_{p1}}{d\tau} = \gamma^3\Big\{\frac{i}{g_{b1}}(g_{p1}-g_{p2})\tilde{a}_{p1}^*\tilde{a}_{p2} +\frac{1}{2g_{b1}}(g_{p1}-g_{p2})|\tilde{a}_{p1}|^2\tilde{a}_{p1} -\frac{\tilde{\omega}_b^2 q_1}{g_{b1}}\Big(\tilde{a}_{b1}-\frac{1}{2}i\tilde{a}_{b1}^*\tilde{a}_{b2}-\frac{1}{8}|\tilde{a}_{b1}|^2\tilde{a}_{b1}-\frac{1}{4}|\tilde{a}_{p1}|^2\tilde{a}_{b1}\Big) \times\exp(-i(w_b-w_p)) +\frac{\tilde{\omega}_b^2 q_1}{2g_{b1}}\Big(i\tilde{a}_{b1}^*\tilde{a}_{p2}+\frac{1}{4}\tilde{a}_{b1}^*\tilde{a}_{p1}^2\Big)\exp(i(w_b-w_p)) -\frac{\tilde{\omega}_b^2 q_2}{g_{b1}}\Big(i\tilde{a}_{b1}^*\tilde{a}_{b2}+\frac{1}{2}\tilde{a}_{p1}^*\tilde{a}_{b1}^2\Big)\exp(-2i(w_b-w_p))\Big\}, \quad (A9)$$

$$-4i\sqrt{\frac{g_{p1}}{g_{b1}\gamma^{-3}}}\frac{d\tilde{a}_{p2}}{d\tau} = \gamma^3\Big\{\frac{(4g_{p1}-g_{p2})}{g_{b1}}\tilde{a}_{p2} +\frac{i}{2g_{b1}}(g_{p2}-g_{p1})\tilde{a}_{p1}^2 -\frac{1}{2}\frac{\tilde{\omega}_b^2 q_1}{g_{b1}}\tilde{a}_{b1}\tilde{a}_{p1}\exp(i(w_p-w_b)) -\frac{\tilde{\omega}_b^2 q_2}{g_{b1}}\Big(\tilde{a}_{b2}-\frac{1}{2}i\tilde{a}_{b1}^2\Big)\exp(-2i(w_b-w_p))\Big\}. \quad (A10)$$

Substituting expressions (14) into Eqs. (A.3) and (A.4) does not change the structure of the equations for δ, w_p, and w_b; the only difference is that the constant phase shift $\xi\tau$ drops out of the exponentials and the amplitudes are indicated by a tilde. To save space, we do not write out these resulting equations, especially because Eqs. (A.5)–(A.10) provide a complete analysis of the problem.

Note that the above collective Cherenkov resonance condition should be regarded as an equation for determining the wavenumber k_z at which the beam–plasma instability under discussion grows at the fastest rate.

REFERENCES

1. B. I. Aronov, L. S. Bogdankevich, and A. A. Rukhadze, Plasma Phys. **16**, 101 (1976).
2. M. V. Kuzelev and A. A. Rukhadze, Fiz. Plazmy **26**, 250 (2000) [Plasma Phys. Rep. **26**, 231 (2000)].
3. M. V. Kuzelev, O. T. Loza, A. A. Rukhadze, *et al.*, Fiz. Plazmy **27**, 710 (2001) [Plasma Phys. Rep. **27**, 669 (2001)].
4. M. A. Agafonov, A. V. Arzhannikov, V. S. Koĭdan, *et al.*, Plasma Phys. Controlled Fusion **38**, A93 (1996).
5. A. K. Berezin and Ya. B. Faĭnberg, Zh. Éksp. Teor. Fiz. **76**, 193 (1976) [Sov. Phys. JETP **44**, 101 (1976)].
6. M. V. Kuzelev, A. A. Rukhadze, and P. S. Strelkov, *Plasma Relativistic Microwave Electronics* (Bauman State Technical Univ. Press, Moscow, 2002).

7. V. P. Maslov and M. V. Fedoryuk, *Quasi-Classical Approximation in Quantum Mechanics* (Nauka, Moscow, 1976; Reidel, Dordrecht, 1981).
8. M. V. Kuzelev and A. A. Rukhadze, *Electrodynamics of Dense Electron Beams in a Plasma* (Nauka, Moscow, 1990).
9. Yu. V. Bobylev, M. V. Kuzelev, and A. A. Rukhadze, Zh. Éksp. Teor. Fiz. **118**, 105 (2000) [JETP **91**, 93 (2000)].
10. Yu. V. Bobylev, M. V. Kuzelev, and A. A. Rukhadze, Radiotekh. Élektron. (Moscow) **47**, 166 (2002).
11. M. V. Kuzelev, A. A. Rukhadze, Yu. V. Bobylev, and V. A. Panin, Zh. Éksp. Teor. Fiz. **91**, 1620 (1986) [Sov. Phys. JETP **64**, 956 (1986)].
12. M. V. Kuzelev, A. A. Rukhadze, and G. V. Sanadze, Zh. Éksp. Teor. Fiz. **89**, 1591 (1985) [Sov. Phys. JETP **62**, 921 (1985)].
13. A. T. Bogdanov and M. V. Kuzelev, Pis'ma Zh. Tekh. Fiz. **14**, 1404 (1988) [Sov. Tech. Phys. Lett. **14**, 612 (1988)].
14. J. Weiland and H. Wilhelmsson, *Coherent Nonlinear Interaction of Waves in Plasmas* (Pergamon Press, Oxford, 1976; Énergoizdat, Moscow, 1981).
15. A. I. Akhiezer, I. A. Akhiezer, R. V. Polovin, *et al.*, *Electrodynamics of Plasma* (Nauka, Moscow, 1974; Pergamon Press, Oxford, 1975).
16. A. A. Ivanov, *Physics of Highly Nonequilibrium Plasma* (Atomizdat, Moscow, 1977).
17. V. D. Shapiro and V. I. Shevchenko, Izv. Vyssh. Uchebn. Zaved. Radiofiz. **19**, 767 (1976).
18. M. V. Kuzelev, Zh. Tekh. Fiz. **53**, 1029 (1983) [Sov. Phys. Tech. Phys. **28**, 623 (1983)].

Translated by I.A. Kalabalyk

Plasma Physics Reports, Vol. 30, No. 5, 2004, pp. 398–412. Translated from Fizika Plazmy, Vol. 30, No. 5, 2004, pp. 434–449.

PLASMA OSCILLATIONS AND WAVES

Self-Consistent Model of an Inductive RF Plasma Source in an External Magnetic Field

A. F. Aleksandrov*, G. É. Bugrov*, K. V. Vavilin*, I. F. Kerimova*, S. G. Kondranin*, E. A. Kral'kina*, V. B. Pavlov*, V. Yu. Plaksin*, and A. A. Rukhadze**

** Physics Department, Moscow State University, Vorob'evy gory, Moscow, 119899 Russia*

*** Prokhorov Institute of General Physics, Russian Academy of Sciences, ul. Vavilova 38, Moscow, 119991 Russia*

Received June 4, 2003; in final form, September 17, 2003

Abstract—A theory is developed that makes it possible to calculate RF power absorption in an inductive plasma source. Conditions are determined under which most of the power is deposited in the plasma. It is shown that these conditions correspond to the excitation of spatial waves (an oblique Langmuir wave and a helicon wave). A simple self-consistent model of a plasma source is proposed that describes all of the experimentally observed distinctive properties of plasma sources well. © *2004 MAIK "Nauka/Interperiodica".*

1. INTRODUCTION

Papers [1–3] presented a series of investigations on the development and construction of an RF plasma source whose operation is based on the excitation of electrostatic waves in a plasma in a permanent external magnetic field. The ion source that was designed had a diameter of 92 mm, operated at frequencies of 41–81 MHz, and made it possible to produce beams of ions of noble and chemically active gases with currents of 5–150 mA (the current density being 0.05–2.5 mA/cm^2) at input powers of 10–150 W. While being tested as part of industrial technological devices, the ion source proved capable of operating reliably and stably, especially in such applications as the modification of material surfaces, ion assistance, and reactive etching. However, the tests revealed a number of drawbacks of the source, such as the saturation of the extracted ion current when the RF power was increased above 150 W, a high external magnetic field (20–40 mT), and low operation efficiency at an industrial frequency of 13.56 MHz. It is most likely that these drawbacks are related both to the method for exciting an electrostatic wave with the help of a zigzag antenna [1] (which induces a surface charge on the side wall of the source) and to the short length (3 cm) of the gas-discharge chamber of the source.

In order to overcome the above drawbacks, the authors of [1–3] began a new series of investigations on the development of ion and plasma sources that would be capable of operating highly efficiently at an industrial frequency of 13.56 MHz and in which the plasma would be created and maintained by an inductive RF discharge in an external magnetic field. One of the goals of these investigations was to develop large-diameter ion and plasma sources. However, since strong magnetic fields in large volumes are technically difficult to produce, the problem was to reduce the working external magnetic field to the lowest possible level. The first results of experimental research in this direction [4] confirmed that such an approach holds considerable promise: the source operated stably at a frequency of 13.56 MHz in an external magnetic field no stronger than 10 mT, and the extracted ion current increased with increasing input power. At the same time, the first experiments revealed some features of the discharge that were not observed in the source operating with a zigzag antenna, namely, discharge disruptions at a certain magnetic field (which depended on both the input power and the magnitude of the extracted ion current) and a hysteresis effect in the dependence of the plasma parameters on the external magnetic field. It is obvious that these purely physical effects can have negative effect on the operation of a plasma source.

In this review, in order to understand the physical reasons for the new features of the discharge that were observed in experiments and to analyze the possibility of developing workable sources, we present the results of mathematical simulations of the operation of an ion source based on an inductive RF discharge in an external magnetic field. We consider the case in which the plasma is heated by its eigenwaves excited by a purely inductive ring antenna positioned at the side surface of the gas-discharge chamber. Earlier, plasma heating by eigenwaves excited by antennas of different shapes was studied in [5–9]. In the present paper, we investigate the mechanism for depositing the RF power into a plasma with a relatively low density (10^9–10^{12} cm^{-3}) in a weak external magnetic field (1–100 mT). We analyze the operation of the source using a self-consistent model that makes it possible to calculate the RF fields in the plasma from the geometric parameters of the source and from the parameters of the plasma maintained by the absorbed RF power. Numerical simulations were

1063-780X/04/3005-0398$26.00 © 2004 MAIK "Nauka/Interperiodica"

carried out for argon as the working gas and for an ion source 5–50 cm in diameter and 5–30 cm in length.

2. EXCITATION OF EIGENWAVES IN AN INDUCTIVE RF PLASMA SOURCE IN AN EXTERNAL MAGNETIC FIELD

2.1. Formulation of the Problem

The load, consisting of an antenna and a plasma coupled to it, is supplied by the RF power from an oscillator through a matching device, which, in turn, serves to maximize the input power. When the load is matched to the oscillator, the oscillator power P is related to the antenna power P_{ant} and to the power P_{pl} deposited in the plasma through the expression

$$P = P_{ant} + P_{pl}. \quad (2.1)$$

Obviously, the optimum operating modes of the plasma sources are those in which the following condition is satisfied:

$$P \approx P_{pl} \gg P_{ant}. \quad (2.2)$$

One possible way to satisfy this condition is to excite eigenwaves, because they are efficiently absorbed by a low-pressure plasma in a permanent external magnetic field [4–9]. In order to determine the conditions for exciting eigenwaves in particular models of the plasma source, we solved the electrodynamic problem of calculating the electric and magnetic RF fields in a cylindrical source of radius R and length L (see Fig. 1) in which the plasma is maintained by an azimuthal surface current I of frequency ω:

$$I = \int_{-L/2}^{L/2} j_{\varphi 0}(z, t)dz, \quad (2.3)$$

where the current density is given by the expression $j_{\varphi 0}(z, t) = j_0 \exp(i(\pi z/L - \omega t))$, with j_0 being a constant.

In investigating plasma sources analytically, the following inequalities need to be satisfied:

$$\Omega_i \ll \omega_{Li} \leq \omega, \quad V_{Te}/R, \quad V_{Te}/L \ll \Omega_e \ll \omega_{Le}. \quad (2.4)$$

Here, ω_{Li} and ω_{Le} are the Langmuir frequencies of the ion and electron plasma components with given densities n_i and n_e, ω is the RF field frequency, $V_{Te} = \sqrt{T_e/m}$ is the electron thermal velocity, and $\Omega_{e,i}$ are the electron and ion gyrofrequencies in a uniform magnetic field $\mathbf{B}_0 \parallel \mathbf{z}$.

The typical experimental parameters and conditions are as follows. The source radius and length are $R \sim 2$–10 cm and $L \sim 5$–15 cm, the electron plasma density is $n_e \sim 10^{10}$–10^{12} cm^{-3}, the uniform magnetic field is $B_0 \sim 1$–10 mT, the electron temperature is 3–8 eV ~ (3–9) × 10^4 K, and the working gas pressure is $p_0 \sim 10^{-4}$–10^{-2} torr (i.e., $n_0 \sim 3 \times 10^{12}$–$3 \times 10^{14}$ cm^{-3}). The degree of ionization is fairly high, so that the electron collision frequency is about $\nu_e \sim \nu_{ei} + \nu_{en} \sim (1–10) \times 10^6$ s^{-1},

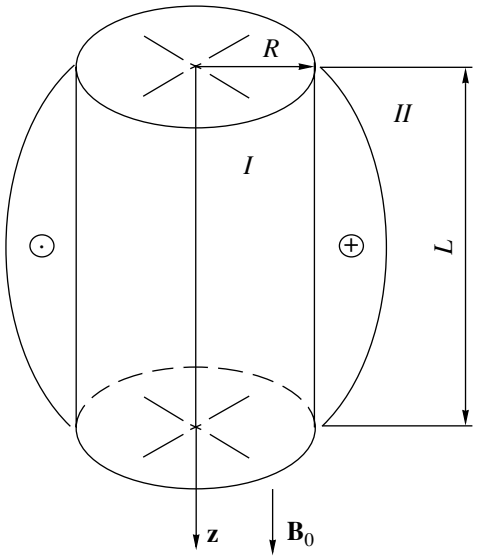

Fig. 1. Schematic of a plasma source.

where ν_{ei} and ν_{en} are the electron–ion and electron–neutral collision frequencies, respectively. The experiments are usually carried out with heavy gases whose atomic masses are about 10^2 of that of hydrogen. Under these conditions, the ions are unmagnetized ($\omega \gg \Omega_i$); moreover, in solving the problem, the ion contribution can always be neglected. For a magnetic field of about 1 mT, the working frequency is only two times lower than the electron gyrofrequency Ω_e. This indicates that the next to last (strong) inequality in conditions (2.4) fails to hold (we will take this point into account in further analysis). As for the last inequality, it is satisfied by a large margin. By the way, it is this circumstance that makes it possible to ignore the ion contribution regardless of the value of the ratio ω/Ω_e.

The basic equations for the problem as formulated are Maxwell's equations. For simplicity, we restrict ourselves to axisymmetric geometry and assume that $\partial/\partial\varphi = 0$. Using the representation $f(r)\exp(-i\omega t + ik_z z)$ for all the quantities that depend on time and coordinates, we write the following equations for the fields within the plasma volume in cylindrical coordinates:

$$ck_z E_\varphi = -\omega B_r, \quad (2.5.1)$$

$$ik_z cE_r - c\left(\frac{\partial E_z}{\partial r}\right) = i\omega B_\varphi, \quad (2.5.2)$$

$$cr^{-1}\left(\frac{\partial (rE_\varphi)}{\partial r}\right) = i\omega B_z, \quad (2.5.3)$$

$$k_z cB_\varphi = \omega(\varepsilon_\perp E_r + igE_\varphi), \quad (2.5.4)$$

$$ik_z cB_r - c\left(\frac{\partial B_z}{\partial r}\right) = -i\omega(-igE_r + \varepsilon_\perp E_\varphi), \quad (2.5.5)$$

$$cr^{-1}\left(\frac{\partial(rB_\varphi)}{\partial r}\right) = -i\omega\varepsilon_\parallel E_z. \quad (2.5.6)$$

Here, $k_z = \pi/L$ and the plasma dielectric tensor $\varepsilon_{ij}(\omega)$ has the form

$$\varepsilon_{ij}(\omega) = \begin{pmatrix} \varepsilon_\perp & ig & 0 \\ -ig & \varepsilon_\perp & 0 \\ 0 & 0 & \varepsilon_\parallel \end{pmatrix}, \quad (2.6)$$

where

$$\varepsilon_\perp = \varepsilon_\perp' + i\varepsilon_\perp'' = 1 - \frac{\omega_{Le}^2}{\omega^2 - \Omega_e^2} + i\frac{\omega_{Le}^2(\omega^2 + \Omega_e^2)\nu_e}{\omega(\omega^2 - \Omega_e^2)^2}$$

$$+ i\sqrt{\frac{\pi}{8}}\frac{\omega_{Le}^2}{\omega k_z V_{Te}}\left[\exp\left(-\frac{(\omega - \Omega_e)^2}{2k_z^2 V_{Te}^2}\right) + \exp\left(-\frac{(\omega + \Omega_e)^2}{2k_z^2 V_{Te}^2}\right)\right],$$

$$g = g' + ig'' = \frac{\omega_{Le}^2\Omega_e}{\omega(\omega^2 - \Omega_e^2)} + i\frac{2\omega_{Le}^2\Omega_e\nu_e}{(\omega^2 - \Omega_e^2)^2} \quad (2.7)$$

$$+ i\sqrt{\frac{\pi}{8}}\frac{\omega_{Le}^2}{\omega k_z V_{Te}}\left[\exp\left(-\frac{(\omega - \Omega_e)^2}{2k_z^2 V_{Te}^2}\right) - \exp\left(-\frac{(\omega + \Omega_e)^2}{2k_z^2 V_{Te}^2}\right)\right],$$

$$\varepsilon_\parallel = \varepsilon_\parallel' + i\varepsilon_\parallel'' = 1 - \frac{\omega_{Le}^2}{\omega^2} + i\frac{\omega_{Le}^2\nu_e}{\omega^3}$$

$$+ i\sqrt{\frac{\pi}{2}}\frac{\omega_{Le}^2\omega}{k_z^3 V_{Te}^3}\exp\left(-\frac{\omega^2}{2k_z^2 V_{Te}^2}\right).$$

In these equations, we take into account both of the mechanisms for the absorption of the RF field by the plasma: collisional absorption and collisionless (Cherenkov and cyclotron) absorption. The reason is that, in a weak magnetic field region in which ω is slightly lower than Ω_e and is slightly higher than $(k_z V_{Te})$, these absorption mechanisms are both important.

On the other hand, it should be noted that, since the plasma density is high [see inequalities (2.4)], all the elements of the tensor $\varepsilon_{ij}(\omega)$ are large. Thus, for the above parameters, we have $k_z V_{Te} \sim 10^8$ s^{-1}, so that the tensor elements are estimated as

$$\varepsilon_\perp' \sim g' \sim 2\times 10^4, \quad \varepsilon_\perp'' \sim g'' \sim 10^3,$$
$$\varepsilon_\parallel' \sim 5\times 10^4, \quad \varepsilon_\parallel'' \sim 2\times 10^3. \quad (2.8)$$

Equations (2.5) are solved separately for the plasma region ($r < R$) and for the region outside the plasma ($r > R$). In Fig. 1, these regions are indicated as region *I* and region *II*, respectively. The solutions obtained are then joined at the plasma surface with the help of the boundary conditions

$$B_{zII} - B_{zI} = -4\pi j_{\varphi 0}(z,t)/c, \quad E_{zII} - E_{zI} = 0,$$
$$B_{\varphi II} - B_{\varphi I} = 0, \quad E_{\varphi II} - E_{\varphi I} = 0. \quad (2.9)$$

At this point, the formulation of the problem is complete. To conclude this section, we present the formula [10, 11] that was used in numerical simulations to determine the RF field power deposited in the plasma:

$$P_{\rm pl} = \frac{L\omega}{4}\int_0^R rdr\{\varepsilon_\perp''|E_r|^2 + \varepsilon_\perp''|E_\varphi|^2$$
$$+ ig''(E_\varphi E_r^* - E_r E_\varphi^*) + \varepsilon_\parallel''|E_z|^2\}. \quad (2.10)$$

2.2. Solution to the Electrodynamic Problem for Arbitrary Magnetic Fields

Without loss of generality, it is convenient to reduce Eqs. (2.5) to two coupled second-order equations for the E_z and B_z field components:[1]

$$\Delta_\perp E_z + \frac{\varepsilon_\parallel}{\varepsilon_\perp}\left(\frac{\omega^2}{c^2}\varepsilon_\perp - k_z^2\right)E_z + \left(-i\frac{gk_z\omega}{\varepsilon_\perp c}\right)B_z = 0,$$
$$\Delta_\perp B_z + \left(\frac{\omega^2}{c^2\varepsilon_\perp}(\varepsilon_\perp^2 - g^2) - k_z^2\right)B_z + \left(i\frac{gk_z\omega\varepsilon_\parallel}{\varepsilon_\perp c}\right)E_z = 0. \quad (2.11)$$

Here, we have introduced the notation $\Delta_\perp = \frac{1}{r}\frac{\partial}{\partial r}r\frac{\partial}{\partial r}$.

We find it convenient to reduce Eqs. (2.5) to Eqs. (2.11) because, if Eqs. (2.11) were decoupled, which is the case for small values of the parameter $\omega^2\varepsilon_\perp/k_z^2c^2$, then the first of them would describe a purely longitudinal wave and the second would describe a purely transverse wave (a helicon) [10, 11].

The solution to Eqs. (2.11) within the plasma should be sought in the form

$$E_z = E_{z1}J_0(\varphi_1 r) + E_{z2}J_0(\varphi_2 r),$$
$$B_z = B_{z1}J_0(\varphi_1 r) + B_{z2}J_0(\varphi_2 r). \quad (2.12)$$

Substituting representations (2.12) into Eqs. (2.11), we obtain two independent biquadratic equations for φ_1^2 and φ_2^2:

$$\varphi_i^4 - \varphi_i^2(x_b + x_e) + x_b x_e - q_b q_e = 0, \quad i = 1, 2. \quad (2.13)$$

[1] In the literature, in solving particular problems, Eqs. (2.5) are conveniently reduced either to two second-order equations for two of the field components or to one fourth-order equation for one of the field components (see, e.g., [10, 11]).

These equations have the solutions

$$\varphi_{1,2}^2 = \frac{(x_b + x_e) \pm \sqrt{(x_b - x_e)^2 + 4q_b q_e}}{2}. \quad (2.14)$$

where we have introduced the notation

$$x_e = \frac{\varepsilon_\parallel}{\varepsilon_\perp}\left(\frac{\omega^2}{c^2}\varepsilon_\perp - k_z^2\right), \quad x_b = \frac{\omega^2}{c^2\varepsilon_\perp}(\varepsilon_\perp^2 - g^2) - k_z^2,$$

$$q_e = -i\frac{gk_z\omega}{\varepsilon_\perp c}, \quad q_b = \varepsilon_\parallel q_e.$$

We again substitute representations (2.12) into Eqs. (2.11) to obtain the relationships between $E_{z1,2}$ and $B_{z1,2}$:

$$B_{z1,2} = \frac{\varphi_{1,2}^2 - x_e}{q_e}E_{z1,2}. \quad (2.15)$$

Outside the plasma ($\varepsilon_\perp = \varepsilon_\parallel = 1$, $g = 0$), Eqs. (2.11) split into two independent equations:

$$\Delta_\perp E_z + \left(\frac{\omega^2}{c^2} - k_z^2\right)E_z = 0,$$
$$\Delta_\perp B_z + \left(\frac{\omega^2}{c^2} - k_z^2\right)B_z = 0, \quad (2.16)$$

which have the following solutions in the frequency range $\omega < k_z c$:

$$E_z = E_{z3}K_0(pr), \quad B_z = B_{z3}K_0(pr), \quad (2.17)$$

where $p = \sqrt{k_z^2 - \frac{\omega^2}{c^2}} \approx k_z$.

In order to join solutions (2.11) with solutions (2.16), we use boundary conditions (2.9) for the field components E_z, B_z, E_φ, and B_φ. Inside the plasma, the last two components are given by the expressions

$$E_\varphi = \frac{i\omega}{\varphi_1 c}B_{z1}J_1(\varphi_1 r) + \frac{i\omega}{\varphi_2 c}B_{z2}J_1(\varphi_2 r),$$
$$B_\varphi = -\frac{i\omega}{\varphi_1 c}\varepsilon_\parallel E_{z1}J_1(\varphi_1 r) - \frac{i\omega}{\varphi_2 c}\varepsilon_\parallel E_{z2}J_1(\varphi_2 r); \quad (2.18)$$

and, outside the plasma, they are given by

$$E_\varphi = -\frac{i\omega}{pc}B_{z3}K_1(pr), \quad B_\varphi = \frac{i\omega}{pc}E_{z3}K_1(pr). \quad (2.19)$$

As a result, boundary conditions (2.9) for B_z and E_z become

$$B_{z1}J_0(\varphi_1 R) + B_{z2}J_0(\varphi_2 R) - B_{z3}K_0(pR) = \frac{4\pi}{c}j_0,$$
$$E_{z1}J_0(\varphi_1 R) + E_{z2}J_0(\varphi_2 R) - E_{z3}K_0(pR) = 0; \quad (2.20)$$

and, for B_φ and E_φ, they take the form

$$-\frac{i\omega}{c}\varepsilon_\parallel\left(\frac{E_{z1}J_1(\varphi_1 R)}{\varphi_1} + \frac{E_{z2}J_1(\varphi_2 R)}{\varphi_2}\right) = -\frac{i\omega}{c}\frac{E_{z3}K_1(pR)}{-p},$$
$$\frac{i\omega}{c}\left(\frac{B_{z1}J_1(\varphi_1 R)}{\varphi_1} + \frac{B_{z2}J_1(\varphi_2 R)}{\varphi_2}\right) = \frac{i\omega}{c}\frac{B_{z3}K_1(pR)}{-p}. \quad (2.21)$$

Taking into account relationships (2.15), we obtain from boundary conditions (2.20) and (2.21) the following expression for the amplitude of the longitudinal electric field component:

$$E_{z1,2} = \frac{\Delta_{1,2}}{\Delta}, \quad (2.22)$$

where

$$\Delta_1 = \frac{4\pi j_0}{c}\left(J_0(\varphi_2 R) + \varepsilon_\parallel\frac{J_1(\varphi_2 R)}{\varphi_2}p\frac{K_0(pR)}{K_1(pR)}\right),$$

$$\Delta_2 = -\frac{4\pi j_0}{c}\left(J_0(\varphi_1 R) + \varepsilon_\parallel\frac{J_1(\varphi_1 R)}{\varphi_1}p\frac{K_0(pR)}{K_1(pR)}\right),$$

$$\Delta = \frac{\varphi_1^2 - x_e}{q_e}\left(J_0(\varphi_1 R) + \frac{J_1(\varphi_1 R)}{\varphi_1}p\frac{K_0(pR)}{K_1(pR)}\right)$$
$$\times\left(J_0(\varphi_2 R) + \varepsilon_\parallel\frac{J_1(\varphi_2 R)}{\varphi_2}p\frac{K_0(pR)}{K_1(pR)}\right)$$
$$-\frac{\varphi_2^2 - x_e}{q_e}\left(J_0(\varphi_1 R) + \varepsilon_\parallel\frac{J_1(\varphi_1 R)}{\varphi_1}p\frac{K_0(pR)}{K_1(pR)}\right)$$
$$\times\left(J_0(\varphi_2 R) + \frac{J_1(\varphi_2 R)}{\varphi_2}p\frac{K_0(pR)}{K_1(pR)}\right).$$

Substituting formulas (2.12), (2.15), and (2.22) into Eqs. (2.5), we can determine the amplitudes of the remaining field components:

$$E_{\varphi i} = \frac{i\omega}{\varphi_i c}B_{zi} = \frac{i\omega}{\varphi_i c}\frac{\varphi_i^2 - x_e}{q_e}E_{zi}, \quad B_{\varphi i} = -\frac{i\omega}{\varphi_i c}\varepsilon_\parallel E_{zi},$$
$$E_{ri} = -\frac{i}{\varphi_i c\varepsilon_\perp}\left(k_z c\varepsilon_\perp + ig\omega\frac{\varphi_i^2 - x_e}{q_e}\right)E_{zi}, \quad (2.23)$$
$$B_{ri} = -\frac{ik_z}{\varphi_i}\frac{\varphi_i^2 - x_e}{q_e}E_{zi}.$$

Formula (2.10) for the power $P_{\rm pl}$ deposited in the plasma now yields

$$P_{\rm pl} = R_{\rm pl}I^2, \quad (2.24)$$

where $R_{\rm pl}$ is the equivalent active resistance of the plasma, which determines the RF power deposited in it.

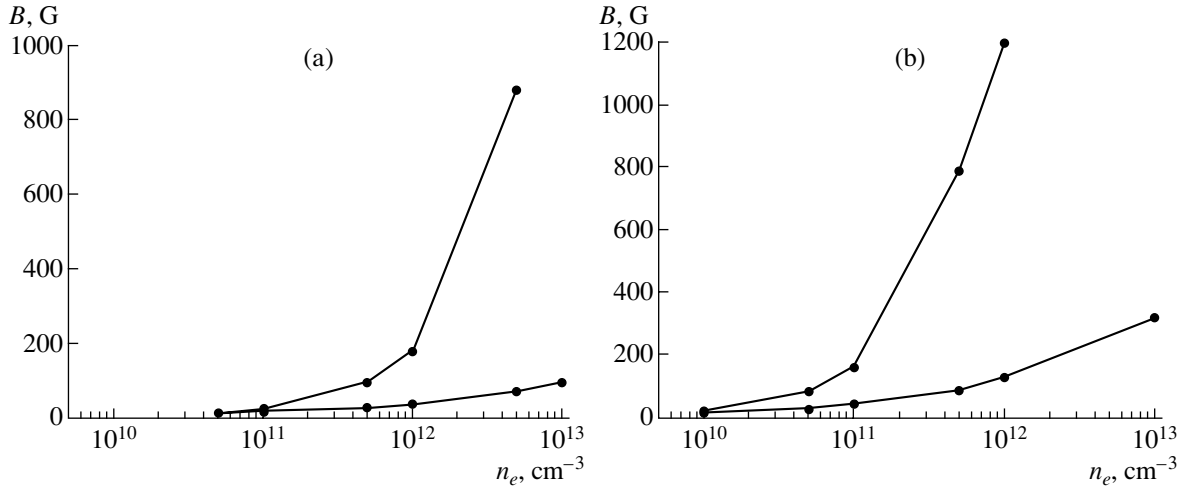

Fig. 2. Ranges of existence of the spatial waves corresponding to the first and the second solution to Eq. (2.14) for two sources having equal radii but different lengths: (a) $R = 2.5$ cm and $L = 10$ cm and (b) $R = 2.5$ cm and $L = 30$ cm.

Below, we will be interested in the magnitude of the deposited power.

The RF fields and the equivalent plasma resistance were calculated from formulas (2.22)–(2.24) using specially developed software. The calculations were carried out for plasma sources 5–50 cm in diameter and 5–30 cm in length and for an argon plasma with an electron density of 10^9–10^{13} cm^{-3} at a pressure of 10^{-4}–10^{-2} torr in an external magnetic field of 1–100 mT.

2.3. Numerical Results

In presenting the numerical results, we first consider the range of the plasma source parameters in which the solutions to Eq. (2.14) describe spatial waves with frequencies $\omega \ll \Omega_e$. Recall that, to zero order in the small parameter $\omega^2\varepsilon_\perp/k_z^2c^2 \ll 1$, the first solution to Eq. (2.14) describes an oblique Langmuir wave and the second describes a helicon [10, 11]. In the literature, oblique Langmuir waves are often referred to as a Trivelpiece–Gould waves [5–9]. Below, the wave described by the solution with the argument $\varphi_1 r$ will be called a Trivelpiece–Gould wave, and the wave described by the solution with the argument $\varphi_2 r$ will be called a helicon. Figure 2 illustrates the ranges of magnetic fields B and electron densities n_e in which $\varphi_{1,2}^2 > 0$ and in which spatial waves exist in two plasma sources of different lengths.

The lower bound on the range in which internal waves can exist is the same for the two solutions and is given by the condition $\omega^2\varepsilon_\perp < k_z^2c^2$, while the upper bound refers only to the helicon and is determined by the equality of the two terms in the numerator of formula (2.14).

As was expected, for each value of the magnetic field, there exists a threshold electron density below which a spatial helicon cannot be excited; moreover, the weaker the magnetic field, the lower the threshold electron plasma density. However, in each plasma source, a spatial helicon cannot be excited at electron densities below a certain minimum threshold density, regardless of the value of the magnetic field. From Fig. 2, we see that, as the length of the plasma source decreases, the minimum threshold electron plasma density increases considerably and the range in which a spatial helicon can exist becomes narrower.

We consider the behavior of the electric field components under conditions in which spatial waves can be generated over a wide range of plasma parameters. Figure 3 illustrates how the amplitudes of the electric field components corresponding to the first and second solutions to the electrodynamic problem [see formulas (2.12)] depend on the magnetic field. The results shown in the figure pertain to a relatively long plasma source ($L \geq 10$ cm) operating at a low argon pressure p ($p \sim 10^{-3}$ torr).

As was expected, for the electron density range under consideration and for magnetic fields stronger than 2–3 mT, the azimuthal component of the electric field corresponding to the first solution exceeds the azimuthal component of the electric field corresponding to the second solution; moreover, the stronger the magnetic field, the larger the difference between the components. In contrast, for electron densities of $n_e < 10^{12}$ cm^{-3}, the longitudinal and radial components of the helicon electric field are, respectively, smaller than the longitudinal and radial components of the electric field of an oblique Langmuir wave. However, at high electron densities ($n_e \geq 10^{12}$ cm^{-3}), the relationship between the longitudinal components and that between the radial com-

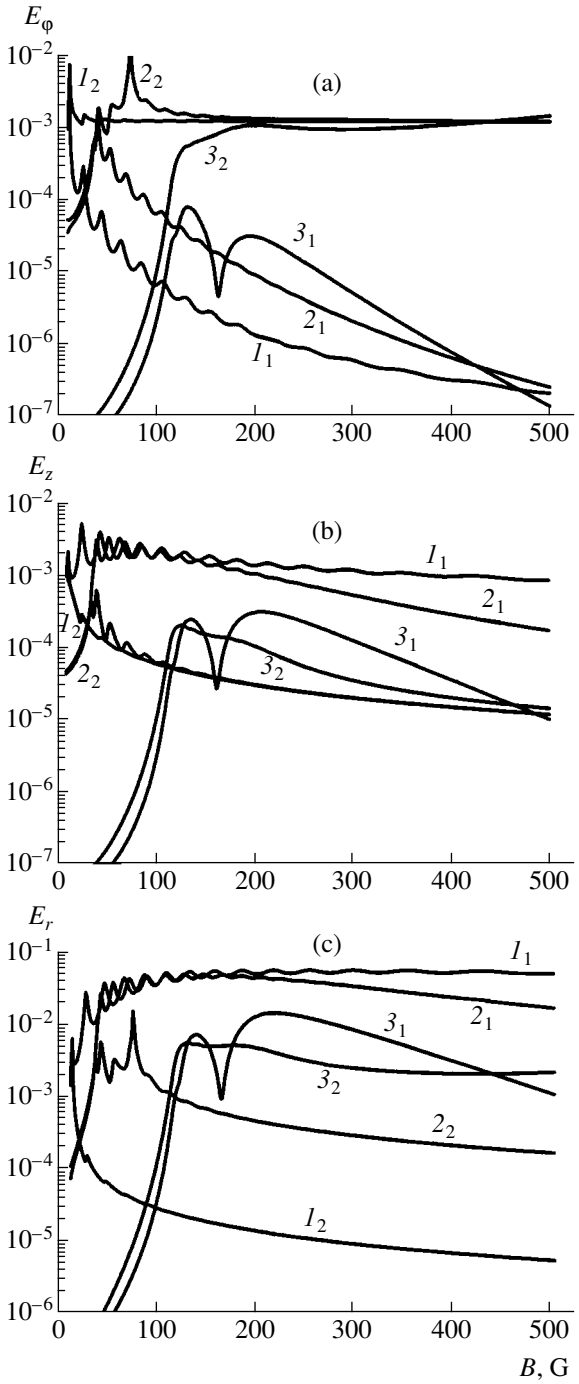

Fig. 3. Dependence of the amplitudes of the (a) azimuthal, (b) longitudinal, and (c) radial components of the RF electric field on the external magnetic field in a source with R = 5 cm and L = 50 cm. Curves *1–3* were calculated for electron densities of 10^{10}, 10^{11}, and 10^{12} cm^{-3}, respectively. Subscript 1 refers to the Trivelpiece–Gould wave, and subscript 2 stands for the helicon.

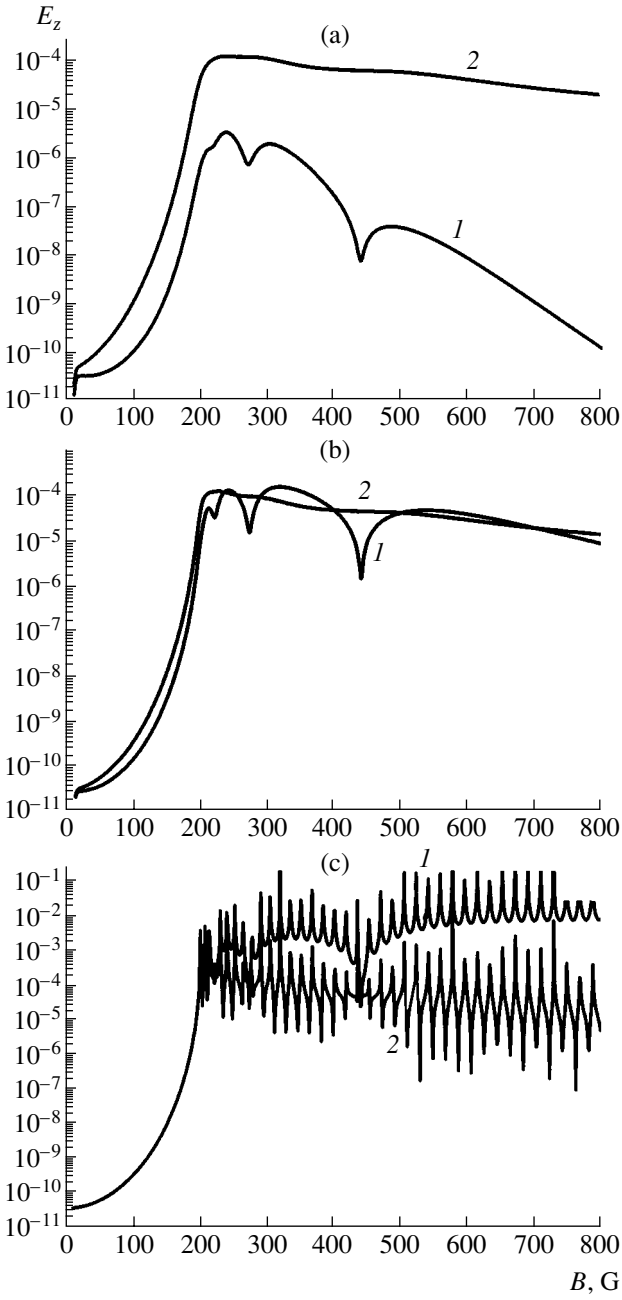

Fig. 4. Amplitude of the longitudinal component of the RF electric field calculated as a function of the magnetic field for R = 5 cm, L = 20 cm, and $n_e = 3 \times 10^{12}$ cm^{-3} (a) with allowance for both electron–neutral and electron–ion collisions, (b) with allowance for electron–neutral collisions only, and (c) without allowance for collisions. Curves *1* refer to the Trivelpiece–Gould wave, and curves *2* refer to the helicon.

ponents depend substantially on the magnetic field and gas pressure, as well as on the diameter and length of the gas-discharge chamber of the source. Figure 4 shows the dependence of the amplitudes of the longitudinal electric fields of a Trivelpiece–Gould wave and a helicon on the magnetic field, calculated for an electron density of 3×10^{12} cm^{-3} in the following three cases: with allowance for electron–neutral and electron–ion collisions, with allowance for electron–neutral collisions only, and without allowance for electron colli-

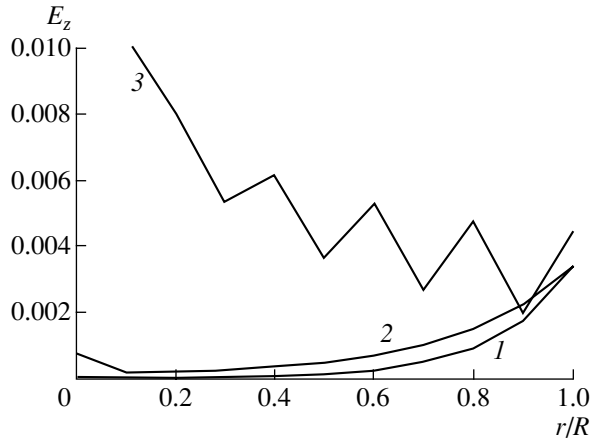

Fig. 5. Radial profiles of the amplitude of the longitudinal electric field of the Trivelpiece–Gould wave for $R = 5$ cm, $L = 20$ cm, $n_e = 3 \times 10^{11}$ cm^{-3}, and $B = 500$ G. Curve *1* was calculated with allowance for both electron–neutral and electron–ion collisions, curve *2*, with allowance for electron–neutral collisions only, and curve *3*, without allowance for collisions.

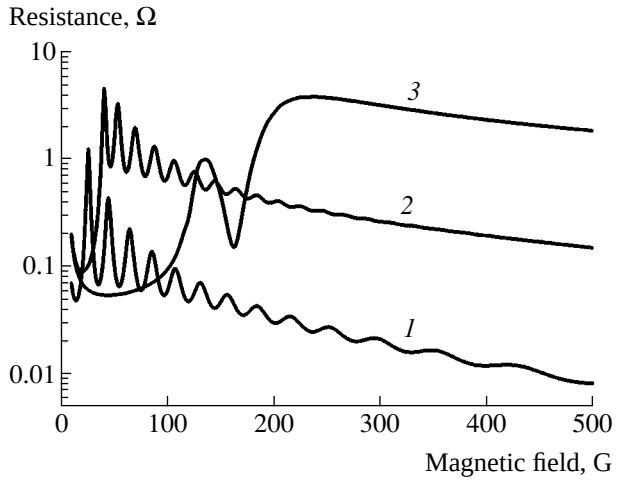

Fig. 6. Dependence of the effective plasma resistance on the magnetic field for $R = 5$ cm and $L = 20$ cm. Curves *1–3* were calculated for electron densities of 10^{10}, 10^{11}, and 10^{12} cm^{-3}, respectively.

sions. As is seen, the characteristic feature of the solutions obtained in the collisionless limit is that the behavior of the longitudinal electric field as a function of the magnetic field is oscillatory, with a short period in the magnetic field. Electron collisions are seen to suppress the oscillations and completely stabilize them. Such behavior of the solutions can be explained using formula (2.22). When electron collisions are ignored, oscillations in the solutions are associated with oscillations in the functions $J_0(\varphi_1 r)$ when the magnetic field is varied. When electron collisions are taken into account, i.e., when $\frac{\nu_e}{\omega} > \frac{\Delta B}{B} \approx \frac{L}{R}\frac{\omega}{\Omega_e}$, the oscillations are stabilized. However, the stabilization of oscillations is not the only consequence of a transition to a collision-dominated plasma. From Fig. 4, we can also see that, under the conditions in question, when electron–ion collisions dominate over electron–neutral collisions, electron collisions considerably reduce the amplitude of the Trivelpiece–Gould wave but essentially do not change the helicon amplitude. This effect is explained by the facts that the collisional dissipation of a helicon is weak (is proportional to the very small parameter $\frac{\Delta H}{H} \approx \frac{\nu_e}{\Omega_e}$) and that the collisional dissipation of a Trivelpiece–Gould wave is strong (is proportional to the large parameter ν_e/ω). Moreover, as the collision frequency increases, a spatial Trivelpiece–Gould wave evolves into a surface Trivelpiece–Gould wave, while the penetration depth of the helicon into the plasma does not change. This effect is readily seen in Fig. 5. Figures 4 and 5 clearly demonstrate why an increase in the electron density in the range $n_e \geq 10^{12}$ cm^{-3} lowers the amplitudes of the electric field components of the Trivelpiece–Gould wave to a much greater extent than those of the helicon. At low electron densities, the collision frequency is determined by the frequency of the electron–neutral collisions and is independent of n_e, so that the ratio of the amplitudes of the longitudinal electric fields of the waves does not depend on the electron density. However, at high electron densities, electron–ion collisions dominate: the electron–ion collision frequency increases with n_e, reducing the amplitudes of the electric field components of the Trivelpiece–Gould wave. The collision frequency also increases with gas pressure; consequently, an increase in the gas pressure lowers the amplitudes of the longitudinal and radial components of the electric field of the Trivelpiece–Gould wave to a greater extent than those of the helicon, so that the spatial Trivelpiece–Gould wave becomes a surface wave.

The above features of the excitation of waves in plasma sources can also be seen in the dependence of the equivalent plasma resistance $R_{\rm pl}$ on the magnetic field. Figure 6 shows representative profiles of $R_{\rm pl}$ calculated as functions of the magnetic field for an argon pressure of 10^{-3} torr and for different electron densities. The functions $R_{\rm pl}$ are seen to exhibit an oscillatory behavior; moreover, the oscillation period at low electron densities ($n_e < 10^{12}$ cm^{-3}) differs markedly from that at high densities ($n_e \geq 10^{12}$ cm^{-3}). The amplitude of oscillations in the equivalent plasma resistance decreases with increasing pressure and vanish at 10^{-2} torr.

Another interesting feature of the behavior of the equivalent plasma resistance is illustrated in Fig. 7. An increase in the electron density leads to a considerable displacement of the maximum in the equivalent plasma

resistance toward stronger magnetic fields. This indicates that, at a fixed value of B_0, the resistance R_{pl} decreases as the electron density increases above a certain high critical density. The stronger the magnetic field, the higher the critical plasma density, an increase above which is accompanied by a decrease in the equivalent plasma resistance.

To conclude this section, we consider the results that are of practical interest. Figures 8–10 show how the plasma resistance depends on the magnetic field in plasma sources of different radii and lengths. In practice, for a plasma source of diameter 5 cm and length 10 cm, it is difficult to satisfy condition (2.2), i.e., to deposit power into the plasma, because the plasma resistance is lower than 1 Ω. Plasma sources with gas-discharge chambers of lengths 15–20 cm are expected to be the most beneficial in providing power deposition in the plasma because, in such sources, the plasma resistance is high over a broad range of magnetic field strengths at electron densities typical of practical applications. Since plasma sources should be capable of operating over a wide range of ion current densities, it seems that, in large-diameter ion sources, too, it is worthwhile to use gas-discharge chambers of the same length (15–20 cm). The reason is that, for longer gas-discharge chambers, the main maximum in the plasma resistance is displaced toward stronger magnetic fields. However, this last effect is undesirable from the point of view of designing working models of sources. Calculations carried out for different operating frequencies of a source showed that an increase in frequency also leads to a displacement of the main maximum in the plasma resistance toward stronger magnetic fields.

According to the above results, the equivalent plasma resistance R_{pl} depends on the strength of the external magnetic field as well as on the discharge parameters: the electron density, the electron temperature, the neutral density, etc. When a certain power is to be fed into a source, the plasma parameters should have quite specific values that would unambiguously determine the plasma resistance and, accordingly, the fraction of the input power that is deposited in the discharge plasma. Hence, in order to simulate the operation of a plasma source and to optimize the source parameters, it is expedient to construct a self-consistent model incorporating the interrelationships between the electron density, the plasma resistance, and the power absorbed by the plasma.

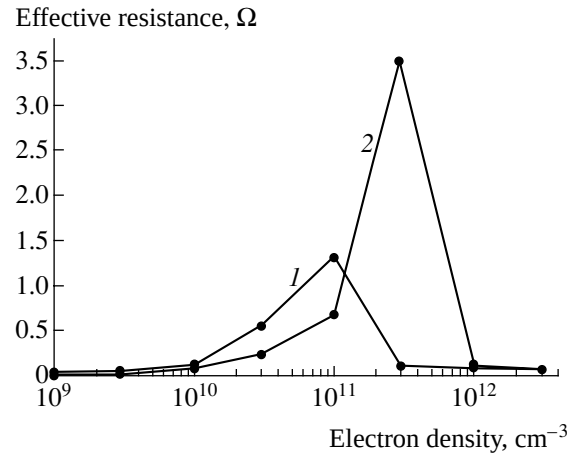

Fig. 7. Dependence of the equivalent plasma resistance on the electron density at a pressure of 10^{-3} torr and at magnetic fields of (*1*) 50 and (*2*) 100 G.

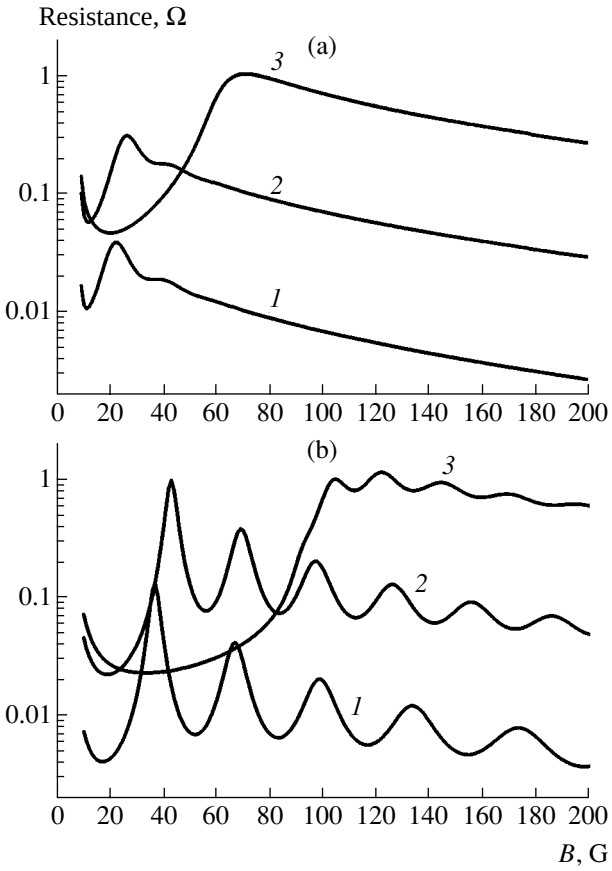

Fig. 8. Dependence of the equivalent plasma resistance on the magnetic field for R = 2.5 cm and L = (a) 10 and (b) 15 cm. Curves *1–3* were calculated for electron densities of 10^{10}, 10^{11}, and 10^{12} cm^{-3}, respectively.

3. RELATIONSHIP OF THE PLASMA PARAMETERS TO THE RF POWER DEPOSITED IN PLASMA

The relationship between the power deposited in the plasma and the plasma parameters can be determined from a simple model of an RF ion source.

The model is based on the following assumptions:

(i) the electron energy distribution function is Maxwellian,

(ii) the ionization is dominated by direct electron-impact ionization,

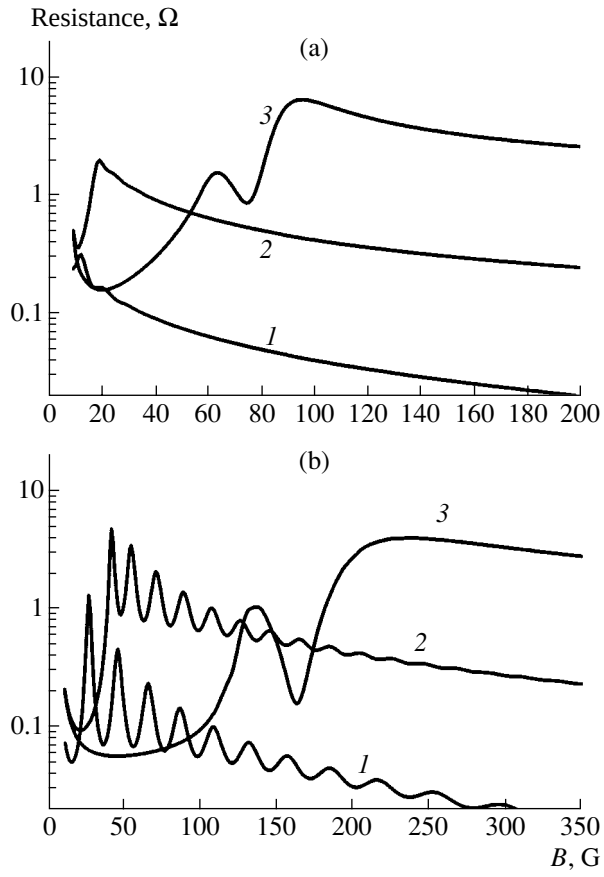

Fig. 9. Dependence of the equivalent plasma resistance on the magnetic field for $R = 5$ cm and $L =$ (a) 10 and (b) 20 cm. Curves *1–3* were calculated for electron densities of 10^{10}, 10^{11}, and 10^{12} cm^{-3}, respectively.

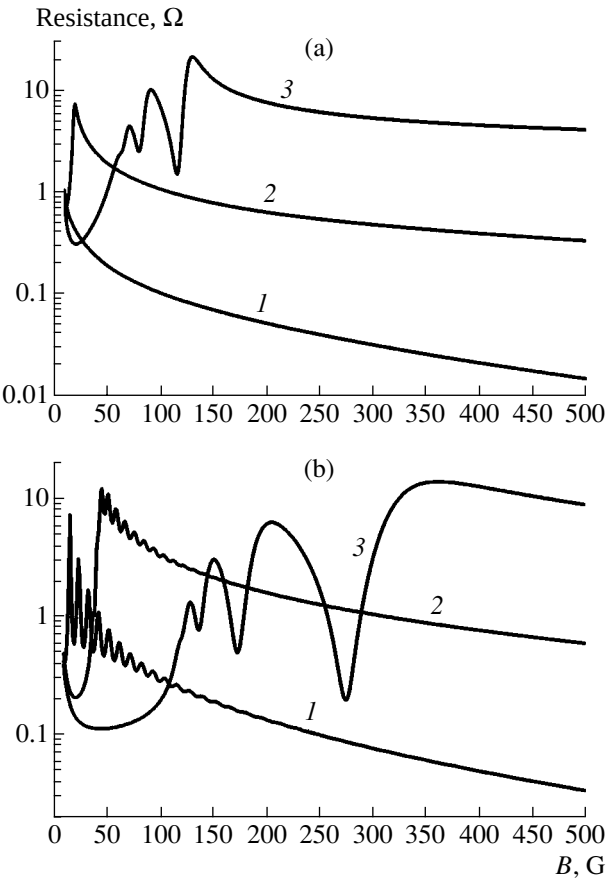

Fig. 10. Dependence of the equivalent plasma resistance on the magnetic field for $R = 10$ cm and $L =$ (a) 10 and (b) 20 cm. Curves *1–3* were calculated for electron densities of 10^{10}, 10^{11}, and 10^{12} cm^{-3}, respectively.

(iii) the density of highly ionized atoms is negligibly low, and

(iv) the density of the ion current to the walls of an ion source is constant at any point.

The model equations are the balance equations for the numbers of ions, electrons, and heavy neutral particles, the power balance equation, and the quasineutrality condition.

The ion balance equation expresses the equality of the number of ions produced within a source of volume V and the number of ions escaping from the plasma volume to the gas-discharge chamber wall of area S:

$$Vn_0n_eZ_{\text{ion}} = 0.4n_iS\sqrt{\frac{2kT_e}{M}}. \qquad (3.1)$$

The electron balance equation expresses the equality of the number of electrons produced within a source of volume V and the number of electrons escaping from the plasma volume to the gas-discharge chamber wall:

$$Vn_0n_eZ_{\text{ion}} = \frac{1}{4}n_eS_e\sqrt{\frac{8kTe}{\pi m}}\exp\left(-\frac{e\phi}{kT_e}\right), \qquad (3.2)$$

where S_e is the area of the wall surface on which the electrons can be lost. In the case when the external magnetic field is absent and the ions are not extracted, the electrons can be lost over the entire surface of the gas-discharge chamber wall; i.e., we have $S_e = S$. Because of the large difference between the ion acoustic velocity and the electron thermal velocity, the possibility of equating the right-hand sides of Eqs. (3.1) and (3.2) is provided by the term that accounts for the negative potential difference ϕ between the plasma and the wall. In the case when the external magnetic field is absent and the ions are extracted, the electrons can be lost over the entire surface of the gas-discharge chamber wall, except for the holes of area S_i through which the ions are extracted; i.e., we have $S_e = S - S_i$. In this case, the potential difference between the gas-discharge

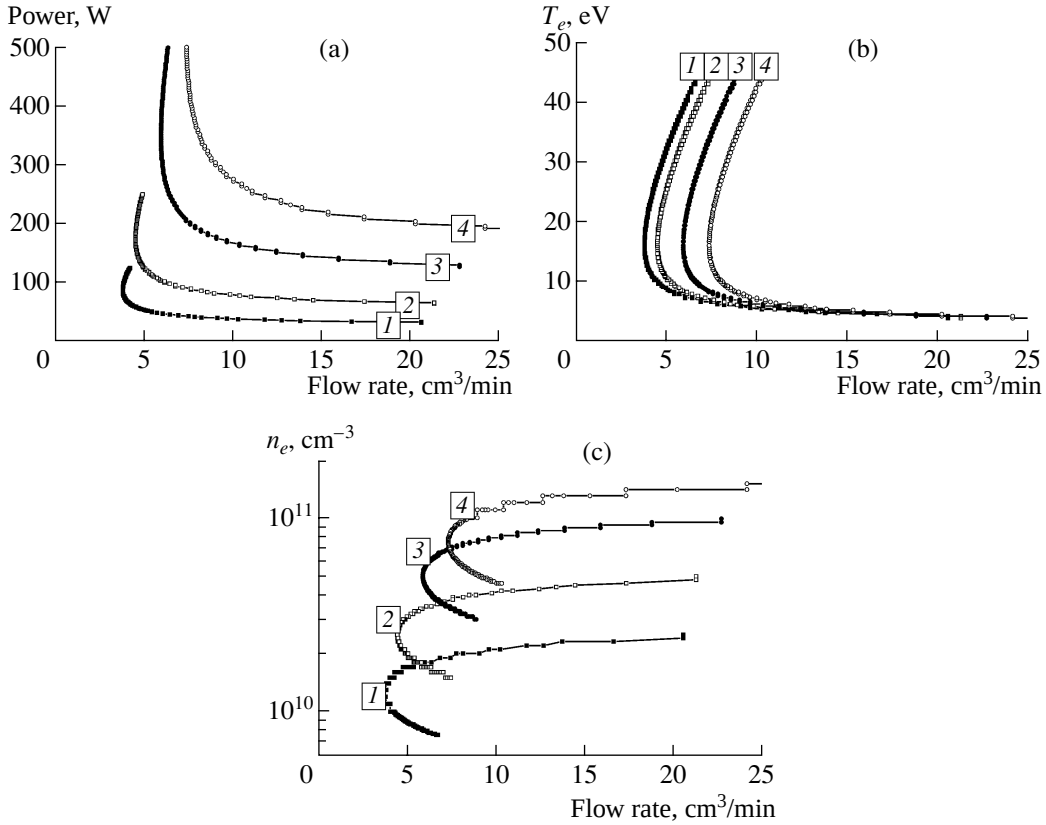

Fig. 11. Dependence of (a) the RF power required to extract an ion current of given magnitude, (b) the electron temperature, and (c) electron density on the argon flow rate. Curves *1–4* were calculated for the following four magnitudes of the ion current extracted from the source: 50, 100, 200, and 300 mA, respectively.

chamber wall and the plasma will obviously be lower. Since the external longitudinal magnetic field reduces the electron mobility in the transverse direction, we can assume for simplicity that, in the presence of the external field, the electrons can only be lost on the end walls of the gas-discharge chamber, except for the holes through which the ions are extracted. Obviously, the smaller the area S_e, the lower the potential difference φ.

The balance equation for heavy neutral particles,

$$N' = 0.4 n_i S_i \sqrt{\frac{2kT_e}{M}} + \frac{1}{4} n_0 S_a \sqrt{\frac{2kT_g}{\pi M}}, \qquad (3.3)$$

expresses the equality of the number N' of atoms (or molecules) of the working gas supplied into the gas-discharge chamber per unit time and the number of atoms (or molecules) and their ions that escape from the chamber through the holes in the ion-optical system at thermal and ion-acoustic velocities, respectively. The transparency of the ion-optical system to atoms can differ from its transparency to ions; that is why, in Eq. (3.3), we have introduced the notation S_i and S_a to denote the areas of the holes through which the ions and atoms are extracted.

The power balance equation expresses the equality of the power deposited into the plasma, on the one hand, and the power carried to the wall by electrons and atoms (as well as the power expended on ionizing and exciting particles in the volume of the system), on the other hand:

$$P_{\text{pl}} = 0.4 e n_i S \sqrt{\frac{2kT_e}{M}} \left(\phi + \frac{2kT_e}{e} + U_i (1 + W(kT_e)) \right), \qquad (3.4)$$

where $W(kT_e)$ is the fraction of power expended on the excitation of atoms (followed by the emission of energy from the system).

The quasineutrality condition has the standard form

$$n_e = n_i. \qquad (3.5)$$

In Eqs. (3.2)–(3.5), n_e and n_i are the electron and ion densities, T_e and T_g are the electron and atom temperatures, M and m are the masses of a heavy particle and an electron, ϕ is the plasma potential relative to the wall, U_i is the ionization potential, $W(kT_e)$ is the fraction of power lost by radiation from the atoms, and P_{pl} is the RF power fed into the plasma.

The ionization rate is given by the formula

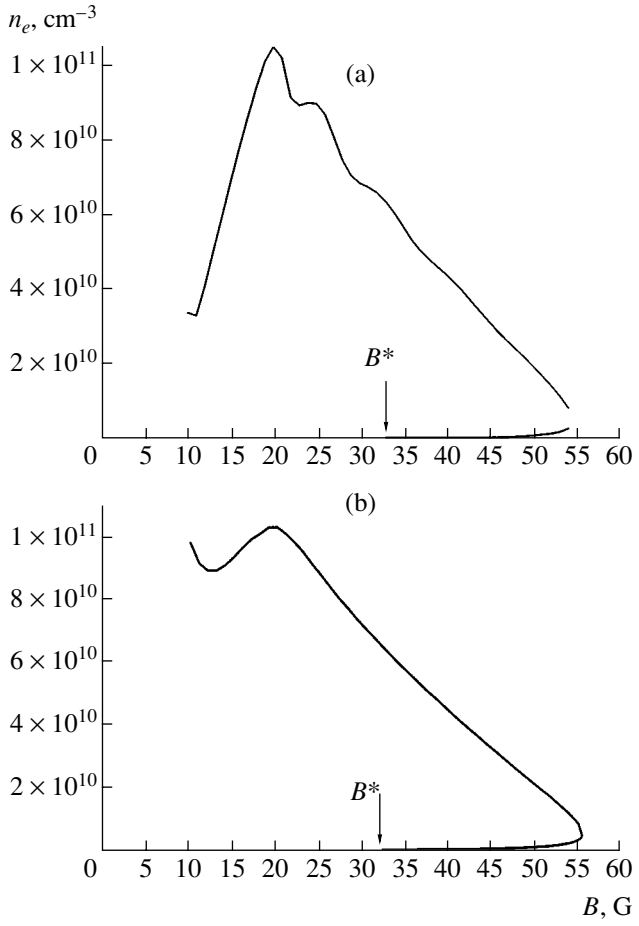

Fig. 12. Solutions to the self-consistent problem for a source of radius 5 cm and length 10 cm at an RF oscillator power of 300 W and at argon gas pressures of p = (a) 10^{-4} and (b) 6×10^{-3} torr.

$$Z_{\text{ion}} = \sqrt{\frac{2m}{M}} \int \sigma_{\text{ion}}(\varepsilon) \sqrt{\varepsilon} f(\varepsilon) d\varepsilon, \tag{3.6}$$

and the fraction of power lost by radiation from the atoms is expressed as

$$W = \frac{\sum E_k \int \sigma_{0k}(\varepsilon) \sqrt{\varepsilon} f(\varepsilon) d\varepsilon}{Z_{\text{ion}}} \sim \frac{\bar{E} \int \bar{\sigma}_{\text{ex}}(\varepsilon) \sqrt{\varepsilon} f(\varepsilon) d\varepsilon}{Z_{\text{ion}}}. \tag{3.7}$$

Here, σ_{ion} is the effective ionization cross section, σ_{ex} is the total excitation cross section for argon, ε is the electron energy, $f(\varepsilon)$ is the electron energy distribution function, and $\bar{E}$ is the mean excitation energy.

The set of nonlinear equations (3.1)–(3.7) was solved by the method of iteration. The required values of the experimental cross sections were taken from [12, 13].

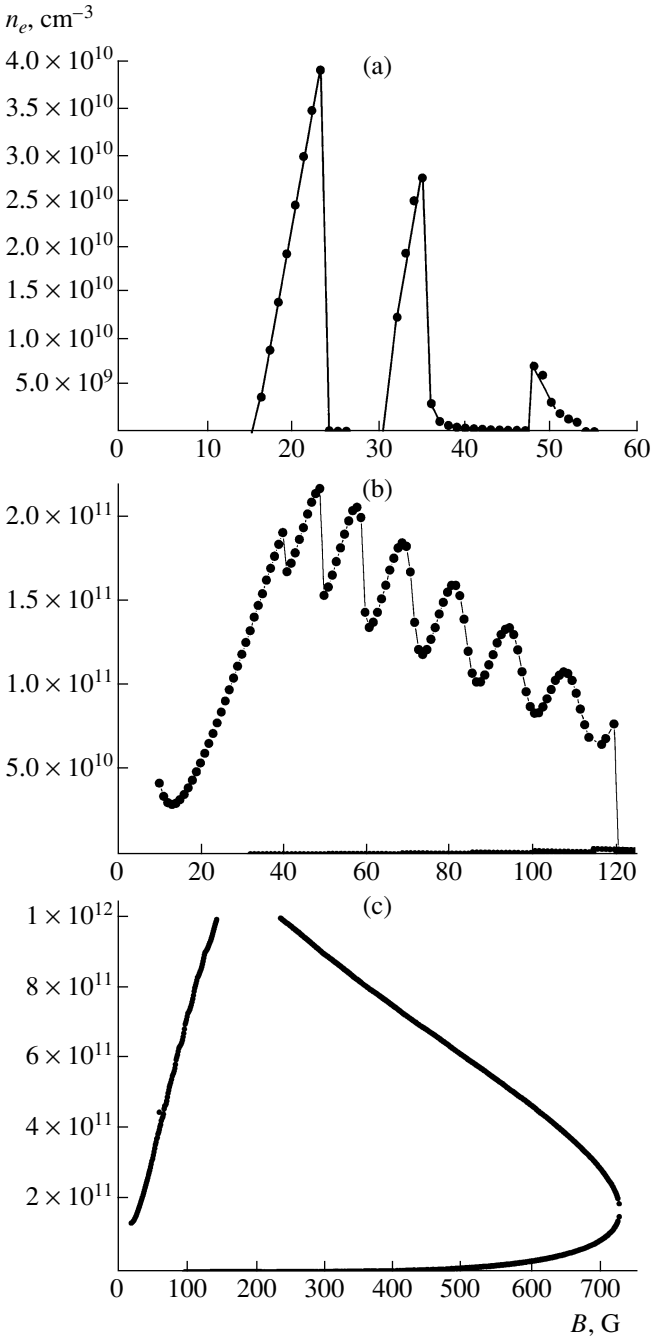

Fig. 13. Solutions to the self-consistent problem for a source of radius 5 cm and length 15 cm at a pressure of 10^{-3} torr and at RF oscillator powers of (a) 100, (b) 500, and (c) 2500 W.

Let us briefly discuss the results of calculating the plasma parameters on the basis of the above simple physical model of the source. These results are illustrated in Fig. 11 in the form of the dependence of the RF power required to extract an ion current of given magnitude, the electron temperature, and electron density on the argon flow rate. According to Fig. 11, we can distinguish between two different modes of operation of

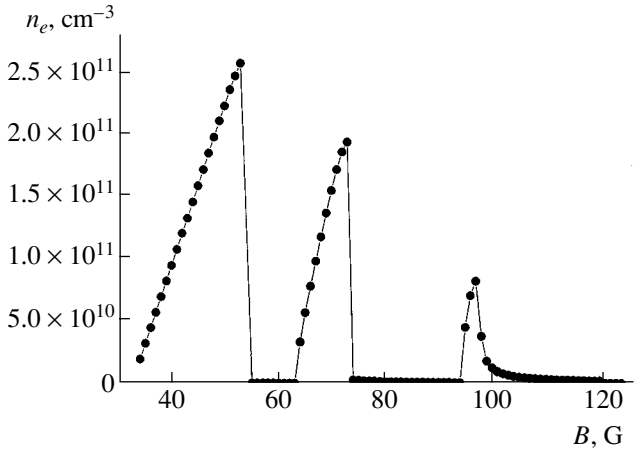

Fig. 14. Solution to the self-consistent problem for a source of radius 2.5 cm and length 15 cm at an RF oscillator power of 700 W and at a pressure of 5×10^{-4} torr.

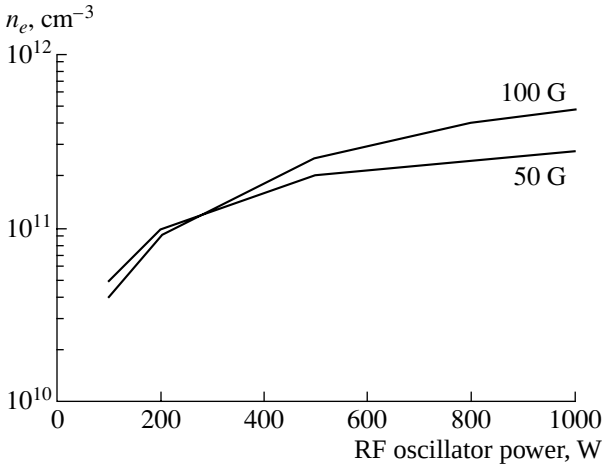

Fig. 15. Dependence of the electron density on the RF oscillator power for a source of radius 5 cm and length 20 cm at a pressure of 10^{-3} torr and at magnetic fields of 50 and 100 G.

an RF ion source: the mode with a low flow rate and that with a high flow rate. The characteristic feature of the first mode is that the RF power deposited in the discharge plasma and the plasma electron temperature both increase sharply as N' decreases. The characteristic feature of the second mode is that the RF power deposited in plasma depends very little on N'. Another important feature of the second mode is that the electron density changes in proportion to the deposited power while the electron temperature remains essentially constant.

We rewrite power balance equation (2.1) as

$$P = I^2(R_{\text{ant}} + R_{\text{pl}}).$$

Generally, the power I^2R_{pl} deposited in plasma is a complicated nonlinear function of the plasma parameters. Recall, however, that, under conditions corresponding to relatively high flow rates of the working gas, the electron density is nearly proportional to the deposited power, the electron temperature being essentially constant. In this case, power balance equation (3.4) becomes

$$I^2R_{\text{pl}}(n_e, T_e, P, B, R, L) = \alpha n_e \equiv 0.4en_iS\sqrt{\frac{2kT_e}{M}}\left(\phi + \frac{2kT_e}{e} + U_i(1 + W(kT_e))\right). \quad (3.8)$$

The set of nonlinear equations (3.1)–(3.8) was solved by iteration. When the calculated values of the electron density were lower than 10^9 cm^{-3}, the equations were regarded as having no solution because such density values are too low to satisfy inequalities (2.4).

Numerical simulations allowed us to explain the following experimentally observed distinctive features of the discharge [4, 7]: discharge disruptions at certain magnetic field strengths, a hysteresis effect in the dependence of the plasma parameters and extracted ion current on the external magnetic field [9, 14], and the fact that, at some magnetic field strengths, the plasma parameters reach their saturation values as the RF oscillator power increases [2, 4, 15].

First of all, simulations showed that, in a number of cases, the problem has several solutions for the same external magnetic field B and the same RF oscillator power P; i.e., there are several values of the electron density that satisfy Eqs. (3.1)–(3.8). Figure 12 shows representative solutions calculated for quite different argon pressures. We can see that, at a fixed RF oscillator power, the electron density increases and reaches its maximum at a comparatively weak magnetic field. A further increase in the field up to a certain value B^* is accompanied by a decrease in the electron density. For stronger magnetic fields, there may exist a second solution, which corresponds to electron densities that are approximately one order of magnitude lower than the densities corresponding to the first stable solutions. The presence of several values of the electron density at a fixed value of B and of P shows that the system can exhibit a hysteresis effect with respect to an increase and a decrease in the external magnetic field. An analysis shows that the extent to which the solutions are stable against small variations in the electron density is different for different strengths of the external magnetic field. The existence of several solutions for the same magnetic field strength and the absence of stable solutions may provide a plausible explanation of the phenomenon that was observed experimentally by Light *et al.* [14], namely, low-frequency oscillations of the electron density at magnetic fields above certain critical values.

There is one more important feature of Eqs. (3.1)–(3.8) that deserves mention here: for a magnetic field above the critical value B_{cr}, they have no solutions in a given range of plasma parameters. The nonexistence of

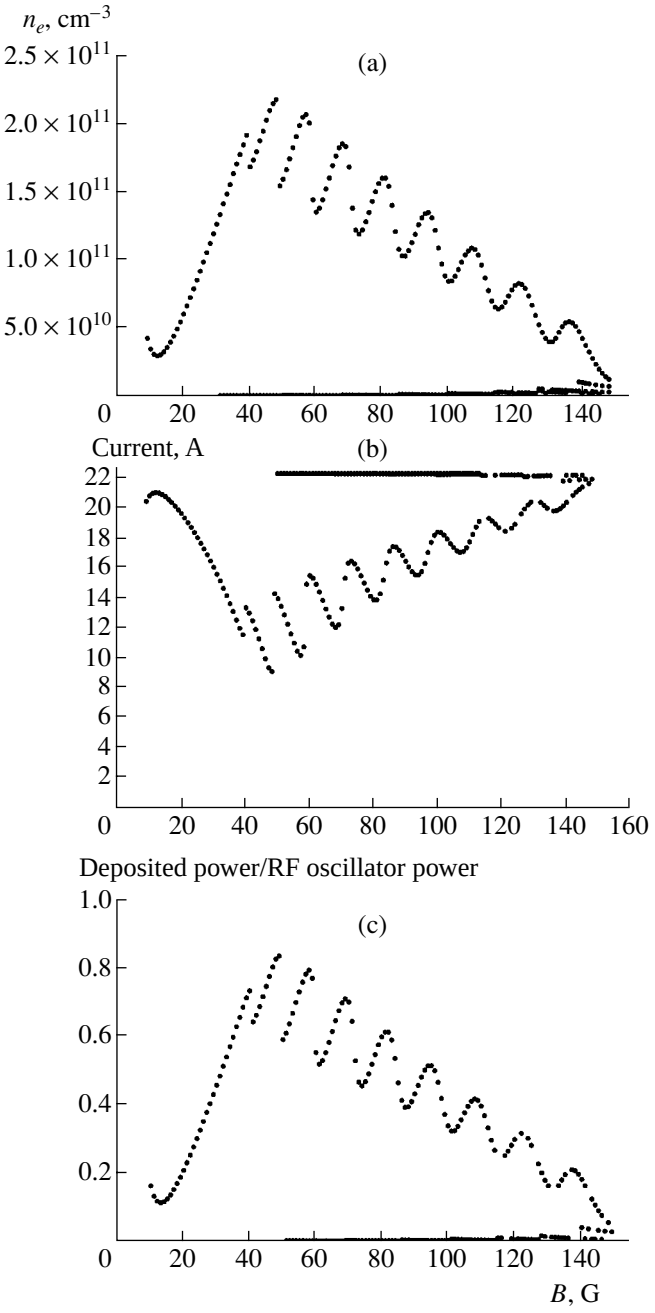

Fig. 16. (a) Electron density, (b) antenna current, and (c) the efficiency of power deposition in a plasma calculated as functions of the external magnetic field from the solution to the self-consistent problem for a source of radius 5 cm and length 15 cm.

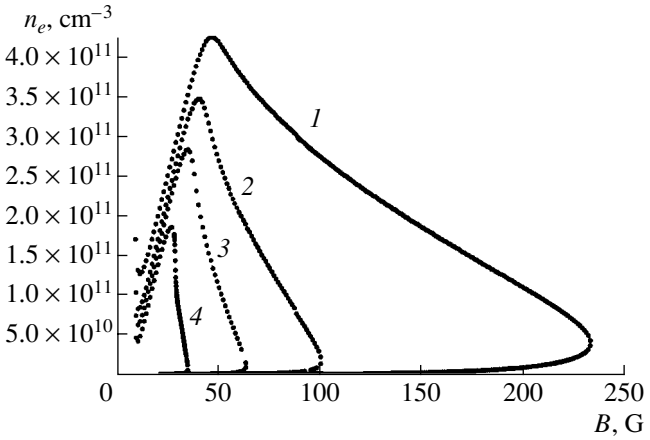

Fig. 17. Electron density calculated as a function of the external magnetic field from the solution to the self-consistent problem for a source of radius 5 cm and length 10 cm at antenna resistances of (*1*) 1, (*2*) 2, (*3*) 3, and (*4*) 5 Ω.

solutions for strong magnetic fields can be explained as follows: since the equivalent plasma resistance decreases as the magnetic field increases, most of the RF oscillator power is lost in the antenna and the power deposited in the plasma is insufficient to maintain the electron density at a level of 10^9 cm^{-3} and higher. Note that, as the pressure increases, the right bound of the range where the solutions can exist is displaced toward larger values of B. Recall that an increase in the electron density is accompanied by the displacement of the maximum in the dependence of R_{pl} on B toward stronger magnetic fields. Consequently, as the RF oscillator power increases, the right bound of the range where the solutions can exist is also displaced toward stronger fields. This result is clearly demonstrated in Fig. 13. However, the following paradoxical situation shown in Fig. 13c is also possible: An increase in the RF oscillator power at weak magnetic fields first leads to an increase in the electron density relative to its values obtained for lower powers. After the critical electron density has been reached, the source loses its ability to operate in a mode with high electron density. Finally, at very strong magnetic fields, the source again becomes capable of operating in such a mode. This unusual feature can be explained by reference to Fig. 7, which illustrates how the equivalent plasma resistance depends on the electron density. At relatively weak magnetic fields, an increase in the electron density above the critical level leads to a sharp decrease in the equivalent plasma resistance and, accordingly, in the power deposited in the discharge plasma. A substantial increase in the magnetic field is accompanied by an increase in both the critical electron density and the equivalent plasma resistance; as a result, the operating mode with a high electron density again becomes possible. It should also be noted that the nonlinear dependence of R_{pl} on B and n_e has the following two interesting consequences. For a low argon gas pressure, the dependence of R_{pl} on B is essentially nonmonotonic, which manifests itself in a very nonmonotonic dependence of the electron density on the magnetic field B (see Fig. 14). As was shown above, an increase in the electron density in the range of its high values is accompanied by a decrease in the equivalent plasma resistance. This explains the phenomenon that was observed experimentally in [2, 4, 15]—the saturation of the

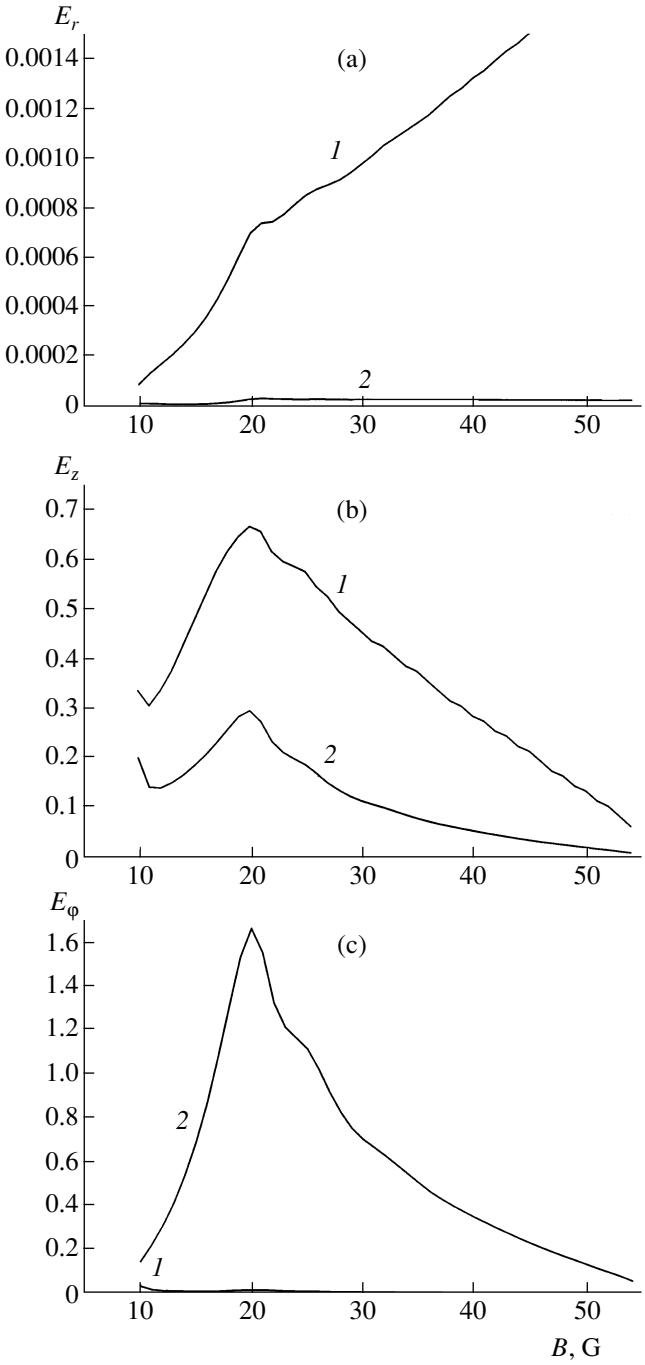

Fig. 18. Dependence of the amplitudes of the (a) radial, (b) longitudinal, and (c) azimuthal components of the electric fields of (*1*) a Trivelpiece–Gould wave and of (*2*) a helicon on the external magnetic field.

plasma density with increasing RF oscillator power. Figure 15 displays the electron density profiles calculated as functions of the oscillator power for several different values of the magnetic field. It can be seen that the calculated profiles are analogous to those observed experimentally.

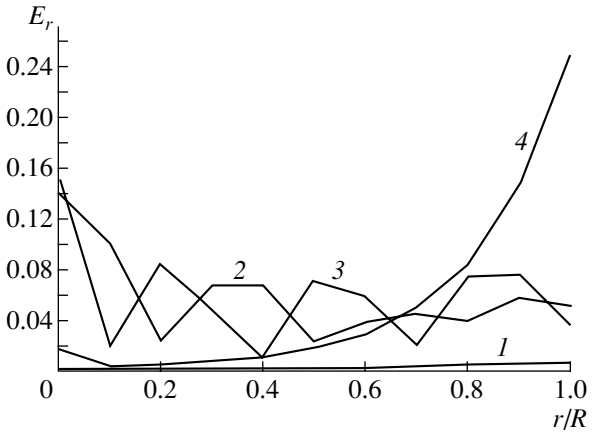

Fig. 19. Radial profiles of the amplitude of the radial component of the RF electric field for different values of the external magnetic field: (*1*) 25, (*2*) 60, (*3*) 100, and (*4*) 460 G.

Shamrai and Taranov [16] showed that discharge disruptions in plasma sources can also be caused by a decrease in the power deposited in the plasma due to the decoupling between an RF oscillator and a plasma. This decoupling is the result of a change in the active and reactive components of the load resistance when the external magnetic field changes. The phenomenon mentioned in [16] can and must make the above effects more pronounced.

Let us consider in more detail what happens in a plasma source when the magnetic field increases. Figure 16 shows the dependence of the electron density, the antenna current, and the efficiency of power deposition in the plasma on the magnetic field B. In the range in which the solution corresponding to high electron densities n_e can exist, an increase in the magnetic field is, as a rule, initially accompanied by an increase in the electron density. As the plasma density increases, the antenna current decreases, which indicates an increase in the amount of power deposited in the plasma. As a result, the power absorption in the discharge plasma becomes more efficient (Fig. 16c). Thus, for an input RF power of 500 W and a magnetic field of about 4 mT, the fraction of the input power deposited in the plasma amounts to 90%.

The numerical calculations described above were carried out for an antenna resistance of 1 Ω. Figure 17 illustrates how the behavior of the system changes with changing antenna resistance. We can see that, by decreasing the resistance of the external circuit, it is possible to achieve efficient power deposition in the plasma over a wide range of magnetic fields.

Simulations showed that, when the electron density and working gas pressure are not too high, the radial electric field of the Trivelpiece–Gould wave is the strongest among the wave fields in the plasma (see Fig. 18). The longitudinal electric field of the Trivelpiece–Gould wave is stronger than that of the helicon,

and the azimuthal electric field of the Trivelpiece–Gould wave is weaker than that of the helicon. On the whole, the relationships between the electric field components of the Trivelpiece–Gould wave and of the helicon are determined by the particular values of the electron plasma density and by the radius and length of the plasma source, in accordance with the results of Section 2.3. Figure 19 shows the radial profiles of the RF electric fields calculated for different values of the external magnetic field. We see that, at magnetic fields close to the field B_{max} (which corresponds to the maximum electron density), the electric field of the waves penetrate into the plasma, whereas, at magnetic fields far stronger and far weaker than B_{max}, the waves in question are surface waves.

4. CONCLUSIONS

In conclusion, we briefly summarize the results of our work.

(i) We have developed a general theory of the absorption of an RF field in a plasma cylinder excited by a purely inductive field source.

(ii) We have shown that, at low plasma densities such that the inductive field excited by the source is screened by the plasma and is concentrated near the surface of the plasma cylinder, the RF power is mainly deposited via the absorption of electrostatic waves (oblique Langmuir waves, or the Trivelpiece–Gould modes), which are, in turn, excited by inductive surface fields. It is the resonant absorption of spatial electrostatic waves that governs the active plasma resistance, which under these conditions considerably exceeds the active antenna resistance.

(iii) We have constructed a simple self-consistent model of a plasma source that takes into account the inflow of gas into the entire volume of the plasma cylinder, gas ionization by an RF field, and losses of charged particles from the plasma volume.

(iv) Using this simple model, we have qualitatively explained a number of phenomena observed in experiments with inductive plasma sources: first, the weak dependence of the RF power deposited in the plasma on the neutral gas density at high gas flow rates; second, the existence of several values of the magnetic field for each of which there are several values of the equilibrium electron plasma density (this phenomenon manifests itself in a hysteresis effect and the onset of instability); and third, the decrease in the active plasma resistance at strong magnetic fields, in which case the efficient operation of the source is impossible.

(v) The results of calculations by our simple self-consistent model agree qualitatively with the experimental observations [2, 4, 8, 9, 12, 15].

REFERENCES

1. A. F. Aleksandrov, G. É. Bugrov, N. F. Vorob'ev, *et al.*, Prikl. Fiz., No. 1, 3 (1995).
2. K. P. Shamrai, A. F. Alexandrov, G. E. Bougrov, *et al.*, in *Proceedings of the 23rd International Conference on Phenomena in Ionic Gases, Toulouse, 1997*; J. Phys. (France), Suppl. **3**, 4365 (1997).
3. A. F. Alexandrov, E. A. Kralkina, V. A. Obukhov, *et al.*, J. Mosc. Phys. Soc. **6** (1), 113 (1996).
4. A. F. Alexandrov, G. E. Bugrov, E. A. Kralkina, *et al.*, in *Proceedings of the 25th International Conference on Phenomena in Ionic Gases, Nagoya, 2001*.
5. R. W. Boswell, Plasma Phys. Controlled Fusion **26**, 1147 (1984).
6. F. F. Chen, *Introduction to Plasma Physics and Controlled Fusion*, Vol. 1: *Plasma Physics* (Plenum Press, New York, 1984).
7. F. F. Chen and G. Chevalier, J. Vac. Sci. Technol. A **10**, 1389 (1992).
8. F. F. Chen and D. Amush, Plasma Phys. **4**, 3411 (1997).
9. J. Rayner and A. Cheetham, Plasma Sources Sci. Technol. **8**, 79 (1999).
10. V. L. Ginzburg and A. A. Rukhadze, *Waves in Magnetized Plasmas* (Nauka, Moscow, 1970).
11. A. F. Aleksandrov, L. S. Bogdankevich, and A. A. Rukhadze, *Principles of Plasma Electrodynamics* (Vysshaya Shkola, Moscow, 1988; Springer-Verlag, Berlin, 1984).
12. A. Muller, E. Salzborn, R. Frodl, *et al.*, J. Phys. B **13**, 1877 (1980).
13. F. J. de Heer, R. H. J. Jansen, W. van der Kaay, *et al.*, J. Phys. B **12**, 979 (1979).
14. M. Light, F. F. Chen, and P. L. Colestock, Plasma Sources Sci. Technol. **11**, 273 (2002).
15. Y. Sakawa, T. Takino, and T. Shoji, Phys. Plasmas **6**, 4759 (1999).
16. K. R. Shamrai and V. B. Taranov, Plasma Sources Sci. Technol. **5**, 474 (1999).

Translated by O.E. Khadin

Plasma Physics Reports, Vol. 30, No. 5, 2004, pp. 413–421. Translated from Fizika Plazmy, Vol. 30, No. 5, 2004, pp. 450–458.

PLASMA OSCILLATIONS AND WAVES

On the Possibility of Reflection of Alfvén Waves in a Curvilinear Magnetic Field

N. G. Mazur, E. N. Fedorov, and V. A. Pilipenko

Schmidt Institute of the Physics of the Earth, Russian Academy of Sciences, ul. Bol'shaya Gruzinskaya 10, Moscow, 123995 Russia

Received April 25, 2003; in final form, October 8, 2003

Abstract—The propagation of Alfvén waves in a plasma immersed in a curvilinear magnetic field is investigated by using a 2D model. The waves are described by a 1D equation that formally coincides with the equation for the case of a quasi-uniform straight magnetic field with a modified Alfvén velocity that takes into account the longitudinal dependence of the Lame coefficients. It is shown that toroidal and poloidal Alfvén modes depend differently on the magnetic-field geometry. In the case of a 2D plane-parallel configuration of the magnetic field, poloidal modes are efficiently reflected from regions where the magnetic field lines sharply converge or diverge. This effect can result in the formation of open-field-line Alfvén quasi-resonators. © *2004 MAIK "Nauka/Interperiodica".*

1. INTRODUCTION

One of the basic mechanisms for the energy transport of nonsteady perturbations in near-Earth, solar, and laboratory plasmas involves Alfvén waves. Long-wavelength Alfvén waves, which are only slightly affected by kinetic and dispersion effects, can propagate without attenuation over large distances along magnetic field lines. It follows from the wave equation for Alfvén waves that these waves have no reflection points. It would seem, therefore, that no longitudinal (along the field lines) resonators in which the wave energy could be accumulated can form for these waves. However, if there are regions with sharp longitudinal variations in Alfvén velocity in the plasma, then Alfvén waves can be partially reflected from these regions [1]. For perturbations with a wavelength comparable to the inhomogeneity scale, the geometric-optics approximation is violated, so that a substantial fraction of the wave energy can be reflected. Such a reflection can limit the influx of the wave energy into the solar corona [2] or the Jovian magnetosphere [3]. In addition, it can lead to the formation of quasi-resonators, such as an ionospheric Alfvén resonator in the upper ionosphere [4–7] and resonators in the regions of the magnetospheric cusp [8] and coronal solar loops [2]. Alfvén oscillations can be excited either directly by fast particles with nonequilibrium distributions [9, 10] or due to the resonant transformation of magnetosonic perturbations when the external source frequency is close to the eigenfrequency of an Alfvén resonator [11, 12]. The accumulation of wave energy in Alfvén resonators can significantly affect long-scale plasma dynamics.

However, in all of the above papers, the propagation of Alfvén waves was described using models in which the magnetic field lines were assumed to be straight. In the present paper, we will show that, under certain conditions, a sharp local change in the geometry of magnetic field lines, such that the field lines sharply converge or diverge, also results in the reflection of Alfvén waves, which can lead to the formation of open-field-line quasi-resonators even in the absence of conducting ends or sharp plasma density gradients.

2. EQUATIONS FOR ALFVÉN WAVES IN A CURVILINEAR MAGNETIC FIELD

The propagation of magnetohydrodynamic (MHD) waves in a curvilinear magnetic field will be examined in a linearized ideal MHD model. In this approach, the transverse component of the polarization current is equal to $\mathbf{j}_\perp = (\mu_0 V_A^2)^{-1}\partial_t \mathbf{E}_\perp$. Assuming the plasma to be perfectly conducting along the main magnetic field $\mathbf{B}_0(\mathbf{r})$, $\sigma_\parallel = \infty$ (in this case, the longitudinal component of the electric field is zero, $\mathbf{E}_\parallel = 0$), we write Maxwell's equations in the form

$$\partial_t \mathbf{B} + \nabla \times \mathbf{E}_\perp = 0, \quad \partial_t \mathbf{E}_\perp - V_A^2 [\nabla \times \mathbf{B}]_\perp = 0, \quad (1)$$

where $\mathbf{E}_\perp$ is the transverse (with respect to $\mathbf{B}_0$) component of the electric field and $V_A = B_0/\sqrt{\mu_0 \rho}$ is the Alfvén velocity.

To study MHD perturbations in a plasma immersed in a curvilinear magnetic field, we will use a curvilinear coordinate system (CS) related to the geometry of the magnetic field $\mathbf{B}_0(\mathbf{r})$. We assume that, in the region under study, the magnetic field can be expressed through a scalar potential Ψ: $\mathbf{B}_0 = -\nabla\Psi$. We introduce the following CS: $x^1 = \Phi_1(x, y, z)$, $x^2 = \Phi_2(x, y, z)$ and $x^3 = \Psi(x, y, z)$ such that the line of intersection of the

1063-780X/04/3005-0413$26.00 © 2004 MAIK "Nauka/Interperiodica"

surfaces $\Phi_1(x, y, z) = \text{const}$ and $\Phi_2(x, y, z) = \text{const}$ with the equipotential surface $S_3(x^3 = \Psi(x, y, z) = \text{const})$ are the lines of curvature on the surface S_3, i.e., the lines tangents to which in each point of S_3 belong to one of two orthogonal planes of the principal normal sections. The local basis of this CS is formed by the vectors $\mathbf{e}^1 = \nabla\Phi_1$, $\mathbf{e}^2 = \nabla\Phi_2$, and $\mathbf{e}^3 = \nabla\Psi = -\mathbf{B}_0$, and the Lame coefficients $h_n = |\mathbf{e}^n|^{-1}$ are related to the diagonal elements of the metric tensor as $h_n^{-2} = g_{nn}$.

In view of the fact that the magnetic field $\mathbf{B}_0$ is nondivergent, an element of the magnetic flux $d\chi = \mathbf{B}_0 \cdot d\mathbf{S}_3$ in a flux tube dx^1dx^2 is conserved along the tube. Taking into account that $\mathbf{B}_0 = -\mathbf{e}^3$ and the element of the cross-sectional area of the flux tube is $d\mathbf{S}_3 = h_1dx^1h_2dx^2h_3\mathbf{e}^3$, we obtain the following expression for a magnetic flux element:

$$d\chi = -\frac{h_1h_2}{h_3}dx^1dx^2.$$

It follows from the conservation of the magnetic flux that the ratio h_1h_2/h_3 is constant along the flux tube. Let $h_1h_2/h_3 = 1$ on a certain equipotential surface; the equality

$$h_3 = h_1h_2 \tag{2}$$

then takes place in the entire volume under study. Taking into account equality (2), the components of Eq. (1) for an individual temporal harmonic $\propto \exp(-i\omega t)$ in the chosen CS can be written as

$$\begin{aligned}
i\omega h_2^2 B_1 + \partial_3 E_2 &= 0,\\
i\omega h_1^2 B_2 - \partial_3 E_1 &= 0,\\
i\omega B_3 - \partial_1 E_2 + \partial_2 E_1 &= 0,\\
i\omega h_2^2 V_A^{-2} E_1 - \partial_3 B_2 + \partial_2 B_3 &= 0,\\
i\omega h_1^2 V_A^{-2} E_2 + \partial_3 B_1 - \partial_1 B_3 &= 0,
\end{aligned} \tag{3}$$

where $\partial_n = \partial/\partial x^n$.

The analysis of the MHD oscillation spectrum in a confined nonuniform plasma system showed [13, 14] that the spectral properties of Alfvén oscillations are described by two ordinary differential (with respect to the longitudinal coordinate x^3) equations that play a role of nonlocal dispersion relations and correspond to different transverse structures of oscillations. For definiteness, we assume that the Alfvén velocity varies more rapidly along the coordinate x^1 (as compared to variations along the coordinate x^2). One class of perturbations corresponds to a case in which the oscillation field varies along the coordinate x^1 ($\partial_1 \simeq ik_1$) much more rapidly than along the coordinate x^2 ($\partial_2 \simeq ik_2$) (i.e., $|k_1| \gg |k_2|$). In the other case, to the contrary, perturbations vary more rapidly along the coordinate x^2 (i.e., $|k_2| \gg |k_1|$).

Let us show that, in these important limiting cases, a set of equations describing Alfvén oscillations with $B_3 \longrightarrow 0$ can be separated out from the complete set (3). Magnetosonic oscillations, in which the component of the longitudinal magnetic field B_3 is finite, will not be considered.

Assuming that $k_1 \longrightarrow \infty$, we find from Eqs. (3) that $E_2 \longrightarrow 0$ and $B_3 \longrightarrow 0$ (while k_1E_2 and k_1B_3 should not necessarily tend to zero). Thus, by virtue of the first equation of set (3), we also have $B_1 \longrightarrow 0$. As a result, the second and fourth equations of set (3) yield the closed set of equations for the components B_2 and E_1:

$$i\omega h_1^2 B_2 - \partial_3 E_1 = 0, \quad i\omega h_2^2 V_A^{-2} E_1 - \partial_3 B_2 = 0,$$

which, after eliminating B_2, reduces to one second-order equation

$$\left(\frac{1}{h_2^2}\partial_3\frac{1}{h_1^2}\partial_3 + \frac{\omega^2}{V_A^2}\right)E_1 = 0. \tag{4}$$

Alfvén oscillations described by Eq. (4) will henceforth be referred to as mode 1. They are polarized so that the electric field is directed along the coordinate x^1, while the magnetic field perturbations and plasma displacements are directed along the coordinate x^2. These oscillations are primarily excited by long-scale (with small k_2) sources.

In the case of perturbations rapidly varying along the coordinate x^2 ($k_2 \longrightarrow \infty$), we have $E_1 \longrightarrow 0$ in Eqs. (3) (while k_2E_1 and k_2B_3 should not necessarily tend to zero). In this case, by virtue of the first equation of set (3), we also have $B_2 \longrightarrow 0$. As a result, the first and fifth equations yield the closed set of equations:

$$i\omega h_2^2 B_1 + \partial_3 E_2 = 0, \quad i\omega h_1^2 V_A^{-2} E_2 + \partial_3 B_1 = 0,$$

which reduces to the second-order equation

$$\left(\frac{1}{h_1^2}\partial_3\frac{1}{h_2^2}\partial_3 + \frac{\omega^2}{V_A^2}\right)E_2 = 0. \tag{5}$$

The polarization of Alfvén oscillations described by Eq. (5) differs from that of mode 1: the electric field is directed along the coordinate x^2, while the magnetic field perturbations and plasma displacements are directed along the coordinate x^1. We will refer to these oscillations as mode 2. These oscillations are mainly excited by localized (with large k_2) sources, e.g., by kinetic instabilities of the hot plasma component [9, 10, 15].

In was shown in [13, 14] that differential equations (4) and (5), supplemented by necessary boundary conditions, can be used to determine the spectrum of Alfvén oscillations even in a 3D case.

Equations (4) and (5) can be rewritten in an invariant form [16] in which the influence of the geometrical factor—the magnetic field curvature—on the propagation of Alfvén waves is expressed explicitly. Let us introduce, along with x^3, the longitudinal coordinate s, equal to the distance along the field line. In view of relation (2), the change of variable $ds = h_3 dx^3$ in Eqs. (4) and (5) reduces them to the form

$$\begin{aligned}[\partial_{ss} + (K_1 - K_2)\partial_s + \omega^2 V_A^{-2}]E_1 &= 0,\\ [\partial_{ss} + (K_2 - K_1)\partial_s + \omega^2 V_A^{-2}]E_2 &= 0.\end{aligned} \tag{6}$$

The quantities $K_i = -\partial_s(\ln h_i)$ in Eqs. (6) are the principal curvatures of an equipotential surface $x^3 = \text{const}$ and characterize the rate at which the field lines converge (or diverge).

The eigenfrequencies of Alfvén oscillations of the geomagnetic shell are somewhat different for modes with different polarizations described by Eqs. (4) and (5). As was shown in [16], this polarization splitting of the spectrum is related to the different influence of the geomagnetic field curvature on the spectrum of oscillations in which the plasma is displaced along and across the shell (more precisely, to the difference between the principal curvatures of equipotential surfaces or, in other words, to the difference in the rates at which the field lines converge or diverge in two orthogonal surfaces containing the given field line). If the principal curvatures coincide in the intersection points of the equipotential surfaces with the given field line, $K_1 = K_2$ (i.e., the field lines converge or diverge at the same rate), the polarization splitting of the spectrum is absent.

It is convenient to rewrite Eqs. (4) and (5) in a form similar to the equation for Alfvén waves propagating in a uniform external magnetic field. Substituting $d\xi = h_1^2 dx^3$ in Eq. (4) reduces it to

$$\left[\partial_{\xi\xi} + \left(\frac{\omega}{V_A^{(1)}}\right)^2\right]E_1 = 0, \tag{7}$$

and Eq. (5), after substituting $d\eta = h_2^2 dx^3$, becomes

$$\left[\partial_{\eta\eta} + \left(\frac{\omega}{V_A^{(2)}}\right)^2\right]E_2 = 0. \tag{8}$$

The modified Alfvén velocities in Eqs. (7) and (8) are determined by the formulas

$$V_A^{(1)} = \frac{h_1}{h_2}V_A = \frac{1}{h_2^2\sqrt{\mu_0\rho}}, \quad V_A^{(2)} = \frac{h_2}{h_1}V_A = \frac{1}{h_1^2\sqrt{\mu_0\rho}}. \tag{9}$$

Thus, the propagation of Alfvén waves in a curvilinear magnetic field can be described by Eqs. (7) and (8), which are similar to the equation that corresponds to the case of a straight field and in which V_A is replaced with the modified Alfvén velocities $V_A^{(1)}$ and $V_A^{(2)}$.

Equations (6) allow us to suppose that the most efficient reflection of Alfvén waves from a region with a curvilinear magnetic field will happen when the principal curvatures K_1 and K_2 differ greatly from one another. For curvatures of the same sign, this takes place at $K_2 \ll K_1$. Therefore, in the next section, we will consider the limiting case of a plane-parallel field $\mathbf{B}_0(\mathbf{r})$, when $K_2 = 0$. In this case, in accordance with geophysical terminology, modes 1 and 2 will be referred to as a toroidal and a poloidal mode, respectively.

3. PROPAGATION OF ALFVÉN WAVES IN 2D PLANE-PARALLEL GEOMETRY

Let us consider some general relationships describing the geometry of a 2D plane-parallel magnetic field and the propagation of Alfvén waves in it. Let x, y, and z are Cartesian coordinates. We assume that the field $\mathbf{B}_0(\mathbf{r})$ does not depend on the coordinate y ($\mathbf{B}_0 = \mathbf{B}_0(x, z)$) and its force lines do not leave parallel planes $y = \text{const}$.

We denote the magnetic scalar potential by Ψ and introduce the corresponding complex potential $W(w) = \Phi(w) + i\Psi(w)$, where $w = x + iz$. The function of a complex variable $W(w)$ determines the conformal mapping of a plane w into a plane W. This mapping allows us to introduce a curvilinear CS in space (x, y, z) with the help of relationships

$$x^1 = \Phi(x, z), \quad x^2 = y, \quad x^3 = \Psi(x, z). \tag{10}$$

The coordinate x^1 labels magnetic shells (e.g., the magnetic flux inside a shell), while the coordinate x^3 is a longitudinal coordinate along a field line. The Lame coefficients h_1 and h_3 are defined by the expressions

$$h_1 = |\nabla\Phi(x, z)|^{-1}, \quad h_3 = |\nabla\Psi(x, z)|^{-1},$$

and, according to (2), coincide with one another. In the given CS, related to the conformal mapping $w \longrightarrow W$, they are expressed through the derivative of the complex function $W(w)$:

$$h_1 = h_3 = h = |W'(w)|^{-1}. \tag{11}$$

We recall that the metric coefficient h is directly related to the absolute value of the magnetic field, $h = B_0^{-1}$.

Let us consider a situation in which Alfvén waves propagate from infinity along the field lines with a small curvature and then fall into a region where the field line geometry changes sharply (the field lines undergo a break and rapidly converge).

In 2D plane-parallel geometry ($h_2 = 1$), Eq. (7), which describes toroidal Alfvén modes, takes the form

$$(\partial_{\xi\xi} + \mu_0\rho\omega^2)E_1 = 0.$$

The equation for toroidal modes contains the effective Alfvén velocity, which is determined by the plasma density only, because the effects of the longitudinal

nonuniformity of the magnetic field and the magnetic field curvature completely cancel one another. In the absence of a density gradient, these modes do not "feel" the magnetic field curvature and are not reflected.

In contrast, Eq. (8) for poloidal modes reduces to

$$(\partial_3^2 + \mu_0\rho\omega^2 h^4)E_2 = 0. \quad (12)$$

Here, the variable η, in fact, coincides with the coordinate x^3, because $d\eta = h_2^2 dx^3$ and $h_2 = 1$. In a curvilinear magnetic field, the effective Alfvén velocity in Eq. (8) is highly nonuniform along the longitudinal coordinate x^3 even in the case of a constant plasma density, because the Lame coefficient depends on the fourth power of this coordinate. The quantity $h(x^3)$ quantitatively characterizes the "distance" between close field lines, i.e., the degree to which the field lines converge.

4. EXAMPLE: SUPERPOSITION OF A UNIFORM MAGNETIC FIELD AND THE FIELD OF A LINEAR CURRENT

As an example illustrating the influence of the field line curvature on the propagation of Alfvén waves, we consider a magnetic field that is a superposition of a uniform magnetic field $\mathbf{B}_0 = B_0\hat{\mathbf{z}}$ ($B_0 > 0$) and the field produced by a linear current with the density $\mathbf{j}_0 = -I_0\delta(x)\delta(z)\hat{\mathbf{y}}$. For definiteness, we assume that the current $\mathbf{j}_0$ is antiparallel to the y axis ($I_0 > 0$). The plasma density ρ is assumed to be uniform over the entire space.

The complex magnetic potential W of such a field superposition is equal to

$$W = -\frac{\mu_0 I_0}{2\pi}\ln w - B_0 w.$$

We normalize W to the quantity $\mu_0 I_0(2\pi)^{-1}$, the magnetic field to B_0, and the spatial coordinates to the characteristic scale length $r_0 = \mu_0 I_0(2\pi B_0)^{-1}$. Physically, the scale length r_0 corresponds to the distance at which the field of the linear current becomes comparable to the uniform field. Then, retaining the previous notation for normalized quantities, we obtain

$$W = -\ln w - w, \quad \Phi = -\ln r - x, \quad \Psi = -\varphi - z,$$

where $r = (x^2 + z^2)^{1/2}$ and $\varphi = \arctan(z/x)$. According to Eq. (11), the Lame coefficients can be found by differentiating the complex potential:

$$h_1 = h_3 = h = \left|1 + \frac{1}{w}\right|^{-1} = \left[\frac{x^2 + z^2}{(x+1)^2 + z^2}\right]^{1/2} = \left(1 + \frac{2\cos\varphi}{r} + \frac{1}{r^2}\right)^{-1/2}.$$

In normalized variables, wave equation (12) takes the form

$$(\partial_3^2 + \Omega^2 h^4)E_2 = 0. \quad (13)$$

The normalized frequency $\Omega = \omega r_0/V_A^{(\infty)}$ is determined by the nonuniformity scale length r_0 and the Alfvén velocity at infinity $V_A^{(\infty)} = B_0(\mu_0\rho)^{-1/2}$.

In the equations for magnetic field lines, $\Phi(x, z) = x_0^1$ and $y = x_0^2$ (where x_0^1 and x_0^2 are given constants), the coordinate z can be explicitly expressed through x:

$$z = \pm\sqrt{\exp[-2(x + x_0^1)] - x^2}.$$

The family of surfaces $\Psi(x, z) = x_0^3$, which are orthogonal to the magnetic field lines, also allows one to explicitly express x through z:

$$x = -z\cot(x_0^3 + z).$$

The coordinate grid in the upper half-plane y = const is shown in Fig. 1. The intersection points of the field lines $\Phi(x, z) = x_0^1$ = const with the x axis can be found from the equation $\Phi(x, 0) = x_0^1$; i.e.,

$$x + \ln|x| = -x_0^1. \quad (14)$$

This equation has one real root at $x_0^1 < 1$ and three real roots at $x_0^1 > 1$, two of which merge at $x_0^1 = 1$ at the point $x_0^1 = -1$. The field line $\Phi(x, z) = 1$, which corresponds to the merging of two roots of Eq. (14), is the separatrix that separates finite and infinite magnetic field lines. It can be seen in Fig. 1 that, at $|x|, |z| \le r_0$, infinite field lines undergo a break and rapidly converge to the right of the linear current ($x \ge 0$) and diverge to the left of the current ($x/r_0 \le -1$). Below, we will consider how these regions affect the propagation of Alfvén waves.

5. NUMERICAL CALCULATION OF THE REFLECTION COEFFICIENT

The specific features of wave propagation can be quantitatively characterized by the coefficient of reflection from a barrier arising due to the convergence and divergence of field lines. Let an Alfvén wave with a unit amplitude arrive from infinity (e.g., from the side of large positive values of the coordinate x^3) at the region with a curvilinear magnetic field. The wave is partially reflected from this region and partially penetrates through it. In other words, the asymptotes of the corresponding solution to Eq. (13) have the form

$$\begin{aligned}&\exp(-ik_\infty x^3) + R\exp(ik_\infty x^3) \quad (x^3 \longrightarrow +\infty),\\ &D\exp(-ik_\infty x^3) \quad (x^3 \longrightarrow -\infty).\end{aligned} \quad (15)$$

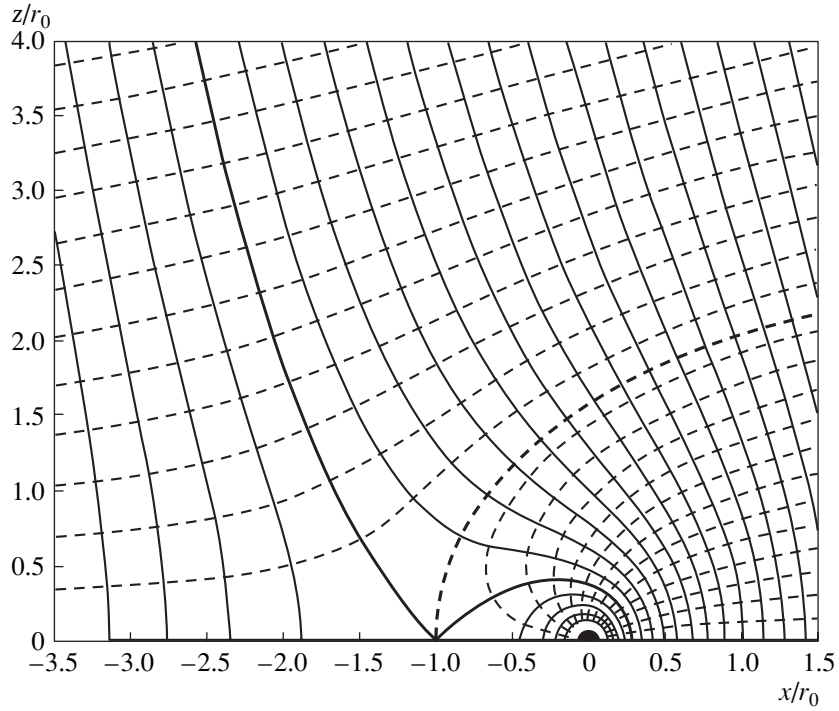

Fig. 1. Coordinate lines of the 2D model: the magnetic field lines (solid lines) and the surfaces orthogonal to them (dashed lines) in a plane orthogonal to the linear current passing through the point (0, 0). The heavy line shows the separatrix that separates the finite and infinite magnetic field lines.

Here, $k_\infty = \omega/V_A^{(\infty)}$ is the wavenumber of the Alfvén wave far from the region with a nonuniform magnetic field. The quantities R and D are the reflection and transmission coefficients, respectively, so that $|R|^2 + |D|^2 = 1$.

We note that asymptotes (15) take place only when the velocity $V_A^{(2)}$ sufficiently rapidly tends to a constant value as $x^3 \longrightarrow \pm\infty$. In the case at hand, we have $h(x^3) - 1 = O(|x^3|^{-2})$, which is quite sufficient for the solution to arrive at the above asymptotes.

The dependence $h(x^3)$ on a given field line can be found by numerically inverting formulas (10), which define the curvilinear CS. Equations (10) along a field line have been solved by successive approximations by the Newton method.

Figure 2 shows typical field lines passing through the regions where the field lines converge ($x \geq 0$) and diverge ($x \leq -r_0$). The profiles of the normalized Alfvén wavenumber squared $k_A^2(x^3)/k_\infty^2 = h^4$ along the same field lines as in Fig. 2 are shown in Fig. 3. It can be seen from these figures that the modified Alfvén velocity changes sharply in the regions where the magnetic field lines rapidly diverge ($h \gg 1$ at $x^3 \longrightarrow 0$ for $x/r_0 < -1$ in Fig. 3a) or converge ($h \ll 1$ at $x^3 \longrightarrow 0$ for $x > 0$ in Fig. 3b).

The calculated dependences of the absolute value of the reflection coefficient $|R|$ on the normalized frequency $\Omega = \omega r_0/V_A^{(\infty)}$ for the same field lines (Fig. 4) show that, in both cases, the reflection coefficient of the Alfvén wave is fairly large. The reflection of an Alfvén

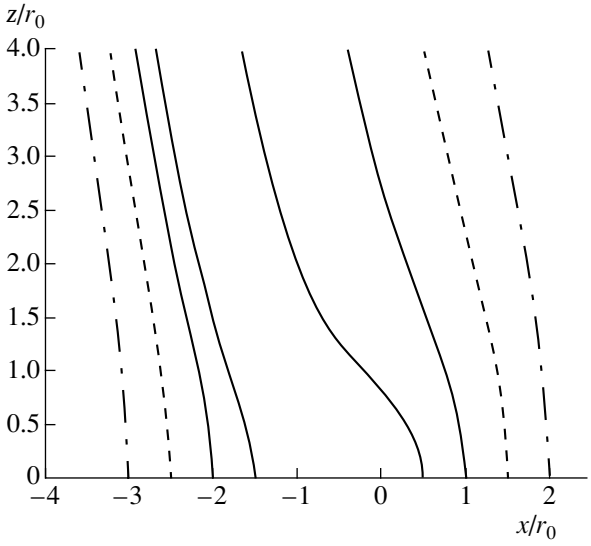

Fig. 2. Typical field lines in the upper half-plane of the 2D model.

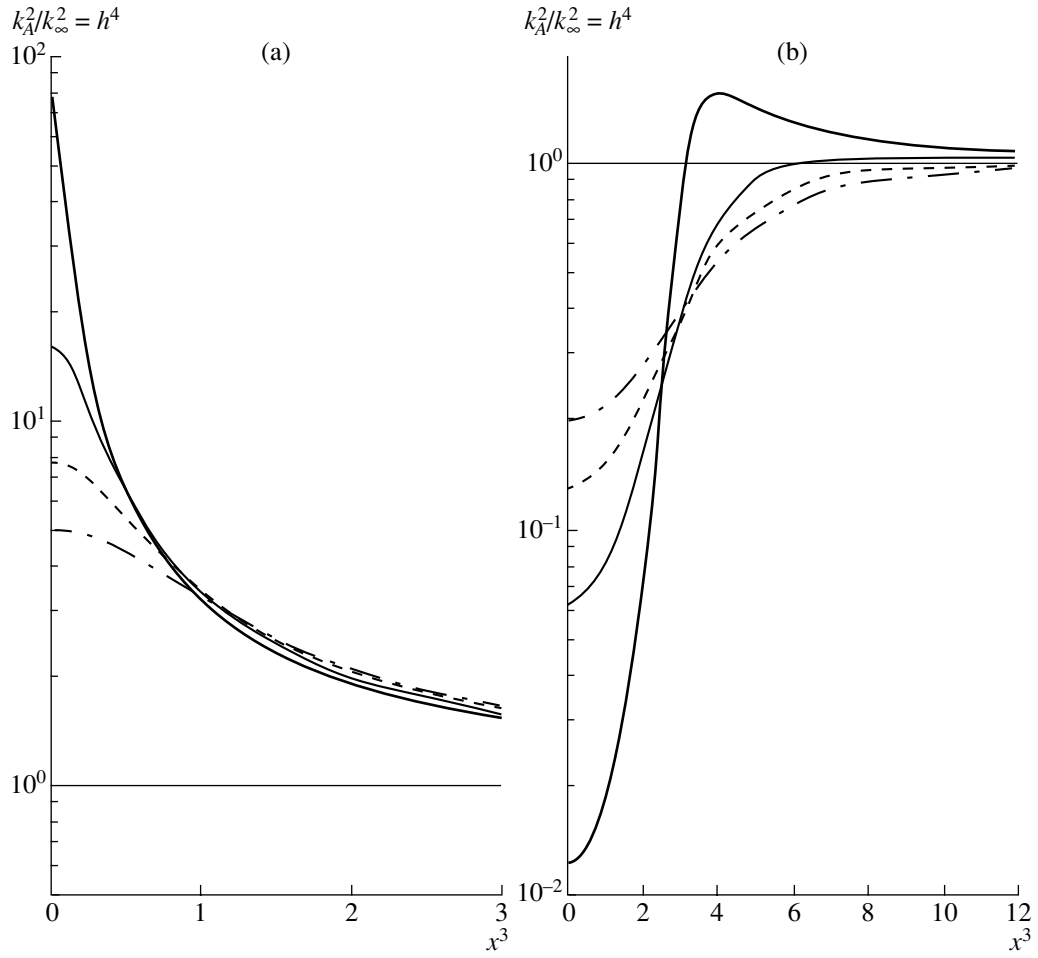

Fig. 3. Profiles of the normalized Alfvén wavenumber squared $k_A^2 = h^4(x^3)$ along the corresponding field lines shown in Fig. 2 at (a) $x/r_0 < -1$ and (b) $x > 0$.

wave whose wavelength is comparable to the nonuniformity scale length r_0 can be as high as 80–90%.

We note that the dependence $R(\Omega)$ is nonmonotonic. For high-frequency waves ($\Omega \gg 1$), the reflection coefficient is small, which is quite natural for waves that can be described in the Wentzel–Kramers–Brillouin (WKB) approximation. In the range of very low frequencies, which, in fact, corresponds to the case of dc perturbations, the reflection coefficient R also tends to zero.

The effect of the geometrical factor arising due to the convergence or divergence of the field lines can formally be separated from the effect related to the dependence of V_A on the magnetic field strength. The ignoring of the geometrical factor corresponds to the transition from $V_A^{(2)}$ to V_A, i.e., the replacement of h^4 with h^2 in Eq. (13). Figure 5 compares the values of $|R|$ on the field line crossing the x axis at the point $x_0 = 1$ for the cases corresponding to the solutions to Eq. (13) and the same equation in which h^4 is replaced with h^2. It can be seen from this figure that the large reflection coefficient is mainly achieved due to the change in the magnetic field geometry, rather than to the nonuniformity of the Alfvén velocity.

6. QUALITATIVE CRITERIA OF REFLECTION

Let us formulate qualitative criteria of the reflection and transmission of Alfvén waves that could be used for an arbitrary geometry of the magnetic field. For a given field line, there is a frequency range in which the coefficient of reflection from the region where the field lines converge (or diverge) is maximum. The bounds of this range are determined by scale lengths characteristic of the given field line. As will be shown below, there are two such scale lengths: one of them determines the upper bound of the frequency range corresponding to efficient reflection, while the other determines the lower bound.

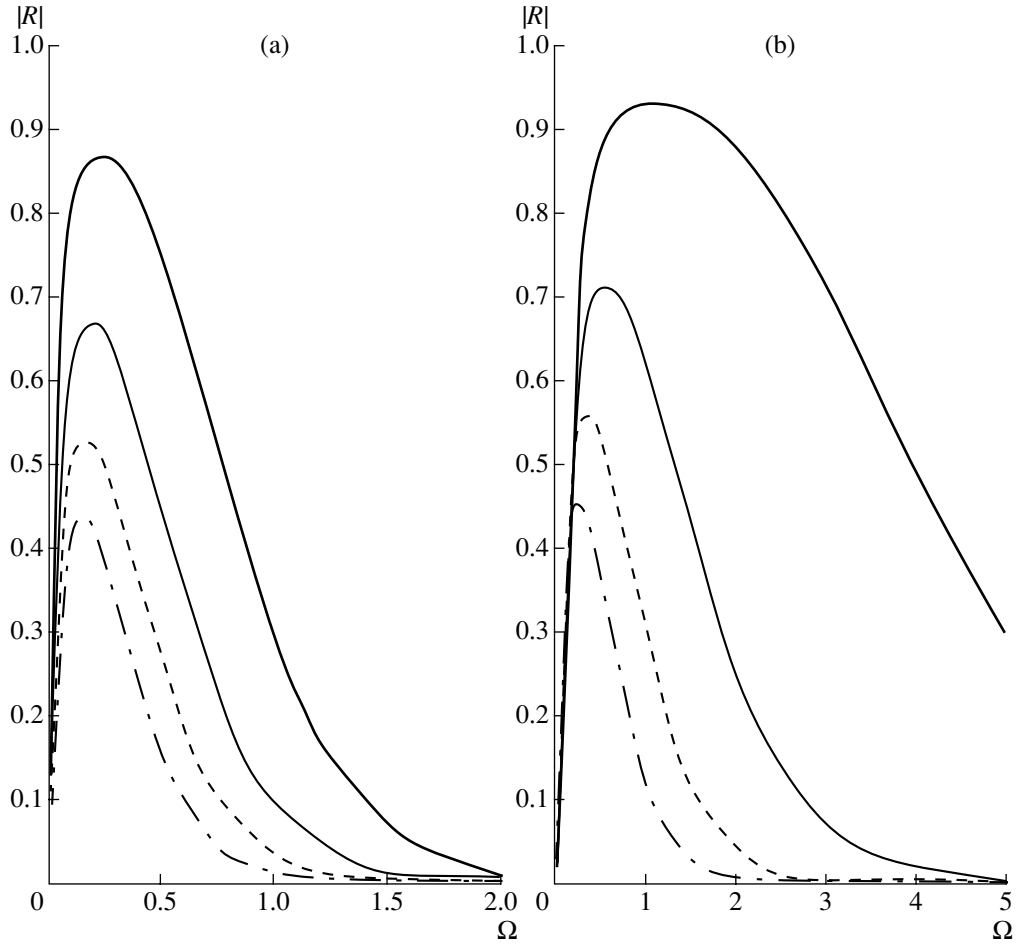

Fig. 4. Reflection coefficients of the poloidal Alfvén modes propagating along the field lines shown in Fig. 2. The curves $|R(\Omega)|$ and the corresponding field lines in Fig. 2 are shown by the same type of line: heavy, light, dashed, and dashed-and-dotted.

In the high-frequency limit ($\Omega \longrightarrow \infty$) the solution to Eq. (13) can be found in the WKB approximation, whose applicability range is local in character. In the vicinity of any point on a field line, there is, on the one hand, the local scale length related to the wavelength of the Alfvén wave, $\bar{\lambda} = \lambda/2\pi = \Omega^{-1}h^{-2}$, and, on the other hand, the scale length related to variations in the coefficient in Eq. (13), $L = h^4|\partial_3 h^4|^{-1} = \frac{1}{4}h|\partial_3 h|^{-1} = \frac{1}{4}|\partial_3 \ln h|^{-1}$. Note that we are speaking here about scale lengths in terms of the normalized variables in which Eq. (13) is written.

The WKB approximation is locally applicable if the condition $\bar{\lambda} \ll L$ is satisfied; i.e.,

$$\Omega \gg \frac{4|\partial_3 h|}{h^3}.$$

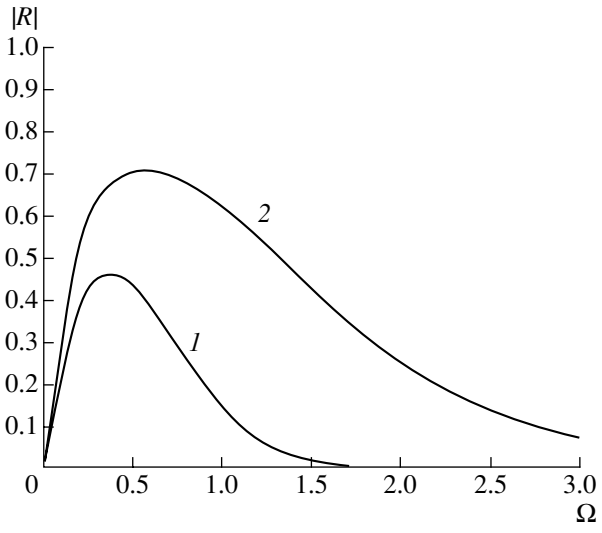

Fig. 5. Comparison of the reflection coefficients of Alfvén waves calculated (*1*) without and (*2*) with allowance for the geometrical factor.

The right-hand side of this inequality reaches its maximum in the region where the field lines converge (or diverge) at the highest rate. Thus, if

$$\Omega \gg \Omega_+ = 4\max\left\{\frac{|\partial_3 h|}{h^3}\right\},$$

then the WKB approximation is valid and the reflection coefficient $|R|$ is small over the entire field line. It can be shown that, in this case, the reflection coefficient decreases exponentially with increasing Ω. The quantity Ω_+ is the upper bound of the frequency range corresponding to efficient reflection.

In the range of low frequencies ($\Omega \longrightarrow 0$), the asymptotes of the solution to Eq. (13) are determined by the integral scale length of the nonuniformity of the function $\Omega^2 h^4$. In particular, the reflection coefficient is described by the approximate formula

$$|R| \simeq \frac{\Omega}{2}\left|\int_{-\infty}^{\infty}[h^4(x^3)-1]dx^3\right|.$$

It follows from this formula that the lower bound of the frequency range corresponding to efficient reflection ($|R| \sim 1$) is determined by the expression

$$\Omega_- = 2\left|\int_{-\infty}^{\infty}[h^4(x^3)-1]dx^3\right|^{-1}.$$

It is necessary to take into account that, as the nonuniformity becomes smoother, so that the function $h(x^3)$ differs only slightly from its limiting value $h(\pm\infty) = 1$, the upper bound Ω_+ goes down, while the lower bound Ω_- goes up, until the frequency range corresponding to efficient reflection disappears. In the above example, this occurs as the distance between the field line and the linear current that perturbs the uniform magnetic field increases.

7. DISCUSSION: PROBABLE CONSEQUENCES

Situations similar to that considered above frequently occur in space and laboratory plasmas. In real situations, sharp variations in the magnetic field geometry are usually accompanied by variations in the plasma density and magnetic field strength. All this results in a sharp change of the modified Alfvén velocity, thus leading to the efficient reflection of Alfvén waves. In such Alfvén quasi-resonators, the energy of trapped oscillations can increase to fairly high values. This fact stems from the specific transverse structure of Alfvén oscillations. The effect manifests itself for poloidal modes, in which the wave magnetic field is perpendicular to the magnetic shell. For toroidal modes, in which the wave magnetic field is directed along the shell, the wave propagation is only determined by the plasma density.

Strictly speaking, the latter result (i.e., that the field line curvature affects only poloidal modes) applies only to the above 2D plane-parallel magnetic field geometry, in which the coordinate lines x^1, x^3 = const are straight. For other magnetic field configurations, i.e., in the general 2D (e.g., dipole) and 3D cases, the difference between modes 1 and 2 will not be so striking from the point of view of the influence of the field line curvature, although it will, nevertheless, manifest itself to a certain extent. In particular, in [17], the propagation of Alfvén waves in a curvilinear magnetic field was considered by using a model equation (which can be reduced to the well-known Klein–Gordon equation) for a thin oscillating flux tube. For dipole geometry, it was shown that Alfvén waves can be partially reflected before they reach the conducting end of the flux tube (the ionosphere).

In the solar atmosphere, coronal loops form resonators for Alfvén waves with frequencies that are multiples of $V_A/2L$, where L is the length of a loop [2]. These resonances, which decisively affect the penetration of Alfvén waves to into the corona, exist only if the waves undergo reflection on the loop ends. In this case, the equation describing the propagation of waves in a straight magnetic field [1] without allowance for geometrical factors applies only to toroidal modes. For poloidal modes, such a model can yield an underestimated reflection coefficient.

In magnetic mirror devices, uniform axisymmetric compression of the magnetic field does not enhance the reflecting properties of magnetic mirrors. On the other hand, nonuniform "squeezing" of the magnetic field in toroidal devices can result in the trapping of Alfvén oscillations.

In the Earth's magnetosphere too, the propagation of Alfvén waves can be significantly affected by local variations in the geometry of the geomagnetic field. Thus, the field lines emerging from the night-time high-latitude ionosphere undergo a sharp break and rapidly converge in the current sheet of the geomagnetic tail of the magnetosphere. After the field lines of the polar cap have been reconnected with the interplanetary magnetic field, their geometry changes sharply as the field lines pass through the magnetopause. Quasi-dipole field lines can be strongly perturbed in the equatorial magnetosphere by an intense ring current. In all these regions, harmonic oscillations can be excited whose period is determined by the dimensions of Alfvén quasi-resonators.

As an Alfvén wave propagates in a medium that is nonuniform in a transverse direction, the wave vector component parallel to the direction of nonuniformity, $\hat{k}_1 = k_1/h_1$, increases due to the effect of scale-length degradation. As a result, Alfvén waves in a curvilinear magnetic field acquire a specific transverse dispersion

and group velocity [18]. It was shown in [18, 19] that, in the course of such transverse propagation, the wave polarization changes from poloidal to toroidal over a distance of $S \sim a\hat{k}_2/k_\parallel$, where $\hat{k}_2 = k_2/h_2$ and a is the characteristic scale length (along the coordinate x^1) over which the Alfvén velocity changes substantially [19]. Hence, the change in the wave polarization can be ignored when $S \gg R$, where R is the size of the region where the magnetic field geometry varies rapidly, i.e., when the condition

$$S/R \sim a\hat{k}_2/(k_\parallel R) \gg 1 \quad (16)$$

is satisfied. In all of the situations considered above, this inequality is satisfied by a large margin.

8. CONCLUSIONS

Although Alfvén waves have no reflection points, they can be efficiently reflected from regions where the magnetic field geometry changes sharply (the field lines rapidly converge or diverge). This effect can result in the formation of open-field-line Alfvén resonators in the complex plasma configurations encountered in near-Earth, solar, and laboratory plasmas.

ACKNOWLEDGMENTS

We thank the anonymous referee for his useful remarks. This work was supported by the Russian Foundation for Basic Research, project no. 03-05-64670.

REFERENCES

1. B. Leroy, Astron. Astrophys. **91**, 136 (1980).
2. E. R. Priest, *Solar Magnetohydrodynamics* (Reidel, Dordrecht, 1982; Mir, Moscow, 1985).
3. A. N. Wright and S. J. Schwartz, J. Geophys. Res. **94**, 3749 (1989).
4. S. V. Polyakov and V. O. Rappoport, Geomagn. Aeron. **21**, 816 (1981).
5. R. L. Lysak, J. Geophys. Res. **93**, 5942 (1988).
6. P. P. Belyaev, S. V. Polyakov, V. O. Rappoport, and V. Yu. Trakhtenhertz, J. Atmos. Terr. Phys. **52**, 781 (1990).
7. O. A. Pokhotelov, D. Pokhotelov, A. Streltsov, *et al.*, J. Geophys. Res. **105**, 7737 (2000).
8. E. N. Fedorov, N. G. Mazur, V. A. Pilipenko, and S. Lepidi, Geomagn. Aeron. **38** (2), 60 (1998).
9. A. B. Mikhaĭlovskiĭ and O. A. Pokhotelov, Fiz. Plazmy **1**, 786 (1975) [Sov. J. Plasma Phys. **1**, 430 (1975)].
10. O. A. Pokhotelov, Yu. M. Nezlina, and V. A. Pilipenko, Dokl. Akad. Nauk SSSR **289**, 332 (1986).
11. A. V. Timofeev, in *Reviews of Plasma Physics*, Ed. by M. A. Leontovich (Gosatomizdat, Moscow, 1979; Consultants Bureau, New York, 1982), Vol. 9, p. 205.
12. E. N. Fedorov, N. G. Mazur, and V. A. Pilipenko, Fiz. Plazmy **21**, 333 (1995) [Plasma Phys. Rep. **21**, 311 (1995)].
13. A. L. Krylov, A. E. Lifshits, and E. N. Fedorov, Dokl. Akad. Nauk SSSR **247**, 1095 (1979).
14. A. L. Krylov, A. E. Lifshits, and E. N. Fedorov, Geomagn. Aeron. **20**, 689 (1980).
15. A. S. Leonovich and V. A. Mazur, Fiz. Plazmy **13**, 800 (1987) [Sov. J. Plasma Phys. **13**, 461 (1987)].
16. A. L. Krylov, A. E. Lifshits, and E. N. Fedorov, Izv. Akad. Nauk SSSR, Fiz. Zemli, No. 6, 49 (1981).
17. V. S. Semenov, N. V. Erkaev, and D. Langmayr, in *Proceedings of the 4th International Conference "Problems of Geocosmos," St. Petersburg, 2002*, p. 95.
18. A. S. Leonovich and V. A. Mazur, Planet. Space Sci. **41**, 697 (1993).
19. D. Yu. Klimushkin, J. Geophys. Res. **105**, 23303 (2000).

Translated by A.S. Sakharov

Plasma Physics Reports, Vol. 30, No. 5, 2004, pp. 422–431. Translated from Fizika Plazmy, Vol. 30, No. 5, 2004, pp. 459–468.

PLASMA DIAGNOSTICS

First Results Obtained with a Sweeping Pulsed Radar Reflectometer in the Globus-M Tokamak

E. A. Azizov*, A. V. Babarykin*, A. V. Voronin, V. K. Gusev**, A. Yu. Malyshev*, V. K. Markov*, A. A. Petrov*, V. G. Petrov*, Yu. V. Petrov**, V. V. Rozhdestvenskiĭ**, and N. V. Sakharov****

** Troitsk Institute for Innovation and Fusion Research, Troitsk, Moscow oblast, 142190 Russia*

*** Ioffe Physicotechnical Institute, Russian Academy of Sciences, Politekhnicheskaya ul. 26, St. Petersburg, 142190 Russia*

Received July 29, 2003; in final form, October 1, 2003

Abstract—A sweeping pulsed radar reflectometer designed for measuring the spatial electron density distribution in the Globus-M spherical tokamak with a minor plasma radius of $a = 24$ cm, a major radius of $R = 36$ cm, a toroidal field of $B_T = 0.5$ T, a plasma current of $I_p = 200$ kA, and an average density of $n = (3–10) \times 10^{13}$ cm^{-3} is described. The reflectometer operation is based on the reflection of microwaves with a carrier frequency f from a plasma layer with the critical density $n = (0.0111f)^2$, where n is the electron density in units of 10^{14} cm^{-3} and f is the microwave frequency in GHz. By simultaneously probing the plasma at different frequencies, it is possible to recover the electron density profile. Microwave pulses with different frequencies are obtained by frequency sweeping. To increase the range of measured densities, channels with fixed frequencies are also used; as a result, the instrument has eleven frequency channels: a 19.5-GHz channel, eight channels in the 26- to 40-GHz frequency range, a 51.5-GHz channel, and a 60-GHz channel, which corresponds to eleven points in the density profile: 0.47×10^{13} cm^{-3}, eight points in the $(0.8–1.95) \times 10^{13}$-cm^{-3} range, 3.27×10^{13} cm^{-3}, and 4.5×10^{13} cm^{-3}. The reflectometer allows detailed measurements of the density profile with a time resolution of several tens of microseconds, which can be useful, in particular, in studying the processes related to the formation of an internal transport barrier in plasma. The first results obtained using this reflectometer in the Globus-M tokamak under various operating conditions are discussed. © *2004 MAIK "Nauka/Interperiodica".*

1. INTRODUCTION

Microwave reflectometers, along with multichannel interferometers and Thomson scattering diagnostics, are widely used to measure the electron density profiles in magnetic confinement devices [1]. Reflectometer operation is based on the reflection of microwaves with a carrier frequency f from a plasma layer with the density n that is critical for this frequency. The plasma is usually probed by an ordinary wave (the wave electric field is directed along the toroidal magnetic field of a tokamak). It is well known [2] that, in this case, the following simple relation holds:

$$n = (0.0111f)^2, \tag{1}$$

where n is the electron density in units of 10^{14} cm^{-3} and f is the microwave frequency in GHz. By probing the plasma at several frequencies, one can obtain information about the positions of several reflection layers. The electron density in each of these layers is unambiguously related to the given probing frequency. The distance to these layers can be determined by measuring the time during which the microwaves propagate to the reflection point and back. The propagation time τ can be measured directly or calculated using the expression [3]

$$\tau = \frac{\partial \Phi}{\partial \omega}, \tag{2}$$

where Φ is the phase shift of the wave with a circular frequency ω in the plasma. When probing the plasma by an ordinary wave, the refractive index $\eta(\omega, x)$ does not depend on the external magnetic field and the group delay time τ_{gr} is equal to

$$\begin{aligned}\tau_{gr}(x, \omega) &= \frac{\partial \Phi(\omega, x)}{\partial \omega} \\ &= \frac{2}{c}\int_0^{x_c} \eta(\omega, x)dx + \frac{2\omega}{c}\int_0^{x_c} \frac{\partial \eta(\omega, x)dx}{\partial \omega},\end{aligned} \tag{3}$$

where x_c is the coordinate of the reflection point.

From the measured (or calculated using formula (2)) delay times τ_k for each of the frequencies, the density profile can be recovered by assuming that it is mono-

1063-780X/04/3005-0422$26.00 © 2004 MAIK "Nauka/Interperiodica"

tonic and using the recurrence formula for a linear-spline approximation [4]

$$x_k = x_{k-1} - \left(\frac{c\tau_k}{4} + a - \sum_{i=1}^{k-1} (x_{i-1} - x_i)/(\sqrt{1 - n_{i-1}/n_k} + \sqrt{1 - n_i/n_k}) \right) \times \sqrt{1 - n_{k-1}/n_k}, \quad (4)$$

where x_k is the coordinate of the reflection point for the kth frequency, τ_k is the measured delay time for this frequency, n_k is the corresponding critical density, and a is the plasma radius. The delay time is measured with respect to the delay time in the absence of a plasma. The coordinate x_0 corresponds to the plasma boundary ($n_0 = 0$), which, at the first step, can be assumed to coincide with the chamber wall. At the next step, this coordinate can be taken from magnetic measurements or determined from the data obtained using the two lowest frequency radar channels. All coordinates in formula (4) are measured from the center of the discharge chamber. The problem of choosing the plasma boundary (i.e., the initialization problem) is of great importance in reflectometer measurements. Note that the results of recovering the density profile depend not only on the choice of the plasma boundary, but also on the type of density profile.

The version with direct measurements of τ is implemented in a multichannel pulsed radar reflectometer, in which the electron density profile is recovered from the delay times of microwave pulses with different frequencies, which are reflected from the plasma layers with the corresponding critical densities. In this case, each frequency channel consists of a microwave source, a receiver, and a measuring circuit [4]. The number of frequency channels in this version determines the number of experimental points in the density profile.

The second version is implemented in a frequency-sweeping phase reflectometer, in which the delay time is determined from phase measurements at different frequencies after their hardware or software differentiation according to formula (2). This version allows one, in principle, to substantially reduce the number of measuring channels and, accordingly, the cost of the instrument. In this case, however, better access to the object under study should be provided in order to exclude the possible ambiguity of measurements caused by multiple antenna–plasma reflections [5–7].

A radar reflectometer in which the propagation time of a microwave pulse to the reflection layer and back is measured directly has obvious advantages over phase reflectometers. First, during a single measurement (each of which lasts for several nanoseconds), the plasma column can be considered immobile. Second, time-of-flight measurements allow one to avoid the ambiguity of measurements (characteristic of phase reflectometry).

When choosing the operating frequency range of a reflectometer intended for measuring the density profile in small and moderate tokamaks (such as T-11, T-10, and Globus-M), in which the electron density in the central region of an ohmically heated plasma is no higher than 10^{14} cm^{-3}, the upper frequency of the reflectometer, according to Eq. (1), can be limited to 60–80 GHz, because the error of reflectometer measurements increases substantially as the cutoff point approaches the center of the plasma column, where the density gradient tends to zero. The lower frequency is usually chosen so that it ensures about a tenfold dynamic range of the density measurements. Note that the choice of the lowest frequency substantially affects the accuracy of the density profile measurements. The point is that uncertainty in the unknown (not measured) part of the profile most strongly influences the low-density measurements; the higher the frequency, the weaker this influence. From this standpoint, the lower probing frequency should be as low as possible; however, as the frequency is decreased, problems related to the coupling between the antenna system and the plasma arise and the accuracy of determining the coordinate of the reflecting layer decreases.

2. DESIGN OF THE SWEEPING PULSED RADAR REFLECTOMETER

The reflectometer is based on the pulsed probing of plasma; i.e., the instrument measures the propagation time of specially formed short-duration (~5 ns) microwave pulses with a rise time of no longer than 2 ns. This method allows one to avoid multiple parasitic reflections in the transmission line and in the tokamak vessel by using time-window filtering [4], as well as to improve the reliability of measurements, since the reflectometer directly measures the pulse delay time in plasma [8] rather than the phase shift, as in conventional phase reflectometers. In this case, however, one faces the problem of precisely measuring rather short (~1 ns) delay times of a microwave pulse reflected from a plasma. This problem was successfully solved in designing our reflectometer.

Microwave pulses with different carrier frequencies are obtained by fast (~15 μs) frequency sweeping. This allows us to substantially reduce the number of the measuring channels, thus lowering the cost of the instrument, and, at the same time, to retain the capability of recovering the density profile in the measurement range with a sufficient accuracy. However, the dynamic frequency range of state-of-the-art commercial frequency-sweeping microwave voltage-controlled oscillators (VCOs) is no higher than 1.5, which corresponds to a dynamic density range of no higher than 2.25. Microwave backward-wave tube oscillators (BWTs) ensure the required frequency sweeping range, but can-

Operating frequencies of the sweeping pulsed radar reflectometer and the corresponding critical plasma densities

Frequency, GHz/channel no.	19.5/8	25.99/7	27.17/6	29.26/5	31.64/4	33.75/3	35.95/2	37.97/1	39.83/0	51.5/11	60.5/10
Critical density, 10^{14} cm^{-3}	0.047	0.083	0.091	0.1055	0.123	0.14	0.159	0.1776	0.195	0.327	0.451

not provide the required sweeping speed. Therefore, to achieve the dynamic density range of ~10 required for actual plasma experiments, it is necessary to either use several VCOs with different frequency ranges or to supplement the frequency-sweeping channel with additional channels operating at fixed frequencies. In our reflectometer, we implemented the latter version, which is much cheaper.

Thus, the final version of the reflectometer contains one 26- to 40-GHz frequency-sweeping channel (eight frequencies can be chosen in this range) and three channels with fixed frequencies: 19.5, 51.5, and 60.5 GHz. The table presents the frequencies of the channels and the corresponding critical plasma densities in the given version of the reflectometer, in which the frequencies in the sweeping channel are distributed almost uniformly over the 26- to 40-GHz frequency range. This scheme allows one to obtain information about eight points in the plasma density profile during one sweep (~10 μs). The number of the measured points at the density profile, as well as the probing frequencies, can be varied depending on the task of an experiment, which is a significant advantage of a sweeping pulsed reflectometer over a multichannel reflectometer using fixed probing frequencies.

The lowest frequency channel (19.5 GHz) can be used to determine the position of the plasma boundary. Along with the measurements of the plasma density profile, the reflectometer can also be used to study low-frequency (below 30 kHz) plasma density fluctuations.

Figure 1 shows the topology of cutoffs and electron cyclotron resonances in the Globus-M tokamak. The frequencies are calculated for a parabolic density profile. In calculations, the central plasma density was assumed to be 0.75×10^{14} cm^{-3}, the plasma current was 200 kA, and the toroidal magnetic field at the axis of the plasma column was 0.5 T. Since the current varies during a discharge, the shear at the plasma boundary also varies and, consequently, purely ordinary-wave plasma probing is hardly possible. It can be seen from the figure that, in view of the presence of an extraordinary component in the probing wave, the possible error in determining the position of the reflecting layer does not exceed 2 cm for an upper frequency equal to 60.5 GHz; for other frequencies, the error is smaller. In this paper, we analyze plasma density profiles in the quasi-steady phase of discharges in the Globus-M tokamak, where the shear varies only slightly and the related error is small.

2.1. Functional Diagram of the Reflectometer

As was mentioned above, the microwave part of the reflectometer includes one channel with frequency sweeping and three channels with fixed frequencies (see Fig. 2). The receiving part of the 50- and 60-GHz channels uses a common detector with the separation of the corresponding pulses in time. Impact-ionization avalanche transit-time (IMPATT) diode microwave oscillators operating at fixed frequencies and a frequency-sweeping VCO produce a train of microwave pulses with a repetition rate of 750 GHz, stabilized by a quartz resonator. Master pulses are fed to the oscillators from the control unit. A fraction of the microwave power (about –20 dB) is directed by waveguide directional couplers (DCs) to monitoring detectors. The detected pulse is amplified by low-noise pulse amplifiers and is fed to a threshold-tracking former (TTF)—a unit allowing exact timing with respect to the leading edge of the pulse [8]. The pulse is then fed through a digital switch to the Start input of a time-to-amplitude converter (TAC). This method for generating the Start signal (unlike that used previously in [9]) provides exact timing with respect to the beginning of microwave generation, thus allowing one to achieve an accuracy of delay-time measurements corresponding to the total jitter of the recording system (~5 ps) [10].

The bulk of the microwave radiation launched into the tokamak plasma is emitted by three horn antennas (antenna *1* for frequencies of 51.5 and 60.5 GHz, antenna *3* for frequencies 26–40 GHz, and antenna *5* for a frequency of 19.5 GHz). A microwave pulse reflected from the plasma or from the inner wall of the tokamak chamber is received by antennas *6*, *4*, and *2* and is fed to measuring detectors and then, through a system of pulse amplifiers, the TTF, and a digital switch, to the Stop input of the TAC.

High-sensitivity Shottky barrier diodes provide a signal-to-noise ratio of about 20 dB in the reflected signal and have a sufficiently high operating speed for receiving pulses with the given parameters (the noise equivalent power is $NEP < 10^{-11}$ W/Hz$^{0.5}$).

The low-noise pulse amplifiers are built of Hewlett Packard, Siemens, and Mini-Circuit IC chips whose intrinsic rise/fall times are no longer than 1.1 ns. The voltage gain is 10–100, the frequency band is 0.01–1 GHz, and the noise factor is below 5 dB.

The electronic part of the instrument includes the control unit, the TTF unit, the TAC card for delay-time measurements, the ADC with the ISA interface, and an IBM-compatible PC.

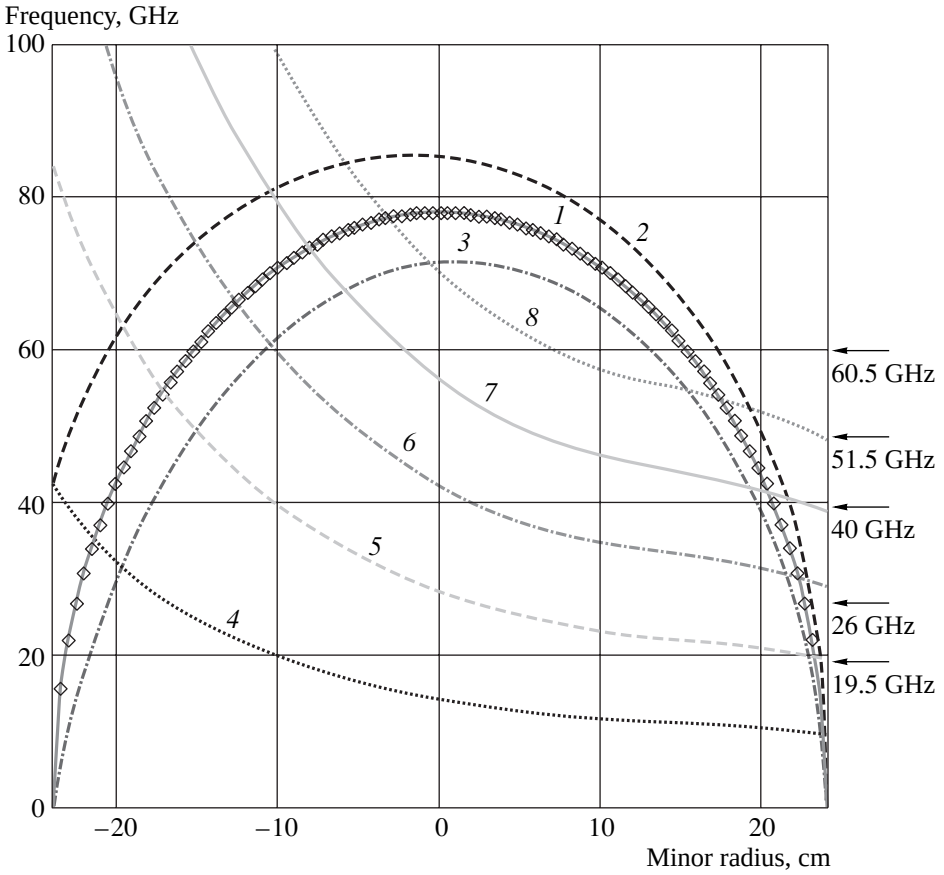

Fig. 1. Topology of cutoffs and electron cyclotron resonances in the Globus-M tokamak: (*1*) cutoff for the ordinary wave, (*2*) upper and (*3*) lower cutoffs for the extraordinary wave, and (*4*)–(*8*) harmonics of the electron cyclotron frequency.

2.2. Parameters of the TAC Card

The parameters of the TAC card are as follows:

the register capacity is 12 bit,

the measurable time interval is 0–10 ns,

the signal level at the Start and Stop inputs corresponds to the transistor–transistor logic (TTL) level,

the Start-up (synchronization) signal level is 10 V,

the frequency-code signal level corresponds to the TTL level, and

the measurement accuracy of time intervals is ~2.5 ps.

All of the input signals are electric-decoupled at voltages of up to 500 V. The card is made to the ISA standard and is installed in a free ISA slot of the PC.

The delay time is measured as follows: The signals from the monitoring and measuring detectors are amplified and fed successively to six TTFs and then to a digital switch controlled by the frequency code (number) of the driving oscillator. The Start and Stop pulses formed at the switch output arrive at the TAC, which is common for the entire system. Two of eight TTFs are used to form pulses of the test channel. The measurement cycle includes twelve delay-time measurements for eleven microwave probing frequencies and one test channel that measures the delay time of an electric pulse in the delay line (cable). The test channel is used to test and adjust the device.

The design of the reflectometer is described in more detail in [11].

2.3. Software Package

The program package developed for the reflectometer serves the following functions:

(i) Data recording to the RAM and hard disk of the data acquisition system PC after receiving the Start-up (synchronization) signal and the transmission of the data through the local network to a remote PC.

(ii) Data processing, the computation of the evolution of the electron density, and the graphical representation of the data and results using a special program operating in the Windows environment.

The data-processing program allows one to load and browse signals from the plasma for all or some of the frequency channels after a tokamak discharge. Raw

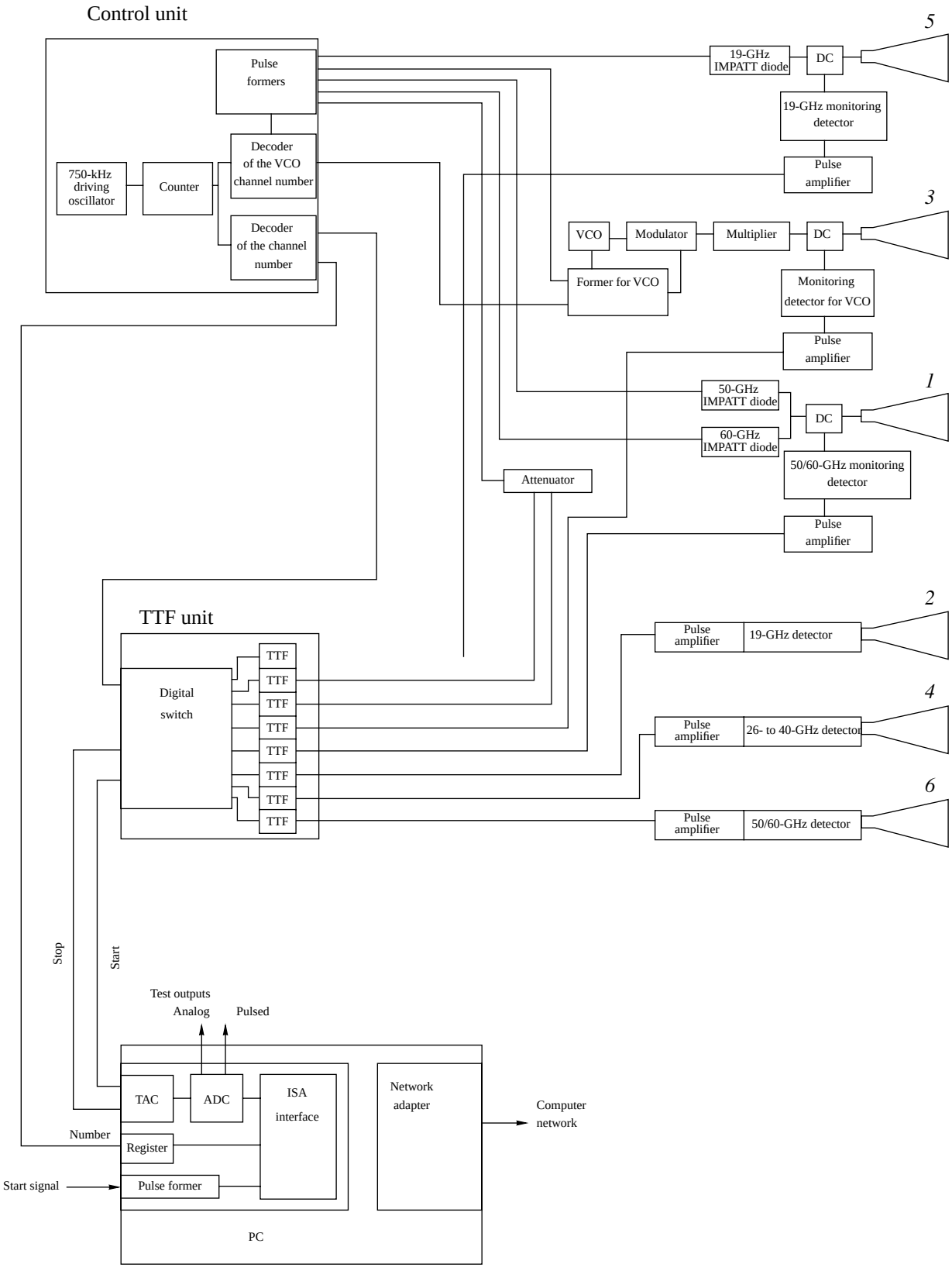

Fig. 2. Functional diagram of the reflectometer: (*1*, *3*, *5*) transmitting antennas of the 50/60-, 26- to 40-, and 19-GHz channels, respectively, and (*2*, *4*, *6*) corresponding receiving antennas.

data (in the ACD codes) or signals after digital filtering can be browsed. The following filters are available: a median filter; an ordinary averaging; low-, high-, and intermediate-frequency filters, and a stop-filter. The program can display signals processed with account taken of the sensitivity of channels and recover a prescribed number of the density profiles in the low-field side of the plasma column during a discharge in any time interval. The plasma density profile is recovered assuming the profile to be monotonic and using recurrence formula (4).

3. EXPERIMENTAL RESULTS

The first measurements with the use of the sweeping pulsed radar reflectometer were carried out in the Globus-M tokamak. Figure 3 shows the general view of the instrument assembled in a nonmagnetic frame in the experimental room of the Globus-M tokamak. Before the reflectometer was installed at the tokamak, it was calibrated on a test bench. In this case, a metal cylinder ~15 cm in diameter was used as a reflecting target. As an illustration, Fig. 4 shows the calibration curve for the channel with a carrier frequency of 26 GHz (the figure shows the segment of the calibration curve that was later used in data processing in tokamak experiments). The time resolution of the reflectometer in test measurements was about 5 ps, and the minimal target displacement detected by the instrument was nearly 1 mm.

After the reflectometer was installed at the tokamak, the antenna systems of all the channels were adjusted so that their axes were directed along the minor radius toward the center of the plasma column. The instrument was mounted on a nonmagnetic frame and was preliminarily adjusted with the help of a screen mimicking the center of the plasma column. The final adjustment was performed after installation at the tokamak.

Figure 5a shows raw reflectometer signals measured in the regime with a rather low density, when nine channels with lower frequencies were operating in the reflection regime (shot no. 05241743). The scatter in the measurements of the delay time in the absence of a plasma was about 25 ps. With the plasma, this scatter increased to 200–300 ps because of the adverse effect of plasma fluctuations and parasitic reflections from the tokamak chamber. In order to provide acceptable accuracy of the measurements of the critical layer position (~1 cm), the signal was filtered. Since, in this case, the 19.5-GHz channel was not calibrated, we used data from the frequency-sweeping channel alone. Figure 5b shows the density profile recovered using these data at the 78th millisecond of the discharge. It can be seen that, in this phase of the discharge, the profile can be fitted well by a parabola.

Figure 6 shows (a) average-density signals from a microwave interferometer, (b) radar signals, (c) the evolution of the density profile, and (d) the comparison

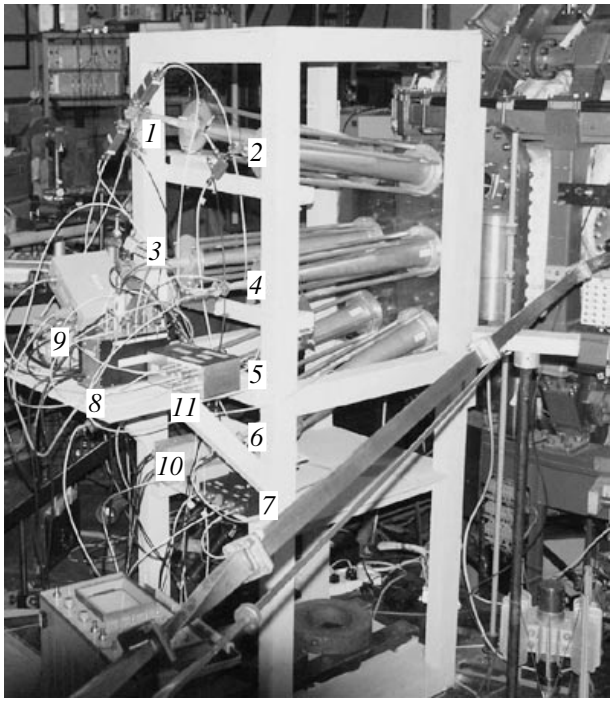

Fig. 3. General view of the reflectometer with antennas in the experimental room of the Globus-M tokamak: (*1*, *3*, *5*) 51.5/60.5-, 26- to 40-, and 19.5-GHz transmitting channels, respectively; (*2*, *4*, *6*) 19.5-, 26- to 40-, and 50/60-GHz receiving channels, respectively; (*7*) supply unit of microwave oscillators; (*8*) control unit; (*9*, *10*) supply units of electronic components; and (*11*) TTF unit.

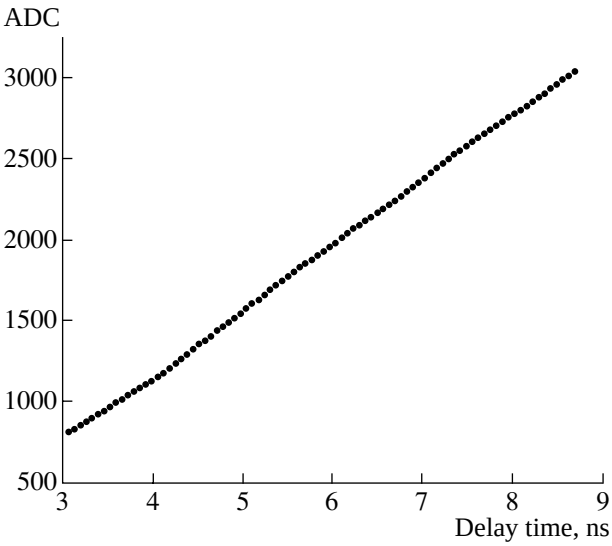

Fig. 4. Calibration curve of the seventh (26-GHz) reflectometer channel (the ADC signal vs. delay time).

of the average densities $\langle nl \rangle$ deduced from the radar and interferometer data for shot no. 02201747/5125.

Since all the three interferometer channels probed the plasma along vertical chords, whereas the reflecto-

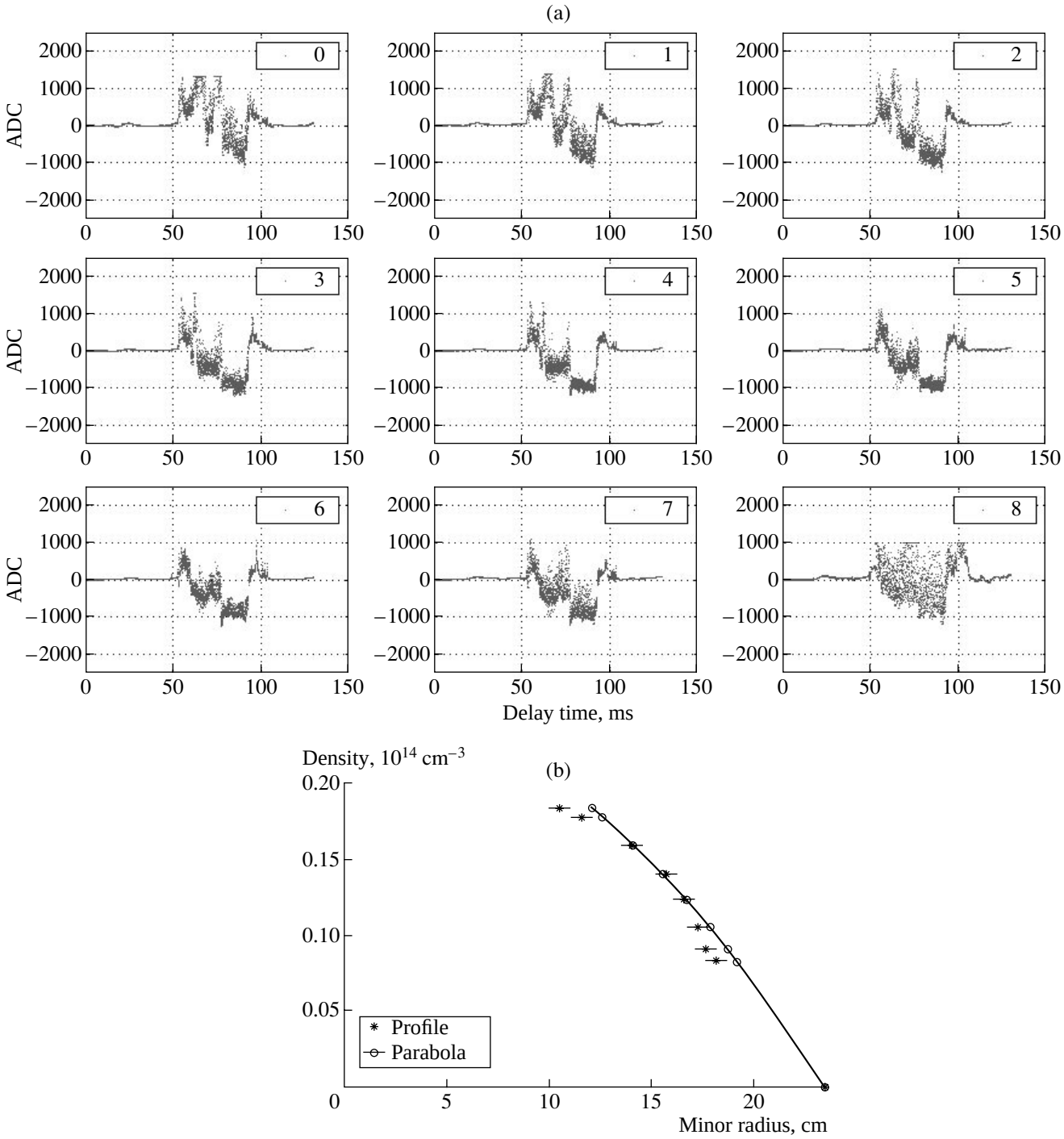

Fig. 5. Shot no. 05241743: (a) raw signals from nine reflectometer signals with lower frequencies of 40–26 and 19.5 GHz and (b) the density profile obtained from processed reflectometer data for the 78th millisecond of the discharge. The accuracy of determining the critical layer position is about ±1.0 cm.

meter was placed in the equatorial plane of the tokamak and measured the profile in the horizontal direction, we reduced the data to the same (horizontal) direction by using the known value of plasma elongation, which was equal to 1.5. It can easily be shown that, for a large class of profiles of the form $n(r) = n(0)(1 - r^2/a^2)^\alpha$, where α is the parabola exponent ($0.8 < \alpha < 3$), the line-averaged density $\langle nl \rangle$ along the 36-cm vertical chord differs from that along the 42-cm chord by a factor of no more than 1.04–1.10. Assuming this factor to be equal to 1.07 and taking into account plasma elongation, we arrive at the result shown in Fig. 6d: the average density esti-

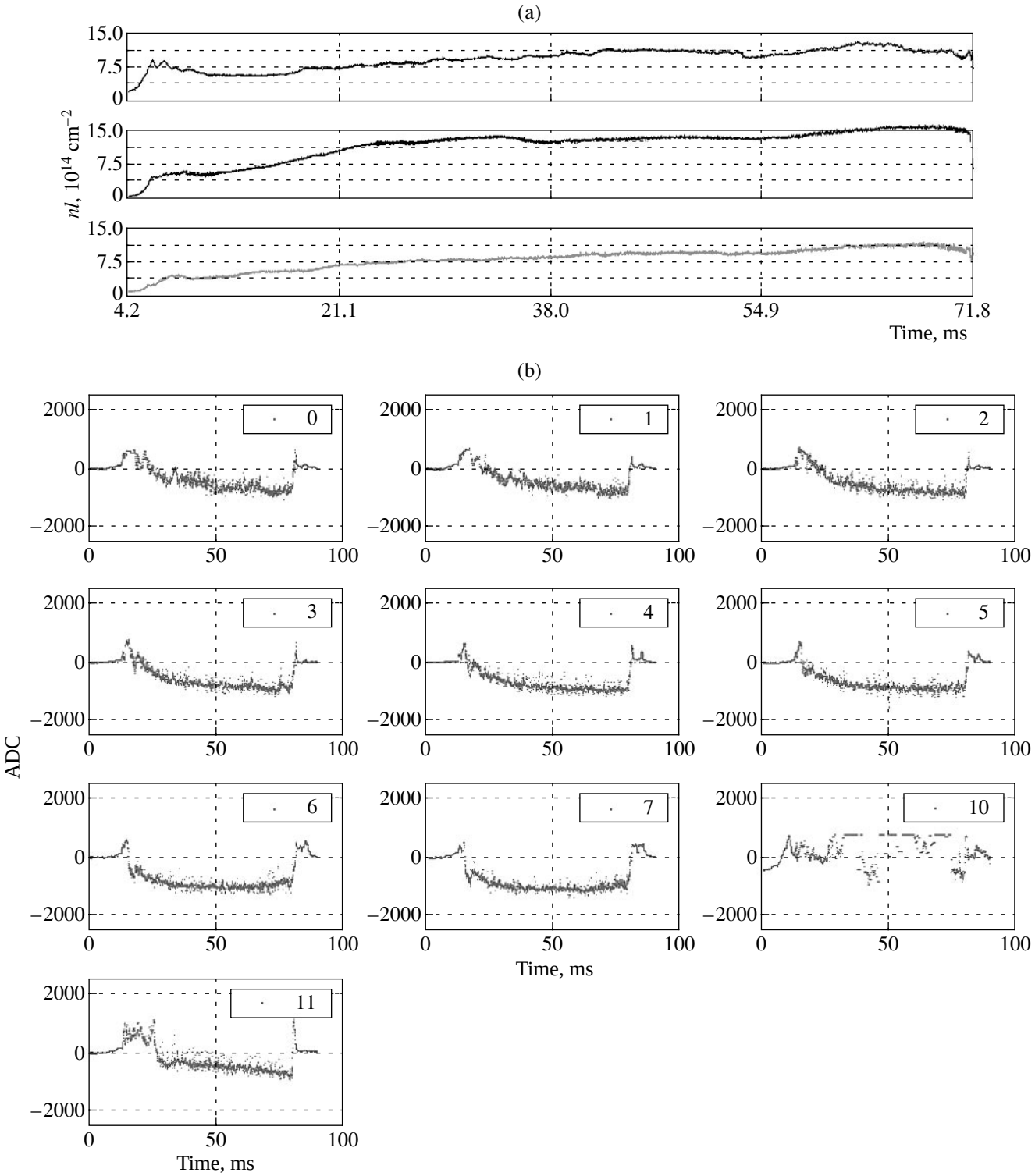

Fig. 6. (a) Average-density signals from a 1-mm microwave interferometer, (b) raw radar signals, (c) evolution of the density profile, and (d) comparison of the average densities $\langle nl \rangle$ obtained from the radar and interferometer data for shot no. 02201747/5125.

mated from the radar data agrees fairly well with the data obtained from the +42-cm interferometer channel. It can be seen from Fig. 6b that the tenth (60.5-GHz) frequency channel operated in the transmission regime; i.e., the central plasma density was below 0.445×10^{14} cm^{-3}. On the other hand, the 51.5-GHz frequency channel, corresponding to a critical density of 0.33×10^{14} cm^{-3}, operated in the reflection regime with a large

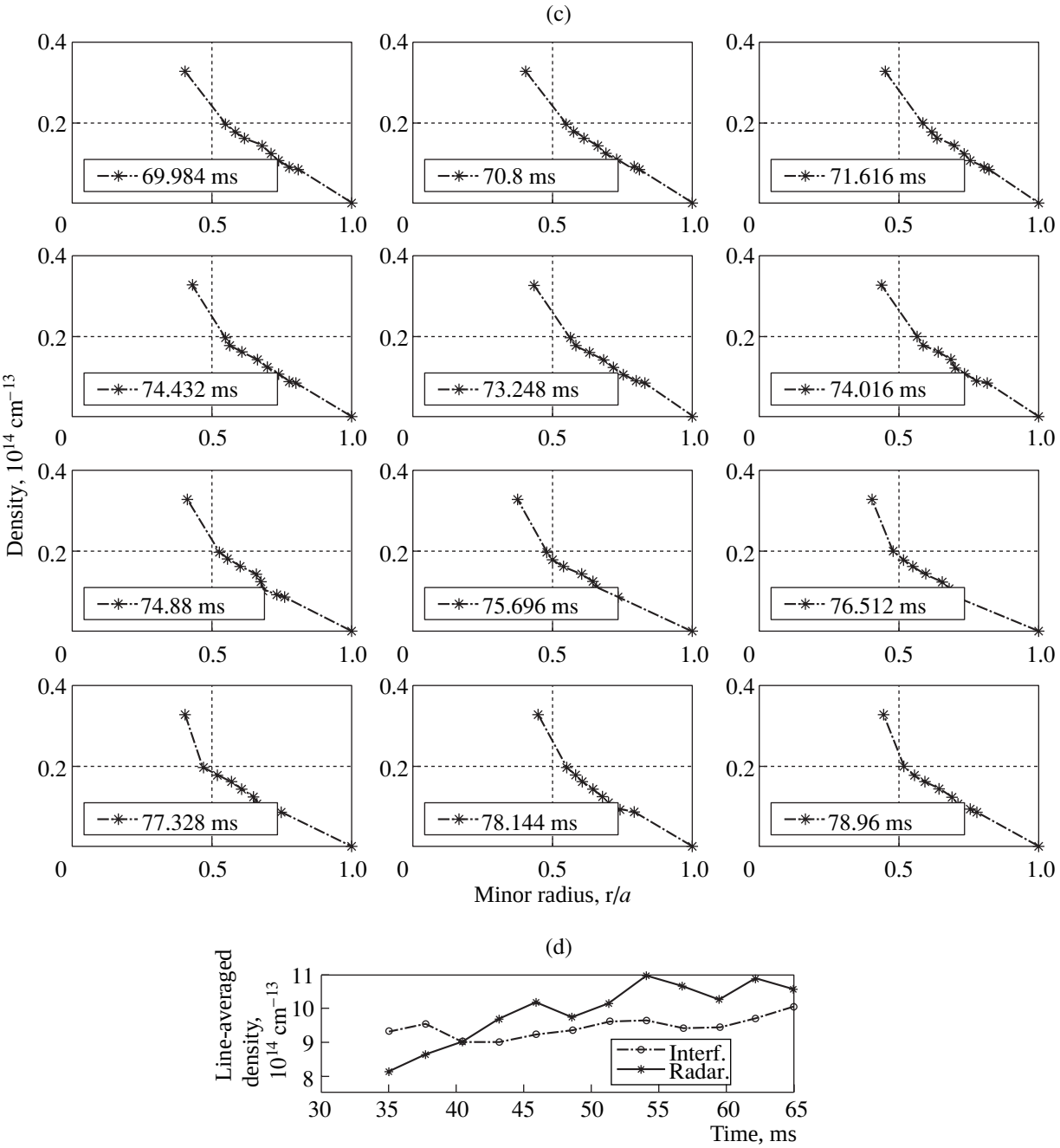

Fig. 6. (Contd.)

margin. For this reason, when estimating the integral from the radar data, the central plasma density was set equal to 0.4×10^{14} cm^{-3} (which is nearly the half-sum of 0.33 and 0.445). It can be seen that, in this case, the error introduced in the line-averaged density does not exceed 10–15%.

4. CONCLUSIONS

A sweeping pulsed radar reflectometer for measuring the electron density profile in magnetic confinement devices has been designed. The instrument combines the advantages of sweeping phase reflectometers and multichannel time-of-flight pulsed reflectometers. The reflectometer allows detailed measurements of the electron density profile in the density range from 4.7×10^{12} to 4.5×10^{13} cm^{-3} with a time resolution of ~16 μs. This can be useful, in particular, in studying the processes related to the formation of an internal transport barrier in plasma.

The first measurements of an electron density profile have been carried out using this reflectometer in the

Globus-M spherical tokamak. The data obtained agree well with those from microwave interferometry.

In future, we plan to use the data from an interferometer and a time-of-flight refractometer [10] to determine the evolution of the entire density profile (over the entire plasma cross section) from the data obtained using the sweeping time-of-flight reflectometer. In addition, the data from the two lowest frequency channels can be used to determine the density gradient in the edge plasma and the position of the plasma boundary. The next step is to use the reflectometer data to study the behavior of the density fluctuations $\delta n/n$ during a discharge in the Globus-M tokamak.

ACKNOWLEDGMENTS

We thank V.A. Yagnov for his assistance in carrying out this work and V.V. Bulanin for fruitful discussions. This work was supported by the International Science and Technology Center (project no. 1126).

REFERENCES

1. M. E. Manso, Plasma Phys. Controlled Fusion **35**, B141 (1993).
2. V. E. Golant, *Fundamentals of Plasma Physics*, Ed. by A. A. Galeev and R. M. Sudan (Énergoatomizdat, Moscow, 1984; Wiley, New York, 1980), Vol. 2.
3. V. L. Ginzburg, *The Propagation of Electromagnetic Waves in Plasmas* (Nauka, Moscow, 1967; Pergamon, Oxford, 1970).
4. V. Shevchenko and M. J. Walsh, Rev. Sci. Instrum. **68**, 2040 (1997).
5. E. Mazzucato and R. Nazikian, Plasma Phys. Controlled Fusion **33**, 261 (1991).
6. E. Mazzucato, Phys. Fluids B **4**, 3460 (1992).
7. J. Sanchez, B. Branas, T. Estrada, *et al.*, Rev. Sci. Instrum. **63**, 4654 (1992).
8. V. F. Shevchenko, A. A. Petrov, and V. G. Petrov, Int. J. Infrared Millim. Waves **14**, 1755 (1993).
9. V. F. Shevchenko, A. A. Petrov, V. G. Petrov, and Yu. A. Chaplygin, Fiz. Plazmy **20**, 33 (1994) [Plasma Phys. Rep. **20**, 27 (1994)].
10. A. A. Petrov, V. G. Petrov, A. Yu. Malyshev, *et al.*, Fiz. Plazmy **28**, 877 (2002) [Plasma Phys. Rep. **28**, 806 (2002)].
11. V. G. Petrov, A. A. Petrov, A. Yu. Malyshev, *et al.*, Prib. Tekh. Éksp., No. 4, 91 (2003).

Translated by N.F. Larionova

Plasma Physics Reports, Vol. 30, No. 5, 2004, pp. 432–436. Translated from Fizika Plazmy, Vol. 30, No. 5, 2004, pp. 469–474.

PLASMA DIAGNOSTICS

Laser Spectroscopy Measurements of the Effective Temperature of Argon Ions in the PNX-U Plasma Neutralizer

I. V. Moskalenko, N. A. Molodtsov, V. A. Zhil'tsov, A. A. Skovoroda, and D. A. Shcheglov

Nuclear Fusion Institute, Russian Research Centre Kurchatov Institute, pl. Kurchatova 1, Moscow, 123182 Russia

Received May 13, 2003; in final form, July 7, 2003

Abstract—Laser spectroscopy measurements of the effective temperature of Ar^{1+} ions in the PNX-U multipole trap, in which argon plasma is ionized and heated by microwaves under electron-cyclotron-resonance conditions, are performed using a narrow-band tunable dye laser. The absorption profile of the 611.5-nm line is examined. In a microwave power range of 5–50 kW, the observed behavior of the effective temperature of argon ions $T_{i,\,\mathrm{eff}}$ indicates an anomalous mechanism for ion heating. It is shown that certain information about the electron temperature can be deduced from measurements by the laser-induced fluorescence (LIF) technique. The measurements performed also serve to test the laser technique and apparatus that is presently being developed for diagnosing additives to the ITER divertor plasma by the LIF method. © *2004 MAIK "Nauka/Interperiodica".*

1. INTRODUCTION

The PNX-U plasma neutralizer was built at the Russian Research Center Kurchatov Institute within the framework of the research program for studying systems for the NBI heating of plasma in the ITER tokamak reactor. The use of plasma instead of gas for neutralizing megaelectronvolt beams of negative hydrogen ions makes possible a radical improvement of the energy characteristics of the injection system. This, however, requires that the power necessary to sustain plasma in the neutralizer be sufficiently low. To enable continuous production of a low-temperature highly ionized dense plasma in large volumes at low energy expenditure, we used a microwave electron-cyclotron-resonance (ECR) discharge in a multicusp magnetic confinement system with a peripheral magnetic field (a "magnetic wall"). The design and technical characteristics of the device, the magnetic field configuration, and the method for igniting discharges are described in detail in [1–3].

The plasma parameters in the PNX-U neutralizer are as follows: the working gas is argon at a pressure lower than 10^{-2} Pa; the plasma density is $\sim 10^{18}$ m^{-3}; the electron temperature varies from 5–10 eV in the middle of the device to 20–30 eV at the periphery (in the ECR region); the energy spread of the ions escaping from the system along the field lines is ~5 eV; and the plasma potential is positive and increases toward the periphery, reaching a maximum value of 50 V in the ECR region. Thus, the conditions are present for the electrostatic confinement of ions in the central region of the PNX-U neutralizer. High radiative losses [1–3] somewhat decrease the electron temperature and, consequently, the potential in the central region. The above parameters were deduced mainly from probe measurements that were performed at a relatively low microwave power and a frequency of 7 GHz. To measure the parameters of argon plasma at a high microwave power (~50 kW), we employed the laser spectroscopy technique.

Laser spectroscopy is also considered to be a promising diagnostics for ITER. The laser-induced fluorescence (LIF) technique is primarily intended to measure the density and temperature of helium and injected impurities (Ne, Ar, and Kr) in the divertor plasma [4]. The injection of inert gases is required to reduce thermal loads on the most heavily stressed elements of the vacuum vessel by spatially equalizing the distribution of the loss power by transforming it into the line emission of the impurities (e.g., argon) [5]. The program for creating ITER diagnostics requires proof-of-principle tests of the developed apparatus in existing devices with allowance for the particular requirements of ITER diagnostics. The experiments performed in the PNX-U device allowed us to resolve some of the above problems.

2. LIF DIAGNOSTICS IN PNX-U

The mounting of the LIF diagnostics in the PNX-U facility required a significant modification in the vacuum chamber. In particular, three branch pipes with quartz windows for the radiation input/output and a light trap at the output of laser radiation were installed.

2.1. Scheme of the Experiment

The arrangement of the LIF diagnostics is shown in Fig. 1. Figures 1 and 2 show the positions of the magnetic coils with an inner diameter of 0.6 m and the

1063-780X/04/3005-0432$26.00 © 2004 MAIK "Nauka/Interperiodica"

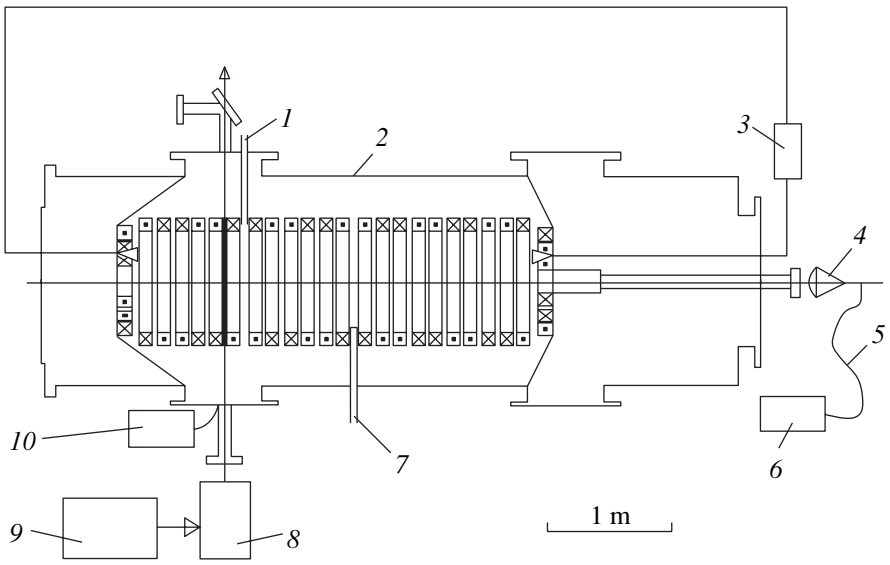

Fig. 1. Arrangement of the diagnostic apparatus in the PNX-U facility: (*1*, *7*) microwave power inputs, (*2*) vacuum chamber, (*3*) 4-mm interferometer, (*4*) lens, (*5*) optical fiber, (*6*) monitoring spectrometer, (*8*) dye laser, (*9*) excimer laser, and (*10*) LIF spectrometer.

directions along which the laser beam was input in the system and the fluorescence radiation was output from it. The main measurements were performed in the central region of the plasma (at $R < R_0/2$, where R_0 = 30 cm), where the magnetic field was relatively low. It is this plasma region that is used for ion beam neutralization.

The probing dye-laser beam passed through the plasma axis in a horizontal direction. The dye laser was optically pumped by a XeCl excimer laser with a pulse repetition rate of 100 Hz. The induced fluorescence radiation was collected by lens *2* (see Fig. 2), which was a part of an optomechanical unit. The unit allowed one to scan the absorption line and to focus the LIF radiation onto the input end of an optical fiber, the output of which was connected to the entrance slit of an MDR-23 monochromator. The spatial resolution along and across the laser beam was 4 and 0.3 cm, respectively.

The spectral width of the probing dye-laser beam was $\delta\lambda_L \approx 3.6$ pm. The profile of the absorption line was measured point-by-point by tuning the laser wavelength and gathering statistics at each λ_L value. The spectral region containing the fluorescence line was separated by a monochromator. An FEU-84-5 or a Hamamatsu R562 photomultiplier served as photodetector *5*. The signals from the photomultiplier were recorded using a system consisting of an S8-14 oscilloscope, a video camera, and a PC. LIF measurements require the careful monitoring of the discharge parameters. In these experiments, we monitored the electron density $N_e(t)$ using a 4-mm interferometer and the optical line intensities using the emission spectroscopy diagnostics with an auxiliary spectrometer.

2.2. Specific Features of the LIF Measurements in the PNX-U Facility

The measurements were performed by a three-level spectroscopic scheme with a common upper level (see Fig. 3). Optical pumping from the $3d'\ ^2G_{9/2}$ metastable

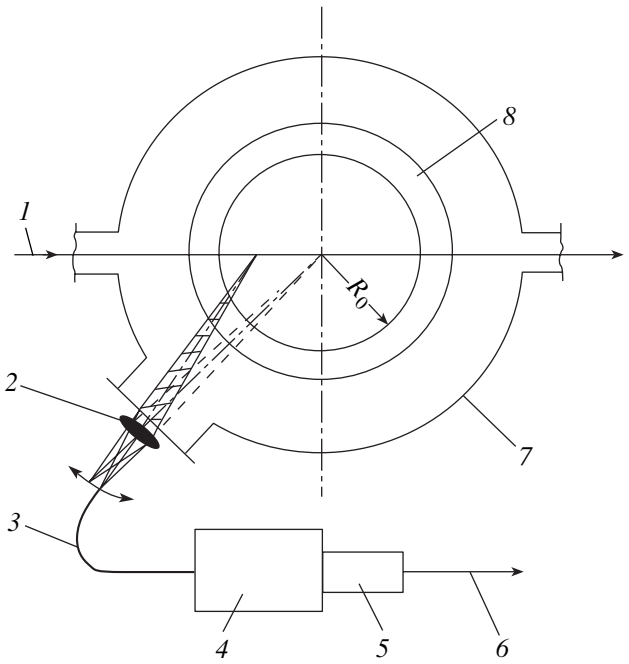

Fig. 2. Arrangement of the LIF diagnostics in the transverse cross section of the PNX-U facility: (*1*) laser beam, (*2*) lens, (*3*) optical fiber, (*4*) MDR-23 monochromator, (*5*) photomultiplier, (*6*) to the system for recording photomultiplier signals, (*7*) vacuum chamber, and (*8*) magnetic coil.

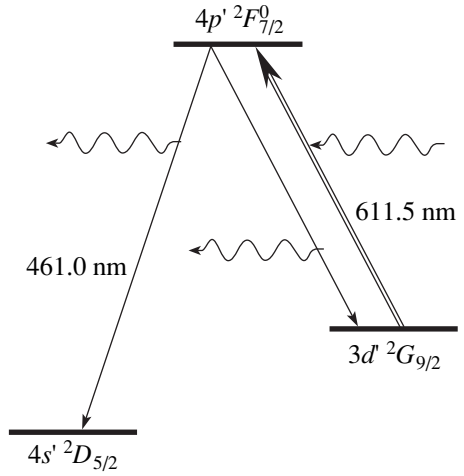

Fig. 3. Diagram of the Ar^+ ion levels involved in the LIF measurements: the 611.5-nm is used for optical pumping, while the 461.0-nm line is used for LIF measurements.

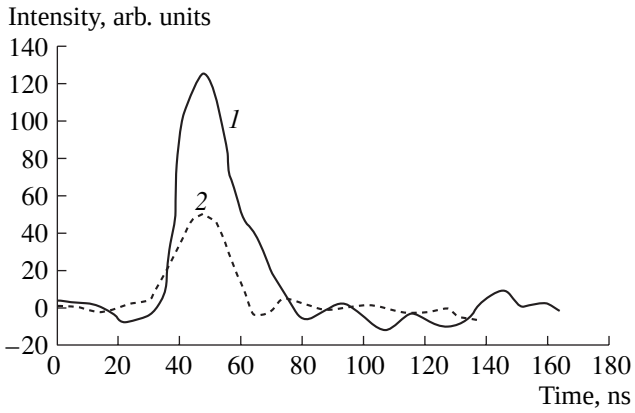

Fig. 4. LIF signals at the Ar^+ 461-nm line for (*1*) R = 14.6 cm and P_{mw} = 12.8 kW and (*2*) R = 0 and P_{mw} = 12.7 kW.

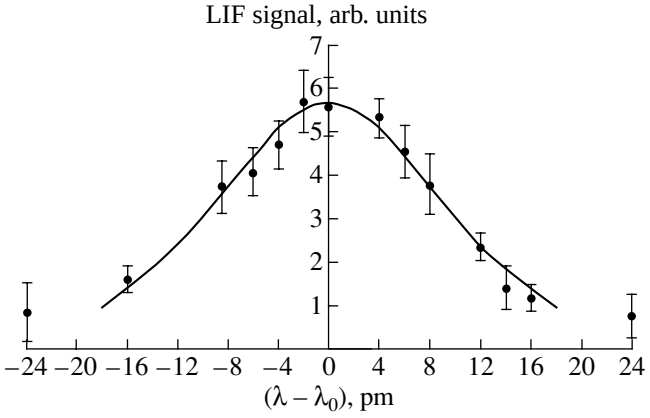

Fig. 5. Measured profile of the Ar^+ 611.5-nm absorption line for R = 0 cm and P_{mw} = 12.7 kW.

level was produced at a wavelength of λ_L = 611.5 nm. The fluorescence signals were monitored at a wavelength of $\lambda_{FLU} \approx 461$ nm. An advantage of this scheme was that the λ_{FLU} line was detuned from the lasing line λ_L. This allowed us to avoid the parasitic effect of radiation scattered by the facility components and the elements of the optical tract.

To correctly estimate the effective ion temperature, which characterizes the ion distribution over velocities, it is necessary to take into account the line-broadening mechanisms other than the Doppler mechanism. Let us consider these mechanisms under the PNX-U conditions.

We note that the measured $T_{i,\,eff}$ values lie mainly within the 6- to 10-eV range, which corresponds to a Doppler broadening $\Delta\lambda_D$ of 18.3 to 23.6 pm. The natural line bandwidth (~0.1 pm) and the Stark broadening of isolated Ar^{1+} lines at an electron density of $N_e < 10^{18}$ m^{-3} are negligibly small [6]. The PNX-U magnetic field decreases sharply toward the plasma axis and does not exceed 0.025 T in the region under study. Simulations of the corresponding Zeeman splitting show that the group width of the π components is also negligibly small (~0.1 pm). Since ^{40}Ar is overwhelmingly dominant among the three argon isotopes ^{36}Ar, ^{38}Ar, and ^{40}Ar (the fraction of the latter is 99.6% [7]), the isotopic shift can also be ignored. Moreover, these isotopes have even–even nuclei; hence, the line under study has no hyperfine structure.

A correction should certainly be made for the instrumental broadening caused by the finite spectral width of the dye-laser line. In our experiments, a Lorentzian profile with a half-width of $\delta\lambda_D \sim 3.6$ pm was taken as an instrumental function. In this case, the measured profile is a convolution of a Gaussian and a Lorentzian profile (a so-called Voigt profile [8]). Table 6.5 in [8] allows one to estimate the half-width of the Doppler profile $\Delta\lambda_D$ using the known half-widths of the Lorentz and Voigt profiles. The obtained $\Delta\lambda_D$ value was used to calculate $T_{i,\,eff}(R, t, P_{mw})$. However, when using a laser as a high-resolution spectral device, one should also take into account so-called "saturation broadening" [9]. At high laser powers, the absorption of photons from the laser-line wings located relatively far from the line center contributes significantly to the formation of the absorption line profile. To avoid this effect, the power of the probing laser was reduced by attenuating the power of the pumping excimer laser with a set of neutral filters.

Thus, the analysis performed shows that, under the PNX-U conditions, a number of the well-known broadening mechanisms can be ignored and the effective argon-ion temperature can be calculated by the formula $T_{i,\,eff} = 1.68 \times 10^8\ (\Delta\lambda_D/\lambda_0)^2 A$, where A is the ion mass in atomic units and $T_{i,\,eff}$ is in electronvolts.

3. MEASUREMENT RESULTS

Figure 4 shows typical waveforms of the fluorescence signals. The absorption line profiles $I_{EXP}(\Delta\lambda)$, where $\Delta\lambda = \lambda - \lambda_0$, were measured by the above scheme at different instants t, different spatial points, and different values of the input microwave power. An example of the line profile measured at the axis of the plasma column is shown in Fig. 5. After introducing corrections for the instrumental function, the line is described by a Doppler profile, which points to a Maxwellian distribution of ions in the plasma core.

At the plasma periphery, the situation is quite different. Figure 6 shows the radial profiles of the effective ion temperature measured at different microwave powers. It can be seen that, in the central region of the plasma, the ion temperature depends slightly on the microwave power and radius. However, as the plasma periphery is approached, the average ion energy increases appreciably and the absorption line profile is deformed. When the effective ion temperature is significantly lower than the radial variations in the plasma potential, such behavior can be attributed to the ion acceleration in this potential.

Additional confirmation of such acceleration is the weak dependence of $T_{i,\,\mathrm{eff}}$ on time (see Fig. 7). The point close to the instant $t = 0$ deserves special attention. A detailed study of this stage of a discharge showed that a power one order of magnitude higher than that transferred to Ar^+ ions via electron–ion collisions is required to heat the ions to the observed temperature. Actually, the ions acquire energy in a potential field that is very rapidly established in the plasma.

We note that the results of the LIF measurements can be used to derive information about the radial profile of the electron temperature in the PNX-U facility. It can be seen from Fig. 4 that the amplitude of the fluorescence signal increases with R. A collisional-radiative model developed for calculating the populations of the excited levels of Ar^+ ion predicts that, for electron densities of $N_e < 10^{18}$ m^{-3}, typical of the PNX-U facility, the population ratio between the metastable level and the ground level, $N_{\mathrm{meta}}/N_{\mathrm{ground}}$, does not depend on N_e and is a function of the electron temperature only (see Fig. 8). The data obtained using emission spectroscopy and probe measurements show that, in the region $R < R_0/2$, in which LIF measurements were performed, the radial profile of the Ar^+ ion density is flat. Therefore, if the electron temperature is measured (or estimated) independently at some point of the region under study, then the temperature at any other point can be estimated using the ratios between signal amplitudes, such as those shown in Fig. 4 (taking into account the correction for the width of the absorption line profile if necessary).

It can be seen from Fig. 5 that, in the center of the PNX-U facility, the ions obey a Maxwellian distribution. Hence, under our experimental conditions, when

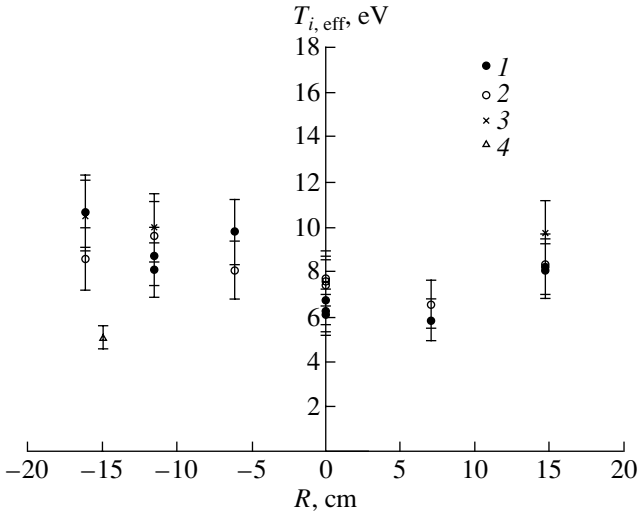

Fig. 6. Radial profile of $T_{i,\,\mathrm{eff}}$ for different heating powers: P_{mw} = (*1*) 11, (*2*) 19, (*3*) 37, and (*4*) 6 kW.

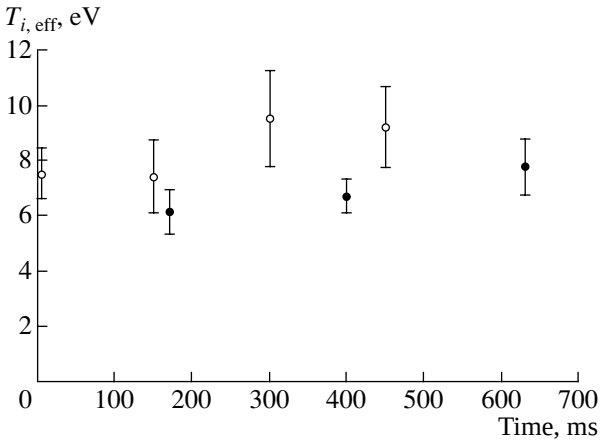

Fig. 7. Evolution of the effective temperature of Ar^+ ions at $R = 0$ for $P_{\mathrm{mw}} \approx$ (open circle) 21 and (closed circle) 12.7 kW.

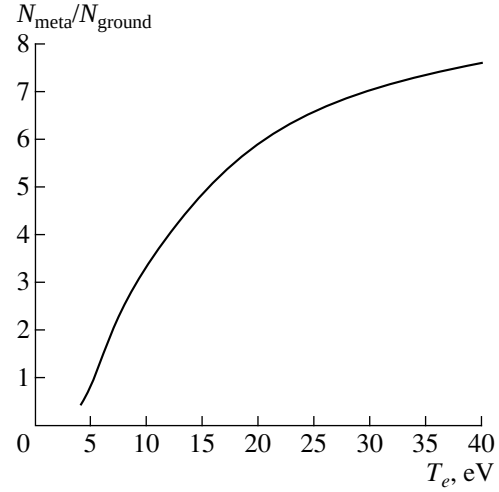

Fig. 8. Calculated relative population of the $3d'\,{}^2G_{9/2}$ metastable level of an Ar^+ ion vs. electron temperature.

Requirements to LIF measurements in ITER and the results obtained in the PNX-U facility

	Measured parameter	Parameter range	Spatial resolution	Accuracy
ITER	$T_{i,a}$	0.3–200 eV	10 cm along the divertor "leg" and 3 mm across the "leg"	20%
PNX-U	$T_{i,\,\mathrm{eff}}\,(Ar^+)$	4–25 eV (experiment)	$\Delta l_{\parallel} = 4$–5 cm, $\Delta l_{\perp} < 3$ mm	≈10–20% in different discharges

the ion confinement time is longer than the time required for equalizing the electron and ion temperatures, the central electron temperature can be estimated using the ion temperature determined from the LIF measurements. Under these conditions, the radial profile of the electron temperature obtained from the ratio of the fluorescence signals turns out to be close to that obtained from probe measurements.

4. CONCLUSIONS

Laser spectroscopy measurements of the effective temperature of Ar^+ ions (in combination with microwave interferometry and emission spectroscopy) have shown that the experimental data obtained in the PNX-U device can be explained in terms of specific acceleration mechanisms for heating argon ions in self-consistent electric fields.

Under certain conditions, the LIF technique makes it possible to determine the spatial distribution of the electron temperature.

The table compares the main requirements for the LIF diagnostics of the divertor plasma parameters in ITER and the experimental results obtained in the PNX-U neutralizer with a prototype laser radiation source that is part of the LIF system developed for ITER.

The PNX-U measurements were performed using the 611.5-nm absorption line of argon ions (an atomic mass of $A = 40$). When recalculated for helium (for the same value of $\Delta\lambda_D$ and the 587.6-nm absorption line), these data give an equivalent helium ion temperature of $T_{i,\,\mathrm{He}} \sim 0.5$–2.7 eV, which approximately corresponds to the lower helium ion temperature required for diagnosing the divertor plasma in ITER. Thus, the experiments performed in the PNX-U device have demonstrated the applicability of this diagnostics to the ITER plasma.

ACKNOWLEDGMENTS

This study was supported by the Department of Atomic Science and Technology of the Ministry of Atomic Energy of the Russian Federation, contract no. 870.

REFERENCES

1. V. A. Zhil'tsov, E. Yu. Klimenko, P. M. Kosarev, *et al.*, Nucl. Fusion **40**, 509 (2000).
2. V. M. Kulygin, E. D. Dlougach, E. P. Gorbunov, *et al.*, Nucl. Fusion **41**, 355 (2001).
3. A. A. Skovoroda and V. A. Zhil'tsov, Plasma Phys. Controlled Fusion **43**, 929 (2001).
4. A. J. H. Donne, O. I. Buzhinskij, A. E. Costley, *et al.*, in *Proceedings of the 10th International Conference on Laser-Aided Plasma Diagnostics, Fukuoka, 2001*, p. 389.
5. R. Jaspers, E. Busche, T. Krakor, and B. Unterberg, in *Proceedings of the 24th EPS Conference on Plasma Physics and Controlled Fusion, Berchtesgaden, 1997*; ECA **21A**, 1713 (1997).
6. H. R. Griem, *Spectral Line Broadening by Plasmas* (Academic Press, New York, 1974; Mir, Moscow, 1978).
7. A. A. Radtsig and B. M. Smirnov, *Reference Data on Atoms, Molecules, and Ions* (Atomizdat, Moscow, 1980; Springer-Verlag, Berlin, 1985).
8. W. Wiese, in *Plasma Diagnostic Techniques*, Ed. by R. H. Huddlestone and S. L. Leonard (Academic Press, New York, 1965; Mir, Moscow, 1967), Chap. 6.
9. W. Demtröder, *Laser Spectroscopy: Basic Concepts and Instrumentation* (Springer-Verlag, New York, 1981; Nauka, Moscow, 1985).

Translated by N.N. Ustinovskiĭ

Plasma Physics Reports, Vol. 30, No. 5, 2004, pp. 437–441. Translated from Fizika Plazmy, Vol. 30, No. 5, 2004, pp. 475–480.

LOW-TEMPERATURE PLASMA

Characteristics of a Transverse RF Discharge in Xe/Cl_2 Mixtures

A. K. Shuaibov, A. I. Dashchenko, and I. V. Shevera

Uzhgorod National University, vul. Pidgirna 46, Uzhgorod, 88000 Ukraine

Received April 23, 2003; in final form, October 1, 2003

Abstract—Results are presented from the study of the electrical and optical characteristics of a transverse RF discharge in Xe/Cl_2 mixtures at pressures of $p \le 400$ Pa. The working mixture was excited by a modulated RF discharge ($f = 1.76$ MHz) with a transverse electrode configuration ($L \le 17$ cm). The emission spectrum in the spectral range of 210–600 nm and the waveforms of the discharge current, discharge voltage, and plasma emission intensity were investigated. The UV emission power from the discharge was studied as a function of the pressure and composition of a Xe/Cl_2 mixture. It is shown that a discharge in a xenon–chlorine mixture acts as a planar excimer–halogen lamp operating in the spectral range of 220–450 nm, which contains a system of overlapping XeCl(*D*, *B*–*X*; *B*, *C*–*A*) and Cl_2(*D*'–*A*') bands. Transverse RF discharges in Xe/Cl_2 mixtures can be used to create a wideband lamp with two 50-cm^2 planar apertures and the low circulation rate of the working mixture.

1. INTRODUCTION

At present, high-power sources of spontaneous UV emission from noble gas monohalogenides and molecular halogens are widely used in microelectronics, photochemistry, and medicine [1, 2]. In these sources, the active medium is usually produced by a dc glow discharge [3–5] or a high-voltage repetitive dielectric barrier discharge [6, 7]. The discharges are ignited in cylindrical quartz tubes of different lengths and diameters; hence, the emitting apertures of such lamps are cylindrical in shape. To uniformly illuminate a large-area flat surface, it is reasonable to employ the emission from a low-pressure transverse discharge. To increase the stability and uniformity of the plasma of a moderate-pressure transverse discharge in electronegative gaseous media, it seems more expedient to use RF excitation rather than the excitation by a dc glow discharge [8]. In [9], the results of optimizing the output characteristics of a low-pressure XeCl lamp with a Xe/Cl_2 working mixture excited by a low-current inductive RF discharge were presented. To increase the UV emission power and produce the active medium in a planar moderate-pressure excimer–halogen lamp, the high-current stage of a transverse RF discharge (TRFD) in the mixtures of heavy noble gases with halogen-containing components can be used. At moderate values of the parameter *pd* (where *p* is the gas mixture pressure and *d* is the interelectrode distance), the TRFD plasma consists mainly of electrode sheaths with an emission intensity higher than the emission intensity from the positive column plasma [10, 11]. In this case, both metallic electrodes act as cathodes, whereas the positive column plasma acts as an anode. In [12–14] a fairly high efficiency of He/Cl_2 ($\lambda = 200/257$ nm) and Kr/Cl_2 ($\lambda = 200/222/257$ nm) excimer–halogen lamps operating with the plasma of a negative cathode glow of a cage dc discharge was demonstrated. Hence, in such lamps, it seems promising to use the extended plasma of the electrode sheaths of a TRFD in the mixtures of noble and halogen-containing gases. Data on the conditions for the production of excimer molecules in this type of discharge are still lacking.

This paper is devoted to studying the characteristics of a transverse RF discharge in xenon–chlorine mixtures.

2. EXPERIMENTAL SETUP

A schematic of the experimental setup for studying an excimer–halogen lamp with planar aperture is similar to that described in [5]. The optical characteristics of the TRFD plasma were studied in the 210- to 600-nm spectral range using an MDR-2 monochromator and a FEU-106 photomultiplier. We monitored the waveforms of the discharge voltage, the discharge current, and the total UV emission power ($\Delta\lambda = 310$–230 nm) from the side apertures of a transverse discharge. The vertical cross section of the electrode system and plasma is shown in Fig. 1. Depending on the pressure and composition of a Xe/Cl_2 mixture, the electrode sheaths of a TRFD occupied from 50 to 70% of the total plasma volume. The RF discharge was ignited in a $17 \times 3 \times 2.2$-cm^3 volume (here, $d = 2.2$ cm is the interelectrode distance). The electrode system consisted of a flat nickel electrode and a massive 17-cm-long nickel-coated electrode with a radius of curvature of the working surface of 3 cm and a base area of 6×17 cm^2. The electrodes were mounted on a dielectric flange placed in a metal 10-l-volume discharge chamber. When recording emission spectra, the plasma emission from

1063-780X/04/3005-0437$26.00

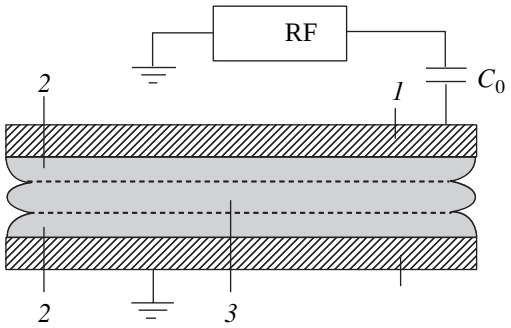

Fig. 1. Schematic of the electrode system and the TRFD plasma: (*1*) transverse discharge electrodes, (*2*) electrode sheath plasma, and (*3*) positive column plasma; RF is the RF power supply and C_0 is the blocking capacitance.

the electrode sheaths at one of the ends of the plasma volume was collected with a quartz lens. A pulsed Foton photomultiplier connected to a C1-99 oscilloscope was set at the other end to monitor the total emission intensity in the spectral range of 210–600 nm. Preliminary studies performed with the use of filters, as well as spectral measurements, showed that the main contribution to the total plasma emission comes from the XeCl(*D*,*B*,*C*–*X*) bands.

The transverse discharge was fed by an amplitude-modulated RF source with an average power of 250 W. The source generated RF voltage pulses with a carrier frequency of $f = 1.76$ MHz, an amplitude of up to 6 kV, and a duration of up to 12 ms. To prevent dc current from flowing through the discharge circuit, the RF voltage was supplied to the discharge gap via a 200-pF blocking capacitance. The discharge voltage and current were measured with a capacitive divider and a low-inductance shunt (r_{sh} = 1–5 Ω), respectively. The total UV emission power from the two working apertures ($S = 2 \times 50$ cm^2) of the lamp was estimated by the method described in [15].

3. ELECTRICAL AND OPTICAL CHARACTERISTICS

The main part of the UV emission spectrum from a TRFD in a Xe/Cl_2 mixture is shown in Fig. 2. Because of the incomplete processes of vibrational relaxation at low total pressures [15, 16], the XeCl(*B*–*X*, *D*–*X*) and Cl_2(*D*'–*A*') bands overlapped and formed a single broad band in the spectral range of 220–310 nm. The main maxima of the XeCl(*B*–*X*) band were found to be shifted to the short-wavelength part of the spectrum and were observed at λ = 306 and 289 nm. They overlapped with less intense Cl_2(*D*'–*A*') 257-nm and XeCl(*D*–*X*) 235-nm bands. As the xenon partial pressure increased from 40 to 400 Pa, the width of the XeCl(*B*–*X*) band decreased, while its intensity increased greatly. In the long-wavelength part of the UV emission spectrum,

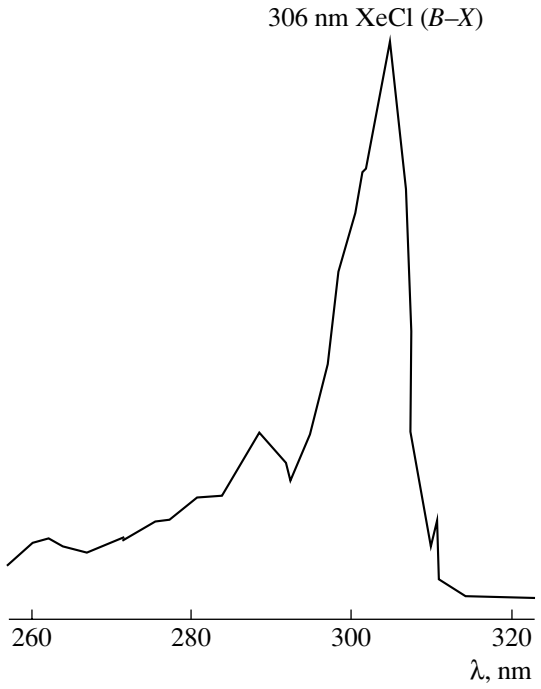

Fig. 2. UV emission spectrum of the discharge plasma in a Xe/Cl_2 mixture with $p(Xe)/p(Cl_2)$ = 40/80 Pa.

there were two broad bands with maxima at λ = 390 and 430 nm. The width of the XeCl(*C*–*A*) 390-nm band was approximately 2.3–3 times the width of the XeCl(*B*–*A*) 430-nm band. The overlapping of all the bands of XeCl and Cl_2 molecules enabled UV emission in the spectral range of 220–450 nm. On the long-wavelength side, the line emission spectrum was dominated by Xe atomic lines. The most intense of these was the XeI (6*s*–7*p*) 467.1-nm line.

Figure 3 shows the waveforms of the RF voltage *U* across the discharge gap, the discharge current *I*, and the plasma emission intensity J_F for the case of a Xe/Cl_2 mixture. The envelopes of *U*, *I*, and J_F, which are determined by the TRFD power supply, are shown in Fig. 4. As the gas pressure increased from 100 to 400 Pa, the amplitude of RF oscillations increased to 5 kV. As the chlorine partial pressure decreased from 160 to 80 Pa, the maximum TRFD current decreased from 1.6 to 0.8 A. The phase shift between the discharge voltage and current increased with the pressure of the Xe/Cl_2 mixture. The maximum half-period of the RF current and voltage was 300–350 ns. The emission intensity from the TRFD plasma consisted mainly of a slowly varying component, which was modulated in amplitude with a frequency twice as high as the pumping RF frequency. At low partial chlorine pressures of $p(Cl_2) \leq$ 80 Pa, the percentage of the slowly varying component in the plasma emission intensity increased from 40–50% at $p(Xe) \leq 80$ Pa to 70–80% at $p(Xe) = 400$ Pa. The maxima of the plasma emission intensity corre-

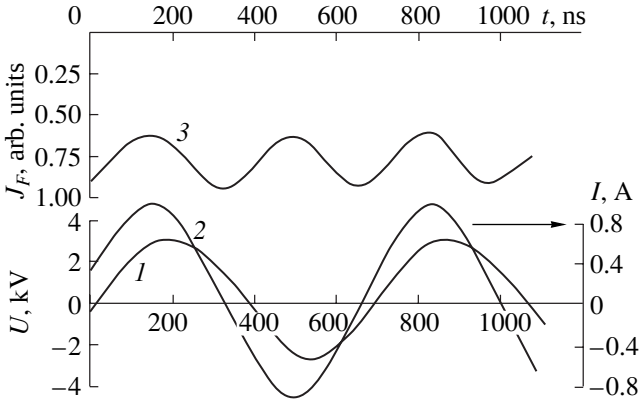

Fig. 3. Waveforms of the (*1*) RF voltage, (*2*) RF current, and (*3*) plasma emission intensity in a Xe/Cl_2 mixture with $p(Xe)/p(Cl_2)$ = 400/80 Pa.

sponded to the ascending and descending segments of the RF component of the discharge current (Fig. 3). The presence of the slowly varying component of the plasma emission intensity, as well as its increase with p(Xe), points to the presence of an efficient channel for the continuous production of XeCl molecules in a TRFD. For a dc glow discharge in low-pressure mixtures of heavy noble gases with chlorine or hydrogen chloride, harpoon reactions such as

$$Xe(6s, 6s') + Cl_2(HCl) \longrightarrow XeCl(A,B,C,D) + Cl(H)$$

prevail in the production of the corresponding excimer molecules [3, 17]. To enable the continuous operation of the harpoon channel for the production of XeCl* molecules, it is necessary to ensure the steady-state density of metastable xenon atoms. This is possible when the density of metastable xenon atoms is maintained at a certain nonzero level, rather than decreasing to zero during the RF pulse.

Let us consider the envelopes of the RF voltage, RF current, and plasma emission intensity in more detail. It can be seen from Fig. 4 that the time evolution of the emission intensity is quite different at the leading and trailing edges of the RF pulse. The dependence of the voltage U at which the plasma emission arises (decays) on the pressure and composition of the Xe/Cl_2 mixture shows hysteresis. The threshold value U at which the plasma emission arises (at the leading edge of the RF pulse, where the gap breakdown occurs) increases from 1 to 2 kV as the xenon partial pressure increases from 80 to 400 Pa (at $p(Cl_2)$ = 80 Pa). For a TRFD in a $p(Xe)/p(Cl_2)$ = 200/160-Pa mixture, the breakdown voltage was 1.5 kV. The maximum duration of the RF

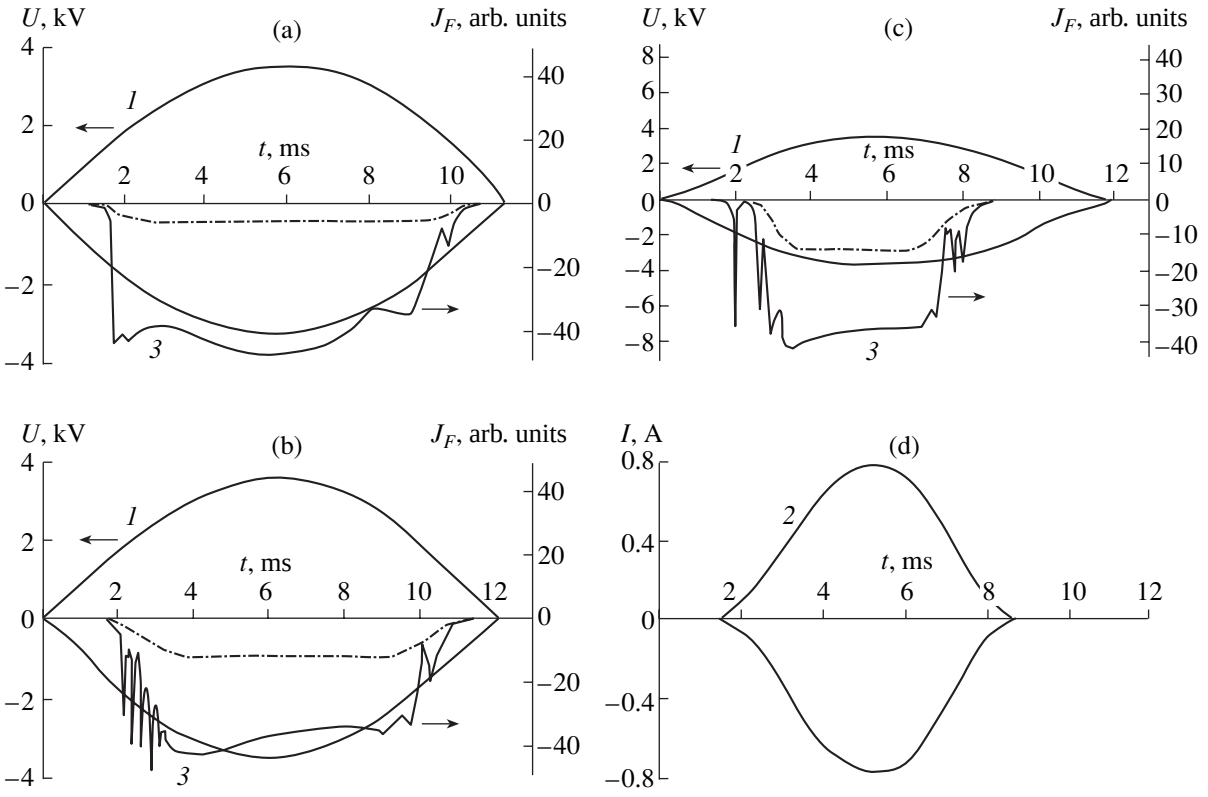

Fig. 4. Envelopes of the (*1*) voltage, (*2*) current, and (*3*) emission intensity from a TRFD in Xe/Cl_2 mixtures with $p(Xe)/p(Cl_2)$ = (a) 80/80, (b) 200/180, and (c) 400/80 Pa. The dashed line shows the slowly varying component of plasma emission.

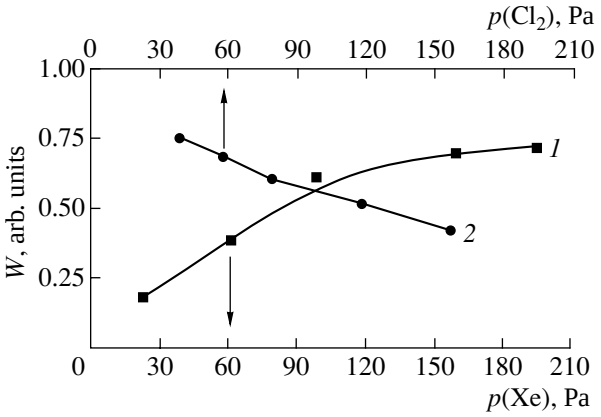

Fig. 5. Average power of the UV emission from a TRFD in Xe/Cl_2 mixtures vs. (*1*) xenon partial pressure at $p(Cl_2)$ = 60 Pa and (*2*) chlorine partial pressure at p(Xe) = 200 Pa.

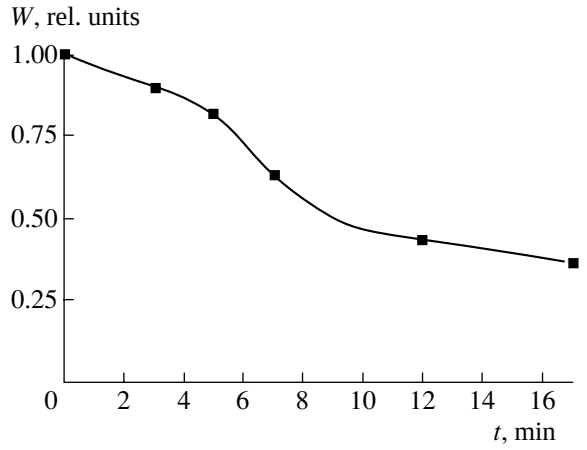

Fig. 6. Average UV emission power from a TRFD in a Xe/Cl_2 mixture with p(Xe)/$p(Cl_2)$ = 200/80 Pa as a function of the continuous operation time on a single gas fill.

current pulse was 7–9 ms (Fig. 4c). It decreased from 9 to 7 ms as the xenon partial pressure increased. At $p(Xe,Cl_2) \geq 80$ Pa, the emission intensity at the leading and trailing edges of the RF pulse had a spiked structure. For a low-pressure discharge (e.g., in a $p(Xe)/p(Cl_2) \leq 80/80$-Pa mixture), this structure was slightly pronounced at the leading edge of the RF pulse, whereas at the trailing edge, there was only one maximum. As p(Xe) increased to 200 Pa, four clearly pronounced narrow maxima arose at the leading edge of the voltage envelope and two broader maxima arose at the trailing edge. As p(Xe) increased to 400 Pa, the sequence of the spikes at the leading edge was no longer equidistant in time (the spikes gathered in two groups, 1 + 3). At pressures of $p(Xe, Cl_2) \geq 80$ Pa, the UV emission intensity slightly decreased with time. At lower pressures, the emission intensity had a broad maximum that corresponded to the maximum of the current envelope. Such behavior of the UV emission power is related to the heating of the moderate-pressure working mixture by the RF component of the discharge current.

It was found in [18] that, in a multicomponent plasma of electronegative gases in a moderate-pressure RF discharge [19], jumps in the densities of electrons and positive and negative ions arise. The jumps occur at the plasma–sheath interface. The jump in the electron density is accompanied by a jump in the density of metastable xenon atoms. This jump, in turn, leads to jumps in the density of excimer molecules and the intensity of its UV emission due to the harpoon reaction between metastable xenon atoms and chlorine molecules. The recombination of positive Xe^+ ions with negative Cl^- ions within the jump region can also lead to the formation of one or two jumps in the density of excimer molecules and corresponding jumps in the plasma emission intensity. This is confirmed by the formation of four short spikes at the leading edge of the emission envelope. After the working mixture is heated by the RF pulse for 5 ms, only the spikes related to XeCl molecules produced in harpoon reactions are present at the trailing edge of the emission intensity envelope, because the rate of ion–ion recombination decreases sharply with increasing temperature [20]. Another explanation for the formation of exactly four spikes at the leading edge of the emission intensity envelope is the participation of all four low-lying 6*s* and 6*s*' excited states of the Xe atoms in the formation of XeCl* molecules. However, this is less probable than the formation of the main maxima of UV emission due to ion–ion recombination before the subsequent RF pulse because the sheath plasma of an RF discharge in an electronegative gas consists mainly of positive and negative ions [18]. More detailed information on the nature of the threshold jumps in the plasma emission intensity and the mechanisms for the production of excimer molecules in a TRFD can be obtained from numerical simulations of TRFDs in Xe/Cl_2 mixtures.

Figure 5 shows the dependences of the average UV emission power from a TRFD on the xenon (at fixed $p(Cl_2)$) and chlorine (at fixed p(Xe)) partial pressures. The UV emission power increases with p(Xe) (up to $p(Xe) \leq 100$ Pa). At higher pressures, this dependence saturates and the transverse discharge terminates. As the chlorine partial pressure increases from 40 to 150 Pa, the UV emission power decreases. In our experiments, the optimum pressure ($p(Cl_2)$ = 30 Pa) was determined by the capability of the gas-mixing system to enable the required accuracy in composing the working gas mixture.

The lifetime of the UV lamp in a static-gas regime did not exceed 10–15 min (Fig. 6); this is related to the significant heating of the gas mixture. To increase the lifetime of the lamp on a single gas fill, it is necessary to use a solid generator of high-purity chlorine, a sys-

tem for regenerating the working mixture, and the forced cooling of the electrode system.

The total UV power emitted from the two side apertures attained 30–40 W. Because of the presence of a significant slowly varying component in the TRFD emission, the specific output characteristics of the lamp under study can be compared to the corresponding characteristics of a XeCl lamp pumped by a dc glow discharge. The UV emission power per unit area of the TRFD working aperture is nearly 1.5–2 times higher than that for a lamp pumped by a glow discharge [21]. For a TRFD, the emission power is up to 300 mW/cm^2, whereas for excimer–halogen lamps pumped by a capacitive discharge, it is no higher than 20 mW/cm^2 [21].

4. CONCLUSIONS

The study of the characteristics of a transverse RF discharge in xenon–chlorine mixtures at moderate pressures has shown that the plasma is a source of broadband emission in the spectral range of 220–450 nm. The main maximum in the emission spectrum corresponds to the XeCl(*B*–*X*) 306-nm band. The plasma emission contains both slowly varying and RF components. As the total pressure of the Xe/Cl_2 mixture increases, the contribution of the RF component to the total plasma emission decreases from 50 to 10%. At voltages close to the threshold voltage, short spikes of plasma emission are observed that are presumably related to the formation of jumps in the densities of positive and negative ions at the plasma–sheath interface and to the recombination mechanism for the production of excimer molecules. The optimum mixtures for achieving the maximum UV emission power are Xe/Cl_2 mixtures with $p(Xe)/p(Cl_2)$ = (200–400)/(30–40) Pa. The discharge under study can be used to create a wideband excimer–halogen lamp with a planar aperture of ≤100-cm^2 area and a reasonable circulation rate of the working mixture. A sealed-off operating mode is feasible given the forced cooling of the electrodes and the regeneration of chlorine in the working volume of the lamp.

REFERENCES

1. U. Kogelschatz, B. Eliasson, and W. Egli, Pure Appl. Chem. **71**, 1819 (1999).
2. E. A. Sosnin, V. N. Batalova, and G. B. Slepchenko, Proc. SPIE **4747**, 352 (2002).
3. A. P. Golovitskiĭ and V. F. Kan, Opt. Spektrosk. **75**, 604 (1993) [Opt. Spectrosc. **75**, 357 (1993)].
4. M. I. Lomaev, A. I. Panchenko, É. I. Sosnin, and V. F. Tarasenko, Zh. Tekh. Fiz. **68** (2), 64 (1998) [Tech. Phys. **43**, 192 (1998)].
5. A. K. Shuaibov, A. I. Dashchenko, and I. V. Shevera, Teplofiz. Vys. Temp. **40**, 337 (2002).
6. I. W. Boyd and J.-Y. Zhang, Mater. Res. Soc. Symp. Proc. **617**, J.4.4.1 (2000).
7. M. I. Lomaev and V. F. Tarasenko, Proc. SPIE **4747**, 390 (2002).
8. Yu. P. Raizer, *Gas Discharge Physics* (Nauka, Moscow, 1987; Springer-Verlag, Berlin, 1991).
9. A. P. Glovitskiĭ, Pis'ma Zh. Tekh. Fiz. **24** (6), 63 (1998) [Tech. Phys. Lett. **24**, 233 (1998)].
10. Yu. P. Raĭzer and M. N. Shneĭder, Fiz. Plazmy **13**, 471 (1987) [Sov. J. Plasma Phys. **13**, 267 (1987)].
11. Yu. P. Raĭzer and M. N. Shneĭder, Fiz. Plazmy **18**, 1476 (1992) [Sov. J. Plasma Phys. **18**, 762 (1992)].
12. A. K. Shuaibov, A. I. Dashchenko, and I. V. Shevera, Ukr. Phys. J. **47**, 346 (2002).
13. A. K. Shuaibov, A. I. Dashchenko, and I. V. Shevera, Pis'ma Zh. Tekh. Fiz. **28** (6), 23 (2002) [Tech. Phys. Lett. **28**, 226 (2002)].
14. A. K. Shuaibov, L. L. Shimon, A. I. Dashchenko, and I. V. Shevera, Ukr. Patent No. 53509A, Byull. No. 1 (January 15, 2003).
15. A. K. Shuaibov, L. L. Shimon, A. I. Dashchenko, and I. V. Shevera, Prib. Tekh. Éksp., No. 1, 104 (2002).
16. V. V. Datsyuk, I. A. Izmaĭlov, and V. A. Kochelap, Usp. Fiz. Nauk **168**, 439 (1998) [Phys. Usp. **41**, 379 (1998)].
17. A. P. Golovitskiĭ and S. V. Lebedev, Opt. Spektrosk. **82**, 251 (1997) [Opt. Spectrosc. **82**, 227 (1997)].
18. I. D. Kaganovich and L. D. Tsendin, Fiz. Plazmy **19**, 1229 (1993) [Plasma Phys. Rep. **19**, 645 (1993)].
19. I. D. Kaganovich, Fiz. Plazmy **21**, 434 (1995) [Plasma Phys. Rep. **21**, 410 (1995)].
20. M. R. Flannery, in *Applied Atomic Collision Physics*, Vol. 3: *Gas Lasers*, Ed. by H. S. W. Massey, B. Bederson, and E. W. McDaniel (Academic, New York, 1982; Mir, Moscow, 1986).
21. Advertising Prospect of the Institute of High-Current Electronics, Siberian Division, Russian Academy of Sciences (Tomsk, 2001).

Translated by N.N. Ustinovskiĭ